NTNU
Norwegian University of
Science and Technology

Earthquake Soil-Structure Interaction Analyses of Offshore Sub-Sea Structures Founded on Closed Caisson Foundations

Sondre Rørvik
Magnus Todnem

Civil and Environmental Engineering
Submission date: June 2018
Supervisor: Gudmund Reidar Eiksund, IBM
Co-supervisor: Erik Sørlie, Multiconsult AS
Espen Aas Smedsrud, Multiconsult AS

Norwegian University of Science and Technology
Department of Civil and Environmental Engineering

NORGES TEKNISK-
NATURVITENSKAPELIGE UNIVERSITET
INSTITUTT FOR BYGG, ANLEGG OG TRANSPORT

Report Title: **Earthquake Soil-Structure Interaction Analyses of Offshore Sub-Sea Structures Founded on Closed Caisson Foundations**	Date: 11.06.2018 Number of pages (incl. appendices): 177			
	Masteroppgave	X	Prosjektoppgave	
Name of students: Sondre Rørvik & Magnus Todnem				
Professor in charge/supervisor: Gudmund Reidar Eiksund				
Other external professional contacts/supervisors: Erik Sørlie & Espen A. Smedsrud				

Abstract:

Regarding the design of offshore foundations subjected to earthquakes, Multiconsult AS have proposed two new design methods, one based on modal analysis and the other on time series analyses where Det Norske Veritas has contributed in the development. The objective of this master thesis is to compare these two methods, as well as investigating kinematic interaction effects, due to site response amplification. A non-linear site response analysis is performed using NERA.

For the time series analyses, the caisson was modelled in ANSYS Mechanical APDL, represented by Timoschenko beam elements supported by springs. These springs were configured to represent the non-linear behaviour of the soil by the use of p-y curves. To achieve an appropriate hysteretic damping, the p-y curves were approximated by a set of four bi-linear springs in parallel.In NERA, input acceleration time series were adjusted for site response effects. These were integrated using the Newmark-Beta method, to find the total displacement time series. Displacement time series were applied at the end of each spring to represent the earthquake.

Time series analyses were performed for three different cases; applying depth variable time series, applying seabed time series and applying time series from 10 meters depth at each spring. The modal analysis was conducted using an in-house program provided by Multiconsult.

When comparing the results from the two proposed methods, the overall highest response was obtained by the modal analysis. Considering the time series analyses, higher accelerations, moments and shear force were seen when applying the seabed time series at each depth. In contrast, the lowest response values were found when using time series from the reference depth of 10 meters at each spring. To summarise, using only seabed time series yielded a higher response, than when embedment effects are considered. Modal analysis gives a conservative response in comparison to the time series analysis.

Keywords:

1. Time Series Analysis
2. Modal Analysis
3. Kinematic Interaction
4. Suction Caisson

Sondre Rørvik Magnus Todnem
(sign.)

NTNU
Faculty of Engineering Science and Technology
Institute of Civil and Environmental Engineering

MASTER DEGREE THESIS

Spring 2018
for

Magnus Todnem & Sondre Rørvik

Earthquake Soil-structure Interaction Analyses of Off-shore, Sub-sea Structures Founded on Closed Caisson Foundations

BACKGROUND

Suction caissons are frequently applied as manifold foundations, due to their practical installation. In earthquake-related design, there is a need for estimating the earthquake loads that the structure and foundation will be subjected to. In design, 3D finite element models are frequently used. Although the results generated are accurate, there is consensus among market operators that the design costs of foundations based on 3D models are too high. Two alternative analysis methods for design are studied in this thesis; (1) a time series analysis for a soil structure interaction model where the soil is represented by discrete springs and (2) a modal analysis where the rocking and translation mode is included. Both analyses cause a significant reduction in computational time. The methods are also simpler, and the number of unknown effects are thus limited. Both methods are developed by Multiconsult AS, where the time series analysis is developed in cooperation with Det Norske Veritas. In this thesis, ANSYS Mechanical APDL is used for the time series analyses. The modal analysis is conducted in an in-house program from Multiconsult AS.

TASK

The purpose of this thesis is to compare two different methods for calculating the earthquake response of a suction anchor with a sub-sea module on top. One specific soil profile and geometry is considered, and four synthetic earthquake accelerograms are used as dynamic input in the time series analyses.

OBJECTIVES

1. Perform a one-dimensional non-linear site response analysis in NERA to calculate the variation of soil response with depth. A unique acceleration time serie for each depth is obtained from the NERA results. The site response analysis is performed for four different earthquakes.
2. Develop a finite element model to be used in the time series analyses. Model the caisson as a beam supported by the soil springs calculated from objective 2. The soil springs shall represent the soil’s stiffness, and dynamic earthquake time series shall be applied at the end of each spring.

3. Modelling a proper hysteretic behavior to get an appropriate hysteretic damping in the soil springs. Different methods for calculating p-y curves should be studied, as well as testing different spring configurations.
4. Observe trends in the structural response parameters such as acceleration, displacement, rotation, moment and shear force. Compare the results of the time series analyses to the simplified modal analysis.

Professor in charge:

Prof. Gudmund Reidar Eiksund

Department of Civil and Transport Engineering, NTNU
Date: 07.06.2018

Gudmund Eiksund
Professor in charge (signature)

Preface

This master's thesis is written in the spring of 2018, over the course of 20 weeks. The thesis serves as a concluding part of the five-year master's programme in Geotechnical Engineering at the Norwegian University of Science and Technology. The work has been conducted as a collaboration between graduate students Sondre Rørvik and Magnus Todnem, and is roughly partitioned as follows:

- 20% literature survey
- 50% FEM modelling and analyses
- 30% report writing

The proposed thesis is given by Multiconsult AS, as a part of their focus on reducing costs in the design of subsea foundations. It combines both geotechnical engineering and structural engineering.

Trondheim, 2018-10-06

Sondre Rørvik Magnus Todnem

Sondre Rørvik Magnus Todnem

Acknowledgment

First of all, we would like to express our sincere gratitude towards our external supervisors, Erik Sørlie and Espen Smedsrud. Thank you for always being available for questions, and for showing a genuine interest in our work.

We are also very thankful for the advice of Dr. Corneliu Athanasiu at Multiconsult. His knowledge within the subjects has been of great importance, as well as his constructive feedback.

We would also like to thank our main supervisor, Gudmund Reidar Eiksund for always being available for questions, and for valuable input on earthquake engineering.

We also want to acknowledge Multiconsult AS for providing us with an initial ANSYS model creating the geometry and mass, as well as lending us their modal analysis prorgram.

The Geotechnical Division, for the excellent studying environment they have created, including welcoming professors, interesting discussions and social gatherings.

Last but not least, we would like to thank each other for the cooperation.

M.T. & S.R.

Summary

One of the most challenging issues in the design of sub-sea structures founded on closed caisson foundations is their structural response to dynamic loading. Currently, the foundation design is mostly based on fully integrated 3D finite element analyses. There is consensus among market operators that such analyses are too expensive. One of the reasons is the considerable computational time and extensive insight needed by the user. This has induced a major interest in developing more cost-efficient methods for design.

Two of the proposed time-efficient design methods are the simplified modal non-linear analysis method and the simplified time series analysis method. The simplified modal non-linear analysis is developed by Multiconsult AS, and the simplified time series analysis is developed by DNV and Multiconsult AS.

A specific case study is performed to compare the simplified modal non-linear analysis and the simplified time series analysis, in addition to investigating kinematic interaction effects. Only one specific geometry and soil profile is considered in the modelling aspect. For the time series analyses, four different earthquake motions were evaluated.

Time series analyses are conducted in ANSYS Mechanical APDL. The model consists of a beam supported by springs with a module on top. A mass-less rigid link element connects the module to the top of the beam which is situated at seabed level. A site response analysis is conducted in NERA for four different earthquakes, to predict the amplification of seismic waves from bedrock. The time series input from NERA was applied in three different ways, resulting in three different analyses; *(1) depth variable time series was applied at each node, (2) the seabed time series was applied at each node and (3) the reference time series from 10 meters depth was applied at each node..*

The soil when subjected to cyclic loading, were represented by four bi-linear springs in parallel, to account for the hysteretic damping in the system. These springs were adjusted to follow p-y curves, representing the backbone curve. The p-y curves were calculated using different methods based on slender piles and were scaled to better approximate the response of a rigid, large-diameter caisson. The scaling was done to fit a representative horizontal capacity plot from Plaxis, provided by Multiconsult.

The modal analysis was performed using an in-house developed tool by Multiconsult. This program is based on the simplified modal non-linear analysis. Masses and moments of inertia were taken directly from the ANSYS model, and used in the modal analysis, to have a better foundation for comparison.

Relevant results include moment, shear force, acceleration, displacement and rotation of the structure at seabed level. The modal analysis yielded the highest response of the two methods for all response parameters. From the time series analyses, the seabed input provided the highest response values regarding moment, shear force and accelerations. Depth variable time series input gave the largest displacement and rotations. Reference time series input gave the lowest response values.

Sammendrag

Vedrørende design av offshore fundamenter utsatt for jordskjelv, har Multiconsult AS utarbeidet to nye alternative designmetoder. Den ene er basert på modal analyse, og den andre er basert på tidsserieanalyser der Det Norske Veritas(DNV) har bidratt i utviklingen. Det overordnede målet til denne masteroppgaven er å sammenligne resultater fra disse metodene, i tillegg til å undersøke hva slags effekt kinematisk interaksjon har på design. En ikke-lineær site respons analyse er utført i NERA, for å gjøre rede for dybdeeffekter.

Tidsserieanalysene ble utført i elementprogrammet ANSYS Mechanical APDL. Sugeankeret ble modellert som en bjelke, representert ved Timoschenko bjelke-elementer, støttet av fjærer. Fjærene simulerte den ikke-lineære stivheten til leiren, som ble beregnet som p-y kurver. For å oppnå en passende hysteretisk dempning ble fire bi-lineære fjærer i parallell satt på ved hver meters dybde langs bjelken. Disse bi-lineære fjærene ble tilpasset til å følge p-y kurvene. I NERA ble akselerasjonstidshistorier for hver dybde funnet. Ved bruk av Newmark Beta-metoden ble akelerasjonstidshistoriene dobbelintegrert for å finne forskyvningstidshistoriene. Disse ble så satt på i enden av hver fjær, og simulerte jordskjelvet.

Tidsserieanalyser ble utført for tre forskjellige tilfeller; *(1) ved å påføre unike dybdevarierende tidshistorier for hver dybde, (2) ved å påføre tidshistorien fra sjøbunn på hver dybde, (3) og ved å påføre tidshistorien fra en referansedybde ved ti meter på hver dybde.* Dette ble gjort for tre ulike jordskjelv. Den modale analysen ble utført i et egetutviklet program av Multiconsult.

Resultatene fra den modale analysen ga de høyeste verdiene for alle relevante responsparametre, sammenlignet mot resultatene fra tidsserieanalysene. Vedrørende resultater fra tidsserieanalysene, ga analysene hvor sjøbunnstishistorier ble benyttet, de høyeste momentene, skjærkreftene og akselerasjonene. I motsetning ga analysene hvor tidsserier fra referansedybdene ble benyttet den laveste responsen. Bruken av sjøbunnstidshistorien på alle dybder ga en høyere respons enn når dybdeeffekter ble tatt med i analysene. Den modale analysen ga svært konservative verdier sammenlignet med tidshistorieanalysene.

Contents

Preface i
Acknowledgment iii
Summary v
Sammendrag vii

Contents **ix**

List of Figures excluding Appendix **xiii**

List of Tables **xix**

1 Introduction **1**
1.1 Background 1
1.2 Approach 3
1.3 Limitations 4
1.4 Structure of the Report 5

2 Literature Survey and Theory **7**
2.1 Introduction 7
2.2 Closed Caisson Foundations 7
2.3 The Winkler Model 8
2.4 Response of Cyclically Loaded Soil 10
  2.4.1 Nonlinear Cyclic Models 11
  2.4.2 Damping of the Foundation Movement 14
2.5 Failure Mechanisms / Ultimate Behaviour of Piles in Cohesive Soils 16
  2.5.1 Conical Wedge Failure 16
  2.5.2 Flow Around Failure 17

2.6 P-Y methods . . . 19

2.6.1 American Petroleum Institute - API RP 2A Recommendation . . . 19

2.6.2 Stevens and Audibert Recommendation . . . 21

2.6.3 Jeanjean Recommendation . . . 23

2.6.4 Comparison of the Lateral Bearing Capacity Factor . . . 24

2.7 PISA Project- Pile Soil Analysis . . . 26

2.8 The Four-spring Winkler Model Proposed by Gerolymos and Gazetas . . . 29

2.9 Wave Propagation . . . 31

2.9.1 1D Longitudinal Waves . . . 32

2.9.2 1D Torsional Waves . . . 33

2.9.3 3D Waves . . . 34

2.9.4 Surface Waves . . . 36

2.9.5 The Effect of Boundaries on Wave Propagation . . . 37

2.9.6 Wave Attenuation . . . 40

2.10 Single Degree of Freedom System (SDOF) . . . 41

2.11 The Response Spectrum . . . 43

2.11.1 Design Spectrum (Target Response Spectra) . . . 44

2.12 Soil-Structure Interaction . . . 45

2.12.1 Kinematic Interaction . . . 45

2.12.2 Inertial Interaction . . . 46

3 Method 47

3.1 Nonlinear Earthquake Site Response Analysis . . . 47

3.1.1 Basic Calculation Process . . . 49

3.1.2 The Nonlinear and Hysteretic Model in NERA . . . 50

3.2 Simplified Time Series Analysis . . . 52

3.3 Simplified Modal Non-linear Analysis . . . 53

4 Evaluation of Input 57

4.1 Caisson and Module Input . . . 57

4.2 Input Time Histories . . . 58

4.3 Soil profile input . . . 60

4.4 Finite Element Model in ANSYS . . . 63

4.4.1 Added Mass 66
4.5 Modelling the Stiffness and Hysteretic Behaviour of the Soil 66
4.5.1 Choice of p-y Method 66
4.5.2 Bi-linear Springs 68
4.6 Input for Modal Analysis 70
4.6.1 Calculation of Reaction Forces 71

5 Results 72
5.1 Site Response Analysis 73
5.1.1 Description of the Results 75
5.2 Modal Analysis 76
5.3 Time Series Analyses 77
5.4 Summary of TSA and Modal Analysis Results 81

6 Discussion 85
6.1 Credibility of the Finite Element Model 85
6.1.1 Sensitivity Analyses 87
6.2 Evaluation of the Results 92
6.2.1 Comparison of Time Series Analyses to Modal Analysis 95

7 Conclusions and Further Work 99
7.1 Summary and Conclusions 99
7.2 Further Work 100

Bibliography 103

APPENDICES 107

List of Figures in Appendices 108

A Input Time Histories 113

B Derivations 115
B.1 Undamped Natural Frequency 115
B.2 Solution of a Free Vibrating Damped SDOF System 116

C Site Response Results **117**
C.1 NERA Results 117

D Results From Time Series Analyses **123**
D.1 Individual Plots 123
D.1.1 EQ 1A 123
D.1.2 EQ 1S 125
D.1.3 EQ 1R 126
D.1.4 EQ 3A 128
D.1.5 EQ 3S 129
D.1.6 EQ 3R 131
D.1.7 EQ 5A 132
D.1.8 EQ 5S 134
D.1.9 EQ 5R 135
D.1.10 EQ 6A 137
D.1.11 EQ 6S 138
D.1.12 EQ 6R 140
D.2 Comparison Plots 142
D.3 Peak value comparisons 149
D.4 Deformed Caisson & Force Diagrams 152
D.5 Hysteresis Plot 153

List of Figures excluding Appendix

2.1 a) Penetration by self weight b) suction installation (Illustrations from Hossain et al., 2012). 8

2.2 The Winkler foundation model (Illustration from Kerr (1964)) 9

2.3 The Winkler foundation model applied to a pile (Illustration from Hanssen (2016)) 10

2.4 Hyperbolic backbone curve, (Illustration from Kramer (1996)). 12

2.5 a) Shear stress versus time. b) Resulting shear stress versus shear strain. (Illustrations from Kramer (1996)) 13

2.6 Lateral soil reaction vs displacement. X-axis shows displacement in meters, Y-axis shows lateral soil reaction in kN/m. (Adapted from Gerolymos and Gazetas, 06c) 13

2.7 a) $\frac{G}{G_{max}}$ vs cyclic shear strain, γ_c. b) Damping ratio vs cyclic shear strain, γ_c. (Illustrations from Vucetic and Dobry (1991)). 15

2.8 Soil failure mechanisms of laterally loaded piles in soft clay (Illustration from Murff and Hamilton (1993)). 16

2.9 Geometry of characteristic stress mesh and deformation mechanism (Illustrations from Randolph M. F & Houlsby (1984)). 17

2.10 Characteristic mesh for $\alpha = 0$ and $\alpha = 1$ (Illustrations from Randolph M. F & Houlsby (1984)). 18

2.11 Variation of limiting pressure and pile surface stress (Illustrations from Randolph M. F & Houlsby (1984)). 18

2.12 Lateal bearing capacity factor, N_p, vs normalized depth(Illustration from Stevens and Audibert (1979)). 22

2.13 Lateral bearing capacity factor, N_p, vs normalised depth z/D, using the proposed methods by API, Jeanjean and the approximated Stevens and Audibert formulation 25

2.14 Proposed 1D finite model for monopile foundations subjected to lateral loading (Illustration by Byrne et al. (2015)). The lateral displacement is denoted v. 27

2.15 **a)** Short pile response in clay **b)** Cumulative breakdown of components for short piles in clay, calculated using the 1D model with numerical soil reaction curves. H is the lateral load applied (Results from Byrne et al., 2015). 28

2.16 a) Stress distribution on caisson from the adjacent soil. b) The nonlinear four spring Winkler model proposed by Gerolymos and Gazetas.(Illustrations from Gerolymos and Gazetas, 06b). 30

2.17 Longitudinal waves in infinitely long bar (Illustration from Kramer (1996)). 32

2.18 Torsional waves in an infinitely long bar (Illustration from Kramer (1996)). 33

2.19 Body wave propagation. (Illustrations from Kramer and Kaynia (2017)) . . 36

2.20 Surface wave propagation. (Illustrations from Kramer and Kaynia (2017)) 37

2.21 Wave propagation at perpendicular boundary. (Illustrations from Kramer and Kaynia (2017)) 37

2.22 Wave propagation at inclined boundary. (Illustrations from Kramer and Kaynia (2017)). 39

2.23 Wave propagation path in multiple layered body (Illustrations from Kramer and Kaynia (2017)). 39

2.24 Thin element of a Kelvin-Voigt soild exposed to horizontal shear stresses (Illustration from Villaverde (2009)). 40

2.25 Relation between damping, ξ, and dissipated energy W_d(Illustration modified from Khari et al. (2011)). 41

2.26 Single degree of freedom system with earthquake motion input. 42

2.27 Construction of a response spectrum (Illustration from QuakeManager). . . 44

2.28 Design spectra by Eurocode 8, for different ground types. 45

2.29 Kinematic interaction (Illustration from Kramer and Kaynia, 2017). 46

3.1 Geometry of a soil layer over rigid rock (Illustration from Kramer and Kaynia (2017)). 48

3.2 Amplification of soil layer at natural frequencies (Illustration from Kramer (1996)). 48

3.3 Simplifying of soil profiles to use in NERA (not actual soil profile). 49

3.4 Brief overview of the one dimensional spatial discretization (Illustration from Bardet and Tobita (2001)). 50

3.5 Representative illustration of stress-strain model used by Iwan (1967) and Mróz (1967). (Illustration from Bardet and Tobita, 2001). 51

3.6 The tangential modulus, H, for n sliders. (Illustration from Bardet and Tobita, 2001). 51

3.7 Left: backbone curve. Right: hysteretic stress strain loop for two sliders. (Illustration from Bardet and Tobita, 2001). 52

3.8 Model used in STSA (Illustration from Athanasiu et al. (2015)). 53

3.9 Structure model (Illustration from (Athanasiu et al., 2015)). 54

4.1 Shear strength versus depth. 60

4.2 Maximum shear modulus, shear velocity and unit weight versus depth. . . 61

4.3 Shear modulus degradation for the upper eight materials, $\frac{G}{G_{eq}}$ vs shear strain, compared to curves found by Vucetic and Dobry (1991). 62

4.4 ANSYS model discretisation. 65

4.5 Horizontal capacity vs lateral displacement. 68

4.6 Multilinear curve fitted to the nonlinear p-y curve at seabed level. 70

4.7 Response spectra input for modal analysis with 5% damping. 71

5.1 Acceleration time series at 0, 10 m, and 17 m for EQ 1. 73

5.2 Shear strain and shear stresses plotted versus the upper 20 meters. 74

5.3 Maximum values of acceleration, relative velocity and relative displacement plotted versus the upper 20 meters. 74

5.4 EQ 1: Total acceleration of structure at seabed level for time series analyses using depth variable time series (A), the seabed time series (S) and the reference depth time series (R). 78

5.5 EQ 1: Total displacement of structure at seabed level for time series analyses using depth variable time series (A), the seabed time series (S) and the reference depth time series (R). 79

5.6 EQ 1: Rotation of structure at seabed level for time series analyses using depth variable time series (A), the seabed time series (S) and the reference depth time series (R). 79

5.7 EQ 1: Moment at seabed level for time series analyses using depth variable time series (A), the seabed time series (S) and the reference depth time series (R). 80

5.8 EQ 1: Shear force at seabed level for time series analyses using depth variable time series (A), the seabed time series (S) and the reference depth time series (R). 80

5.9 Comparison of peak acceleration at seabed for the various time series analyses. Depth variable time series (A), the seabed time series (S) and the reference depth time series (R). 81

5.10 Comparison of average peak results. Depth variable time series (A), the seabed time series (S) and the reference depth time series. 83

6.1 Acceleration at seabed for EQ 3A, EQ 3S, EQ 3R and free-field seabed from 33 seconds to 35 seconds. 86

6.2 Comparison of stiffness configurations. 88

6.3 Hysteretic response of spring configurations, with two different amplitudes. 88

6.4 Initial part of the loading curve. 90

6.5 Response of structure with and without Rayleigh damping. 90

6.6 Response of structure with and without Rayleigh damping for a smaller time interval. 91

6.7 Moment response of rigid beam versus real stiffness. 92

6.8 Simplified hand calculations 94

6.9 Average moment and shear force at seabed. Depth variable time series (A), the seabed time series (S) and the reference depth time series (R). 95

6.10 Three different spring arrangements. 96

6.11 Comparison of the damping ratios from the three different spring configurations to the modal analysis. 97

List of Tables

2.1 API RP 2A - Load-deflection (p-y) curves for soft clay 21

4.1 Dimensions of caisson and module. 57
4.2 Material properties of caisson and soil plug. 57
4.3 Masses and moment of inertia. 58
4.4 Earthquake input data. 59
4.5 Natural periods and frequencies of the five first modes. 61
4.6 ANSYS model data. 64
4.7 Rayleigh damping. 66
4.8 Spring values 69

5.1 Acceleration and displacement results from the modal analysis. 76
5.2 Moment and shear force at seabed level. 76
5.3 Depth variable displacement time series (A). 82
5.4 Seabed displacement time series at every depth (S). 82
5.5 Reference displacement time series at every depth (R). 82
5.6 Results from modal analysis. Maximal values are from seabed level. 82
5.7 Comparison of results. Values corresponding to figure 5.10. 83

Chapter 1

Introduction

1.1 Background

The introduction of suction caissons in 1982 was a breakthrough when it comes to offshore foundation engineering. This gave the industry a reliable foundation coupled with easy installation. Suction caissons are commonly applied as foundations for offshore wind turbines, jackets and manifolds.

The offshore oil industry is increasingly looking towards deeper waters for their platforms. According to Gourvenec and Randolph (2011), the definition of deep waters is 500 meters and deeper. For such depths, fixed platforms become impractical, and buoyant structures are better suited. Suction caissons are frequently applied as moored anchors for floating structures and as foundations for manifolds, due to their practical installation.

As mentioned above, suction caissons are also used as foundations for offshore wind turbines. As onshore wind farms bring with it noise, visual impact and other negatives, the focus has increasingly shifted to construct offshore wind parks. Benefits such as higher and more constant wind speeds, in addition to larger areas being available, are driving the industry. As the EU has committed to cutting CO2 emissions by a minimum of 40% within 2030 (Europa.eu), the growth in the wind industry is expected to continue.

One of the most challenging aspects in the design of sub-sea structures founded on closed caissons is their response to dynamic loading. The foundation and superstructure are subjected to dynamic loading in the form of wind and wave loads, as well as the possible occurrence of earthquakes.

In earthquake-related design, there is a need for estimating the earthquake loads that the structure and foundation will be subjected to. For design, 3D finite element models are frequently used. The 3D models estimate how the caisson will behave under the given conditions, and show good correspondence with real, observed behaviour. Although the results generated are accurate, there is consensus among market operators that the design costs of foundations based on 3D models are too high. These analyses are generally costly, time-consuming and require extensive insight by the user.

Two alternative analysis methods for design are treated in this thesis; *(1) a time series analysis and (2) a modal analysis*. Both analyses cause a significant reduction in computational time. The methods are also simpler, and the number of unknown effects are thus limited.

Problem Formulation

Multiconsult AS has proposed two conceptually different design methods. One based on modal analysis, and the other on time series analyses where Det Norske Veritas(DNV) was involved in development. The methods were proposed in 2015 at the International Symposium of Frontiers in Offshore Geotechnics(ISFOG) in Oslo. They are elaborated in the article *Simplified earthquake analysis for wind turbines and subsea structures on closed caisson foundations* by Athanasiu et al. (2015). A comparison is needed to address the ratio of conservatism between the two methods.

For a stiff foundation embedded in soft soil, kinematic interaction effects might have a major role in the response of the system. Site response amplification leads to a reduction of ground motion with depth. If these kinematic embedment effects are considered in design, it can lead to a more realistic response, resulting in less conservative design.

Objectives

1. Perform a one-dimensional non-linear site response analysis in NERA to calculate the variation of soil response with depth. A unique acceleration time serie for each

depth is obtained from the NERA results. The site response analysis is performed for four different earthquakes.

2. Develop a finite element model to be used in the time series analyses. Model the caisson as a beam supported by the soil springs calculated from objective 3. The soil springs shall represent the soil's stiffness, and dynamic earthquake time series shall be applied at the end of each spring.
3. Modelling the hysteretic behaviour to get an appropriate hysteretic damping in the soil springs. Different methods for calculating p-y curves should be studied, as well as testing different spring configurations.
4. Evaluate trends in the structural response parameters such as acceleration, displacement, rotation, moment and shear force. Compare the results of the time series analyses to the simplified modal analysis.

1.2 Approach

This thesis compares the results from two conceptually different calculation methods. The first method is a simplified modal analysis, performed in frequency domain using an in-house program, provided by Multiconsult. The second method consists of modelling the caisson as a beam and performing time series analyses, abbreviated TSA's, in ANSYS.

Firstly, a thorough literature study was completed. This study aimed to increase the knowledge within earthquake engineering, in addition to give further insight into the soil's non-linear behaviour during cyclic loading. Additionally, the theory covering the input needed in the analyses was emphasised.

Secondly, a non-linear numerical site response analysis was carried out. This was done using NERA (Non-linear Earthquake site Response Analysis). The acceleration time series, adjusted for depth effects, were integrated to find the total displacement at each depth. These displacement time histories were applied at the end of each spring.

The soil stiffness was represented by p-y curves which were calculated using different recommendations. To better represent the response of large diameter caissons, the p-y curves were corrected to approximate results from Plaxis, provided by Multiconsult. Four bi-linear springs were applied at the beam element nodes to model the hysteretic damping. These were curve-fitted to simulate the non-linear p-y curves.

The FE model was continuously updated, and sensitivity analyses were performed to increase the credibility of the model. Having established a model, time series analyses were performed using four different input earthquake displacement time series. The results from the time series analyses were compared to the modal analysis.

1.3 Limitations

Applied earthquake input is limited to four different excitations. The caisson is modelled as beam elements where soil mass is included. Spring elements in ANSYS are modelled as four bi-linear springs in parallel, to model the hysteretic soil response. Input accelerations from NERA have been integrated to get the displacement time series at each depth. The displacement time series are applied in one horizontal direction only. Soil springs and corresponding time series are applied to the caisson as point loads at each meter with depth. Caisson geometry remains constant in all analyses and no effect of geometry variation is studied. No possibility to account for time-dependent effects such as creep or consolidation. Degradation of soil stiffness due to pore pressure accumulation during cyclic loading is not considered.

1.4 Structure of the Report

- The structure of the report is presented in the following.
  - **Chapter 2: Literature Survey and Theory**

    This chapter provides an introductory literature study, and provides theory concerning geodynamics. The literature study has been conducted to give insight on the soils non-linear cyclic behaviour. Additionally, it presents relevant models developed to calculate the lateral capacity of large diameter caissons.
  - **Chapter 3: Method**

    This chapter summarises the basics behind the analyses methods used in the thesis.
  - **Chapter 4: Case Study**

    This chapter covers the project-specific input given by Multiconsult AS, such as the soil profile and the synthetic accelerograms. Adjustment of p-y curves, the hysteresis configuration and a presentation of the finite element model, is also covered.
  - **Chapter 5: Results**

    This chapter presents the results from the three different time series analyses and the modal analysis.
  - **Chapter 6: Discussion**

    This chapter evaluates both the results from the previous chapter and credibility of the model.
  - **Chapter 7: Conclusions and Further Work**

    This chapter provides a summary and conclusion of the thesis, and describes further work needed.

Chapter 2

Literature Survey and Theory

2.1 Introduction

This literature study is performed to increase knowledge on the subject of earthquake engineering, and ways of representing the soil response when subjected to dynamic loading.

2.2 Closed Caisson Foundations

Caissons are specialised foundations that are predominantly used for bridges, dams, windmills and other structures that need underwater support. A caisson is a prefabricated hollow, watertight box or cylinder that is penetrated into the ground. In comparison to normal piles, caissons are characterised by having a low depth to width ratio, $\frac{D}{B}$, thus attaining a stiffer behaviour. Common depth to width ratios for rigid caissons are typically 0.5 to 4, while flexible caissons have a $\frac{D}{B}$ ratio of 3 to 8 (Gerolymos and Gazetas, 06a).

Two common caisson types are open and closed caissons, whereas only the latter is considered in this thesis. Open caissons are characterised by either having an open top, or both top and bottom being open. At large depths, open caissons become impractical due to installation difficulty. Closed caissons are skirted foundations that are open in the bottom. These are better suited for deep waters, due to the possibility of using suction during installation.

Installation of closed suction caissons can be divided into two phases. The first phase when the caisson penetrates the upper soil by self-weight, while in the second phase, suction brings the caisson to the desired depth. Suction is obtained by pumping water out of the caisson, inducing pore pressure differences between the interior and the exterior of the caisson. As a consequence of the differential pressure, the caisson penetrates the soil further. The principles of the installation procedure is illustrated in figure 2.1.

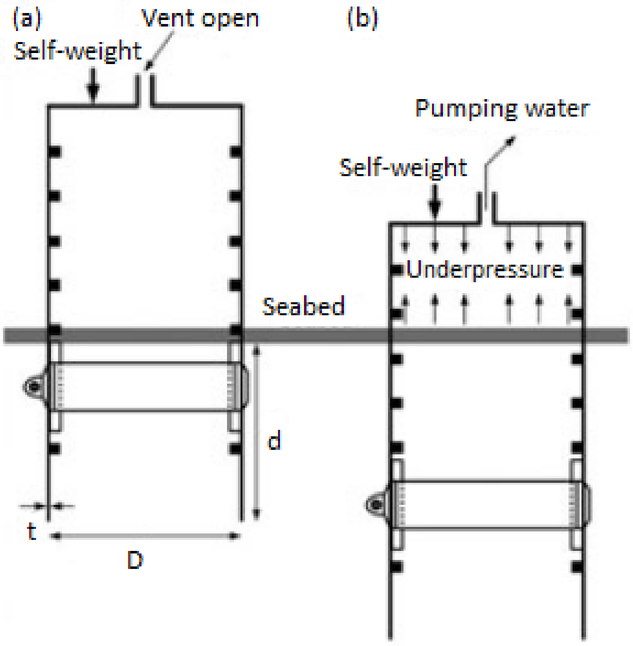

Figure 2.1: a) Penetration by self weight b) suction installation (Illustrations from Hossain et al., 2012).

Suction caissons are frequently applied as anchors for buoyant structures. Such structures are better suited for deep waters compared to fixed structures, due to both water depth and complex load conditions. The platforms are moored to the anchors using cables, transferring loads from the floating facility and holding the platform in place (Gourvenec and Randolph, 2011).

2.3 The Winkler Model

To simplify the three-dimensional problem of a beam with external resistance against deflection from the surrounding soil, Emil Winkler came up with a simplified mechanical subgrade model in 1867 (Hanssen, 2016). In this model, named the Winkler model, the soil is idealised as a set of infinitely many, closely spaced, linear elastic, identical springs. An illustration of the model can be seen in figure 2.2.

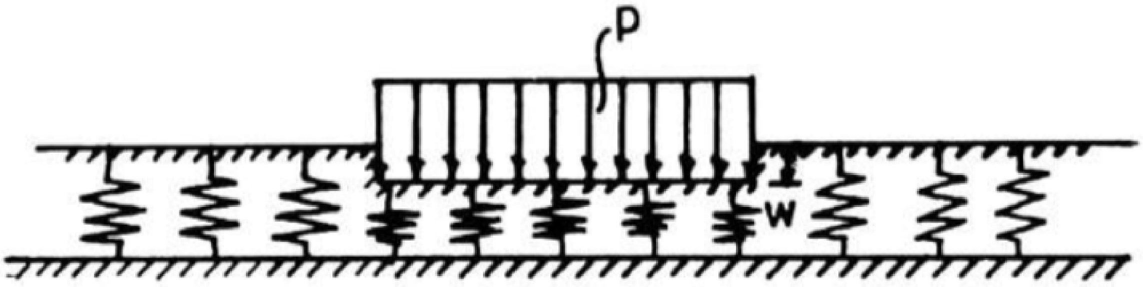

Figure 2.2: The Winkler foundation model (Illustration from Kerr (1964))

The basic concept is that a beam situated on top of an elastic soil medium experiences a distributed resistance against deflection from the soil. In this case, the resistance at one specific point is proportional to the displacement. The assumption of proportionality indicates that the springs are uncoupled, and consequently independent of each other. The mathematical expression representing the resistance of the soil in point i is:

$$p_i = k_i \cdot y_i \tag{2.3.1}$$

In the above equation, p is the subgrade reaction, y is the normal displacement and k is the foundation modulus.

Further, the Winkler model can be applied to piles subjected to lateral loading. In this case, the pile is idealised as a one-dimensional beam with its longitudinal axis oriented vertically, and the elastic foundation is the surrounding soil. This is illustrated in figure 2.3.

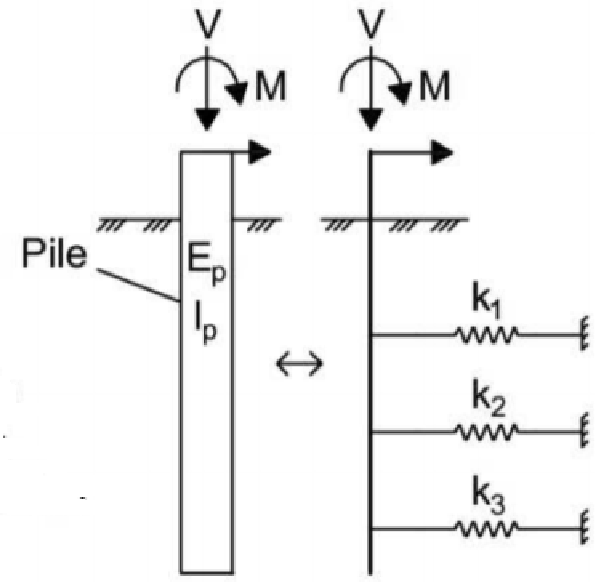

Figure 2.3: The Winkler foundation model applied to a pile (Illustration from Hanssen (2016))

Due to the idealisation of uncoupled springs, the deflection of the foundation is confined only to the loaded region. Consequently, the model lacks continuity in the supporting soil. The model also deviates from reality as it considers the deformation to be uniform under the load. Again, this is a result of the idealisation, as zero interaction between the adjacent springs implies that the model ignores shear effects in the soil. Hence, the Winkler foundation model is often seen as an incomplete approximation of the real mechanical behaviour of the soil.

However, the Winkler foundation method has been the dominating subgrade model to date (Colasanti and Horvath, 2010). Due to complex and varying conditions offshore, it is necessary to check a large number of load cases when designing offshore structures. This makes the Winkler method attractive to use, due to its simplicity and computational cost efficiency (Hanssen, 2016).

2.4 Response of Cyclically Loaded Soil

Because of the soil-caisson interaction, the response of the foundation is directly related to the response of the soil surrounding it. During an earthquake, the soil around the caisson will be subjected to cyclic loading, unloading and reloading due to the pile's oscillation.

For small movements, only elastic strains will occur. If the movement is considerable, the strains developed during loading will be both elastic and plastic. When the dynamic load is reversed, the soil will experience unloading, which initially is elastic and the response is stiffer than during loading. If the size of the load reversal increases further above the yield criterion, it will lead to a decrease in stiffness, in addition to generating additional permanent deformation. Plastic deformations in the soil surrounding the foundation will cause plastic displacements and rotations, thus inducing a nonlinear foundation response (Aasen et al., 2017).

The mechanical behaviour of soils is quite complex under dynamic load conditions. Several soil models have been developed with the purpose of characterising the cyclic soil behaviour. Of these, the equivalent linear models are the simplest but show limitations when it comes to describing many aspects of soil behaviour under cyclic loading. The nonlinear stress-strain behaviour of soils subjected to cyclic loading can be better represented by the use of nonlinear cyclic models, whose ability to represent the development of permanent deformations is an advantage (Kramer, 1996).

2.4.1 Nonlinear Cyclic Models

Several nonlinear models have been developed, and are characterised by a backbone curve and a series of rules that governs unloading/reloading behaviour, stiffness degradation and other effects. A simple example is considered to illustrate the performance of a nonlinear model. The shear stress, τ is described as a function of the shear strain, $F_{bb}(\gamma)$.

$$F_{bb}(\gamma) = \frac{G_{max} \cdot \gamma}{1 + \frac{G_{max}}{\tau_{max}} \cdot |\gamma|} \tag{2.4.1}$$

Equation 2.4.1 describes the backbone curve, represented by a hyperbolic function, and is illustrated in figure 2.4.

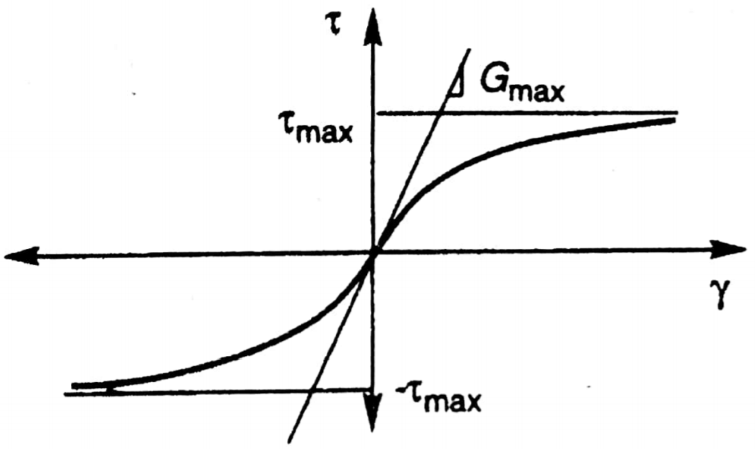

Figure 2.4: Hyperbolic backbone curve, (Illustration from Kramer (1996)).

For this simple example, four rules govern the response of the soil. These are called Masing rules, and models that follow these rules are often referred to as *extended Masing models*. According to Kramer (1996), the rules are the following:

1. During initial loading, the soil's stress-strain curve will follow the backbone curve. This is illustrated as loading from A (where the cyclic loading begins) to B in figure 2.5.
2. If a load reversal occurs at a point i, defined by (τ_i, γ_i), the stress-strain curve will follow a new path, defined by:

   $$\frac{\tau - \tau_i}{2} = F_{bb}(\frac{\gamma - \gamma_i}{2}) \tag{2.4.2}$$

   This new path will evidently have the same shape as the backbone curve, only magnified by a factor of 2. In figure 2.5, this is shown as the load reversal from B to C.
3. If the unloading/reloading curve exceeds the prior strain and subsequently crosses the backbone curve, it will follow the backbone curve until the next load reversal occurs. This rule is illustrated as one moves from B to D, and from D to F.
4. If an unloading or reloading curve crosses an unloading or reloading curve of a previous cycle, the stress-strain curve will follow that of the previous cycle.

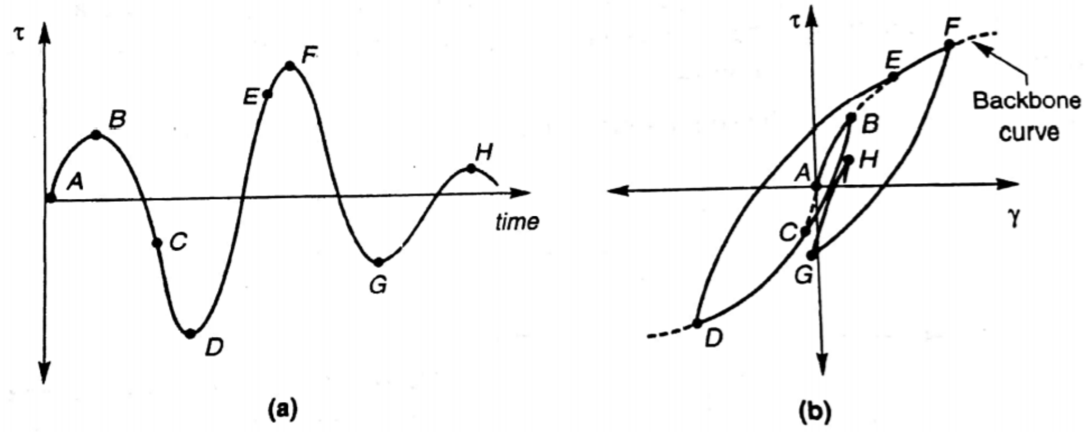

Figure 2.5: a) Shear stress versus time. b) Resulting shear stress versus shear strain. (Illustrations from Kramer (1996))

Figure 6 and the aforementioned Masing rules describe how the permanent strains develop during cyclic loading of the soil. However, this simplified model does not describe how pore pressure under undrained conditions develops, nor does it describe the hardening of the soil during loading. These are both factors that are accounted for in most nonlinear models.

Cyclic nonlinear models can be coupled with pore pressure generation models. This makes it possible to predict changes in effective stresses, hence also changes in the soil stiffness. When pore pressure increases, effective stresses decreases and consequently also maximum shear stress and shear modulus. Hence, increased pore pressure would result in the backbone curve degrading. Such hysteresis loops where it is evident that the backbone curve degrades is shown in figure 2.6.

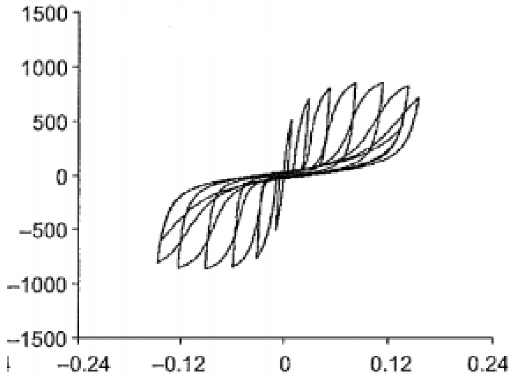

Figure 2.6: Lateral soil reaction vs displacement. X-axis shows displacement in meters, Y-axis shows lateral soil reaction in kN/m. (Adapted from Gerolymos and Gazetas, 06c)

When permanent deformations are developed, energy coming from the earthquake is dissipated (Villaverde, 2009). This is referred to as hysteretic damping and is further discussed in section 2.4.2.

2.4.2 Damping of the Foundation Movement

When foundations are subjected to external forces, energy is dissipated by several mechanisms. These include friction, heat generation and plastic yielding.

When it comes to foundation issues, there are two main types of damping present, radiation damping and hysteretic damping. Radiation damping results from the dispersion of wave energy over a larger volume of material as it moves away from the source and is further explained in section 2.9.6.2.

Hysteretic damping, also known as material or internal damping, is caused by the internal friction that arises by the slippage of grains as the soil deforms. Hysteretic damping is explained further in section 2.9.6.1. The hysteretic damping is dependent on the strain level in the soil, which in turn is affected by the loading history, as soils behave stiffer during unloading and reloading. Also, as previously indicated in section 2.4.1, the shear strains will be influenced by the pore pressure, due to its relation with the shear modulus, $G = \frac{\tau}{\gamma}$.

In 1991 Vucetic and Dobry (1991) published a paper on the effects of the soil's plasticity index (PI) on the cyclic response. While showing the effects of $\frac{G}{G_{max}}$ and γ_c on the damping ratio, Vucetic and Dobry conclude that the plasticity index of the soil is the most influential parameter that affects the damping response of soils subjected to cyclic loading (Vucetic and Dobry, 1991). The influence of the plasticity index on the damping is shown in figure 2.7.

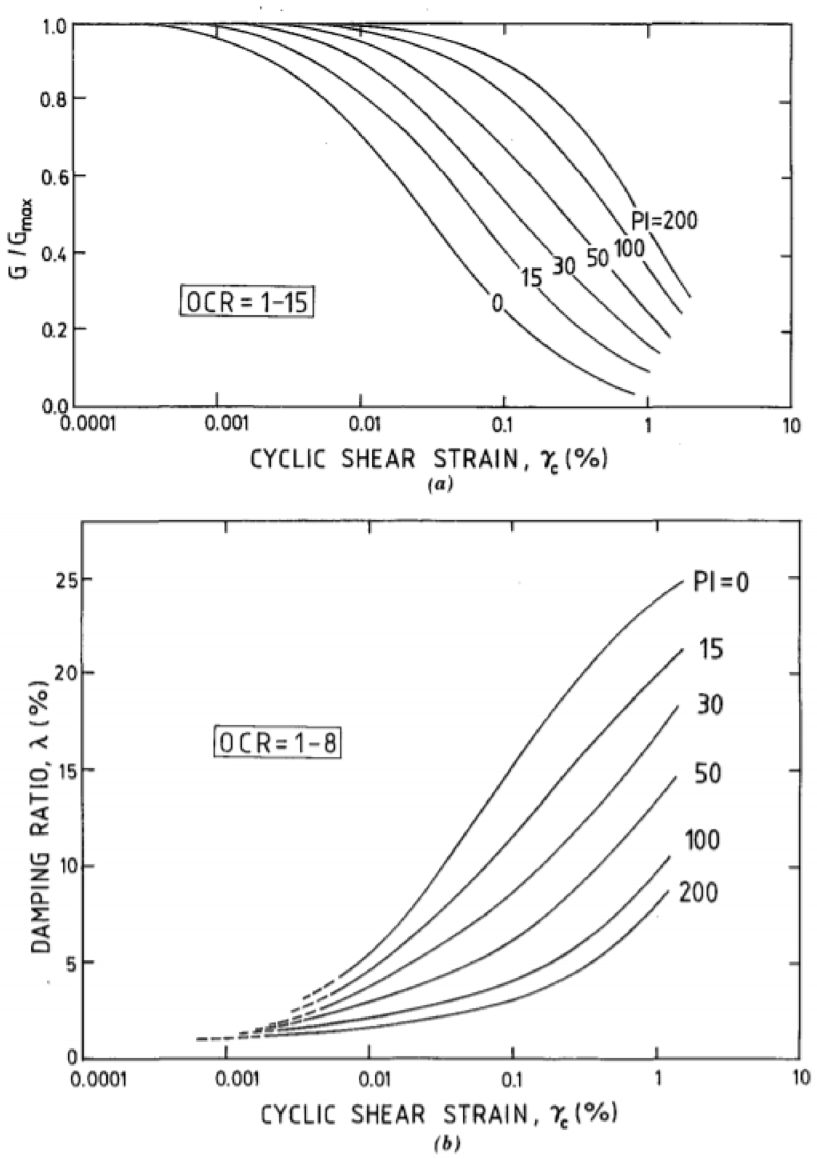

Figure 2.7: a) $\frac{G}{G_{max}}$ vs cyclic shear strain, γ_c. b) Damping ratio vs cyclic shear strain, γ_c. (Illustrations from Vucetic and Dobry (1991)).

2.5 Failure Mechanisms / Ultimate Behaviour of Piles in Cohesive Soils

Before discussing different methods for developing p-y curves, it is appropriate to cover the topic of failure mechanisms around a pile in cohesive soil, as these curves often incorporate the peak unit resistance that can be exerted against the pile. The geometry of the failure mechanism around a pile in cohesive soil can be modelled by separating it into two main failure mechanisms; flow around failure and conical wedge failure. As seen in figure 2.8, the lateral movement of the pile forces a conical wedge to move up and out, while at a certain depth, the soil fails in a localised flow around mechanism.

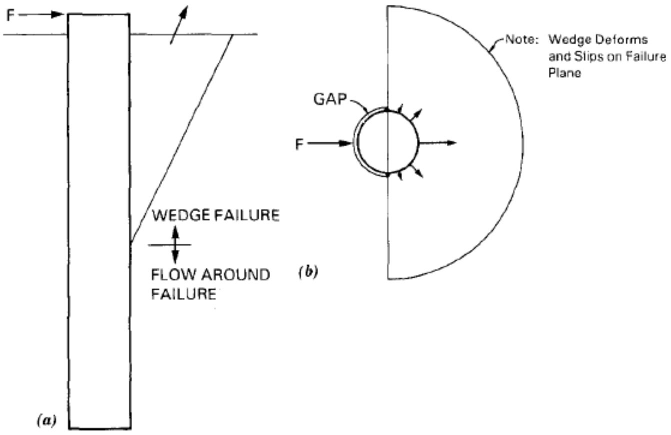

Figure 2.8: Soil failure mechanisms of laterally loaded piles in soft clay (Illustration from Murff and Hamilton (1993)).

2.5.1 Conical Wedge Failure

During lateral loading, the upper part of the soil profile fails in a conical wedge mechanism. If separation arises between the pile and the soil at the rear side of the loading direction, i.e. no suction, a passive wedge will form on the front side of the pile. This is the case illustrated in figure 2.8. In this case, gapping on the rear side might appear. If suction is present, there will also be mobilised an active wedge on the rear side of the loading direction. During fast wave loading, such as in an earthquake, or when the free drainage path is blocked around the pile, it might be suitable to assume suction. Assuming suction results in a higher lateral bearing capacity factor, N_p (Zhang et al., 2016). The ultimate soil capacity is further elaborated in section 2.6.

2.5.2 Flow Around Failure

The paper by Randolph M. F & Houlsby (1984) investigated the limiting pressure on a circular pile loaded laterally in cohesive soil. The flow around failure mechanism surrounding the pile was studied, and the resulting upper and lower bound solutions showed the same limiting pressure. The flow around mechanism arises at a certain depth, as the soil resistance mobilised in this mechanism becomes smaller than in the wedge mechanism.

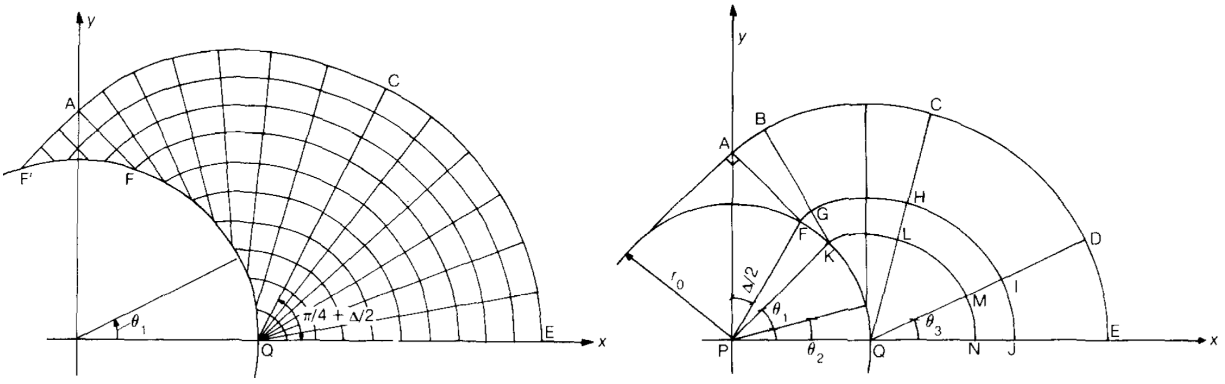

(a) Geometry of the characteristic stress mesh. **(b)** Deformation mechanism.

Figure 2.9: Geometry of characteristic stress mesh and deformation mechanism (Illustrations from Randolph M. F & Houlsby (1984)).

The lower bound solution is derived by assuming a stress distribution and equating it to an external load. The geometry of the assumed stress field around the first quadrant of the pile is shown in fig 2.9a. The lateral movement of the pile causes a zone of high mean stress in front of the pile, and low stress behind the pile. The distribution of stresses forces the soil to flow from the front to the back of the pile. For the upper bound solution, a postulated failure mechanism and associated velocity field is used. By equating the work done by the external load to the rate of energy dissipation within the soil mass, the upper bound collapse load is calculated. Both upper and lower bound solutions yielded the same resulting equation:

$$\frac{P}{cd} = \pi + 2arcsin\alpha + 2cos(arcsin\alpha) + 4\left[cos\frac{arcsin\alpha}{2} + sin\frac{arcsin\alpha}{2}\right] \tag{2.5.1}$$

where P is the ultimate failure load per unit length of the pile, and α is the constant factor of the pile-soil adhesion, a, divided by the soil cohesion, c. By observing figure 2.11a, it can be seen that the ultimate failure load is highly dependent on the α factor, which is an indication of the roughness of the soil-pile interface. A plot showing the cases of $\alpha = 0.0$ and $\alpha = 1.0$ is shown in figure 2.10. An important observation is the size of the stress field, as it expands with an increasing roughness, thus inducing a higher soil resistance.

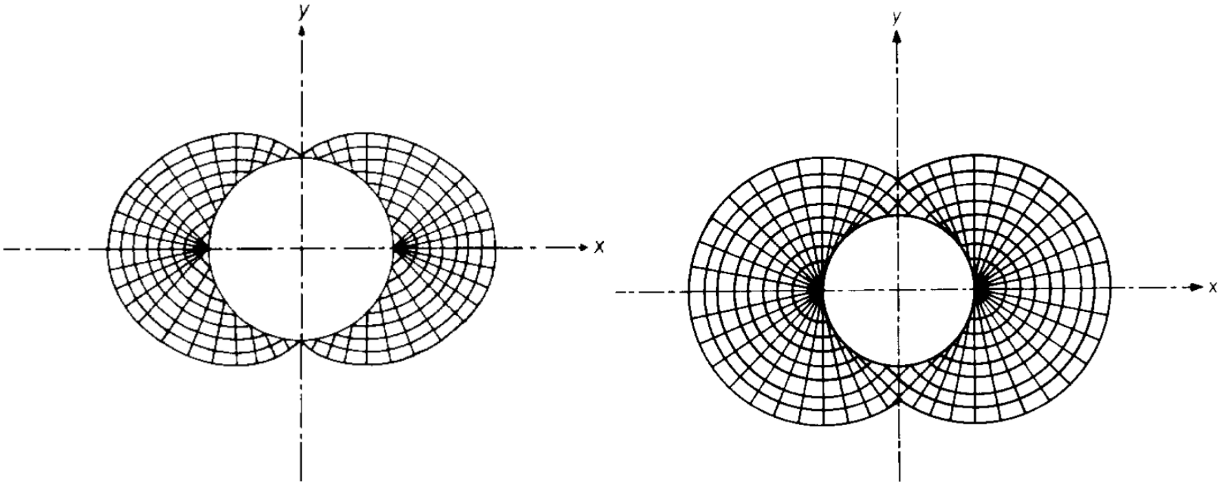

(a) Characteristic mesh at $\alpha = 0$. **(b)** Characteristic mesh at $\alpha = 1$.

Figure 2.10: Characteristic mesh for $\alpha = 0$ and $\alpha = 1$ (Illustrations from Randolph M. F & Houlsby (1984)).

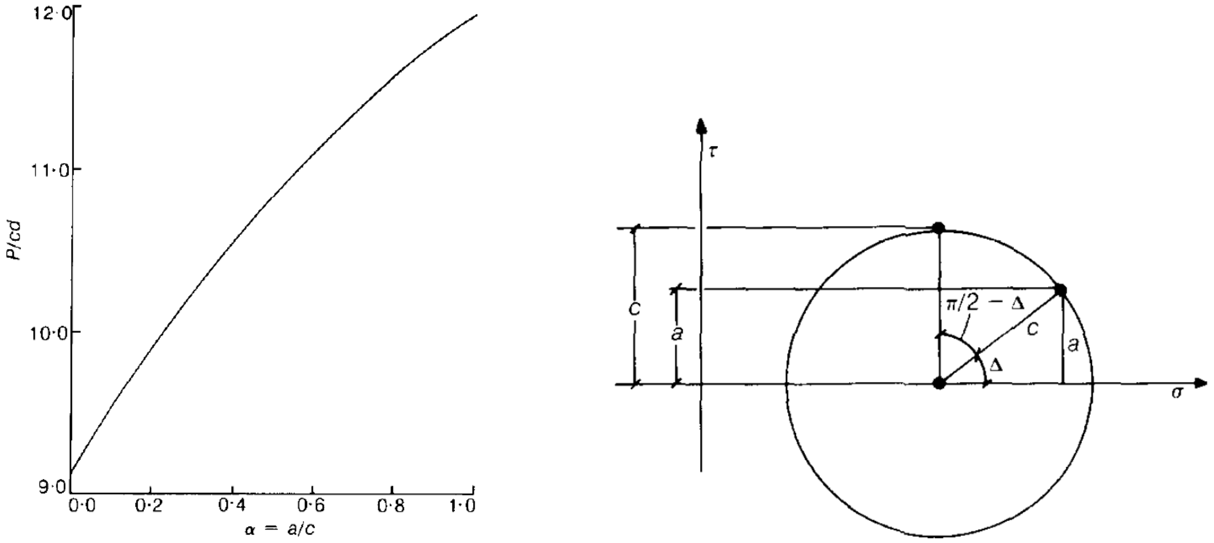

(a) Variation of limiting pressure. **(b)** Pile surface stress.

Figure 2.11: Variation of limiting pressure and pile surface stress (Illustrations from Randolph M. F & Houlsby (1984)).

The results from this paper are believed to yield exact plasticity solutions, but the resulting equation 2.5.1, is only exact for $\alpha = 1.0$. This was due to the localised conflict between the strain rate field and the stress field for $\alpha < 1$ in the upper bound solution, thus including negative plastic work. This interfered with the compliance between the two solutions. This problem was investigated in the paper (Martin, 2006), but the results only showed a difference of 0.65 percentage when comparing the strict exact lower bound solution of Randolph M. F & Houlsby (1984) to the newer upper bound solutions of Martin (2006).

2.6 P-Y methods

Offshore piles and caisson foundations usually have to be designed to withstand lateral loading, such as earthquakes, waves etc. The lateral soil resistance versus horizontal displacement can be represented by p-y curves. These are also called load transfer curves, and describes the lateral stiffness of the soil. Such curves are commonly applied in design. However, there is no industry standard for how these p-y curves are to be represented for large diameter caissons, nor is there an agreement for what is the limiting pile capacity in clay. Hence there exist several methods and recommendations on how to represent the soil's mobilisation during lateral loading. The methods considered in this thesis are proposed for soft clays and are further elaborated in the following subsections.

2.6.1 American Petroleum Institute - API RP 2A Recommendation

The API standard for laterally loaded piles in soft clay is based upon Matlock (1970). Soft clay is here defined as clay with a shear strength up to 96 kPa. The API RP 2A method of constructing p-y curves is widely adopted when designing offshore pile foundations. For static lateral loads, the method is initiated by calculating the ultimate lateral bearing capacity, p_u, of the soft clay (API, 2007). This formula is mainly derived from back analyses of field pile tests performed during the 1950s (Matlock, 1970). Piles considered were long and slender, and the method includes no scaling for larger diameters. Consequently, the applicability of the formula for large diameter piles have long been debated. The API recommendation for the ultimate lateral bearing capacity at a given depth is:

$$p_u = N_p \cdot s_{u,z} \tag{2.6.1}$$

$$N_p = (3 + J \cdot \frac{z}{D}) + \frac{\gamma' \cdot z}{s_{u,z}} \tag{2.6.2}$$

where N_p is the dimensionless ultimate lateral soil resistance coefficient, $s_{u,z}$ is the shear strength at a given depth, z, and γ' is the effective unit weight of the soil. D is the diameter of the pile, and J is an empirical constant with an approximate value of 0.5 for soft offshore Gulf of Mexico clay and 0.25 for stiffer clays (Stevens and Audibert, 1979). When inserted in 2.6.1, the first term in equation 2.6.2 represents the contribution of soil strength, while the second term represents the contribution of soil weight to the lateral bearing capacity, until a localised flow around mechanism at a certain depth is formed (Zhang et al., 2016).

Close to the surface, the soil is usually insufficiently confined, and as the pile deflects, the soil in front will be pushed up and away in a wedge formation. For this kind of failure, Matlock suggests that $N_p = 3$, and that it increases linearly with depth as in equation 2.6.2. For depths where the soil is sufficiently confined, an upper limit of $p_u = 9 \cdot s_u$ is suggested, assuming no suction and a smooth interface. The depth in which the upper limit appears, corresponds to the depth where flow around mechanisms arises (Stevens and Audibert, 1979).

$$p_u = 9 \cdot s_u \text{ for } z \geq z_r \tag{2.6.3}$$

$$z_r = \frac{6 \cdot D}{\frac{\gamma' \cdot D}{s_u} + J} \tag{2.6.4}$$

Having established the ultimate bearing capacity, API RP 2A suggests using table 2.1, showing relationships between deflection, y, and resistance, p, when creating the p-y curve.

Table 2.1: API RP 2A - Load-deflection (p-y) curves for soft clay

$\mathbf{p}/p_u$	$\mathbf{y}/y_c$
0.00	0.0
0.50	1.0
0.72	3.0
1.00	8.0
1.00	∞

where y_c is defined by ϵ_{50}, the strain that occurs at 50% of the maximum stress on undrained compression tests of undisturbed soil samples, and the diameter of the pile/caisson, D, as shown in equation 2.6.5 (API, 2007). Following this procedure will yield a piecewise linear p-y curve.

$$y_c = 2.5 \cdot \epsilon_{50} \cdot D \tag{2.6.5}$$

2.6.2 Stevens and Audibert Recommendation

In the study by Stevens and Audibert (1979), results from lateral load tests on seven piles with a diameter up to 1.5 meters in soft to medium soft clays were compared to p-y values predicted using the methods proposed by Matlock(1970), API(1978) and Reese et al(1975). These methods are all empirically based, and as Stevens and Audibert state, only justifiable if the design conditions are similar to the conditions the methods were based on (Stevens and Audibert, 1979).

The study concludes that the empirical methods significantly overestimate the pile deflections near the ground line. The use of too low N_p values near the ground line, in addition to the linear dependency between y_c and the pile diameter was identified as the two factors which led to the differences between predicted and observed behaviour. On this basis, Stevens and Audibert suggested two modifications for the Matlock(1970) and the API(1978) method.

The first modification is adding a scaling effect to y_c, to reflect diameter effects. The original y_c used by Matlock and API, as expressed in equation 2.6.5, was based on tests on a pile with a 0.32385-meter diameter. Stevens and Audibert's study implemented seven full-scale pile load tests in clays for diameters in the range of 0.28 to 1.5 meters. The tests indicated that the value of y_c was proportional to the square root of the pile diameter, and they suggested a new relationship based on this, which normalises the relationship concerning the reference test pile used by Matlock (Stevens and Audibert, 1979). Their recommendation is the following equation:

$$y_c = 2.5 \cdot \epsilon_{50}(\frac{D}{D_{ref}})^{0,5} \cdot D_{Dref} \quad [\mathrm{m}] \tag{2.6.6}$$

where $D_{ref} = 0.32385$ is the reference diameter used by Matlock. As this scaling is done for piles up to only 1.5 meters in diameter, one should note that it might be inaccurate for piles and caisson foundations with greater diameters and stiffer behaviour.

The second modification is a recommendation of using a different relationship of N_p versus the ratio of depth to pile diameter. Based on the test results, the N_p vs $\frac{z}{D}$ represents the average value minus one standard deviation of the values collected from the study of the different case histories. The relationship is shown in figure 2.12.

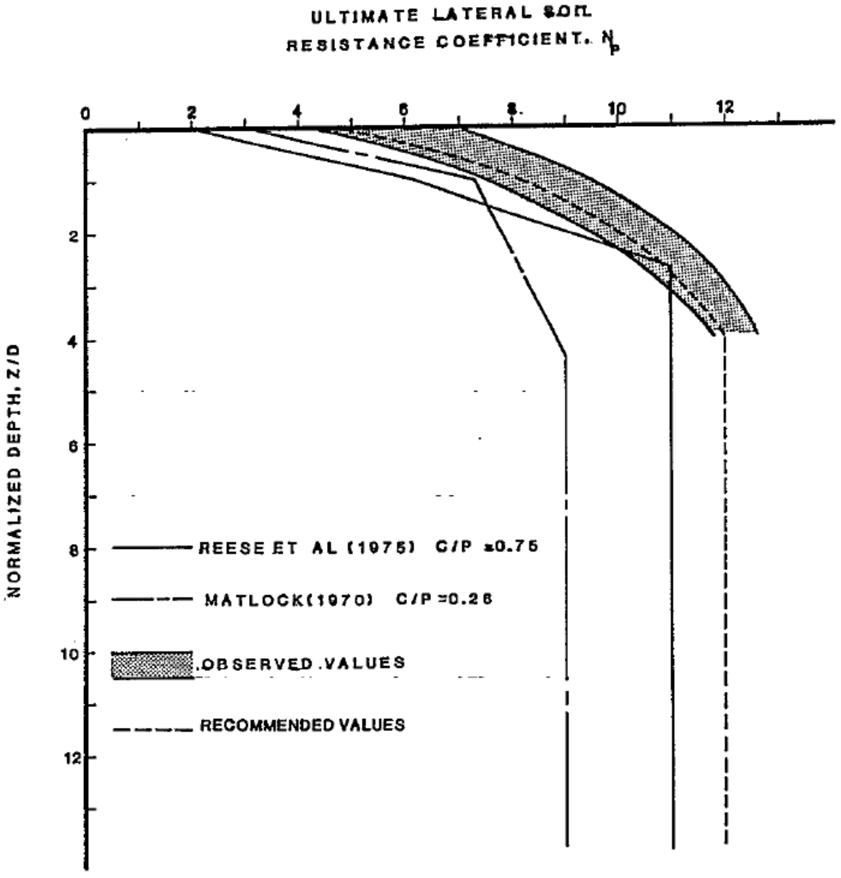

Figure 2.12: Lateal bearing capacity factor, N_p, vs normalized depth(Illustration from Stevens and Audibert (1979)).

This relationship is only shown graphically in Stevens and Audibert (1979), and no explicit formula is specified. Stevens and Audibert recommend an upper limit of N_p=12. An approximate formula which shows good correlation with the recommended values by Stevens and Audibert is suggested in the following equation:

$$N_p = 4,7 + 4,6 \cdot (\frac{z}{D})^{\frac{1}{3}} \tag{2.6.7}$$

With the use of the two modifications, the construction of p-y curves are done following the same procedure as presented in section 2.6.1 for the API method, and can also be used in Matlock's parabolic p-y curve formulation represented in equation 2.6.8 and 2.6.9.

$$p = 0,5 \cdot p_u \cdot (\frac{y}{y_c})^{\frac{1}{3}} \text{ for } y < 8 \cdot y_c \tag{2.6.8}$$

$$p = p_u \text{ for } y \geq 8 \cdot y_c \tag{2.6.9}$$

where p_u is as in equation 2.6.1.

2.6.3 Jeanjean Recommendation

Jeanjean generated p-y curves for monotonic conditions using centrifuge experiments and finite element analysis in lightly over-consolidated clay. The centrifuge experiments were based on a free head well conductor with a diameter of 0.91 meters, length equaling 36.5 meters and a thickness of 50.8 mm, acting similarly to a rather slender pile. Static backbone p-y curves were obtained from a test in which the pile was loaded laterally until the pile head had moved just over 1 pile diameter horizontally. This was done at eight depths. It was found that the centrifuge curves agreed well with the finite element analyses curves both in terms of initial stiffness and ultimate pressure, but that they were stiffer than the API RP 2A(2000) curves. The ultimate pressure observed, also exceeded the value of 9$\cdot s_u$ given by API, an average for the FEA were found to be 12.7$\cdot s_u$, while being 13.4$\cdot s_u$ for the centrifuge tests.

In 1993, Murff and Hamilton (1993) proposed an empirical trial function for calculating the variation of N_p with depth for a soil profile with linearly increasing shear strength, in which Jeanjean adopted. Their proposal is shown in equation 2.6.10.

$$N_p = N_1 - N_2 \cdot e^{\frac{-\xi \cdot z}{D}} \tag{2.6.10}$$

Where N_1 is the upper limiting value at depth, while $(N_1 - N_2)$ is the intercept at the soil surface (Murff and Hamilton, 1993). ξ is defined as a function of λ as follows.

$$\xi = 0,25 + 0,05 \cdot \lambda \text{ for } \lambda < 6$$

$$\xi = 0,55 \text{ for } \lambda \geq 6$$

$$\lambda = \frac{s_{u0}}{s_{u1} \cdot D}$$

Jeanjean adjusted equation 2.6.10 using design values obtained from the centrifuge tests. The value of N_p at the soil surface was set to 8, while the limiting value of N_p was set to 12, as in equation 2.6.11.

$$N_p = 12 - 4 \cdot e^{\frac{-\xi \cdot z}{D}} \tag{2.6.11}$$

The ultimate lateral bearing capacity is calculated using the equation 2.6.1 as in the previous methods. To generate the monotonic backbone curve Jeanjean modified an empirical equation suggested by O'Neill et al. (1990). This formulation assumes a rough interface and suction. Jeanjeans proposed equation is shown in equation 2.6.12.

$$p = tanh\left[\frac{G_{max}}{100 \cdot s_u} \cdot (\frac{y}{D})^{0.5}\right] \cdot p_u \tag{2.6.12}$$

2.6.4 Comparison of the Lateral Bearing Capacity Factor

An important parameter when constructing p-y curves is the lateral bearing capacity factor, N_p, which is calculated differently for each method. Figure 2.13 shows the different variations of N_p versus normalized depth $\frac{z}{D}$ using the three formulations. The graphs in figure 2.13 are project specific, made using the soil input and dimensions given by Multiconsult. The diameter of the caisson is 7.5 meters, while its embedded depth is 17 meters, which yields a $\frac{z}{D} = 2.27$.

The figure shows a remarkable scatter, and it is evident that the API (2007) standard results in a resistance lower than proposed by both Jeanjean (2009) and Stevens and

Audibert (1979). Consequently, it may be hard to choose which method to apply. Different values are due to the various assumptions in which the methods are based on. While the widely adopted industry guideline by API assumes no suction on the rear side of the pile and assumes a smooth soil-pile interface, the proposal by Jeanjean assumes the opposite.

For the dimensions considered in this thesis, the method by Stevens and Audibert yields a lower resistance than the formulation by Jeanjean in the upper meters of the caisson. However, the lateral bearing capacity factor increases faster with an increasing $\frac{z}{D}$, and Stevens and Audibert's proposed method yields a higher resistance for greater depths.

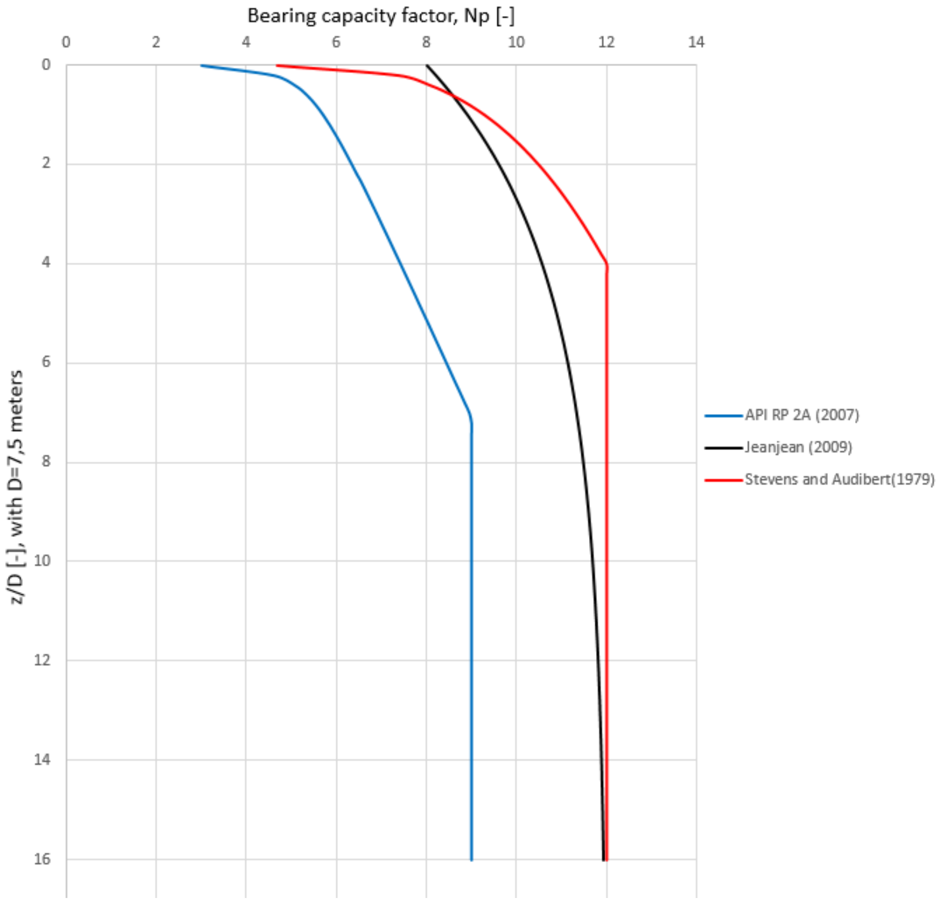

Figure 2.13: Lateral bearing capacity factor, N_p, vs normalised depth z/D, using the proposed methods by API, Jeanjean and the approximated Stevens and Audibert formulation .

The depths in which the limiting N_p values arises, corresponds to the depths where flow around mechanisms is formed. The proposed method by Jeanjean shows no clear indication of where local flow around mechanisms are formed, as its curve only converges towards $N_p = 12$. Compared to the API formulation, the proposed method by Stevens and Audibert predicts that flow around mechanisms form at a lower depth to diameter ratio.

2.7 PISA Project- Pile Soil Analysis

The most applied method of designing piles under lateral loading is based on a Winkler modelling approach, often referred to as the p-y method. The methods presented in section 2.6 were developed for slender piles, and there are concerns that these approaches are inappropriate for large diameter piles and caissons. As a consequence, PISA (Pile Soil Analysis) was established. PISA is a joint industry project formed to develop new design methods for large diameter monopiles and caissons subjected to horizontal loading (Byrne et al., 2015). The project involves three articles which summarises the numerical modelling using a 3D finite element analysis, development of a new design method, and field testing respectively.

The current design formulations by DNV (Det Norske Veritas, 2014) and API (American Petroleum Institute, 2010) are based on the Winkler model by Matlock (1970), where each spring is described by non-linear or piecewise linear functions to describe the subgrade reaction, p, as a function of lateral displacement, y. These methods are based on field tests on slender piles with a high length to diameter ratio. However, the methods have been applied extensively for more rigid foundations (Byrne et al., 2015).

In the traditional p-y method, only the lateral forces developed between the pile and the soil is taken into account. However, to get a more accurate response, Byrne et al. (2015) states that it seems reasonable to include other interaction mechanisms, especially for short, large diameter monopiles. Their proposed 1D finite model for monopile foundations, also valid for caissons, are illustrated in figure 2.14.

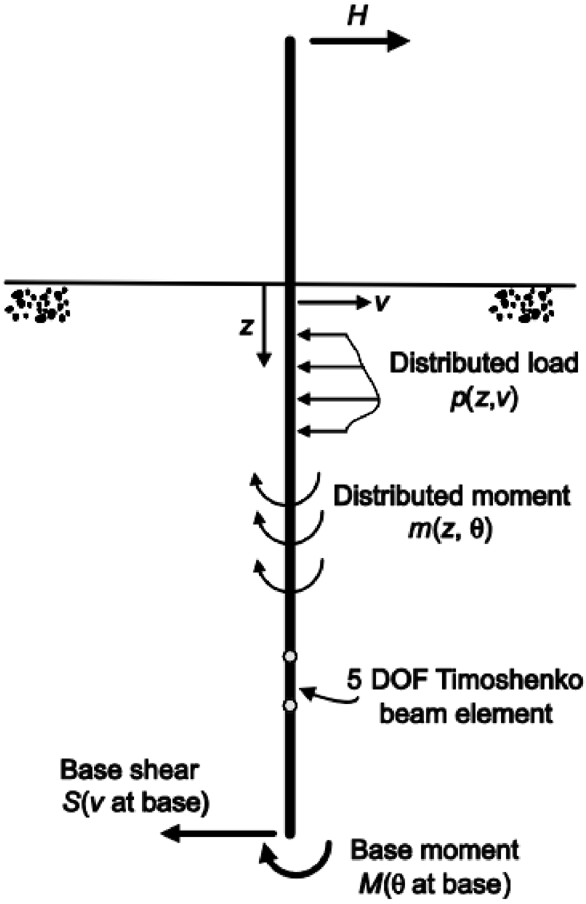
H
v
z
Distributed load
p(z,v)
Distributed moment
m(z, θ)
5 DOF Timoshenko beam element
Base shear
S(v at base)
Base moment
M(θ at base)

Figure 2.14: Proposed 1D finite model for monopile foundations subjected to lateral loading (Illustration by Byrne et al. (2015)). The lateral displacement is denoted v.

To include shear strain effects, the pile is modelled using Timoshenko beam elements with five degrees of freedom. The model includes the following four different components of soil reaction.

- The distributed load curve which defines the distributed lateral load, p, and the lateral pile displacement y (displacement is denoted v in Byrne et al. (2015)). This curve has the same function as a typical p-y curve.
- The distributed moment curve which describes the relationship between the rotation of the pile cross section, θ, and the distributed moment, m. Due to the large surface area of large diameter monopiles, vertical shear stresses acts as a force couple and induce a distributed moment along the pile.
- The base moment curve which describes the relationship between the base moment, M, and the rotation at the base.

- The Base shear curve which describes the relationship between the base shear force, S, and the displacement of the base.

In Byrne et al. (2015) the soil reaction curves used in the 1D model was based on the data determined from the 3D model described in the companion paper by Zdravković et al. (2015). The effect of the additional numerical soil reaction curves is illustrated in figure 2.15.

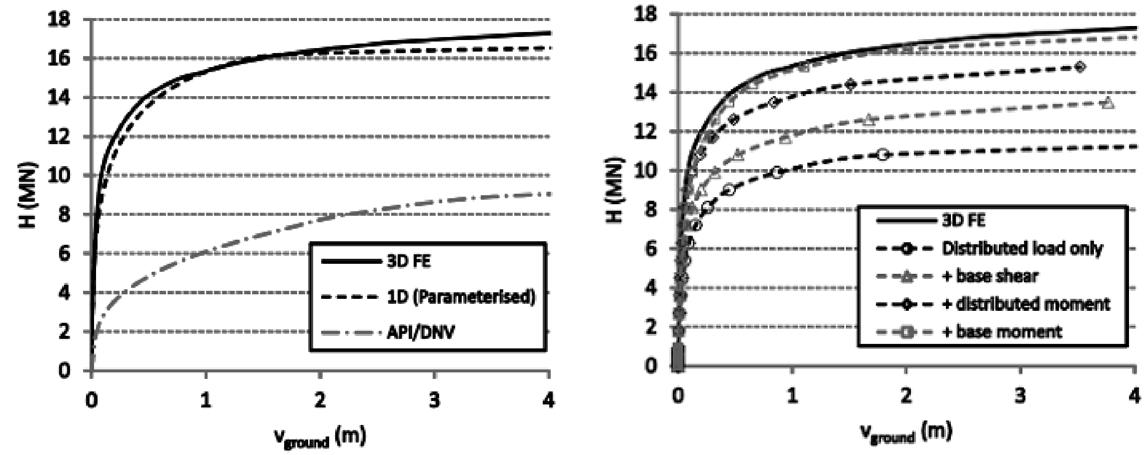

(a) **(b)**

Figure 2.15: **a)** Short pile response in clay **b)** Cumulative breakdown of components for short piles in clay, calculated using the 1D model with numerical soil reaction curves. H is the lateral load applied (Results from Byrne et al., 2015).

In figure 2.15a the response of a pile with a 10-meter diameter and 20 meters length, labelled a short pile, is compared to both a 3D finite element analysis and the API/DNV recommendation. Their 1D method shows good correspondence with the 3D FE analysis, while the API/DNV approach seems inaccurate in comparison. Figure 2.15b shows a cumulative component breakdown using the 1D model for a short pile in clay. The distributed load curves are insufficient to calculate the short pile response alone. Each additional soil reaction curve is observed to offer approximately the same contribution to the calculated lateral load, H.

Computations were also performed on longer piles with a higher length to diameter ratio, while the results are not reproduced here. To summarise, for longer piles, the influence of the additional soil reaction curves were relatively small. Byrne et al. (2015) concluded that for shorter, large diameter piles there is a diameter effect related to an increased influence of the additional soil reaction components.

It should be noted that the proposed model was developed for a monotonic load case, while it is also stated that cyclic behaviour could be incorporated by using simple rule-based methods, such as the Masing rules.

2.8 The Four-spring Winkler Model Proposed by Gerolymos and Gazetas

The three articles by Gerolymos and Gazetas from 2006, proposes a dynamic four-spring Winkler model for rigid caisson foundations. Since the movement of rigid caissons differs from the movement of long, slender piles, the stress distribution also varies. Consequently, the standard p-y method for slender piles becomes insufficient. A stress distribution for rigid caissons is shown in figure 2.16a. The model incorporates distributed translational and rotational springs, and dashpots along the vertical interface of the foundation. In addition, concentrated shear translational and rotational springs and dashpots are incorporated at the base of the caisson.

The interaction between the soil and caisson involves complicated geometric and material nonlinearities. Due to lateral and rotational movement during cyclic loading, it cannot be assumed complete contact between the soil and the caisson shaft. The soils inelasticity, base uplift, gapping between soil and the shaft, and slippage along the soil-caisson interface are some of the nonlinearities. For the model to be realistic, the nonlinear behaviour should be taken into consideration (Gerolymos and Gazetas, 06b).

To account for the nonlinear behaviour upon loading, Gerolymos and Gazetas adapted and further developed the macroscopic Bouc-Wen model. This model, prior to further development by Gerolymos and Gazetas, gives an analytical description of a smooth hysteretic behaviour (Ikhouane et al., 2007). By using the developed model, named the BWGG model, Gerolymos and Gazetas developed interaction springs and dashpots that accounts for hysteretic behaviour(Gerolymos and Gazetas, 06b). An illustration of the model with the nonlinear springs is shown in figure 2.16b.

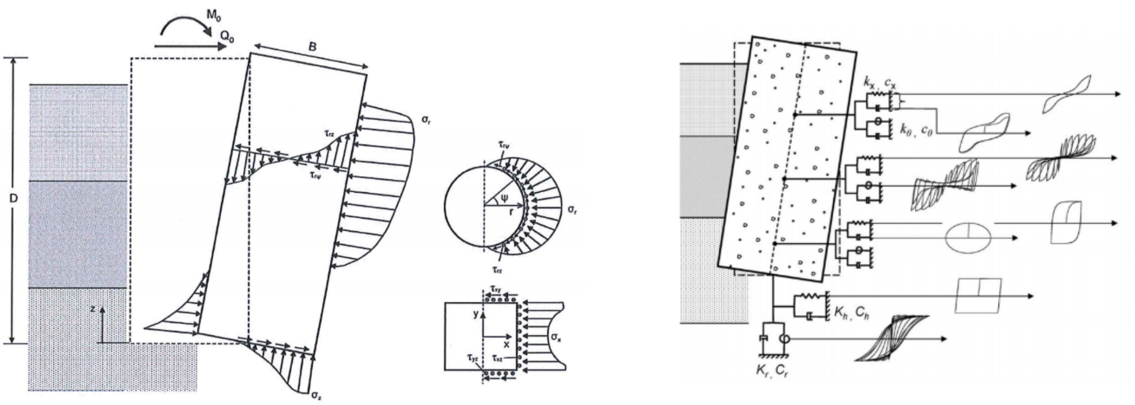

(a) **(b)**

Figure 2.16: a) Stress distribution on caisson from the adjacent soil. b) The nonlinear four spring Winkler model proposed by Gerolymos and Gazetas.(Illustrations from Gerolymos and Gazetas, 06b).

The four nonlinear and inelastic spring types and corresponding viscoelastic dashpots are related to the resisting forces acting on the caisson shaft and base.

- The distributed nonlinear translational springs, k_x, and corresponding dashpots, c_x, represents the horizontal soil reaction on the shaft of the caisson.
- The distributed rotational springs, k_θ, and corresponding dashpots, c_θ, represents the distributed moment caused by the vertical shear tractions on the shaft. At large deformations, translational, rotational springs and dashpots are coupled. Because the ultimate rotational resistance is dependent on the frictional capacity of the soil-caisson interface, which is also related to the normal tractions and thus the horizontal springs.
- The resultant base shear translational spring, K_h, and corresponding dashpot, C_h, represents the resulting horizontal shear force on the base.
- The resultant base rotational spring, K_r, and corresponding dashpot, C_r, represents the moment induced by normal stresses on the base of the function.

Proper choices and assessments of dynamic spring and dashpot coefficients are crucial for the reliability of this Winkler-type model. These coefficients are frequency dependent and are functions of both soil stiffness and the caisson geometry. The methodology for finding the stiffness parameters are presented in Gerolymos and Gazetas (06a) and is not covered in this paper. For cylindrical-shaped caissons, the stiffness parameters were found to be:

$$k_x = 1.60\frac{D}{B}^{-0,13} E_s \tag{2.8.1}$$

$$k_\theta = 0.85\frac{D}{B}^{-1,71} E_s D^2 \tag{2.8.2}$$

$$K_h = \frac{2E_sB}{(2-v_s)(1+v_s)} \tag{2.8.3}$$

$$K_r = \frac{E_sB^3}{1-v_s^2} \tag{2.8.4}$$

Where B and D is the diameter and the height of the caisson respectively, v_s and E_s is the soil's Poisson ratio and Young's modulus respectively. The results are taken from Gerolymos and Gazetas (06b).

While the springs are associated with the resistance mobilised by the soil upon displacement, the dashpots expresses the damping in the system. This damping arises as a result of both radiation of wave energy away from the caisson, and hysteretic dissipation of energy in the soil (Gerolymos and Gazetas, 06a). Hysteresis and damping mechanisms are discussed in section 2.4.

The model showed good correspondence with the 3D finite element analysis performed in ABAQUS. Gerolymos and Gazetas also concluded that interface nonlinearities play an essential role in the response of a caisson (Gerolymos and Gazetas, 06c).

2.9 Wave Propagation

To understand the complex propagation of three-dimensional seismic waves from a near-surface earthquake, it is essential to first examine the theory behind basic wave propagation. This section describes the different types of wave propagation that can occur in the ground, starting with some fundamental wave propagation theory.

A simple one-dimensional unbounded infinitely long bar is used to better understand the concept of wave propagation in an elastic solid. By examining this unbounded bar using basic equilibrium equations, stress-strain and strain-displacement relationships, the equations of motion can be derived. For a one-dimensional thin bar, vibration occurs in three different ways:

- Longitudinal vibration, where the bar extends and contracts without lateral movement.
- Torsional vibration, where the bar rotates about its axis without lateral movement.
- Flexural vibration, where the bar's axis has a lateral motion.

The wave equations for the first two types of vibration are derived and solved in the sections below. The third type of vibration is mostly irrelevant in soil dynamics, and is not further assessed.

2.9.1 1D Longitudinal Waves

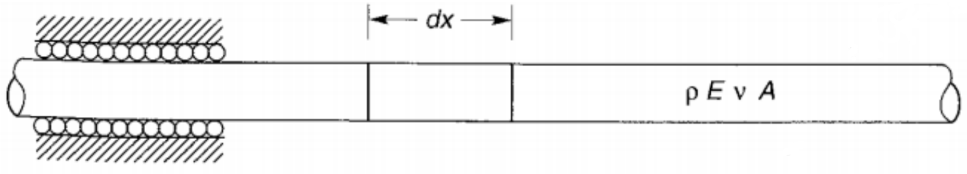

Figure 2.17: Longitudinal waves in infinitely long bar (Illustration from Kramer (1996)).

Dynamic equilibrium of an element in an infinitely long, linear elastic, radially constrained bar, with density ρ, cross-sectional area A, Young's modulus E, and Poisson's ratio ν, gives the following equation:

$$\left(\sigma_{x0} + \frac{\partial \sigma_x}{\partial x dx}\right) A = \rho A dx \frac{\partial^2 u}{\partial t^2} \tag{2.9.1}$$

where the axial stress at the left and right is σ_{x0} and $\sigma_{x0}+\partial\sigma x$ respectively. This simplifies to the following equation of motion for a one-dimensional longitudinal wave:

$$\frac{\partial \sigma_x}{\partial x} = \rho \frac{\partial^2 u}{\partial t^2} \tag{2.9.2}$$

By introducing a stress-strain relationship with the constrained modulus M, we can rewrite the equation in terms of displacement:

$$M = \frac{E(1-\nu)}{(1+\nu)(1+2\nu)} = \frac{\sigma_x}{\epsilon_x}$$

$$\frac{\partial^2 u}{\partial t^2} = \frac{M}{\rho}\frac{\partial^2 u}{\partial x^2} \tag{2.9.3}$$

$$\frac{\partial^2 u}{\partial t^2} = v_p^2 \frac{\partial^2 u}{\partial x^2} \tag{2.9.4}$$

where the parameter v_p, is the wave propagation velocity. An important thing address is that the speed of the propagating wave is dependent only on the stiffness and density of the solid it travels through. Additionally, the velocity of the particles is different than the velocity of the propagating wave. The particle velocity, denoted by $\dot{u}$ is:

$$\dot{u} = \frac{\partial u}{\partial t} = \frac{\epsilon_x \partial x}{\partial t} = \frac{\sigma_x}{\rho v_p} \tag{2.9.5}$$

This points to the proportionality of the particle velocity to the axial stress. The proportionality factor, $\rho \cdot v_p$, is called the specific impedance of the material. Differences between the specific impedance from one material to another, influence the wave propagation behaviour.

2.9.2 1D Torsional Waves

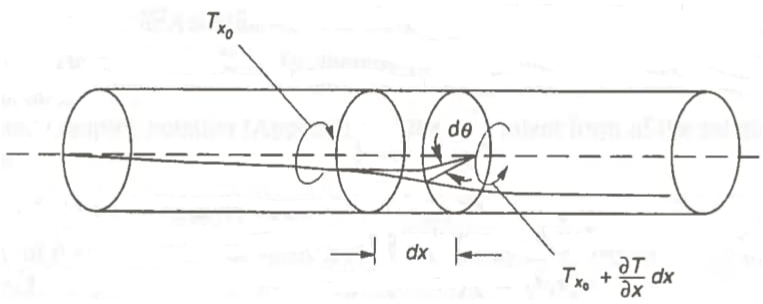

Figure 2.18: Torsional waves in an infinitely long bar (Illustration from Kramer (1996)).

Particle motion for torsional waves is constrained to planes perpendicular to the wave propagation. These waves rotate the bar about its own axis contrary to the lengthening, shortening nature of the longitudinal waves. Looking at a short cylindrical segment of an infinitely long bar with shear modulus G, the following equation can be derived:

$$\left(T_{x0} + \frac{\partial T}{\partial x}\right) - T_{x0} = \rho J dx \frac{\partial^2 \theta}{\partial t^2} \tag{2.9.6}$$

Which simplifies to:

$$\frac{\partial T}{\partial x} = \rho J \frac{\partial^2 \theta}{\partial t^2} \tag{2.9.7}$$

By introducing the torque-rotation relationship, it can be rewritten to:

$$\frac{\partial^2 \theta}{\partial t^2} = \frac{G}{\rho} \frac{\partial^2 \theta}{\partial x^2} = v_s^2 \frac{\partial^2 \theta}{\partial x^2} \tag{2.9.8}$$

where the parameter, v_s is the wave propagation velocity. Once again it should be noted that the velocity of the wave is only dependent on a stiffness modulus and the density of the solid.

2.9.3 3D Waves

Equations of motion for three-dimensional wave propagation is derived by the same principles as the one-dimensional case, within an infinite, unbounded media. The detailed derivations of the equations are not shown in this section but can be further assessed in the book by Kramer (1996). By equilibrium considerations, stress-strain and strain-displacement relationships, the following equations of motion are derived:

$$\rho \frac{\partial^2 w}{\partial t^2} = (\lambda + \mu) \frac{\partial \bar{\epsilon}}{\partial x} + \mu \nabla^2 u \tag{2.9.9}$$

$$\rho \frac{\partial^2 v}{\partial t^2} = (\lambda + \mu) \frac{\partial \bar{\epsilon}}{\partial y} + \mu \nabla^2 v \tag{2.9.10}$$

$$\rho \frac{\partial^2 w}{\partial t^2} = (\lambda + \mu) \frac{\partial \bar{\epsilon}}{\partial z} + \mu \nabla^2 w \tag{2.9.11}$$

where u, v and w represents the displacements in the x, y and z directions respectively, λ and μ are Lamé's constants, $\bar{\epsilon}$ is the volumetric strain. The Laplacian operator ∇^2 represents:

$$\nabla^2 = \frac{\partial^2}{\partial x^2} + \frac{\partial^2}{\partial y^2} + \frac{\partial^2}{\partial z^2} \tag{2.9.12}$$

By differentiating these equations of motion with respect to x, y and z, the wave equation for the dilatational wave can be obtained:

$$\frac{\partial^2 \bar{\epsilon}}{\partial t^2} = \frac{\lambda + 2\mu}{\rho} \nabla^2 \bar{\epsilon} \tag{2.9.13}$$

These types of dilatational waves are called pressure waves or primary waves, and are denoted P-waves. Such waves are travelling through the body at a velocity of:

$$v_p = \sqrt{\frac{\lambda + 2\mu}{\rho}} = \sqrt{\frac{G(2 - 2\nu)}{\rho(1 - 2\nu)}} \tag{2.9.14}$$

A similar expression of the same form can be obtained by eliminating $\bar{\epsilon}$ from the equations of motion and rewriting it to:

$$\frac{\partial^2 \Omega_x}{\partial t^2} = \frac{\mu}{\rho} \nabla^2 \Omega_x \tag{2.9.15}$$

where Ω_x is the rotation of an element about the x-axis. This is a wave equation that describes distortion in the solid and has a velocity of:

$$v_s = \sqrt{\frac{\mu}{\rho}} = \sqrt{\frac{G}{\rho}} \tag{2.9.16}$$

These waves are called shear waves and the particle motion is perpendicular to the direction of the wave propagation, similar to the torsional waves. From a comparison of the wave velocities, it can be shown that the ratio between the two body waves are

$$\frac{v_p}{v_s} = \sqrt{\frac{2 - 2\nu}{1 - 2\nu}} \tag{2.9.17}$$

It is shown in this subsection, that waves travel at different velocities depending on the stiffness and density of the solid. For geological materials which are softer in shear than in volumetric stiffness, the pressure waves will always have a higher velocity than the shear waves. S-waves with horizontal and vertical particle motion are often denoted SH and SV.

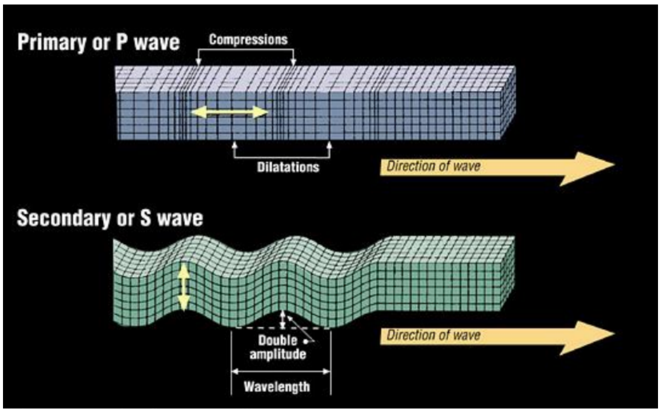

Figure 2.19: Body wave propagation. (Illustrations from Kramer and Kaynia (2017))

2.9.4 Surface Waves

A semi-infinite body with a planar surface is used to model the earth's large spherical shape. The free surface boundary condition makes it possible to derive additional solutions to the equations of motion in the preceding subsection. These solutions describe waves with motion on or near the earth's surface, thus making these surface waves of high importance in the context of earthquake engineering. The two types of surface waves that are most important in earthquake engineering practices are shown in figure 2.20. The love waves consist of horizontal shear waves trapped by multiple reflections in the surficial layer. Their particle motion is confined to the horizontal y-direction, perpendicular to the wave propagation. Rayleigh waves have a propagation shape of a rolling ocean wave and shake the ground both vertically and horizontally.

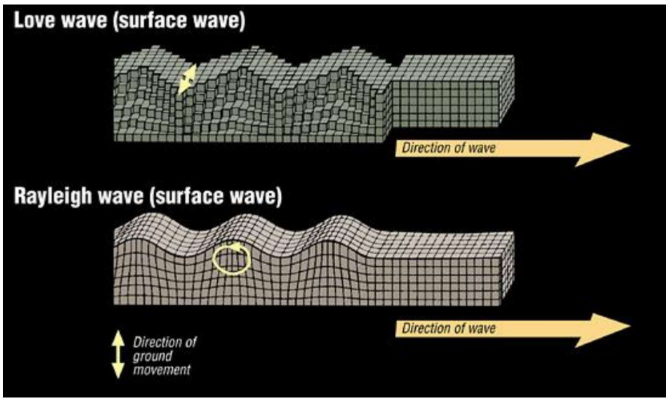
Love wave (surface wave)
Direction of wave
Rayleigh wave (surface wave)
Direction of wave
Direction of ground movement

Figure 2.20: Surface wave propagation. (Illustrations from Kramer and Kaynia (2017))

2.9.5 The Effect of Boundaries on Wave Propagation

To study the behaviour of body waves travelling through a non-homogeneous material, it is important to observe how boundaries affect the propagation of the incoming seismic waves. For a caisson foundation resting in a soft off-shore clay, this is of high importance because of the amplification response at a free surface. Hence, this subsection will cover some brief theory behind boundary effects, with an emphasis on how the impedance ratio influences these effects.

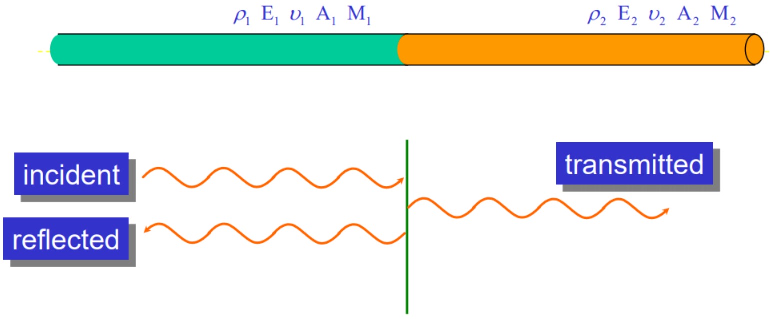
ρ_1 E_1 υ_1 A_1 M_1
ρ_2 E_2 υ_2 A_2 M_2
incident
reflected
transmitted

Figure 2.21: Wave propagation at perpendicular boundary. (Illustrations from Kramer and Kaynia (2017))

At the boundary between the materials, there are two constraints; displacement must be continuous, and equilibrium must be satisfied:

$$A_i + A_r = A_t \tag{2.9.18}$$

$$\sigma_i + \sigma_r = \sigma_t \tag{2.9.19}$$

where A_i, A_r, and A_t are the displacement amplitudes of the incident, reflected, and transmitted wave respectively, while σ_i, σ_r, and σ_t are the stress amplitudes of the incident, reflected and transmitted waves respectively. Introducing compatibility and equilibrium we obtain:

$$A_r = \frac{1-\alpha_z}{1+\alpha_z} A_i \qquad \sigma_r = \frac{\alpha_z - 1}{1+\alpha_z}\sigma_i \tag{2.9.20}$$

$$A_i = \frac{2}{1+\alpha_z} Ai \qquad \sigma_i = \frac{2\alpha_z}{1+\alpha_z}\sigma_i \tag{2.9.21}$$

$$\alpha_z = \frac{\rho_2 \cdot v_2}{\rho_1 \cdot v_1} \tag{2.9.22}$$

Expression 2.9.22, describes the ratio between the product of the mass density and the wave propagation velocity of the two materials. Recalling equation 2.9.5, this product describes the specific impedance of the material. Hence, propagation of waves at the boundary of different materials is controlled by the impedance ratio, α_z.

An infinitely large impedance ratio would thus imply an incident wave encountering a fixed end. This would force a displacement amplitude of zero at the boundary, and the stress would double. With an impedance ratio of zero, meaning the incident wave encountering a free surface, the stress would be zero, and the displacement amplitude would increase by a factor of two. Consequently, amplification of displacement at a free end is of high importance when it comes to earthquake analysis, as most structures are situated at the free surface. Because of the small differences in mass density of geological materials in comparison with differences of wave velocity, the impedance ratio is mostly determined by the ratio of wave velocity between the materials.

2.9.5.1 Inclined Waves

An important effect of earthquake analysis arises when the propagating waves encounter a non-perpendicular boundary. This can alter both the wave type and the direction of the reflected and transmitted wave. In figure 2.22, the propagation of an inclined incident SV wave at a horizontal boundary is shown. Snell's law suggests that waves from a higher velocity material into a lower velocity material will be refracted closer to the normal of the interfaces. Consequently, the refracted SV-waves will have a more perpendicular path to the material boundary.

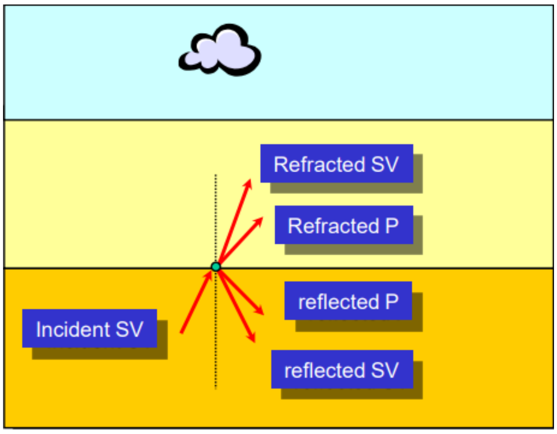
Refracted SV
Refracted P
reflected P
Incident SV
reflected SV

Figure 2.22: Wave propagation at inclined boundary. (Illustrations from Kramer and Kaynia (2017)).

In practice, this means that incoming waves from an earthquake deep underground will be refracted towards an almost vertical propagation path. This is because of the increasing wave propagation velocity with depth. The mechanism is expressed graphically in figure 2.23, and is widely used as a basis for many site response analyses, including NERA.

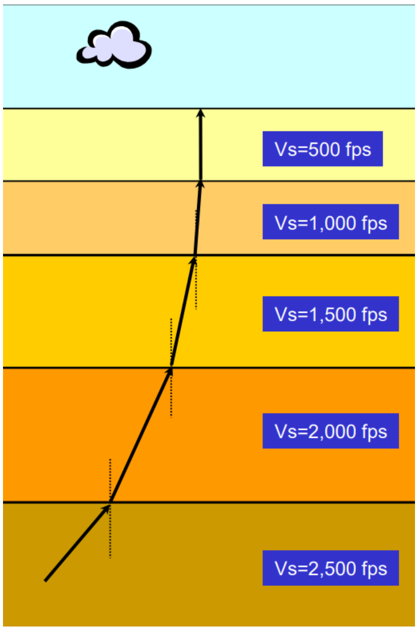
Vs=500 fps
Vs=1,000 fps
Vs=1,500 fps
Vs=2,000 fps
Vs=2,500 fps

Figure 2.23: Wave propagation path in multiple layered body (Illustrations from Kramer and Kaynia (2017)).

2.9.6 Wave Attenuation

The amplitude of a stress wave propagating through a soil medium will decrease with distance. This attenuation is the result of both material and radiation damping (Kramer, 1996).

2.9.6.1 Material damping

As waves propagate through the soil, some of the elastic energy will always be converted to heat or permanent deformations, and the amplitudes of the waves will thus decrease. Due to its mathematical convenience and simple theory, this dissipation of elastic energy is often represented by viscous damping. To explain material damping, soil elements are often modelled as a Kelvin-Voigt solid. This is a thin, linearly visco-elastic material, and it is illustrated in figure 2.24.

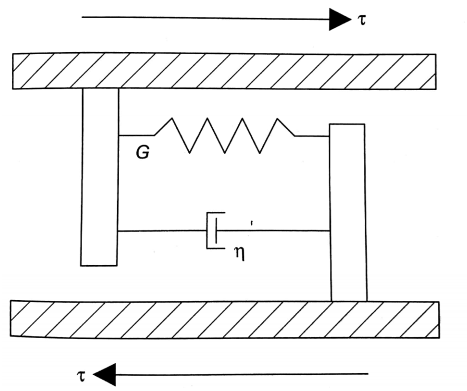

Figure 2.24: Thin element of a Kelvin-Voigt soild exposed to horizontal shear stresses (Illustration from Villaverde (2009)).

The stress-strain relationship is given as:

$$\tau = G \cdot \gamma + \eta \cdot \frac{\partial \gamma}{\partial t} \tag{2.9.23}$$

Where τ is the shear stress, γ is the shear strain, η is the viscosity of the material, G is the shear modulus, and t is time. In one cycle, the elastic energy dissipated is given by the area of the ellipse in figure 2.25, and is expressed as:

$$W_d = \int_{t_0}^{t_0+\frac{2\pi}{\omega}} \tau \frac{\partial \gamma}{\partial t} = \pi \eta \omega \gamma_c^2 \tag{2.9.24}$$

Where W_d is the dissipated elastic energy, ω is the natural frequency of the applied shear stress and γ_c is the cyclic strain. The peak strain energy can be given as:

$$W_s = \frac{1}{2} G \gamma_c^2 \tag{2.9.25}$$

The damping ratio, ξ, is then given as shown in figure 2.25.

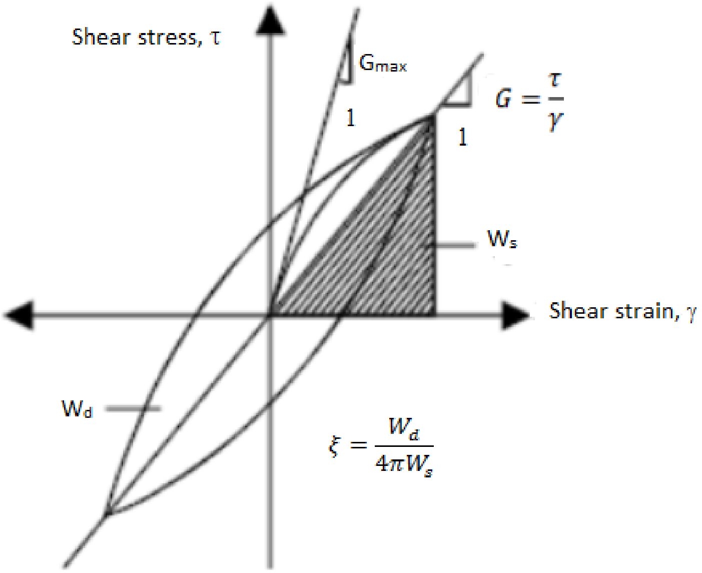

Figure 2.25: Relation between damping, ξ, and dissipated energy W_d(Illustration modified from Khari et al. (2011)).

2.9.6.2 Radiation Damping

Radiation damping is directly related to the geometry of a wave propagating through a soil body. This kind of damping results from the dispersion of wave energy over a larger volume of material as it moves away from the source. The total elastic energy is conserved, but the amplitudes of the waves will decrease with distance.

2.10 Single Degree of Freedom System (SDOF)

To better understand the behaviour of dynamic systems, it is beneficial to know the response of an SDOF system. The SDOF model is the basis of many earthquake engineering topics such as the response spectra, which is covered in the next section. The system is modelled by a simple mass, m resting on top of two mass-less columns with stiffness, k and damping coefficient, c.

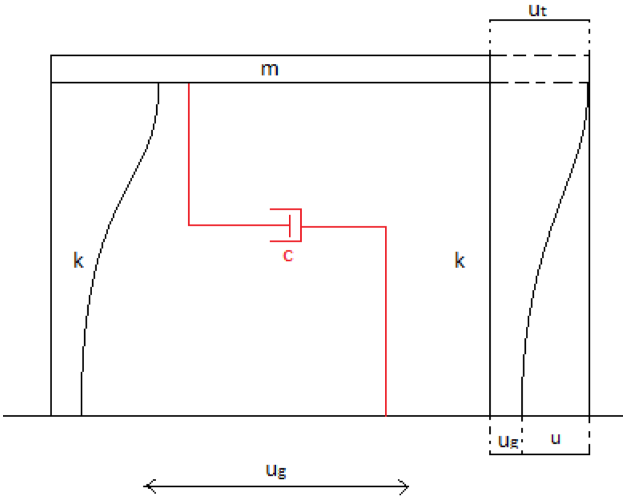

Figure 2.26: Single degree of freedom system with earthquake motion input.

The differential equation for the free vibration undamped system:

$$m\ddot{u} + ku = 0 \tag{2.10.1}$$

By solving this differential equation, the undamped natural circular frequency that satisfies the dynamic equilibrium is found:

$$\omega = \omega_n = \sqrt{\frac{k}{m}} \tag{2.10.2}$$

Derivation of the undamped natural frequency is given in Appendix B.1.

This gives the natural cyclic frequency of vibration, and the natural period of vibration:

$$f_n = \frac{\omega_n}{2\pi} \tag{2.10.3}$$

$$T_n = \frac{1}{f_n} = \frac{2\pi}{\omega_n} \tag{2.10.4}$$

$$\xi = \frac{c}{2m\omega_n} \tag{2.10.5}$$

By taking damping into account, the equation of motion becomes:

$$m\ddot{u}_t + c\dot{u} + ku = 0 \tag{2.10.6}$$

Separating the total displacement into relative displacement, $\ddot{u}$ and ground displacement, $\ddot{u}_g$ gives:

$$\begin{aligned} m(\ddot{u} + \ddot{u}_g) + c\dot{u} + ku &= 0 \\ m\ddot{u} + c\dot{u} + ku &= -m\ddot{u}_g \end{aligned} \tag{2.10.7}$$

Introducing the damping ratio derived in appendix B.2:

$$\xi = \frac{c}{c_c} = \frac{c}{2m\omega} \tag{2.10.8}$$

Where c_c is called the critical damping constant which expresses the damping where no actual vibration arises. The damping ratio describes the fraction of critical damping coefficient in the system.

Writing c in terms of ω, ξ and m, and inserting into (2.10.7) yields:

$$\ddot{u} + 2\xi\omega\dot{u} + \omega^2 u = -\ddot{u}_g \tag{2.10.9}$$

With a given input ground motion $\ddot{u}_g$ it is possible to solve for the response of the single degree of freedom system with boundary conditions $\dot{u}(t=0) = \dot{u}_0$ and $u(t=0) = u_0$. A commonly adapted way of calculating the solution for the SDOF is Newmark's numerical integration method.

2.11 The Response Spectrum

Important parameters from the recorded ground motions include peak relative displacement and peak absolute acceleration. To simplify the reading of these parameters, the recorded ground motion is used as base input in an SDOF equation with different combinations of natural frequency, ω and damping ratio, ξ. For each of these combinations, the peak relative displacement are found and plotted as functions with respect to ξ and natural period, T_n. This plot is called the displacement response spectrum and represents the maximum relative displacement of every structure with natural period T_n.

$$S_a = \omega^2 S_d = \omega S_v \tag{2.11.1}$$

Where S_a is the spectral pseudo acceleration, S_d is the spectral relative displacement, and S_v is the spectral pseudo velocity.

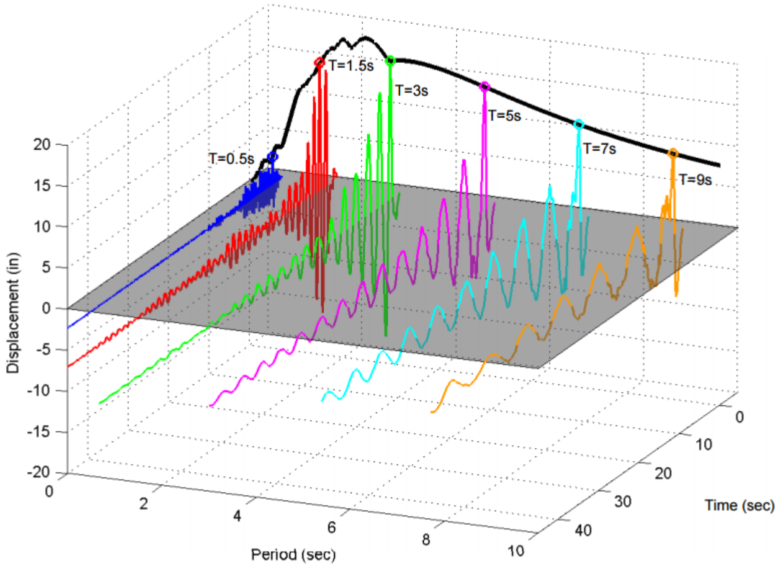

Figure 2.27: Construction of a response spectrum (Illustration from QuakeManager).

2.11.1 Design Spectrum (Target Response Spectra)

A challenging aspect of earthquake design is the fact that acceleration time histories vary significantly from one earthquake to another, thus making each response spectra unique. It is therefore unlikely that the properties of an earthquake are similar to another. Also, the peaks and valleys from the response spectra do not collaborate well with structure design as they show a high level of uncertainty. A smoother curve based on several earthquake motions for the given site is therefore required. These are called design spectra and represent an average design response of structures for a given seismic area. A design spectra borrowed from Eurocode 8 (ec8 (1996)) is shown in figure 2.28.

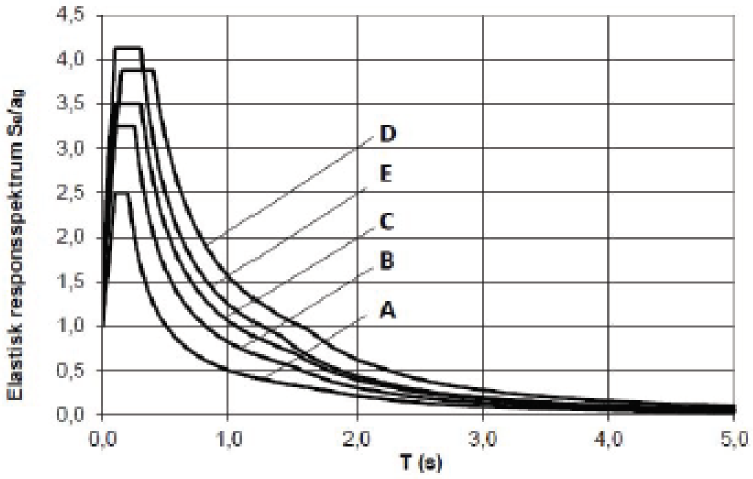

Figure 2.28: Design spectra by Eurocode 8, for different ground types.

2.12 Soil-Structure Interaction

An important aspect regarding the dynamic response of a structure embedded in soil, is the interaction between the structure and the surrounding soil. The two phenomena that cause these effects are kinematic interaction and inertial interaction.

2.12.1 Kinematic Interaction

The presence of a stiff foundation embedded in or laying on top of soil with lower stiffness causes differential motion between the foundation and the free-field motion. The deviance from the free-field motion is caused by an effect called kinematic interaction. The effect is present even if the foundation has no mass, it only has to be rigid enough to prevent it from following the free-field motion. Three different mechanisms can cause deviation of the foundation motion to the free-field motion:

- Wave scattering: scattering of seismic waves off corners and edges of the foundation.
- Base slab averaging: stiffness of the foundation prevents it from matching free field deformations.
- Embedment effects: site response amplification causes a reduction of ground motion with depth.

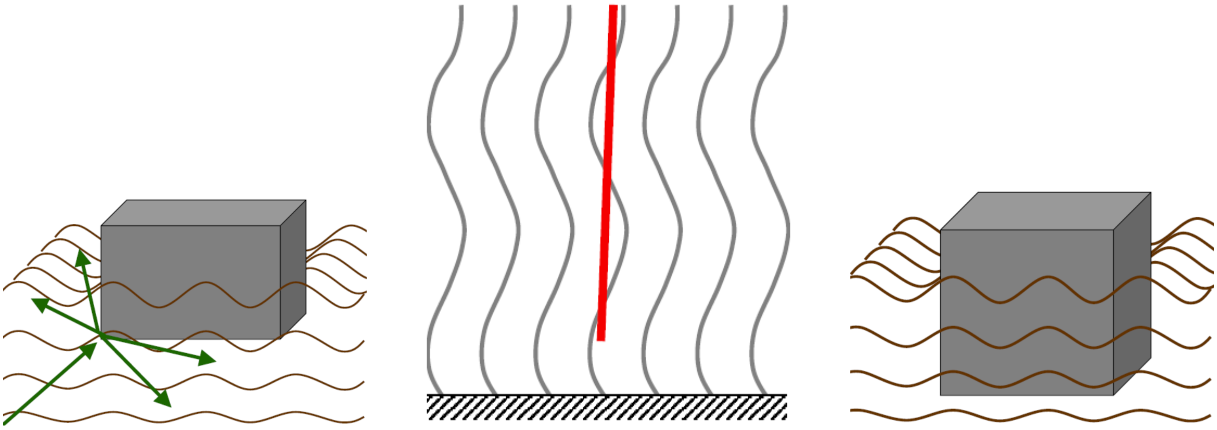

(a) Wave scattering. **(b)** Base slab averaging. **(c)** Embedment effects.

Figure 2.29: Kinematic interaction (Illustration from Kramer and Kaynia, 2017).

2.12.2 Inertial Interaction

When foundation mass is included, inertial interaction is studied. The forces transmitted to the soil by the foundation causes translation relative to free-field. This inertial interaction combined with the kinematic interaction describes the full soil-structure interaction, denoted SSI.

In general, the natural frequency of a soil-structure system is lower than the structure's. Consequently, it is often referred to as a positive effect when looking at structure demands, but since SSI allows rotation and relative translation of the foundation, the overall displacements might also become greater. SSI effects become more significant with increasing relative stiffness between the foundation and the surrounding soil, as it acts as a period lengthening effect. Thus making it an important topic when looking at any stiff sub-sea structure embedded in soft soil.

Chapter 3

Method

3.1 Nonlinear Earthquake Site Response Analysis

To determine the free-field displacement time series at depths along the caisson, non-linear site response analyses are performed for every earthquake. This is done using NERA (Non-linear Earthquake site Response Analysis) which is a non-linear time domain site response analysis program (Bardet and Tobita, 2001).

Measurements of earthquake excitation on a soil surface, compared to a nearby bedrock outcrop will show great variation. In the section covering wave propagation, the impedance ratio, and most importantly the wave velocity was found to influence the propagating path of reflected and refracted waves. The soil stiffness and strength greatly influences how big the amplified response from the incoming input ground motion is. The wave velocity influences the soil's dynamic response, as stiffer soil tends to amplify response at higher frequencies, while softer soil amplifies at lower frequencies.

To describe how the earthquake excitation differs at various depths in a layered soil body over rigid rock, a transfer function is used. In site response, the transfer function relates the input excitation to an output excitation. To derive the transfer function, shearing characteristics of a Kelvin Voigt solid (section 2.9.6.1) are used to rewrite the wave equation to:

$$\rho\frac{\partial^2 u}{\partial t^2} = G\frac{\partial^2 u}{\partial z^2} + \eta\frac{\partial^3 u}{\partial z^2 \partial t} \tag{3.1.1}$$

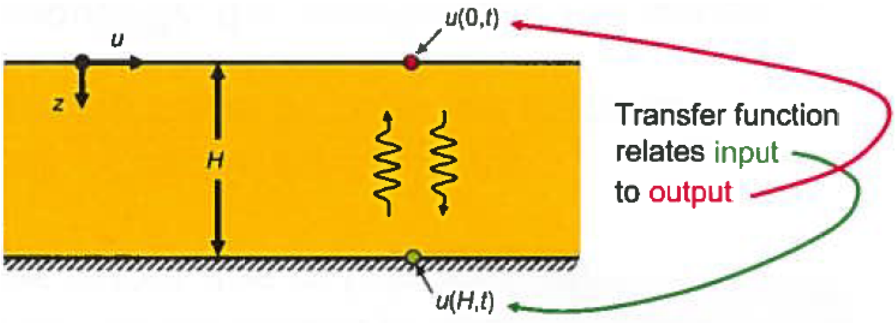

Figure 3.1: Geometry of a soil layer over rigid rock (Illustration from Kramer and Kaynia (2017)).

Solving this equation with boundary conditions for a damped soil on rigid rock (Kramer, 1996), gives a transfer function relating displacements at the top compared to the bottom:

$$|F(\omega)| = \frac{u_{max}(0,t)}{u_{max}(H,t)} = \frac{1}{\sqrt{cos^2\left(\frac{\omega H}{v_s}\right) + \left[\xi\left(\frac{\omega H}{v_s}\right)\right]^2}} \tag{3.1.2}$$

where H is the height of the soil layer, ω is the eigenfrequency of the wave, and v_s is the shear wave velocity. By observation, small damping ratios indicate that the amplification of the excitation is frequency dependent. The amplification is highest at frequencies near the natural frequency of the soil layer, as displayed in figure 3.2. Note that the amplification is highest at the first natural frequency and decays for higher eigenfrequencies. The first eigenfrequency is commonly called the fundamental frequency.

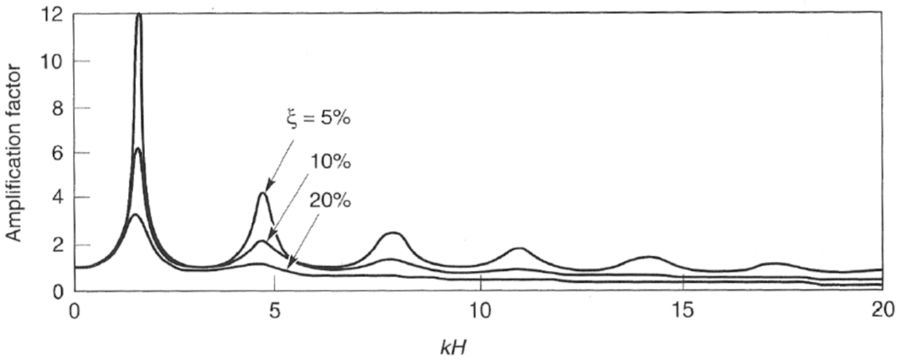

Figure 3.2: Amplification of soil layer at natural frequencies (Illustration from Kramer (1996)).

In this thesis, a one-dimensional site response is performed to obtain input time series for the finite element analysis. The site response analysis will be conducted using the computer program NERA, developed by *The University of Southern California*. The reasoning behind choosing a one-dimensional analysis, is because of the highly unknown two- and three-dimensional soil layering in the ground. Hence, the assumption of a horizontally layered body of soil beneath the ground surface is made.

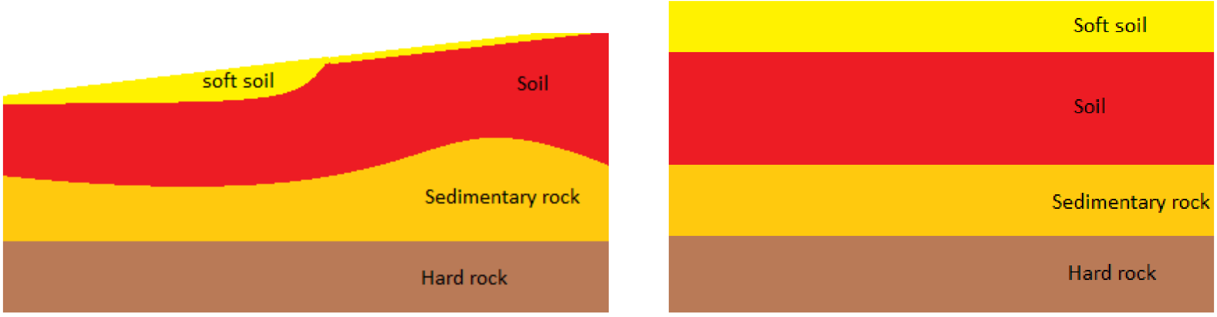

(a) Possible 2D soil layering. **(b)** Simplified soil profile for 1D.

Figure 3.3: Simplifying of soil profiles to use in NERA (not actual soil profile).

3.1.1 Basic Calculation Process

Nonlinear earthquake analysis is done in time domain and uses the wave equation for visco-elastic medium:

$$\rho \frac{\partial^2 d}{\partial t^2} + \eta \frac{\partial d}{\partial t} = \frac{\partial \tau}{\partial z} \tag{3.1.3}$$

where ρ is the mass density, τ is the shear stress, η is the mass-proportional damping coefficient, and d is the horizontal displacement. An easy visual representation of the spatial discretization is shown in figure 3.4.

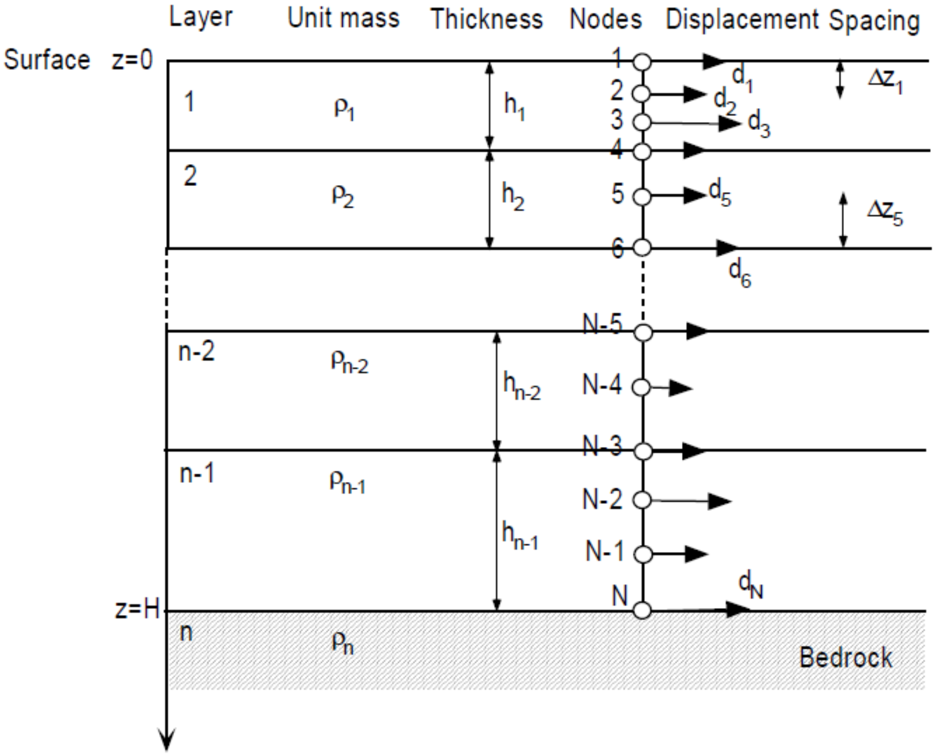
Layer
Unit mass
Thickness
Nodes
Displacement
Spacing
Surface z=0
1
2
n-2
n-1
n
z=H
ρ_1
ρ_2
ρ_{n-2}
ρ_{n-1}
ρ_n
h_1
h_2
h_{n-2}
h_{n-1}
1
2
3
4
5
6
N-5
N-4
N-3
N-2
N-1
N
d_1
d_2
d_3
d_5
d_6
d_N
Δz_1
Δz_5
Bedrock

Figure 3.4: Brief overview of the one dimensional spatial discretization (Illustration from Bardet and Tobita (2001)).

In NERA, direct integration of the wave equation for a visco-elastic medium is used. This is done through the use of a finite difference formulation with the central difference algorithm (Hughes et al., 1986). Integration in small time steps allows the user to apply any linear or nonlinear stress-strain model. At the beginning of an iteration, the stress-strain relationship is calculated to be used within this time step. By doing this, the nonlinear site response program includes the nonlinearity of the soil.

3.1.2 The Nonlinear and Hysteretic Model in NERA

The nonlinear and hysteretic model in NERA is based on the model of Iwan and Mroz and is presented in the program's manual. They proposed an extended Masing model for nonlinear stress-strain curves, using a series-parallel model consisting of n mechanical elements and slip elements to represent the system behaviour. These elements and slip elements all have different stiffnesses, k, and sliding resistances, R. The sliders have increasing resistances, meaning $R_1 < R_2 < R_3 < ... < R_n$. During loading, slider i yields when τ reaches R_i. The basis of the model is illustrated in figure 3.5.

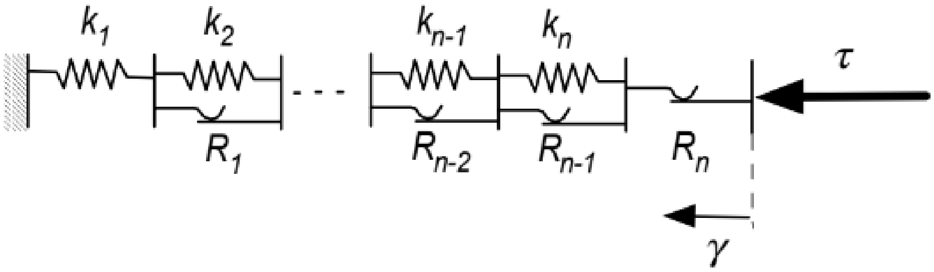

Figure 3.5: Representative illustration of stress-strain model used by Iwan (1967) and Mróz (1967). (Illustration from Bardet and Tobita, 2001).

An illustration of how NERA computes the stress-strain curve is given in figure 3.7. This figure shows the backbone curve and cyclic hysteretic behaviour for a model with two sliders. It is clear that the stress-strain curve is piecewise linear. The stress-strain increment is related through the tangential modulus H which varies in steps, as illustrated in the same figure.

$$H = \frac{d\tau}{d\gamma} \tag{3.1.4}$$

The tangential modulus, H, for n sliders is given in figure 3.6.

$$H = \begin{cases} H_1 = k_1 & \text{if } 0 \le \tau < R_1 \\ H_2 = \left(k_1^{-1} + k_2^{-1}\right)^{-1} & \text{if } R_1 \le \tau < R_2 \\ & \\ H_{n-1} = \left(k_1^{-1} + k_2^{-1} + \ldots + k_{n-1}^{-1}\right)^{-1} & \text{if } R_{n-2} \le \tau < R_{n-1} \\ H_n = \left(k_1^{-1} + k_2^{-1} + \ldots + k_{n-1}^{-1} + k_n^{-1}\right)^{-1} & \text{if } R_{n-1} \le \tau < R_n \\ 0 & \text{if } \tau = R_n \end{cases}$$

Figure 3.6: The tangential modulus, H, for n sliders. (Illustration from Bardet and Tobita, 2001).

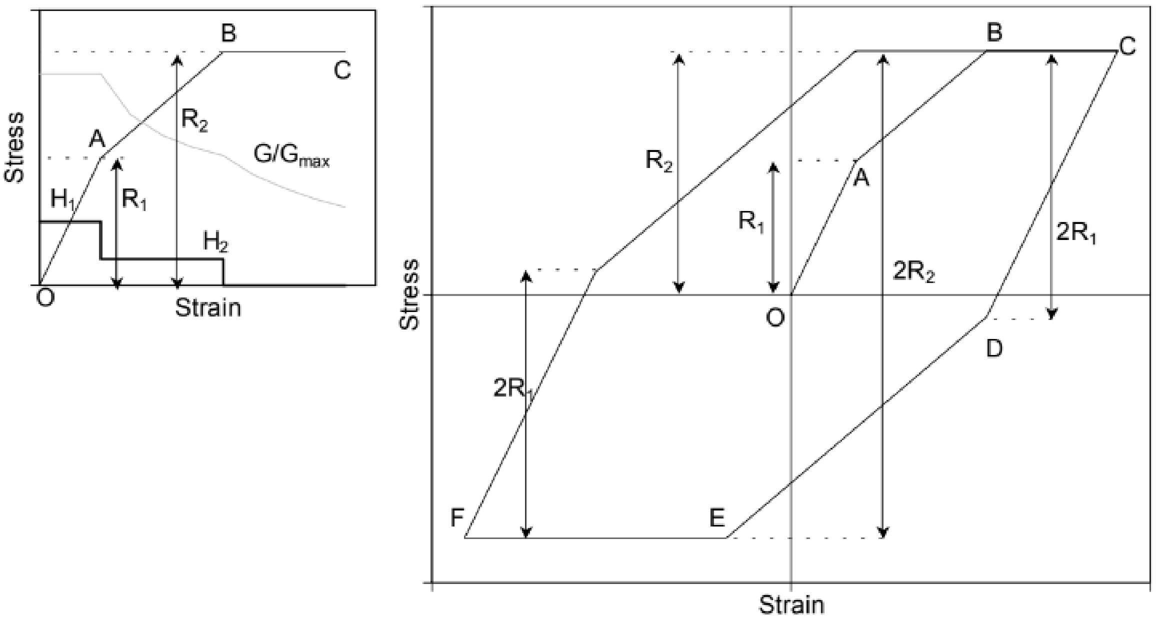

Figure 3.7: Left: backbone curve. Right: hysteretic stress strain loop for two sliders. (Illustration from Bardet and Tobita, 2001).

For further information on the model, the reader is referred to the manual.

3.2 Simplified Time Series Analysis

Simplified time series analysis (STSA) is an approach for determining the dynamic response following an earthquake. In addition, it permits estimating permanent displacements. A description of the basics of the STSA method is given in Athanasiu et al. (2015), and a short summary is given in the following paragraphs.

An alternative to a fully integrated 3D analysis is to represent the bucket foundation as a beam supported by non-linear springs distributed along the beam. Springs are applied in both the horizontal directions and in the vertical direction. These springs represent the stiffness of the soil. Dynamic input in the form of earthquake time series is then applied at the end of each spring, in each of the three orthogonal directions. The simplified model is illustrated in figure 3.8.

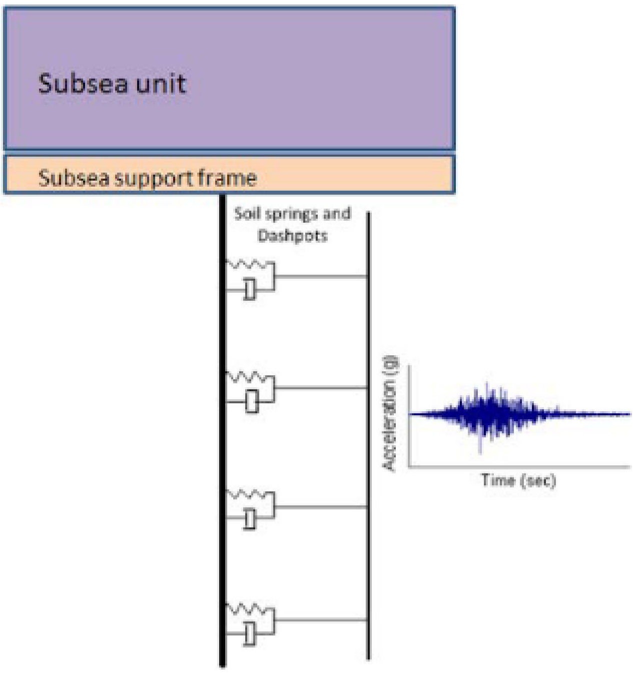

Figure 3.8: Model used in STSA (Illustration from Athanasiu et al. (2015)).

Again, the challenge is to create a representative soil model to adequately represent the soil's dynamic response and the development of permanent displacements. The dynamic response can be captured by using a model following the Masing rule, while permanent displacements can be predicted by modifying the model to follow a rule that adds displacements related to the average and the cyclic components of forces in the springs. Thus, this requires a purpose build material model (Athanasiu et al., 2015).

3.3 Simplified Modal Non-linear Analysis

A simplified and time efficient procedure for the calculation of dynamic loads on sub-sea structures was developed by Athanasiu et al. (2015). This simplified modal non-linear analysis (SMNA) utilizes a yield surface in moment-force space, together with force-displacement and moment-rotation curves to model the structure response. A visual representation of the SMNA model is shown in 3.9. A short summary of the method is provided in this section.

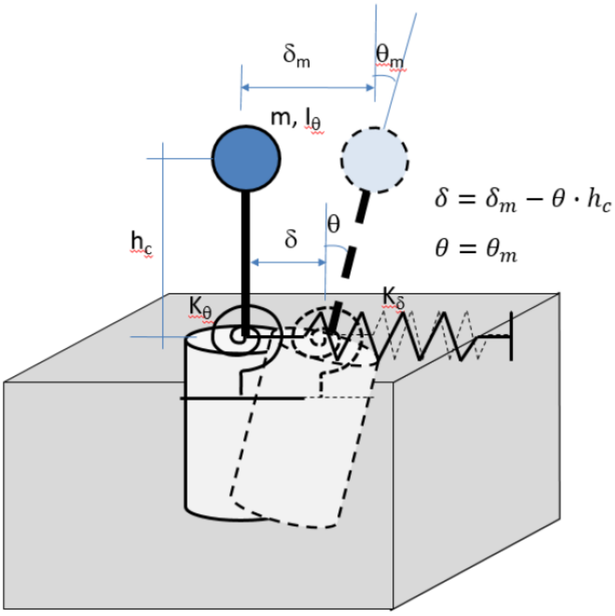

Figure 3.9: Structure model (Illustration from (Athanasiu et al., 2015)).

Equations of motion for the free, undamped vibrations about the centre of mass can be written as:

$$\begin{gathered} m \cdot \ddot{\delta} + K_\delta \cdot (\delta_m - \theta \cdot h_c) = 0 \\ I_\theta \cdot \ddot{\theta} - K_\delta \cdot (\delta_m - \theta \cdot h_c) \cdot h_c + K_\theta \cdot \theta) \end{gathered} \tag{3.3.1}$$

where m is the mass matrix, K_δ is the translational stiffness, and K_θ is the rotational stiffness.

Performing a modal analysis with orthogonality of modes and the site response spectra, the maximum accelerations of each mode, n, can be calculated:

$$\ddot{q}_{n,max} = \frac{L_n}{Mass_n} \cdot PS_a(T_n) = A_n \tag{3.3.2}$$

where L_n is the n^{th} modal excitation factor, $Mass_n$ is the n^{th} modal mass, and A_n is the n^{th} modal acceleration amplitude. Maximum modal force, Q_n and moment, M_n are calculated by:

$$\begin{gathered} Q_n = A_n \cdot m(1,1) \cdot \phi_{n1} \\ M_n = A_n \cdot m(2,2) \cdot \phi_{n2} \end{gathered} \tag{3.3.3}$$

where ϕ_{n1} and ϕ_{n2} are vectors describing the mode shapes. Total force and moment can be calculated by using the square root of the sum of squares. The assumption of using the maxima of each mode, and taking the square root of the sum of squares is typically too conservative. In reality, the maxima occur at different time instants during the earthquake excitation phase.

The yield surface is modelled through the use of soil-caisson finite element analyses. To express the yield surface, different loading ratios h=$\frac{M}{Q}$ are applied until failure and plotted into a Q-M space. To draw the full failure line, equation 3.3.4 is used.

$$\left(\frac{Q}{f \cdot Q_{ult,0}}\right)^{\alpha} + \left(\frac{M}{f \cdot M_{ult,0}}\right)^{\beta} \tag{3.3.4}$$

Where $Q_{ult,0}$ and $M_{ult,0}$ are ultimate values when loaded solely by horizontal force or moment respectively. α and β are curve-fitting parameters.

Initial stiffness's, $K_{\delta max}$ and $K_{\theta max}$, as functions of h, and secant stiffness ratios, $K_{\delta}/K_{\delta max}$ and $K_{\theta}/K_{\theta max}$, as functions of displacement and rotations, are used to form the backbone curve.

To account for the non-linearity of soil, an iterative process with assumed loading ratio h and secant stiffness's are used to perform the modal analysis. This gives an estimate of natural frequencies and periods of dynamic loads, as well as forces, moment, displacement and rotation. The process is repeated until a set of conditions have been satisfied. The reader is encouraged to see the original article, Athanasiu et al. (2015) for a thorough explanation of the method.

Chapter 4

Evaluation of Input

4.1 Caisson and Module Input

This section covers the caisson and module input given by Multiconsult. Dimensions for both caisson and module are presented in table 4.1, while material properties are given in table 4.2. The module is simplified as a box with a height equaling 6 meters and a width of 10 meters. The length to diameter ratio of the caisson equals $\frac{L}{D}$=2.27. For the centre of gravity, reference depth is seabed level.

Table 4.1: Dimensions of caisson and module.

Notation	**Value**	**Unit**	**Description**
D	7.5	[m]	Diameter of caisson
t	0.03	[m]	Thickness of caisson skirt
L	17	[m]	Length of suction caisson
b_{module}	10	[m]	Width of module
h_{module}	6	[m]	Height of module
CoG_{module}	3.2	[m]	Center of gravity of module
CoG_{global}	-6.1	[m]	Global Center of gravity

Table 4.2: Material properties of caisson and soil plug.

Notation	**Value**	**Unit**	**Description**
ρ_{steel}	7850	$[kg/m^3]$	Steel density
E_{steel}	$210 * 10^9$	$[N/m^2]$	Young's modulus for steel
v	0.3	[-]	Poisson ratio
ρ_{soil}	1500	$[kg/m^3]$	Soil density

The masses of the caisson and the module, as well as the different contributions to the global moment of inertia, are given in table 4.3. Due to the module being situated in water, added mass effects are considered. The global moment of inertia was found directly from ANSYS. Since the module was simplified as an equivalent box, its moment of inertia was found by hand calculation as in equation 4.1.1. The moment of inertia due to the added mass was approximated as 30% of the module inertia.

$$I_{module} = \frac{1}{12} \cdot m_{module} \cdot (h_{module}^2 + b_{module}^2) \tag{4.1.1}$$

Table 4.3: Masses and moment of inertia.

Notation	Value	Unit	Description
$m_{caisson}$	94.0	[ton]	Mass of Caisson
$m_{soil\ plug}$	1108.6	[ton]	Mass of soil plug
m_{module}	239.6	[ton]	Mass of module and top plate
m_{added}	71.9	[ton]	Added mass of module
I_{module}	2716	$[ton \cdot m^2]$	Moment of inertia of module+top plate
$I_{added\ mass}$	815	$[ton \cdot m^2]$	Moment of inertia of added mass
I_{total}	74919	$[ton \cdot m^2]$	Global moment of inertia

4.2 Input Time Histories

Dynamic input in the form of seven synthetic earthquake accelerograms were given by Multiconsult. The time series are based on a return period of 3300 years. The soil profile used in NERA was also given by Multiconsult and is discussed in section 4.3. The earthquake time series were given at bedrock outcrop and thus needed to be adjusted to account for depth effects and the transition between layers. To obtain how the acceleration and displacements varies in the soil profile, a nonlinear site response analysis was performed, using the program NERA (Non-linear Earthquake site Response Analysis). The basics of this site response analysis is elaborated in section 3.1.

The artificial earthquake accelerograms are matched to a defined target response spectrum for the specific site. Various methods and assumptions are developed for calculating such accelerograms. Considering that these accelerograms are not real, one could possibly get a more natural structural response using real, observed accelerograms. However, if there are no representative accelerograms available, synthetic accelerograms are a decent alternative.

It was deemed sufficient to consider only four out of the seven synthetic accelerograms. This was partly due to the extensive work needed to create input for the analyses. Peak ground acceleration, duration and significant duration(time between first and last occurrence of an acceleration larger than 0.05g) are given in table 4.4. A visual representation of the input accelerograms can be seen in appendix A.

Table 4.4: Earthquake input data.

Synthetic accelogram	PGA [g]	Duration [sec]	Significant duration [sec]
1	0.439	81.915	18.310
3	0.458	81.915	13.530
5	0.440	81.915	9.170
6	0.439	81.915	20.905

Given the acceleration time history at bedrock as input, the user can define output depths at which time histories, response spectra, and stress-strain relations are obtained. This yields the total acceleration at this depth, as well as the relative velocity and displacement. The total velocity and displacement with depth is not calculated but can be approximated using the Newmark beta-method given in equation 4.2.1 and 4.2.2.

$$v_{n+1} = v_n + (1-\alpha)\Delta t \cdot a_n + \alpha \cdot t \cdot a_{n+1}, \text{ for } 0 < \alpha < 1 \tag{4.2.1}$$

$$d_{n+1} = d_n + \Delta t \cdot v_n + \frac{1}{2}(1-2\beta) \cdot \Delta t^2 \cdot a_n + \beta \cdot \Delta t^2 \cdot a_{n+1}, \text{ for } 0 < 2\beta < 1 \tag{4.2.2}$$

Where the notation d, v and a are for displacement, velocity and acceleration respectively. The parameters β and α are set to $\frac{1}{4}$ and $\frac{1}{2}$ respectively, which yields the average acceleration method. The time step in the analysis, Δt, is set to 0.005 seconds. Consequently, equation 4.2.2 could be simplified to exclude the beta terms. The total displacements for each depth are then used in the finite element analysis.

4.3 Soil profile input

The soil input given by Multiconsult is a 185-meter deep soil profile consisting of high plasticity offshore deepwater clay. Included in the input is a shear strength profile varying linearly with depth, as well as maximum shear modulus, G_{max}, shear wave velocity, v_s, and total unit weight, varying with depth. The shear strength profile is shown in figure 4.1, while the rest is shown in figure 4.2. As the soil profile was given directly as input for NERA, the plots, excluding the Su-plot, are given as stairstep graphs. Underneath the soil profile it is assumed to be bedrock with high stiffness (G_{max}=5000 MPa).

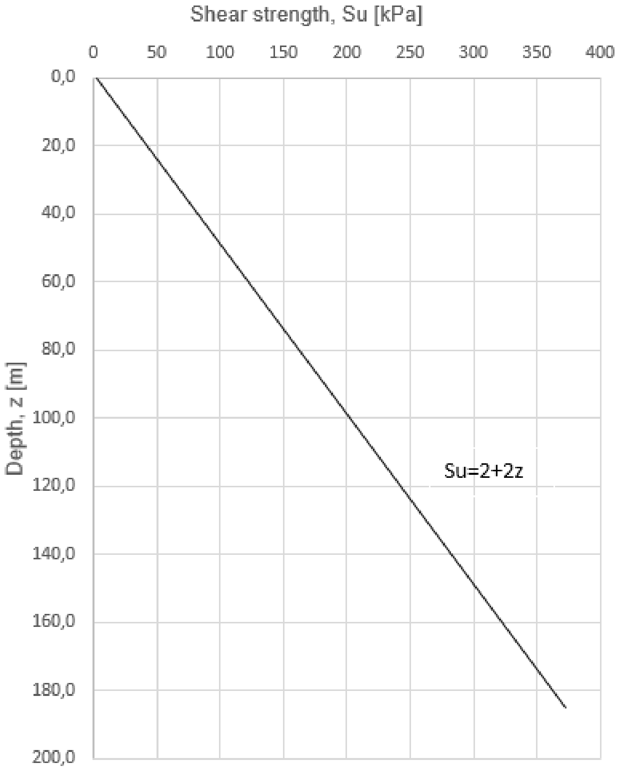

Figure 4.1: Shear strength versus depth.

The closed caisson will be situated in the upper 17 meters of the soil, where the soil consists of soft clay.

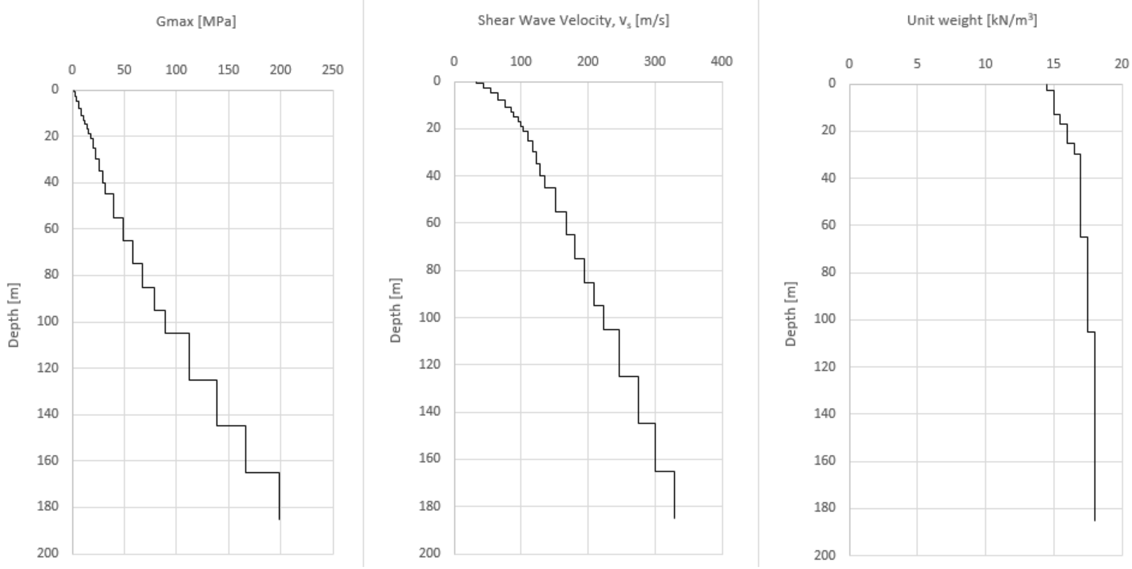

Figure 4.2: Maximum shear modulus, shear velocity and unit weight versus depth.

The weighted average of the shear velocity is 210.2 $\frac{m}{sec}$, and can be used to find the natural periods and frequencies of the soil layer, T_n. This can be done using equations 4.3.1 and 4.3.2.

$$T_n = \frac{4 \cdot H}{(2n-1) \cdot \overline{v_s}}, \text{ for } n = 1, 2, 3... \tag{4.3.1}$$

$$f_n = \frac{1}{T_n}, \text{ for } n = 1, 2, 3... \tag{4.3.2}$$

Where H is the height of the soil profile and $\overline{v_s}$ is the weighted average shear velocity of the soil. The five first natural frequencies are shown in table 4.5. If the incoming earthquake excitation contains a significant amount of frequencies close to these natural frequencies, the soil response will amplify notably.

Table 4.5: Natural periods and frequencies of the five first modes.

n	T_n [sec]	f_n [Hz]
1	3.52	0.28
2	1.17	0.85
3	0.70	1.42
4	0.50	1.99
5	0.39	2.55

The entire soil profile consists of high plasticity offshore deepwater clay, and for calculation accuracy in NERA, the profile is divided into 15 layers with varying material properties.

These materials are denoted 1 to 15, for the top and the bottom layer respectively. Material 1 to 8 covers the upper 17 meters in which the caisson will be situated, and will be emphasised. The shear modulus degradation for the eight first materials is illustrated in figure 4.3.

The cyclic stress-strain behaviour and damping response are often found using a backbone curve and Masing rules. However, this approach does not account for variations in stiffness due to pore pressure accumulation during cyclic loading. According to Yamamoto et al. (2015), the damping ratio curves corresponding to $\frac{G}{G_{max}}$ curves tend to be overestimated, when using the Masing rules. As an alternative to the standard G_{max} method, Yamamoto et al. propose using an equivalent shear modulus, G_{eq}. In contrast to using the $\frac{G}{G_{max}}$ curve and back calculating the damping curve using Masing rules, the desired damping curve is obtained by reducing the initial stiffness, G_{max}, and then back calculating the new $\frac{G}{G_{max}}$ curve. Consequently, one can achieve a more realistic damping curve, at the expense of small strain stiffness. The optimal adjusted G_{max} value is referred to as the equivalent shear modulus, G_{eq}.

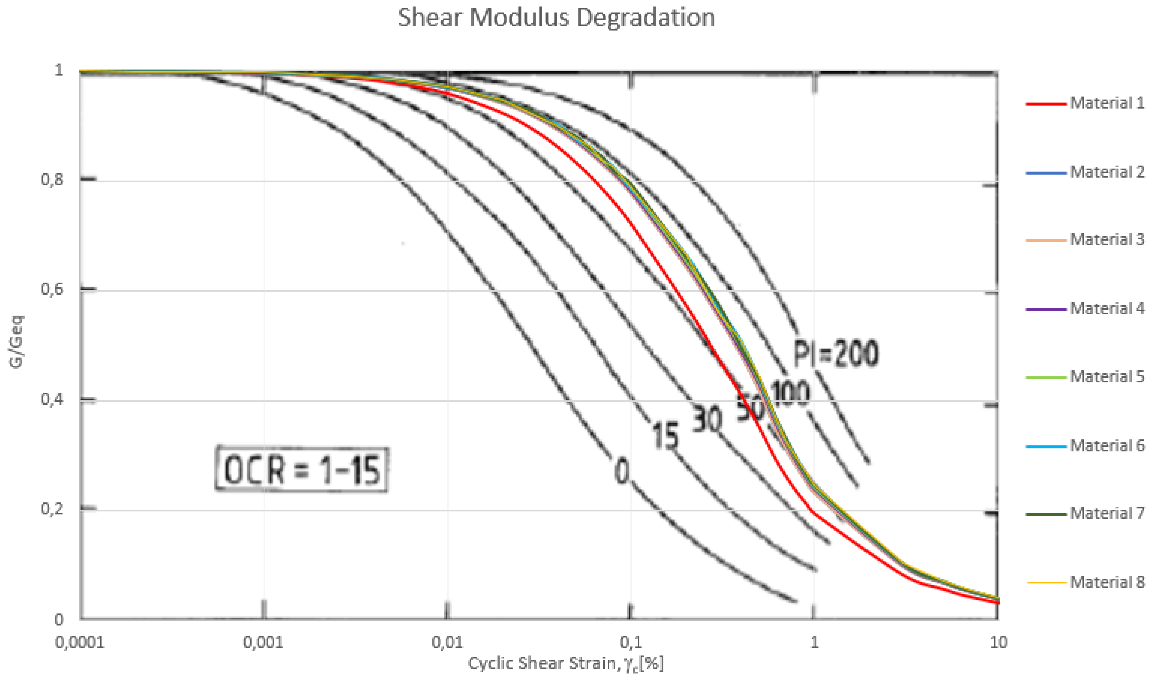

Figure 4.3: Shear modulus degradation for the upper eight materials, $\frac{G}{G_{eq}}$ vs shear strain, compared to curves found by Vucetic and Dobry (1991).

The shear modulus degradation of each material is compared to the Vucetic curves shown in figure 4.3. Furthermore, it indicates the plasticity index of the materials. However, the curves by Vucetic and Dobry (1991) represents the relationship $\frac{G}{G_{max}}$ versus shear strain, while the given material input shows the relationship $\frac{G}{G_{eq}}$ versus shear strain. Consequently, the graphs do not simulate the real plasticity index of the materials. The original $\frac{G}{Gmax}$ curves would probably show a plasticity index in the region of about 30, which is the real value.

4.4 Finite Element Model in ANSYS

The 3D modelling is done using the finite element program, ANSYS Mechanical APDL. A code creating the geometry, mass and inertia was provided by Multiconsult AS as a basis. This code is modified to perform the different time series analyses.

An important part of the time series analyses is the behaviour of the soil springs that act as the interface between the caisson and the surrounding soil. Consequently, an essential part of the modelling is to get a proper hysteretic damping response. Uncertainty about the capabilities of ANSYS regarding the hysteretic response of the spring elements, lead to two sensitivity tests:

- Test of the hysteretic response when using one nonlinear spring with a built-in hysteretic function (COMBIN39 element and sinus displacement load).
- Test of the hysteretic response when using 4 bi-linear springs with a built-in hysteretic function (four COMBIN39 elements and sinus displacement load).

A visual representation of the 3D model is provided in figure 4.4. The caisson itself consists of BEAM188 elements vertically connected at nodes with an equal spacing of 1 m. These elements are based on Timoshenko beam theory and are well-suited for large rotation and large strain nonlinear applications. Soil mass is included in the BEAM188 mass. The module on top and added mass are modelled using the MASS21 element. Input for these elements is concentrated mass components and rotary inertia for each element coordinate direction. For simplicity, the mass and moment of inertia for the frame on top of the caisson and the top plate are added to the module mass and inertia. To create a link between the top module and beam elements, the element MPC184 is applied. This is done to create a rigid component between the two elements for transmitting forces and moments.

To model the soil surrounding the caisson, spring-elements of type COMBIN39 are used. These are applied as parallel bi-linear sets at each node. The reasoning behind the use of bi-linear springs in parallell is discussed further in 4.5.2, and is done to assure an appropriate hysteretic response simulating the cyclic nonlinear soil reaction. The COMBIN39 springs are unidirectional elements with a nonlinear force-deflection capability, and no mass or thermal capacity. The springs are applied in three directions at each caisson node and connected to a soil-node. Because of the time series being applied only in the x-direction, we only consider one-dimensional displacements. Hence, the bi-linear spring sets are only applied in the x-direction. Input stiffness for the four bi-linear springs at each depth is calculated as shown in section 4.5.1.

Table 4.6: ANSYS model data.

Component	**Element**	**Description**
Caisson skirt	BEAM188	Beam elements suited for large strain nonlinear applications
Module	MASS21	Mass element with inertia
Added mass	MASS21	Mass element with inertia
Module link	MPC184	Rigid link element to transfer forces and moments
Springs	COMBIN39	2-node nonlinear spring elements

The discretisation of the model is shown in figure 4.4. The module mass element is situated 3.2 meters above seabed level. The caisson itself is 17 meters long, and a set of four parallel bi-linear springs are placed at each meter. A typical point of rotation for caissons situated in soil with linearly increasing shear strength, is located at about two-thirds down of the caisson length. Hence, a vertical spring is placed at 11 meters depth to prevent any additional moment from the vertical spring force.

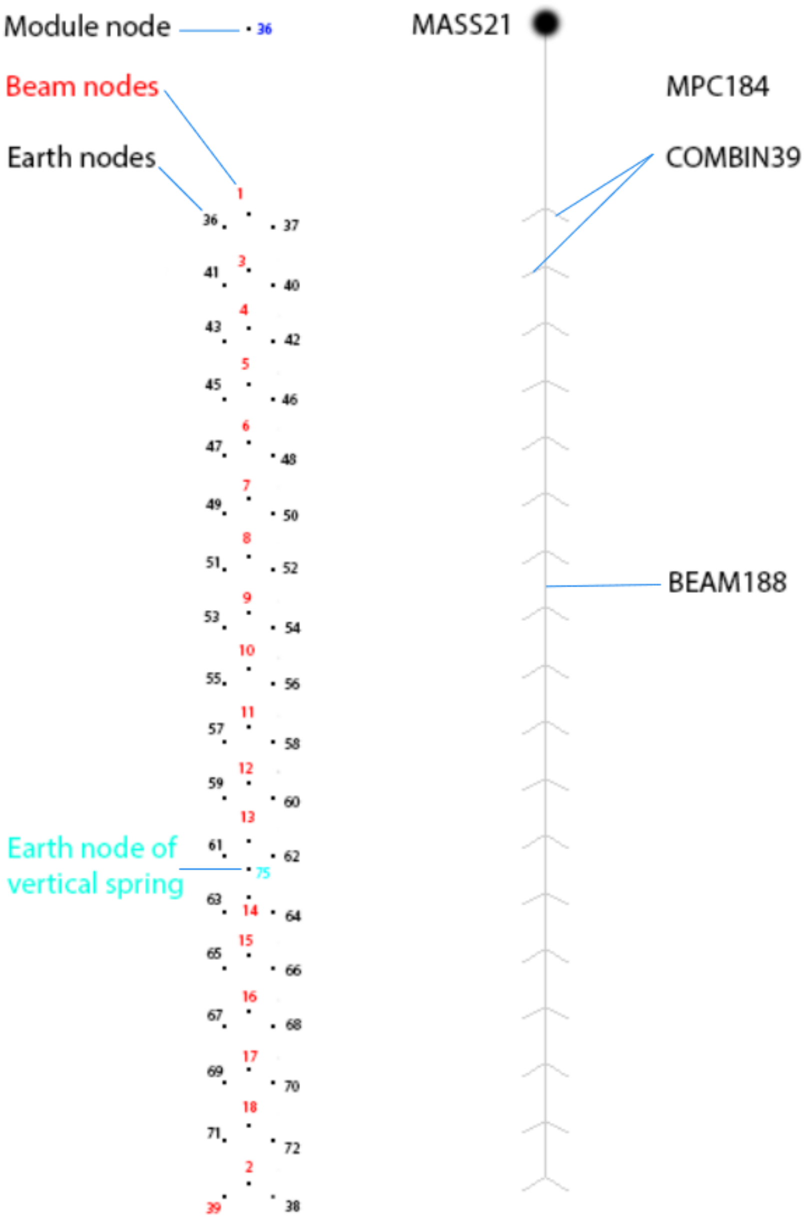
Module node
36
MASS21
Beam nodes
MPC184
Earth nodes
COMBIN39
1
36
37
3
41
40
4
43
42
5
45
46
6
47
48
7
49
50
8
51
52
BEAM188
9
53
54
10
55
56
11
57
58
12
59
60
13
Earth node of vertical spring
61
62
75
63
14
64
15
65
66
16
67
68
17
69
70
18
71
72
2
39
38

Figure 4.4: ANSYS model discretisation.

Earthquake excitation introduces some high frequencies to the system which in the real world would be damped out. In order to obtain the energy dissipation of these higher frequencies in the analysis, 2% Rayleigh damping is applied to the whole system, with damping coefficients as listed in table 4.7.

Table 4.7: Rayleigh damping.

Parameter	description	Value
ξ	Desired Damping ratio	0.02
f_1	First target frequency	0.5 Hz
f_2	Second target frequency	5 Hz
α	Mass proportional damping coefficient	0.1142
β	Stiffness proportional damping coefficient	1.157E-3

4.4.1 Added Mass

When an object is accelerated relative to a surrounding fluid, it appears to have an additional mass component. This added mass increases the inertia effects of such objects. The subsea module on top of the caisson foundation is surrounded by water, hence the added mass will have an effect on the translational response of the subsea structure. In the ANSYS model, an added mass component of 0.3 times the module mass and module inertia is used. These values are recommended by Multiconsult AS.

4.5 Modelling the Stiffness and Hysteretic Behaviour of the Soil

4.5.1 Choice of p-y Method

As the p-y methods used for the calculation of soil stiffness are based on slender piles, the p-y curves were adjusted to better approximate the response of a rigid, large diameter caisson. This adjustment is presented in this section.

As Multiconsult AS previously had calculated the horizontal capacity of the caisson versus lateral displacement using the finite element program PLAXIS 3D, the p-y methods were compared to their results. The lateral capacity, H, is calculated as the average resistance with depth over the average shear strength, $s_{u,ave}$ of the soil profile, and is plotted versus lateral displacement.

$$H = \sum_{i=0}^{L=17} \frac{p_i}{L \cdot s_{u,ave}} \tag{4.5.1}$$

This was done using the p-values for each method, and it was clear that the soil mobilised its strength too slow compared to the PLAXIS results. In this thesis, the diameter of the caisson is set to 7.5 meters with a thickness of 30 mm, while the length is 17 meters. This causes the caisson to act as a stiff beam, and the length to diameter ratio, $\frac{L}{D}$, is significantly smaller than what has been the basis of the different p-y methods presented. Larger shear friction will develop, and the soil will mobilise its strength quicker than predicted by the p-y methods.

The displacement-values, y_0, in which the p-values were plotted against, were scaled further to account for diameter effects. The method proposed by Jeanjean (2009) showed the most promising plot in terms of shape, and it was plotted against a y_{scaled}, using the scaling factor proposed by Stevens and Audibert (1979).

$$y_{scaled} = \frac{y_0}{\sqrt{\frac{D}{D_{ref}}}} = 0.208 \cdot y_0 \tag{4.5.2}$$

Where y_0 is the original, non-scaled displacement for which the p-values were calculated, and D_{ref} is the reference diameter of 0.32385 meters used by Matlock (1970). Using y_{scaled}, the soil reaction was mobilized too quickly. A good fit was achieved by trial, and a corrected displacement value was found to be:

$$y_{corr} = 0.416 \cdot y_0 \tag{4.5.3}$$

The p-values were calculated using y_0, and yielded a somewhat lower horizontal capacity than Plaxis 3D. Hence the horizontal capacity of the Jeanjean method was multiplied by a factor of 1.06. When plotted against y_{corr}, this yielded a horizontal capacity close to PLAXIS. Hence, scaled p-values were plotted versus y_{corr}, to create the backbone curves. The lateral capacity can be seen in figure 4.5. Its capacity is slightly lower for large deformations, but the initial values seem compliant with the PLAXIS results.

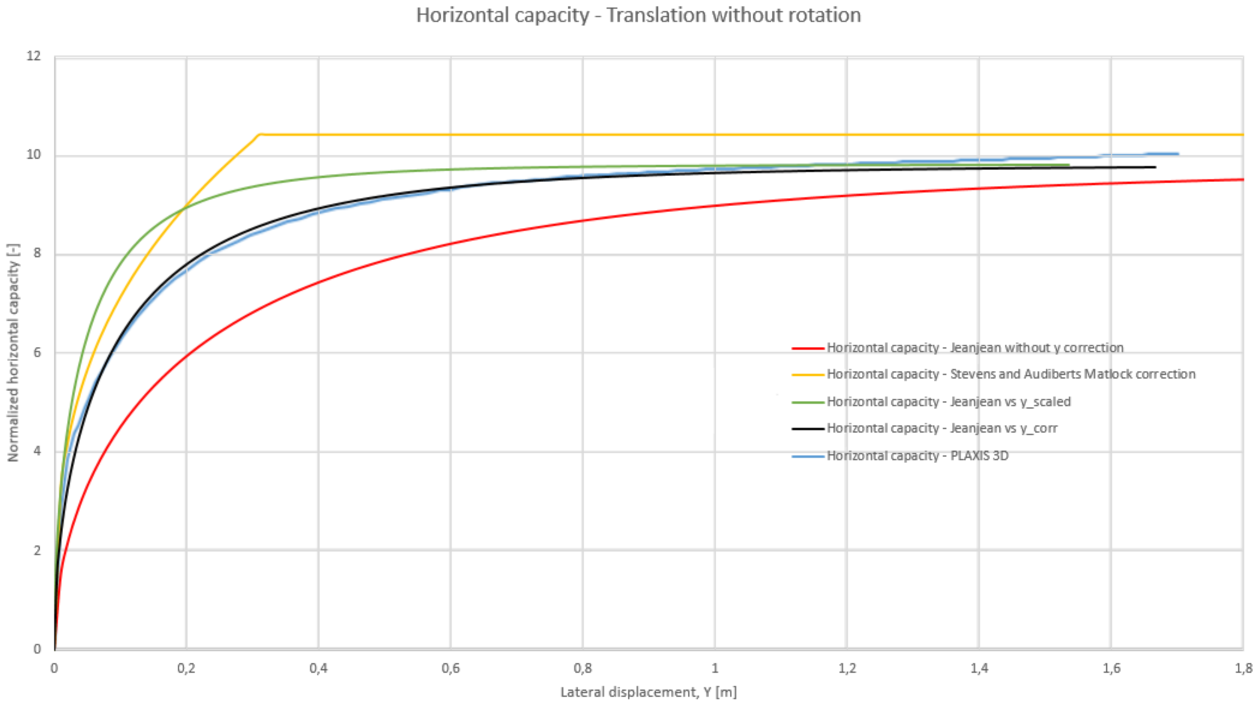

Figure 4.5: Horizontal capacity vs lateral displacement.

To achieve a more accurate lateral capacity, one could consider the added capacity contributions of a rotated caisson. Rotational movement would induce oppositely directed shear stresses on the caisson skirt, working as a force-couple, which would increase the capacity. Additionally, increased resistance at the caisson tip would arise. Therefore, one could possibly get a more accurate response, applying similar additional soil reaction curves as in the PISA model. However, they are neglected in this analysis for simplicity. This is probably the reason why the lateral capacity needed scaling, as PLAXIS 3D executes a full analysis.

This scaling is done based on the soil profile given by Multiconsult AS, and will not necessarily hold for other soil profiles and caisson dimensions.

4.5.2 Bi-linear Springs

When using one nonlinear spring element, the hysteretic curve seemed to give exaggerated damping, and unloading/reloading did not follow the backbone curve. Thus it did not follow the Masing rules, and this model was discarded. An alternative approach was to model the hysteretic response using four bi-linear springs. The reasoning behind this is further elaborated in section 6.1.1.1

The nonlinear back-bone curves were then replaced by piecewise linear curves made up of four bi-linear springs in parallel, each of them defined by its stiffness and ultimate force. This was applied at each depth with one meter spacing. For simplicity and to emphasise the quick mobilisation of the soil, the springs followed the values of table 4.8, with relatively small displacement values for the first three springs. The failure load is assumed to appear at a deformation equal to 10% of the caisson diameter.

Table 4.8: Spring values

Spring no.	y_i [m]	p_i [kN]
1	0.002	$\sim 10 - 15\% \cdot p_{ult,z}$
2	0.02	$\sim 30 - 40\% \cdot p_{ult,z}$
3	0.1	$\sim 60 - 70\% \cdot p_{ult,z}$
4	0.75	$\sim 100\% \cdot p_{ult,z}$

Where $p_{ult,z}$ is the ultimate lateral bearing capacity at depth z. The stiffness of spring i was calculated using equation 4.5.4. While the stiffness of the last spring, spring n, has the stiffness of the last segment of the p-y curve, expressed in equation 4.5.5 (Athanasiu, 1999).

$$k_i = \frac{p_i - p_{i-1}}{y_i - y_{i-1}} - \sum_{j=i+1}^{n} k_j \tag{4.5.4}$$

$$k_n = \frac{p_n - p_{n-1}}{y_n - y_{n-1}} \tag{4.5.5}$$

Where k is the stiffness, p is the force and y is the displacement. The stiffness of each spring is the slope of each segment of the multilinear curve. An illustration of such a spring curve is shown in figure 4.6, valid for the seabed level.

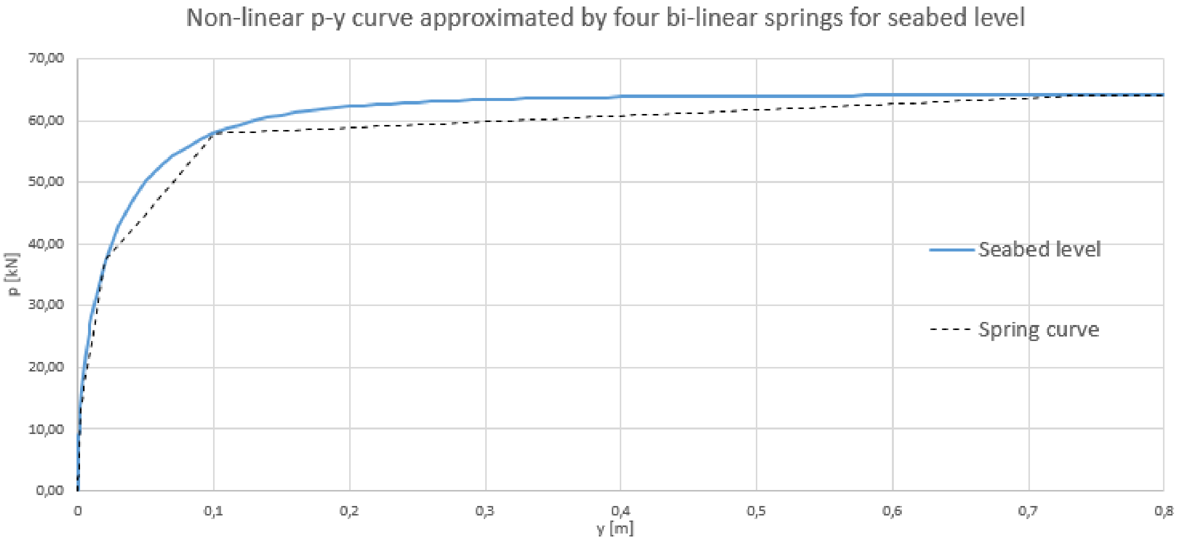

Figure 4.6: Multilinear curve fitted to the nonlinear p-y curve at seabed level.

4.6 Input for Modal Analysis

In this section, the input used in the in-house developed modal analysis program provided by Multiconsult, is presented. The simplified non-linear modal analysis (SMNA) is implemented in this program. The program calculates an equivalent length and an equivalent distributed mass based on the dimensions of the caisson and module, presented in section 4.1.

The program calculates the two first eigenperiods of the caisson. Based on these, it calculates the spectral acceleration from the response spectrum in figure 4.7. The spectrum used in the modal analysis is a typical response spectrum for an area with high seismic activity and soft soil with a high plasticity. The spectra includes 5% damping.

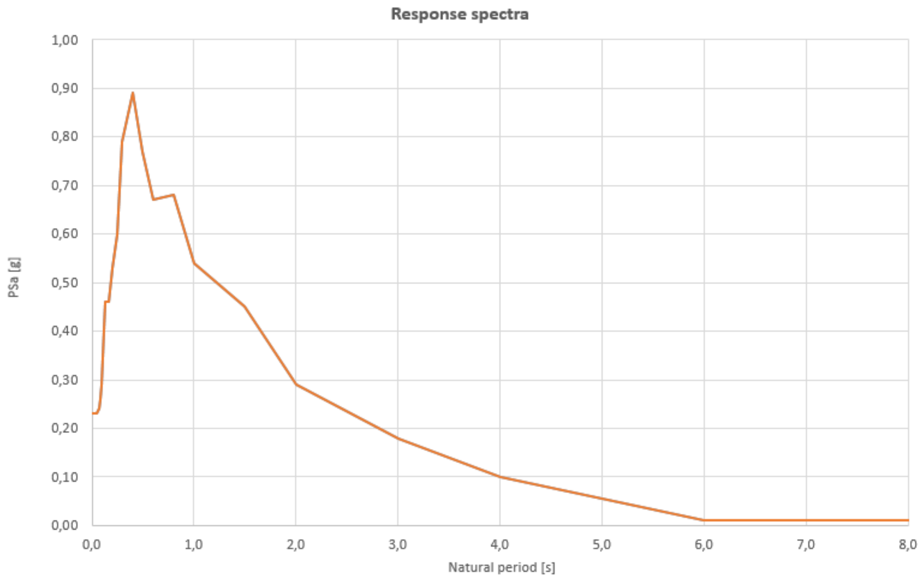

Figure 4.7: Response spectra input for modal analysis with 5% damping.

4.6.1 Calculation of Reaction Forces

Comparable results from the modal analysis include acceleration, displacement and rotation. Equations for simplified calculation of the caisson's bending moment at seabed level is shown in equation 4.6.1. Horizontal force is calculated by multiplying the module mass with the module acceleration.

$$M = m \cdot \ddot{u} \cdot \Delta + I \cdot \omega \tag{4.6.1}$$

where m, $\ddot{u}$ and I are the module mass, acceleration and inertia, respectively. Δ is the moment arm and ω is the angular acceleration.

Chapter 5

Results

5.1 Site Response Analysis

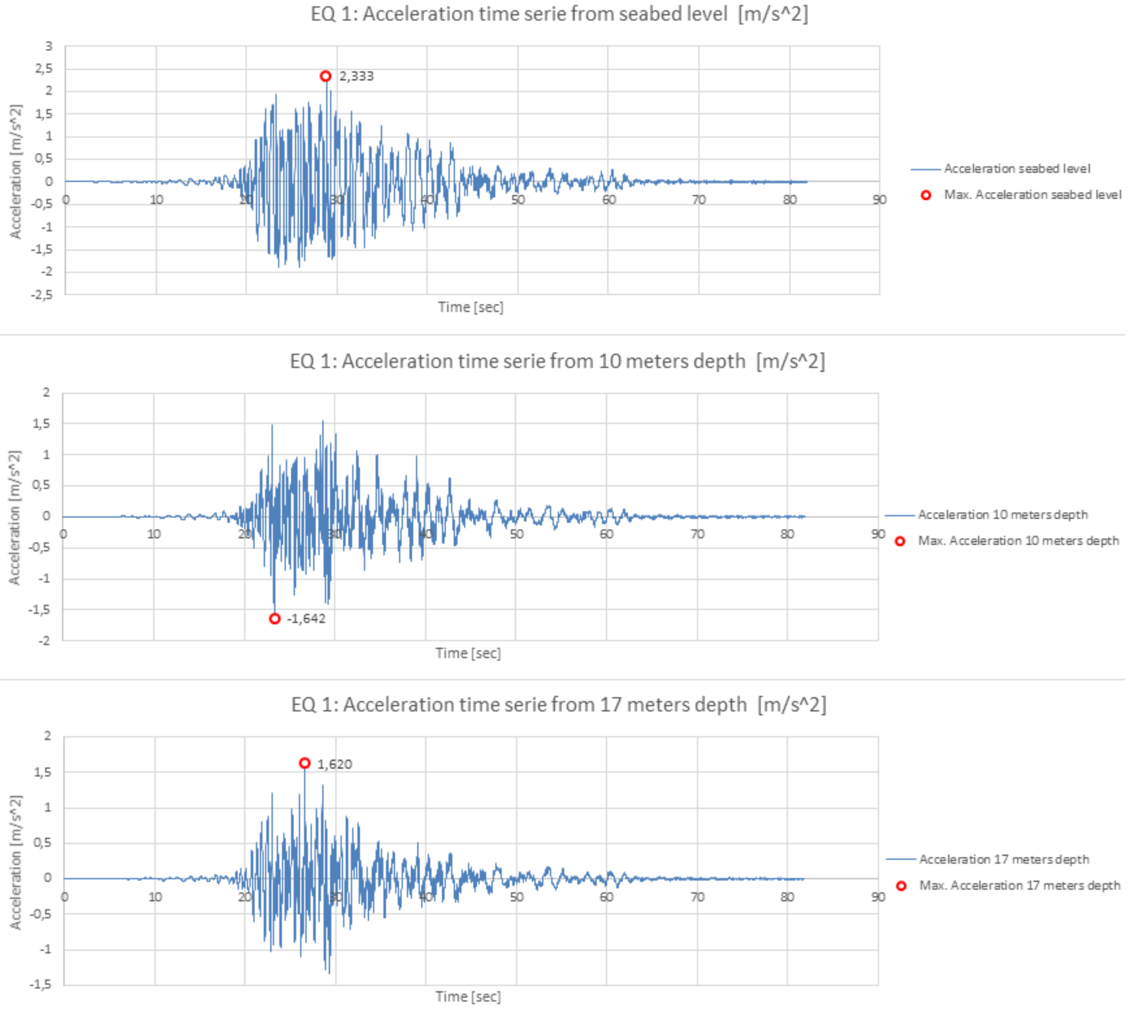

Figure 5.1: Acceleration time series at 0, 10 m, and 17 m for EQ 1.

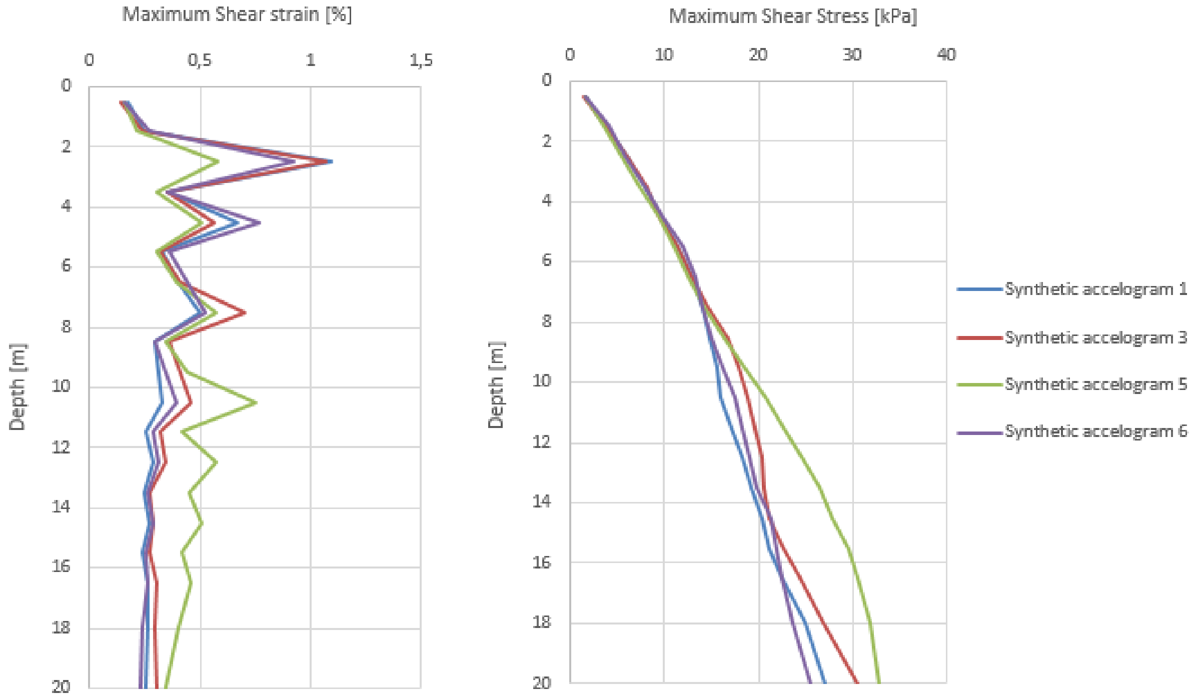

Figure 5.2: Shear strain and shear stresses plotted versus the upper 20 meters.

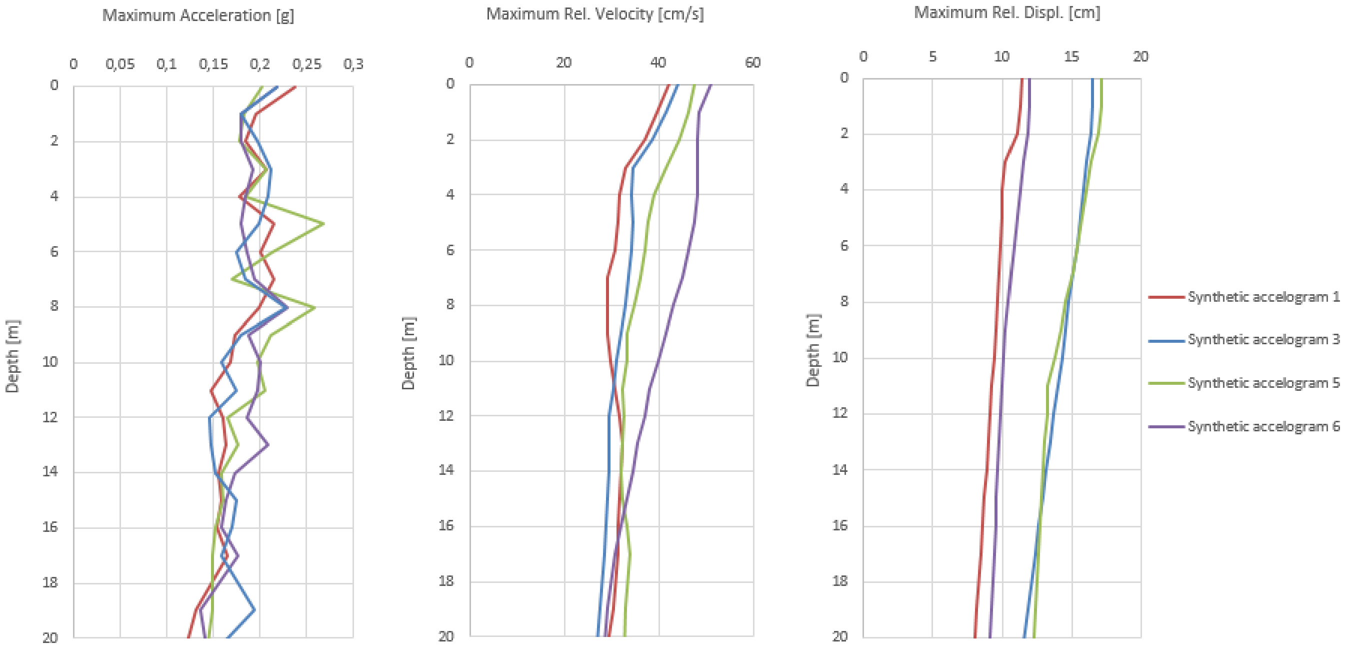

Figure 5.3: Maximum values of acceleration, relative velocity and relative displacement plotted versus the upper 20 meters.

5.1.1 Description of the Results

To accentuate the amplification of earthquake response from bedrock to seabed level, acceleration time series from the seabed level, -10 meters, and -17 meters are plotted in figure 5.1. The upward propagating waves can be observed by a small time lag between the peak amplitudes of the calculated motion. One can also note that the amplification of the whole time series, increases towards the surface layer. Similar plots for the remaining earthquakes are given in appendix C.1.

Figure 5.2 displays the calculated maximum strain and stress of the soil profile. The peak strain is situated at about 2.5 meters depth for all earthquakes except EQ5, where it's observed at 10.5 meters depth. The maximum stress is seen at the bottom as expected. Also, the constraints of zero strain and stress at the top of the profile is satisfied.

An indication of how the maximum acceleration, as well as maximum relative velocity and displacement, varies with depth in the soil profile is given in figure 5.3. According to theory, all three parameters should show an increase towards soil surface. These trends are seen in the velocity and displacement plots, but not in the acceleration plot, where EQ5 peaks at about -4.5 and -8 meters.

For the analyses, a reference depth of -10 meters was chosen. Originally it was meant to be half of the caisson length, but looking at the comparison of the peak accelerations in figure 5.3, the max accelerations seem to have a peak at -8 meters. Consequently, the reference depth was selected at a lower level.

As seen from the plots of shear strain and maximum acceleration, there are some distinct peaks. This is probably due to the profile layers being divided into sublayers in NERA, as smoother curves were obtained when removing the sublayers. However, based on the input given, the profile had to be divided into sublayers in order to obtain unique time histories for every depth. Due to the distinct peaks for the maximum accelerations, caution should be exhibited when choosing reference depths.

5.2 Modal Analysis

Results from the modal analysis are shown in table 5.1.

Table 5.1: Acceleration and displacement results from the modal analysis.

Eigenperiod 1	0.45	[s]
Eigenperiod 2	1.22	[s]
Rotation at CoG	0.791	[deg]
Displacement seabed	0.198	[m]
Acceleration seabed	5.261	[m/s^2]
Displacement at CoG_{module}	0.243	[m]
Acceleration at CoG_{module}	6.18	[m/s^2]

Table 5.2: Moment and shear force at seabed level.

Description	**Value**	**Unit**
Moment at seabed	7.194	[MNm]
Shear force at seabed	1929.560	[kN]
Mobilisation	0.77	[-]

5.3 Time Series Analyses

Time series analyses were performed for four different earthquakes. For each earthquake, three different analyses with different dynamic input were executed. The different dynamic inputs are listed in the following:

- Unique depth variable displacement time series at each depth:
  - EQ 1A, EQ 3A, EQ 5A and EQ 6A
- The seabed displacement time series at each depth:
  - EQ 1S, EQ 3S, EQ 5S and EQ 6S
- Displacement time series from a reference depth at 10 meters applied at each depth:
  - EQ 1R, EQ 3R, EQ 5R and EQ 6R

In the following, comparison plots for acceleration, displacement, rotation, moment and shear force for EQ 1 are presented. Comparison plots for the remaining earthquakes are given in appendix D.2. A comparison of peak values for acceleration for the various earthquakes is given in figure 5.9. Comparisons of peak values for the other response values for the various earthquakes are given in appendix D.3. The individual plots are shown in appendix D.1.

Acceleration

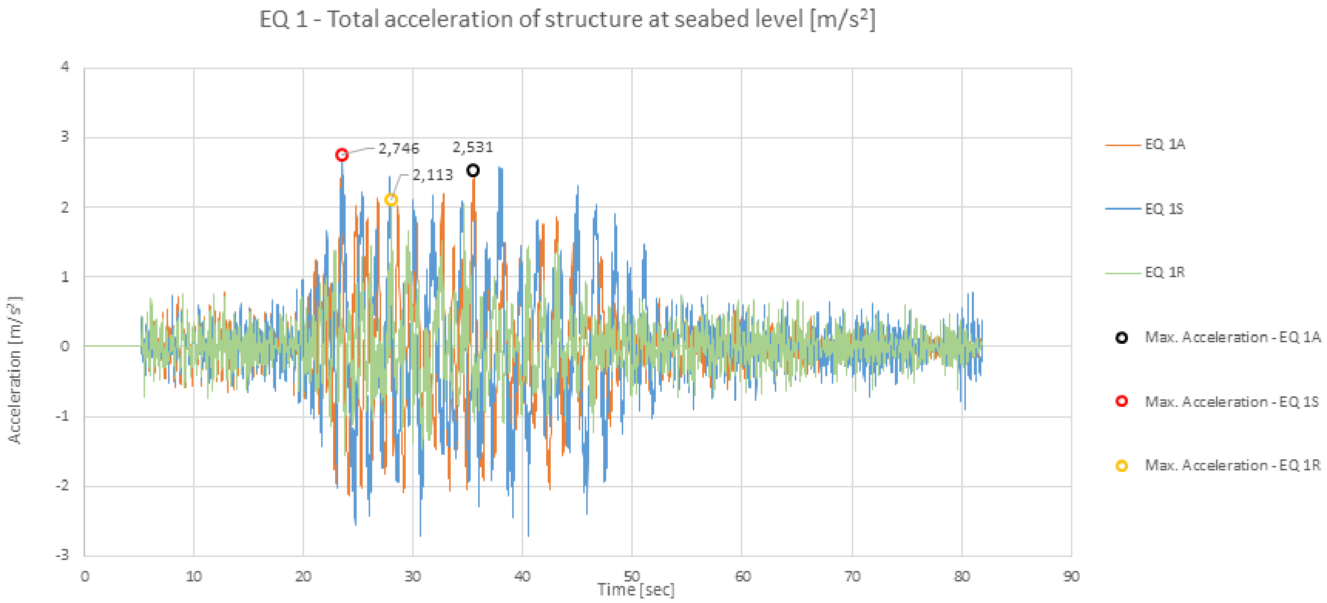

Figure 5.4: EQ 1: Total acceleration of structure at seabed level for time series analyses using depth variable time series (A), the seabed time series (S) and the reference depth time series (R).

Displacement

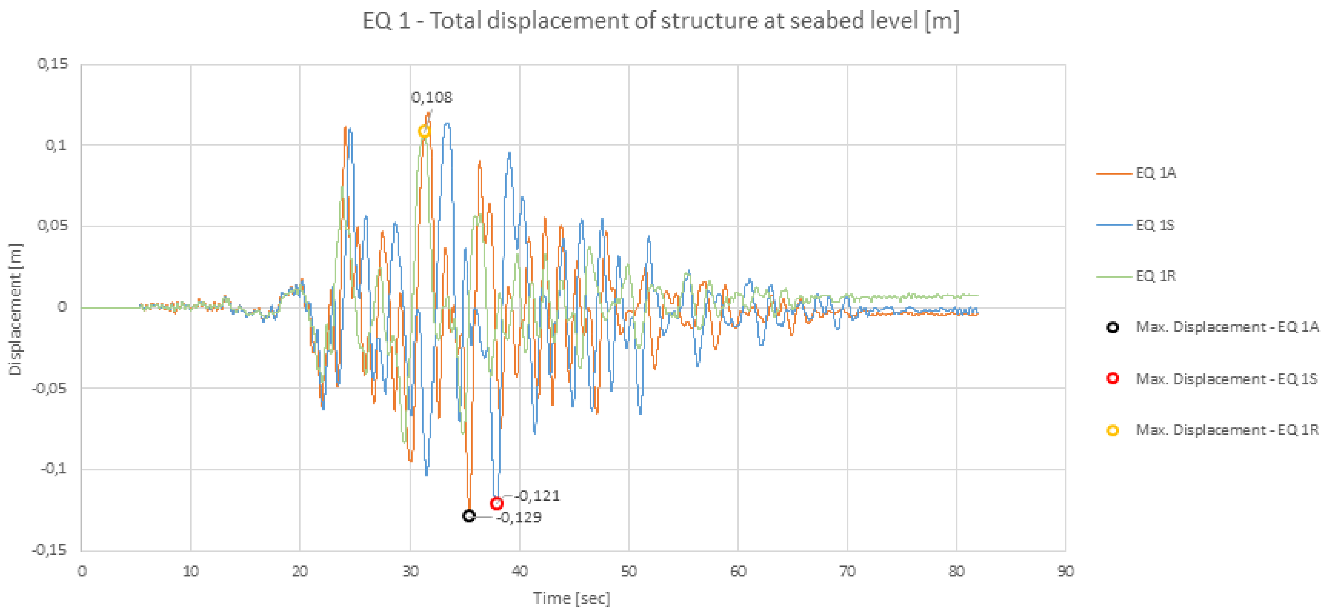

Figure 5.5: EQ 1: Total displacement of structure at seabed level for time series analyses using depth variable time series (A), the seabed time series (S) and the reference depth time series (R).

Rotation

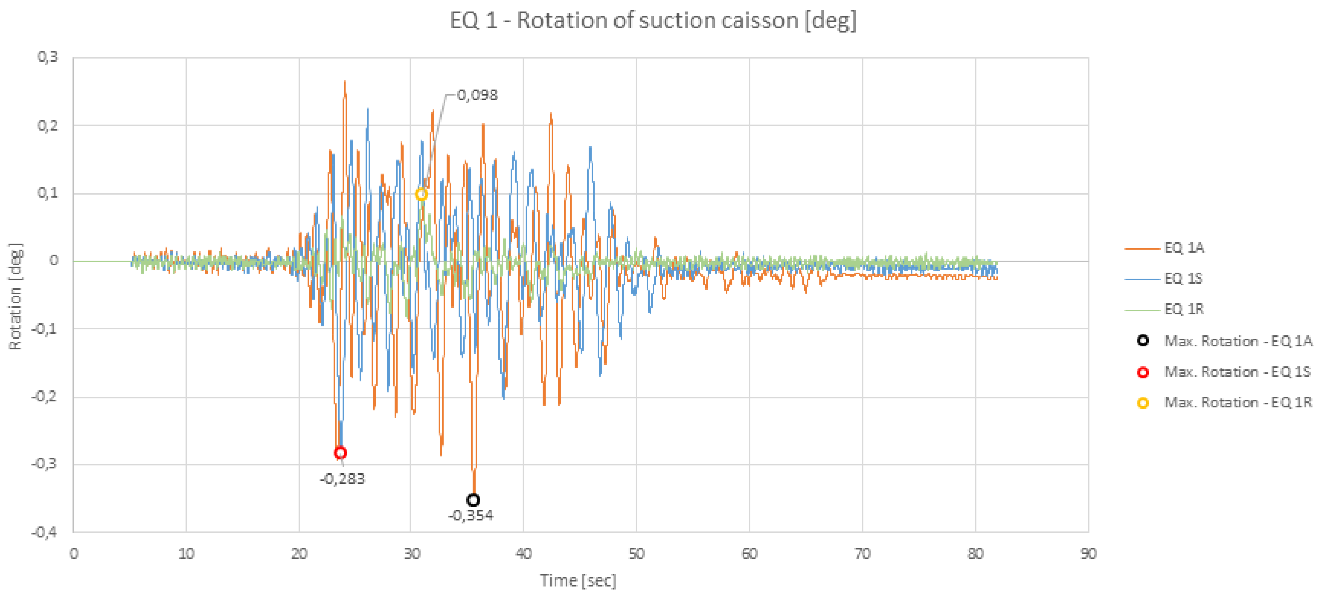

Figure 5.6: EQ 1: Rotation of structure at seabed level for time series analyses using depth variable time series (A), the seabed time series (S) and the reference depth time series (R).

Base moment

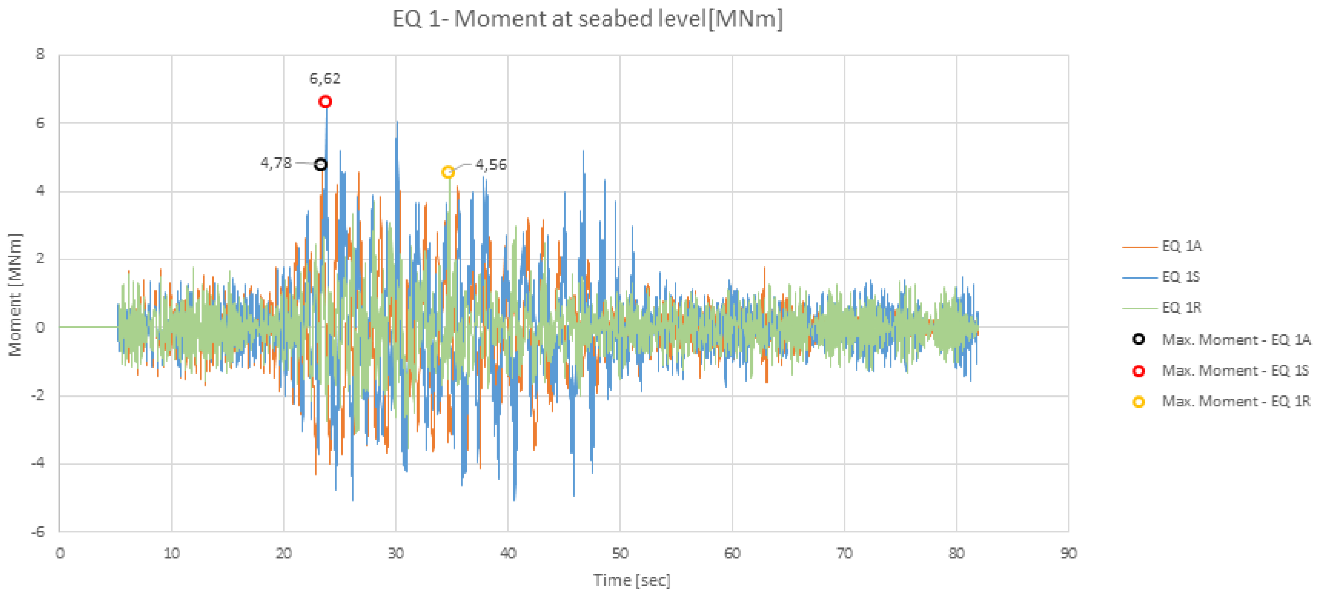

Figure 5.7: EQ 1: Moment at seabed level for time series analyses using depth variable time series (A), the seabed time series (S) and the reference depth time series (R).

Base Shear Force

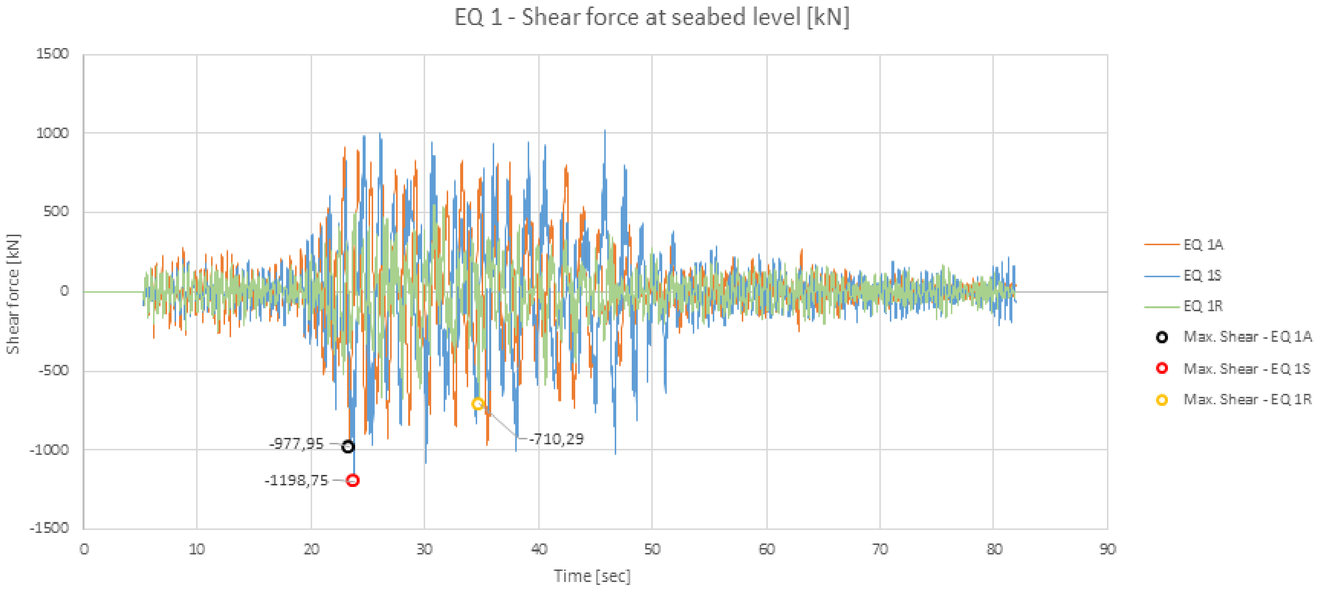

Figure 5.8: EQ 1: Shear force at seabed level for time series analyses using depth variable time series (A), the seabed time series (S) and the reference depth time series (R).

Comparison of Peak Values of Acceleration

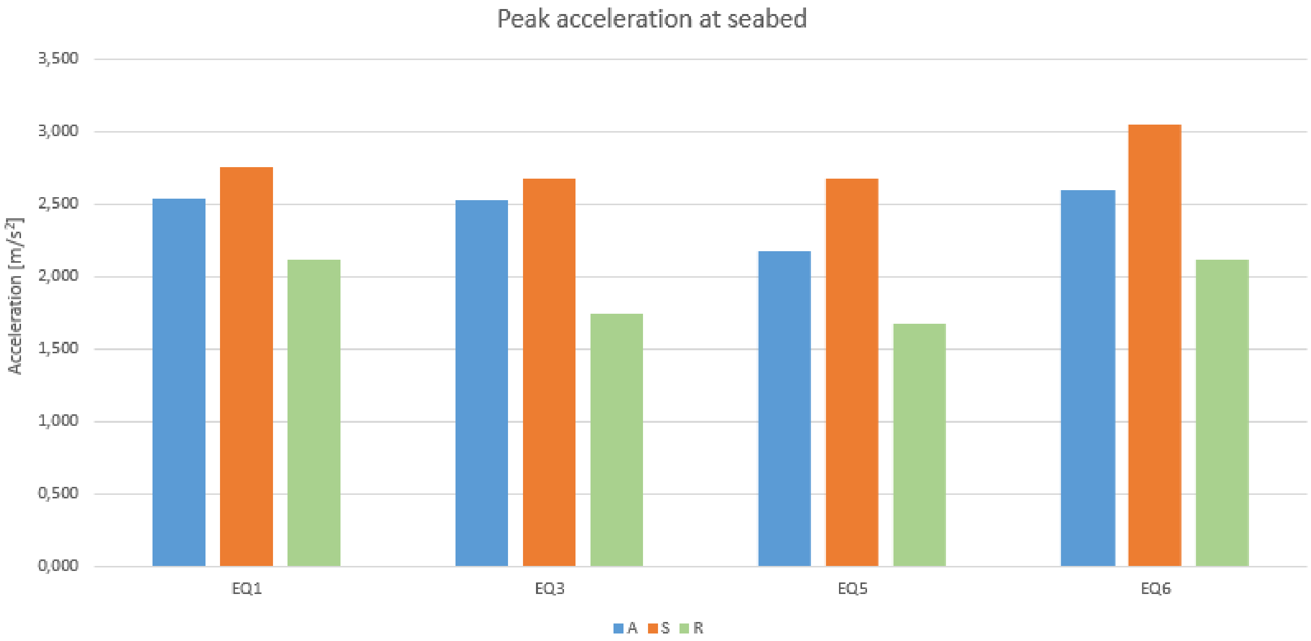

Figure 5.9: Comparison of peak acceleration at seabed for the various time series analyses. Depth variable time series (A), the seabed time series (S) and the reference depth time series (R).

5.4 Summary of TSA and Modal Analysis Results

In tables 5.3 to 5.5, an overview of the maximal values of the plotted graphs are presented. Additionally, the average of the maximal values are calculated to show an indication of how the response varies when applying the different time series. In table 5.6, the results from the modal analysis are presented. A comparison between the different time series analyses and the modal analysis is shown in figure 5.10. The values are presented as a percentage of the average maximum response values of the depth variable TSA. The depth variable TSA's are used as the percentage reference values because of the assumed realness of the site response depth variable time series.

Table 5.3: Depth variable displacement time series (A).

EQ	**Max. Acc. [m/s^2]**	**Max. Total Disp. [m]**	**Max. Rot. [deg]**	**Max. Mom. [MNm]**	**Max. Shear force [kN]**
1A	2.531	0.129	0.354	4.780	977.947
3A	2.526	0.185	0.337	4.501	989.890
5A	2.171	0.249	0.384	4.385	944.901
6A	2.592	0.119	0.377	4.747	1008.448
Average	2.455	0.171	0.363	4.603	980.297

Table 5.4: Seabed displacement time series at every depth (S).

EQ	**Max. Acc. [m/s^2]**	**Max. Total Disp. [m]**	**Max. Rot. [deg]**	**Max. Mom. [MNm]**	**Max. Shear force [kN]**
1S	2.746	0.121	0.283	6.618	1198.748
3S	2.676	0.181	0.222	4.729	1053.971
5S	2.677	0.251	0.229	4.464	901.279
6S	3.05	0.123	0.273	6.811	1115.402
Average	2.787	0.169	0.252	5.656	1067.350

Table 5.5: Reference displacement time series at every depth (R).

EQ	**Max. Acc. [m/s^2]**	**Max. Total Disp.t [m]**	**Max. Rot. [deg]**	**Max. Mom. [MNm]**	**Max. Shear force [kN]**
1R	2.113	0.108	0.098	4.563	710.292
3R	1.741	0.135	0.067	3.604	573.127
5R	1.676	0.193	0.074	4.551	659.608
6R	2.114	0.104	0.088	5.478	843.964
Average	1.911	0.135	0.082	4.549	696.748

Table 5.6: Results from modal analysis. Maximal values are from seabed level.

Max. Acc. [m/s^2]	**Max. Total Disp. [m]**	**Max. Rot. [deg]**	**Max. Mom. [MNm]**	**Max. Shear force [kN]**
5.261	0.198	0.791	7.194	1929.561

Comparison of Results

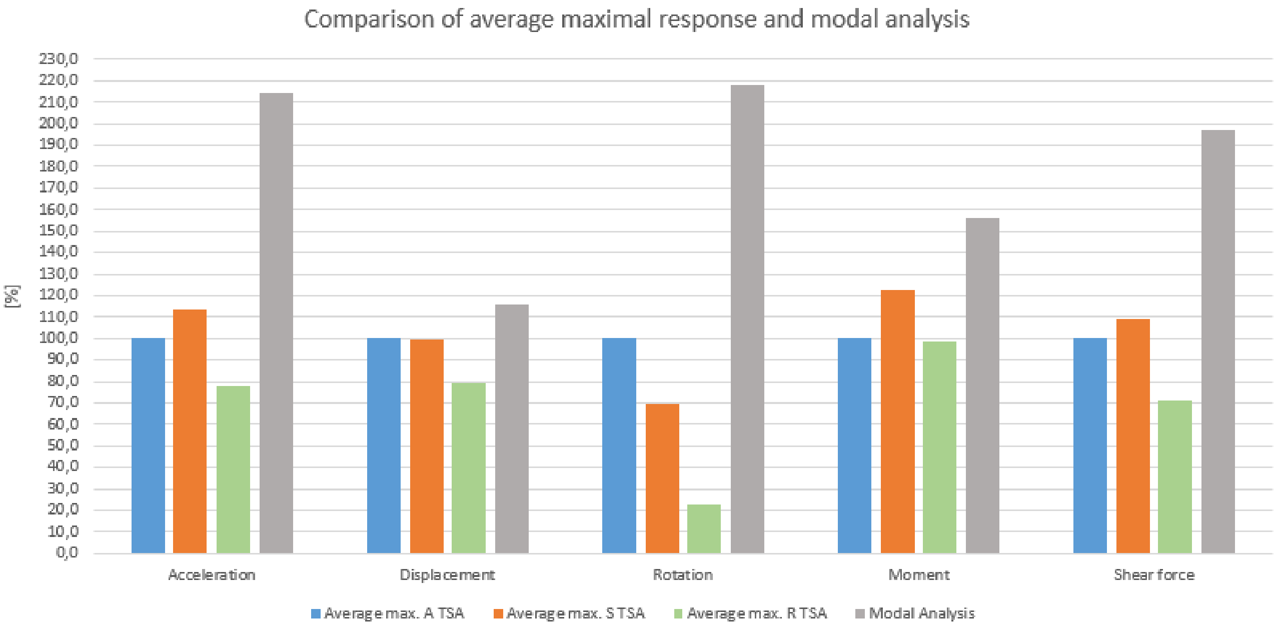

Figure 5.10: Comparison of average peak results. Depth variable time series (A), the seabed time series (S) and the reference depth time series.

Table 5.7 shows the values corresponding to figure 5.10. The average maximal values for the depth variable TSAs are used as the reference.

Table 5.7: Comparison of results. Values corresponding to figure 5.10.

	Acc. [%]	**Disp.** [%]	**Rot.** [%]	**Mom.** [%]	**Shear force** [%]
Average max. A TSA	100.0	100.0	100.0	100.0	100.0
Average max. S TSA	113.5	99.1	69.4	122.9	108.9
Average max. R TSA	77.8	79.2	22.5	98.8	71.1
Modal Analysis	214.3	116.1	217.8	156.3	196.8

Chapter 6

Discussion

Firstly, the credibility of the finite element model and sensitivity analyses is discussed. Secondly, the results from the modal analysis and the time series analyses are evaluated.

6.1 Credibility of the Finite Element Model

For any numerical analysis, its credibility needs to be assessed. Proper modelling of the physical response has been emphasised, however simplifications have been made to shorten the computational time, and limit the complexity of the calculations. Some of the simplifications made are elaborated in the following:

- The spring elements and time series have only been applied at each meter along the caisson skirt. This is considered appropriate, as the caisson has been represented by a beam-model, subjected to a distributed load integrated into point loads.
- The module mass and the mass of the top plate has been modelled as a lumped mass, using typical values provided by Multiconsult. The module itself was modelled as an equivalent box with 6 meters height and 10 meters width.
- To achieve a more realistic soil response when a cylindrical caisson is subjected to lateral loading, the p-y curves have been adjusted to comply with the lateral response calculated in Plaxis, by Multiconsult.
- Pore pressure accumulation during cyclic loading, and thus stiffness degradation,

has not been accounted for.

- 2% Rayleigh damping has been applied in the model, to conveniently represent radiation damping, structural damping and damping due to movement in water.
- Earthquake motions have only been applied in one direction.

A noticeable high acceleration value is observed from the seabed TSA in figure D.61. Figure 6.1 highlights this peak with a value of 2.538 m/s^2 and an arrival at approximately 34.1 seconds. When compared to the free-field acceleration as well as the other analyses, EQ 3S appears to display a distinctive behaviour. Even though the free-field accelerations seem to decrease together with EQ 3A and EQ 3R, a sudden amplification occurs in EQ 3S. Unanticipated large amplification of oscillation could be due to the input approaching a natural frequency of the system. Since the excitation input used in the EQ 3S analysis is in phase, this could be a reason for the sudden amplitude build-up. The most plausible reason, however, could be due to some numerical instability. Either from the input synthetic time series, application of inaccurate damping, the integrated displacements from NERA, or the calculation of the solution within the program code itself.

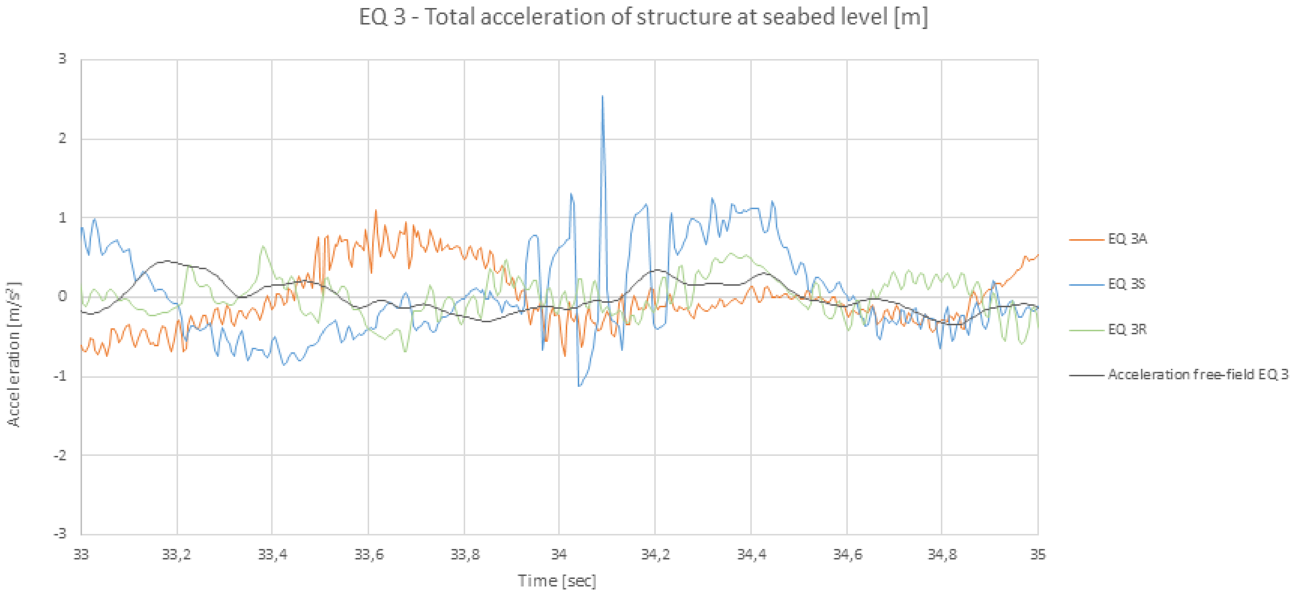

Figure 6.1: Acceleration at seabed for EQ 3A, EQ 3S, EQ 3R and free-field seabed from 33 seconds to 35 seconds.

Since the structure is completely submerged in soil and water, the real damping could possibly be higher than the 2% Rayleigh damping used in the TSA's. Therefore, performing sensitivity tests with increased Rayleigh damping or adding a viscous damper, would be beneficial to further assess the credibility of the model. However, sensitivity tests with various damping are not performed in this thesis.

6.1.1 Sensitivity Analyses

To optimise the credibility of the model, and map its sensitivity to certain aspects, three sensitivity tests were performed. This is a common way of ensuring more accurate results in the final analyses. The various sensitivity analyses performed are presented in the following sections. These are:

- Hysteresis configuration using one non-linear spring, versus four bi-linear springs in parallel.
- Comparison of the response when including Rayleigh damping in the model.
- Modelling the beam using rigid elements.

6.1.1.1 Spring/Soil Response Models

To get a realistic response of the caisson when subjected to an earthquake, modelling the soil response correctly is essential. As previously mentioned in section 3.2, the dynamic response can be captured using a model following the Masing rules. This was emphasised when assessing the hysteresis curves obtained using the different configurations.

Two different spring configurations were tested. The first using one non-linear spring with a built-in hysteresis function in ANSYS. The second configuration used was applying four bi-linear springs in parallel with the same built-in hysteresis function. The stiffness of the one non-linear spring was represented by a p-y curve divided into 20 segments, while the stiffnesses of the bi-linear configuration were calculated as described in section 4.5.2. A visual representation of the input soil stiffnesses is given in figure 6.2.

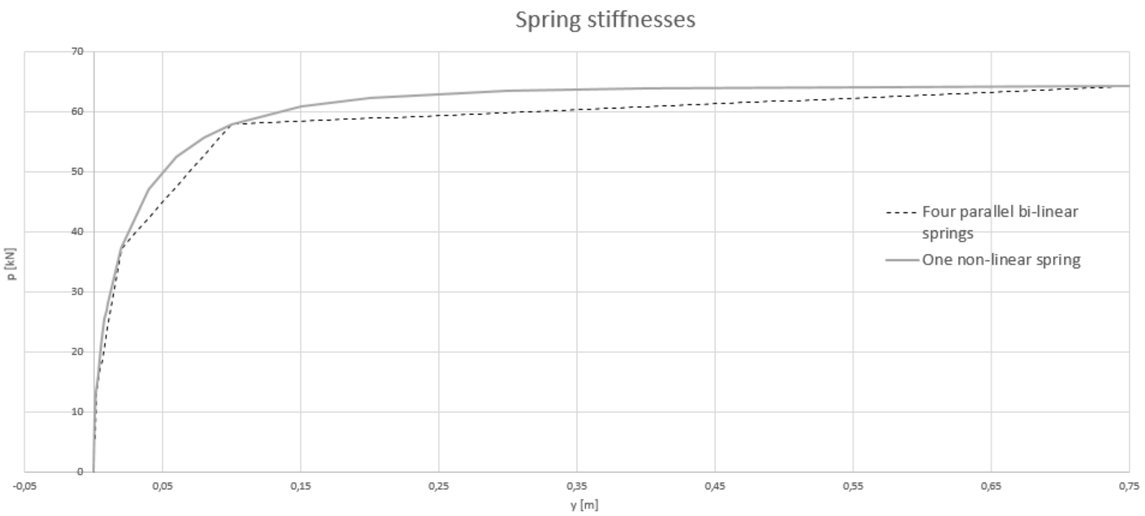

Figure 6.2: Comparison of stiffness configurations.

To get a better foundation for a comparison between the two configurations, load application needed to be simpler than an earthquake time history. Hence, dynamic input in the form of a sinusoidal cycle with a displacement amplitude was applied at each beam node. The resulting unloading-reloading cycles with amplitudes 1.0 meter and 0.5 meter is shown in figure 6.3.

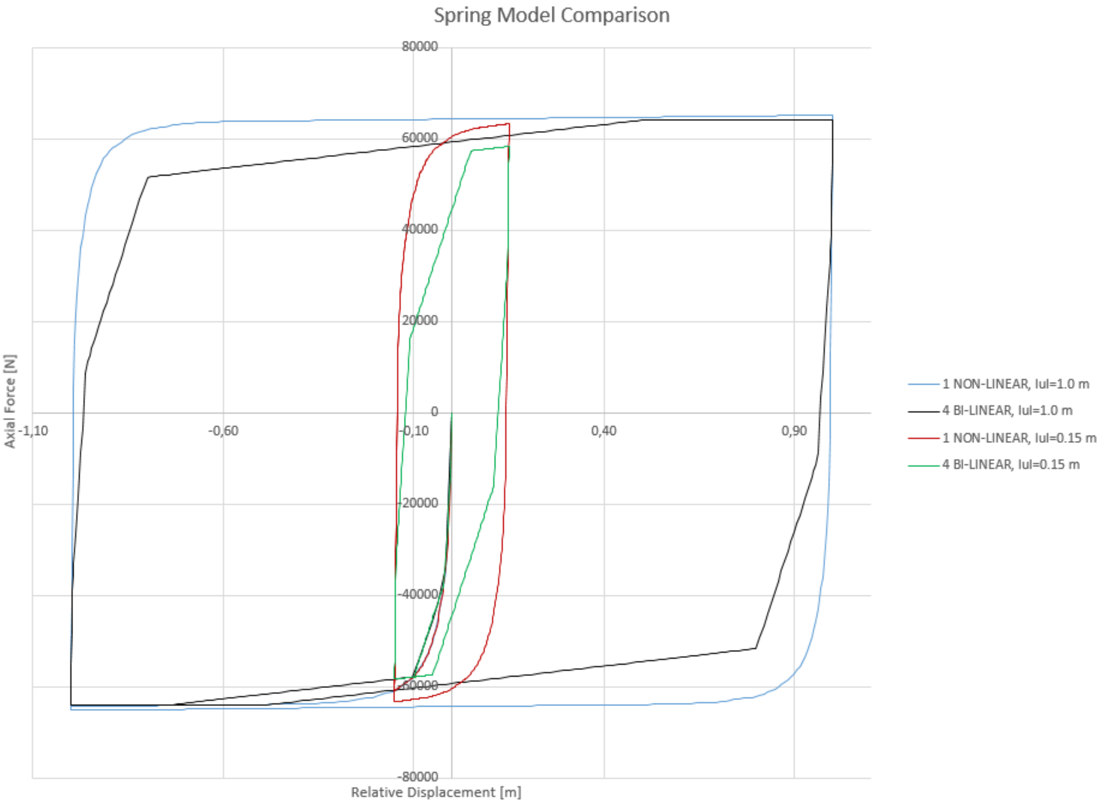

Figure 6.3: Hysteretic response of spring configurations, with two different amplitudes.

The built-in hysteresis function in ANSYS applies a rather simple formulation, as the unloading lines are parallel to the initial slope of the loading curve. Applying it to the one non-linear spring results in an unloading-reloading curve non-compliant with the Masing rules. During unloading the curve follows the initial stiffness until zero force, thus it does not have the same shape as the backbone curve. This is non-compliant with the second Masing rule presented in section 2.4.1, and this configuration results in an exaggerated damping.

6.1.1.2 Rayleigh Damping

Rayleigh damping was introduced in the model to account for radiation damping, as well as the structure's material damping. This is due to both the physical and mathematical convenience of Rayleigh damping. The response of the structure with and without Rayleigh damping was compared. Without Rayleigh damping, the only damping in the system would be a consequence of the soil response, namely the hysteretic damping. Rayleigh damping is introduced to better simulate an actual response.

At lower displacements, only the first spring will be mobilised. Consequently, the springs will still be in the linear elastic area resulting in no hysteretic damping. In reality, damping will be present even at low displacements. In order to realistically model the hysteretic damping, the number of springs may be increased, and the first springs must be mobilised at very low lateral displacements. However as an alternative, the application of Rayleigh damping results in damping, even at small displacements.

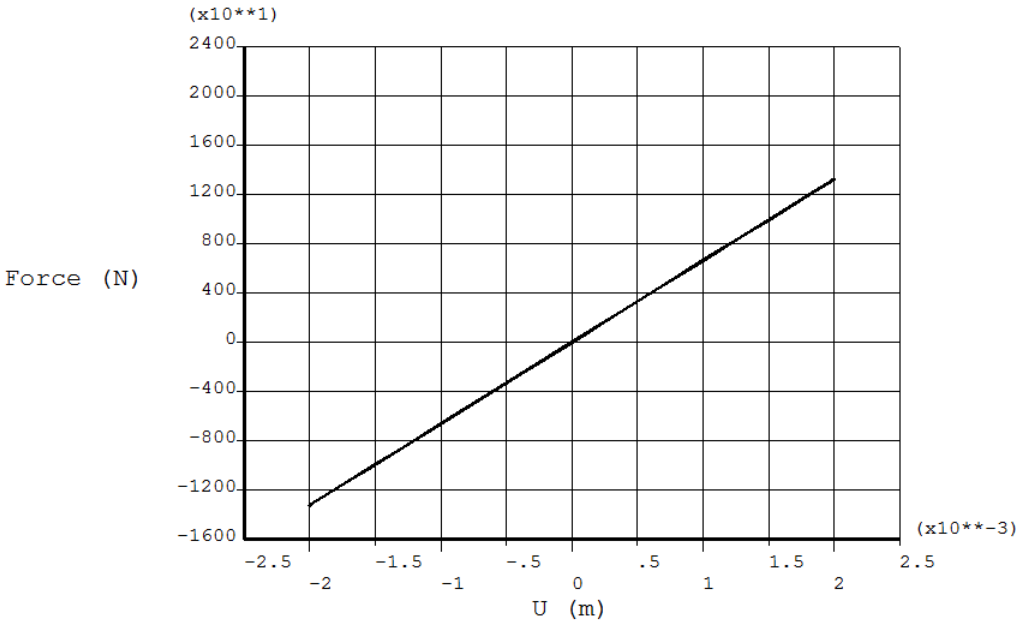

Figure 6.4: Initial part of the loading curve.

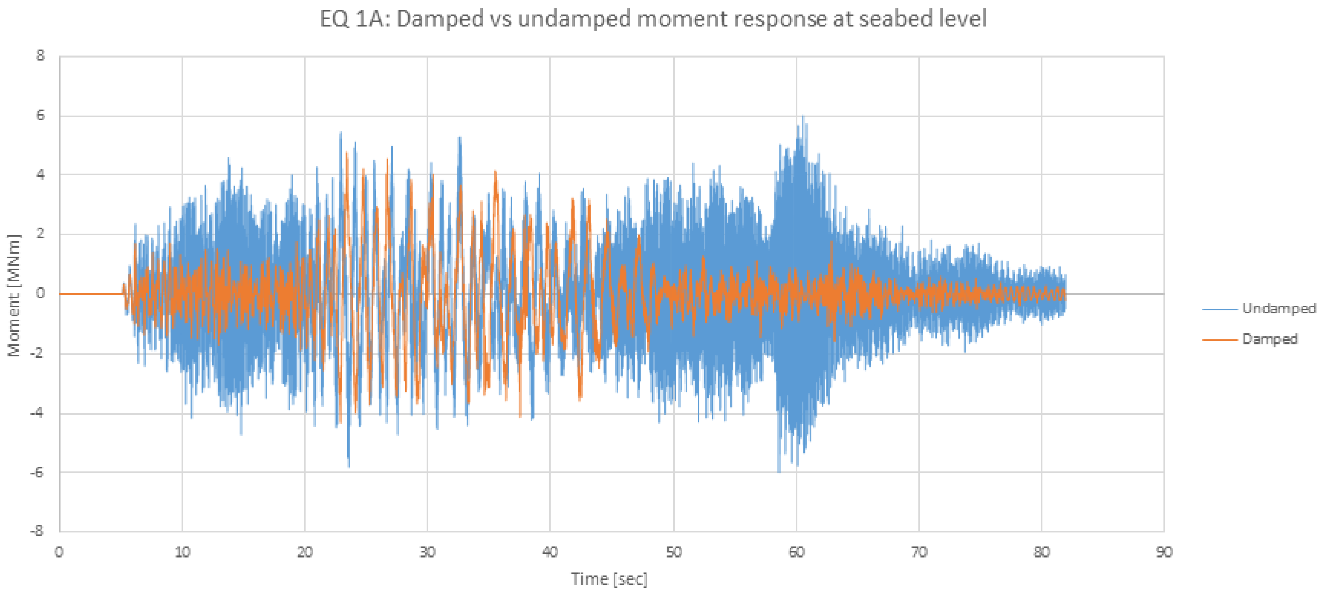

Figure 6.5: Response of structure with and without Rayleigh damping.

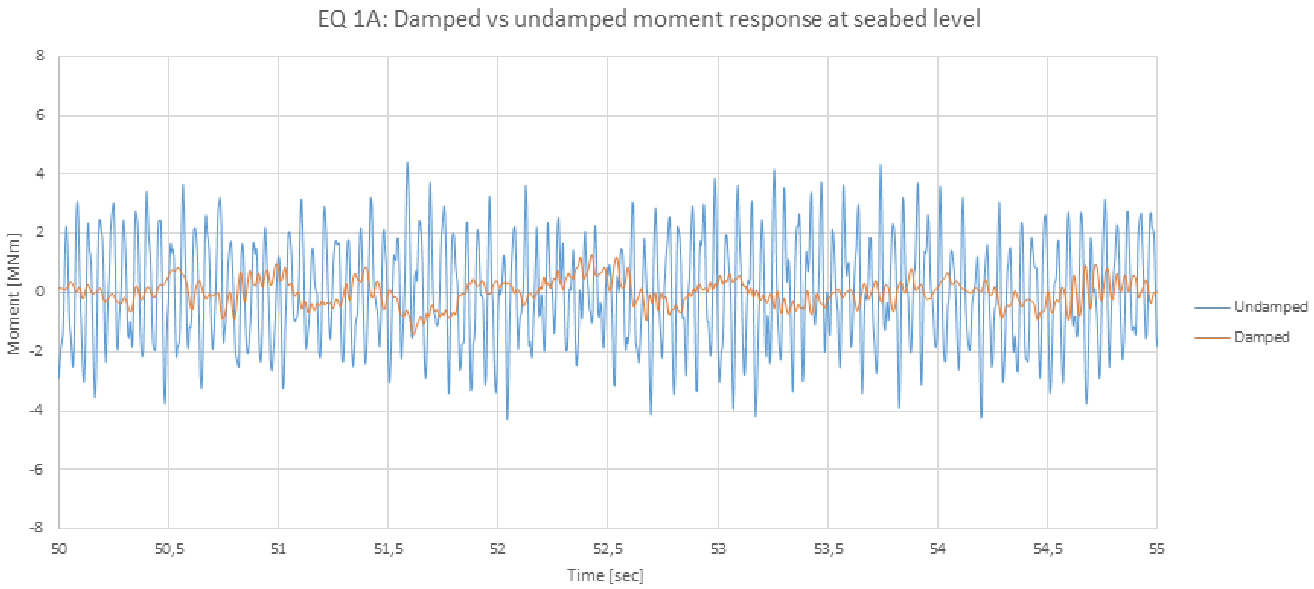

Figure 6.6: Response of structure with and without Rayleigh damping for a smaller time interval.

When plotting the response for a smaller time interval, the effects of the applied Rayleigh damping becomes evident. Without the Rayleigh damping present, it appears that high-frequency modes dominate the response. This results in an unphysical behaviour. The Rayleigh damping filters out the high-frequency vibrations, resulting in the smoother curve observed in figure 6.6.

This is also observed in figure 6.5, where an improbably high moment arises around 57 seconds. Observing the free-field acceleration at around 57 seconds, it can be seen that the time series decreases and stabilises. A build-up of high bending moments in the structure at seabed level as the input starts to die out appears unrealistic. When introducing the Rayleigh damping, this moment build-up disappears resulting in a more realistic response. Consequently, the Rayleigh damping was implemented for the final analyses.

6.1.1.3 Rigid Beam

The modal analysis performed using an in-house program by Multiconsult AS only considers the two first eigenmodes of the system. In general, these are the two main contributors to the structural response. Higher modes imply an unrealistic deformation of the caisson. Taking these higher modes into account will result in a correspondingly unrealistic structural response. To assure that the stiffness of the caisson is sufficiently high to neglect these higher modes, a sensitivity analysis with the implementation of an infinitely stiff beam is performed. For the rigid beam, ANSYS element MPC184 is used to model the caisson.

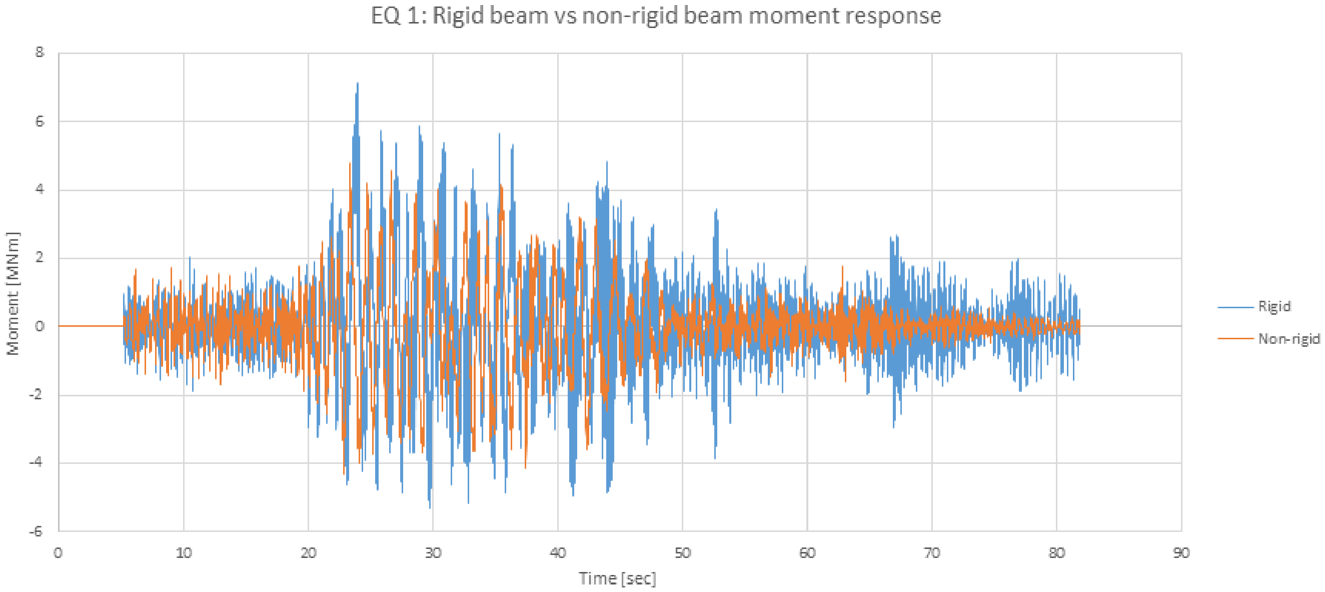

Figure 6.7: Moment response of rigid beam versus real stiffness.

The two different analyses are shown in fig 6.7. Implementing the rigid beam elements resulted in a more unphysical response. As a consequence, it was decided that the system using BEAM188 elements was sufficient.

6.2 Evaluation of the Results

In order to get a realistic view of the results obtained through dynamic analyses such as this, it is important to view the response of the structure together with the dynamic input. To that end, the reader is strongly encouraged to have a copy of the free-field accelerations at hand when examining the results. These are provided in appendix C. To simplify, abbreviations for the three time series analysis types are:

- Depth variable time series analysis - Depth variable TSA
- Seabed time series analysis - Seabed TSA
- Reference depth time series analysis - Reference TSA

When looking at the acceleration values from tables 5.3 to 5.5, it is evident that the overall highest values are obtained from the seabed TSA's. This can also be seen in figures 5.4 and D.61 to D.63. Average maximum acceleration for these analyses are 2.787 m/s^2 while the depth variable TSA's and reference TSA's have an average of 2.455 m/s^2 and 1.911 m/s^2 respectively.

Displacement results from figure 5.5 and figures D.64 to D.66 display a pattern of smaller displacement for the reference TSA compared to the other TSAs. As expected, the smaller amplitude of the reference input corresponds to the lowest displacement amplitudes in the plots. By contrast, the seabed TSA displacements seem to be slightly lower than the depth variable TSA displacements, despite having a larger input amplitude with depth. This difference is even more accentuated in the rotation plots from figure 5.6 and figures D.67 to D.69, where the rotation for the depth variable TSA is generally higher than the other two. This is believed to be a consequence of decreasing amplitudes of input motions, coupled with increasing soil stiffness with depth. Additionally, when applying depth variable time series, the motions are not in phase, as is the case when applying the same input at each depth. When considering a mass-less beam subjected to the same input motion at each depth, a strictly translational movement would occur. However, the values are relatively small, and the differences in displacement and rotation amplitude from the depth variable TSA and seabed TSA will probably have minimal influence in design.

The average maximum moments and shear force are larger when applying seabed time series at every spring. A possible explanation for this is given in the following hand calculations. Note that these are highly simplified, and included to substantiate. Results from the simplified hand calculations are presented in figure 6.8. The simplified earthquake load is calculated as the product of the displacement, D, and the stiffness, proportional to G_{max}. When using scaled displacements, the load varies parabolically versus depth. By contrast, the load will vary linearly with depth when applying only seabed time series. Consequently, the resulting forces when using seabed time series are larger and would give more significant moments and shear forces at seabed level.

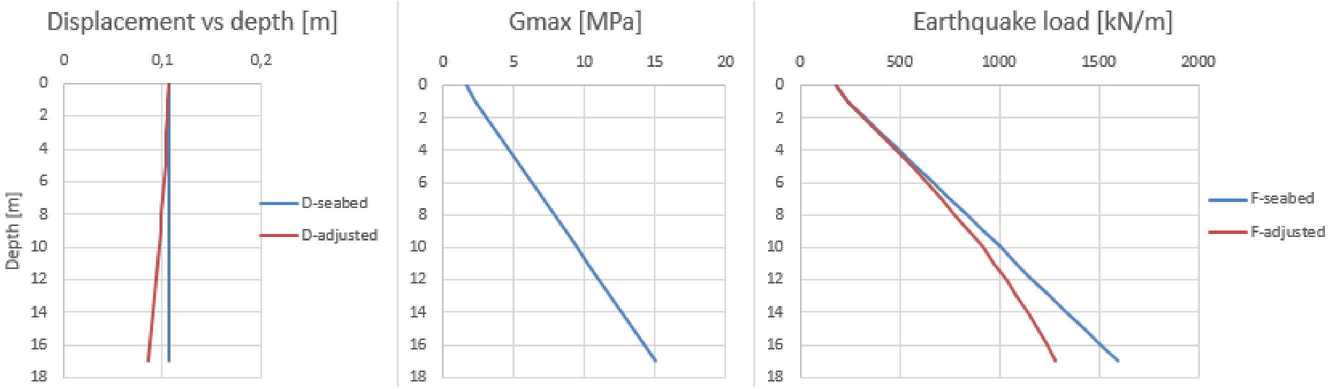

Figure 6.8: Simplified hand calculations

Because of the limited amount of earthquake input time series, a big variation is seen in peak response values. This is presented as a comparison of peak acceleration in figure 5.9. A higher variation of peak acceleration is seen between the depth variable TSA and seabed TSA during EQ 5. While EQ 3 shows little variation. An increased amount of input earthquakes would be beneficial to validate the trends.

Figure 6.9 shows the average moment and shear force for each analysis. It was found by taking the absolute value at each time step and then calculating the average. Although the most interesting values for design are the maximum values, figure 6.9 indicates a clear trend; that the seabed TSAs in general yields higher moments and shear force.

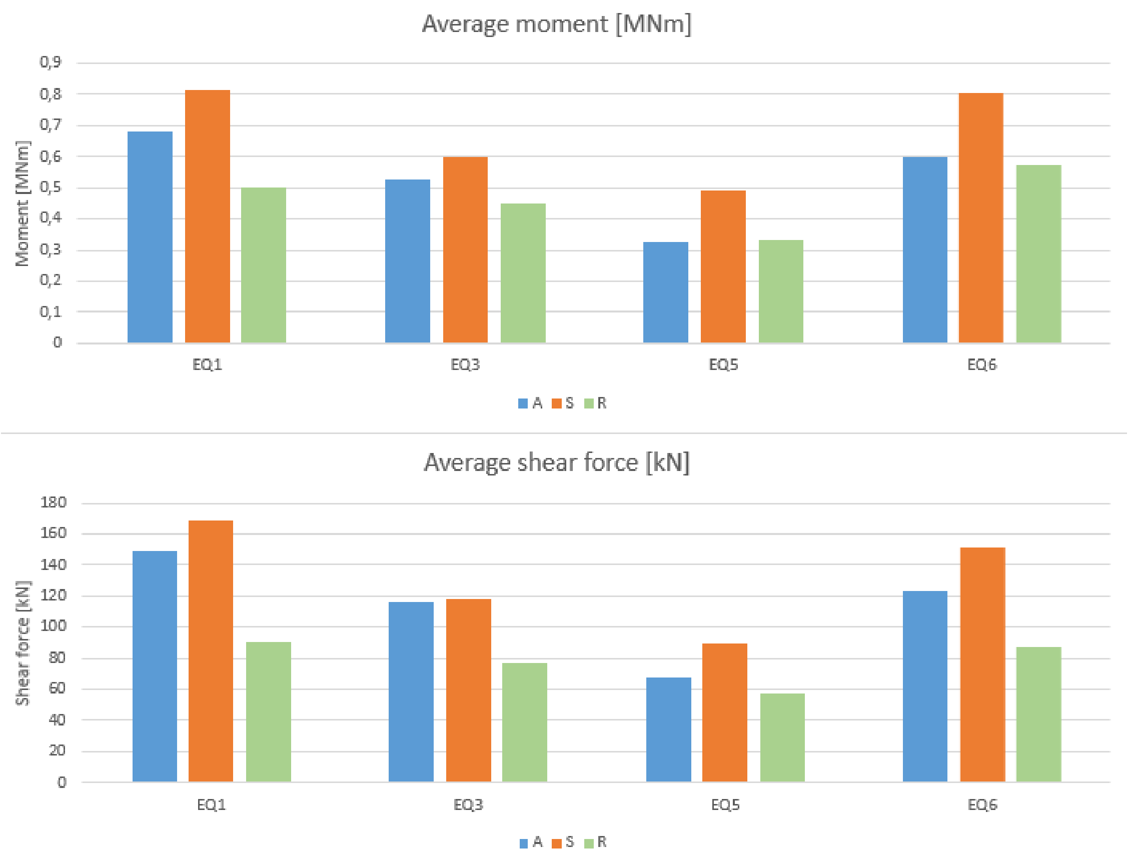

Figure 6.9: Average moment and shear force at seabed. Depth variable time series (A), the seabed time series (S) and the reference depth time series (R).

6.2.1 Comparison of Time Series Analyses to Modal Analysis

The average maximum values of all analyses are presented in tables 5.3 to 5.6, and a graphical representation of aspect ratios are given in figure 5.10.

Figure 5.10 indicates some clear trends regarding the analyses. Seabed TSA's show a higher structural response regarding maximal values of moments, shear force, and acceleration, compared to the other time series analyses. This was expected due to the higher displacement amplitudes of the seabed input time series. Displacement and rotation values, on the other hand, show a different ratio. While the average maximal displacement is similar for the depth variable TSA's and the seabed TSA's, average maximal rotation from the seabed TSA's is considerably lower than the depth variable TSA's. This is believed to be an effect of the time lag difference between the free-field displacements applied to the caisson for the depth variable TSA's, while the other TSA's have free-field displacements applied in phase.

Modal analysis results are shown in table 5.1 and graphically in figure 5.10. The modal analysis shows higher values compared to the time series analyses. Maximum values of base moments, shear forces, and accelerations are often viewed as the limiting design criteria. The modal analysis shows 56.3% higher moment values, 96.8% higher base shear values, and 114.3% higher base acceleration compared to the depth variable TSA's.

Comparing the ratios between the two methods, it is evident that the modal analysis yields a conservative response. As previously covered in section 3.3, the SMNA method combines the maxima of the two first deformation modes when calculating the ultimate response. Thus implying that the eigenfrequencies of the system match the input. By contrast, the time series analyses do not necessarily imply this.

In figure 6.11, damping ratios for the modal analysis and three different spring arrangements are shown. Figure 6.10 shows the spring arrangement used in this thesis, namely spring arrangement three, together with two alternative spring arrangements. Damping ratios for the spring arrangements are calculated using the equations from 2.9.6.1. Because of the Rayleigh damping applied to the ANSYS model, an additional 2% damping is applied at the spring arrangements.

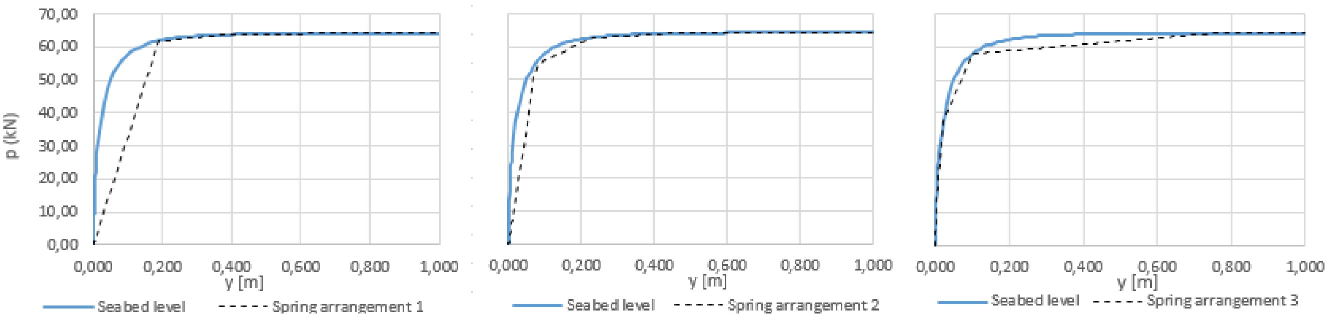

Figure 6.10: Three different spring arrangements.

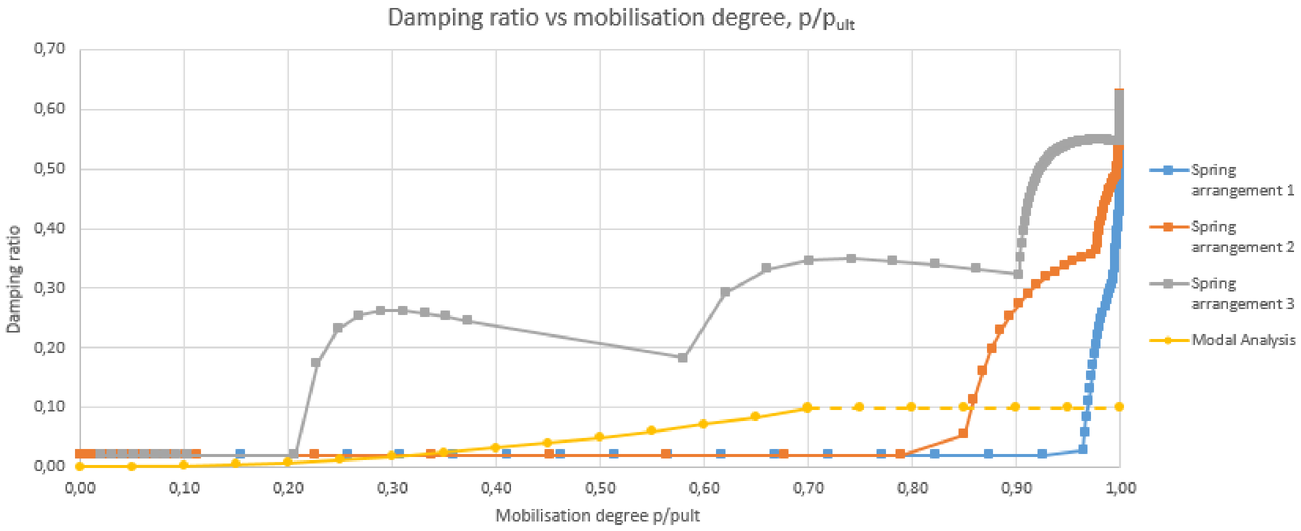

Figure 6.11: Comparison of the damping ratios from the three different spring configurations to the modal analysis.

The modal analysis yields a conservative damping ratio equal to 10% for mobilisation above 0.7. This is the case for the modal analysis performed, with a mobilisation of 0.77. As observed in figure 6.11, the damping applied in the ANSYS model is significantly larger than in the modal analysis. For the modal analysis, this results in larger accelerations, and consequently larger forces and moments. This is likely the main reason to why the modal analysis is conservative compared to the time series analyses.

The bi-linear springs were fitted after p-y curves calculated for a static load case. However, as this is a cyclic load scenario, where the soil stiffness in reality would degrade, the damping based on the p-y curves could be slightly high. The damping could be reduced by reducing the initial stiffness, however, implementing a model that accounts for soil stiffness degradation could better approximate the damping.

Regarding the small displacement damping previously discussed in section 6.1.1.2. The mobilisation degree in figure 6.4 is approximately $p/p_{ult} = 0.2$, hence the mobilisation needed for hysteretic damping is not reached. Rayleigh damping is thus needed to account for damping during small displacement cycles.

Chapter 7

Conclusions and Further Work

7.1 Summary and Conclusions

Simplified time series analyses and a modal analysis were performed for a caisson with a ratio of $\frac{L}{D}$=2.27. This was done to compare the two methods and to investigate kinematic interaction effects. Time series analyses were conducted in the software ANSYS Mechanical APDL, and the modal analysis was done using an in-house program provided by Multiconsult AS. The finite element model was developed in cooperation with Multiconsult AS. Input in the form of calculated p-y curves and displacement time series were implemented into the model.

Regarding kinematic interaction, the TSA results showed some interesting trends, when looking at the average maximal values. Applying seabed time series at each depth yields the highest response when looking at the moment, shear force and acceleration. These are 22.9 %, 8.9% and 13.5% larger respectively than results obtained when applying depth variable time series. This is in accordance with the expectations and simplified hand calculations. However, the seabed TSA's yield 30.6% less rotation and 0.9% less displacement. Applying the reference time series at every depth gives the lowest response values in general. If a reference time serie is to be used in design, caution must be exercised when choosing reference depth, because of the significant scatter in the NERA results.

The results generated in this thesis, show that the modal analysis yields generally higher response values than the time series analyses. For common design values, the modal analysis yields 56.3% and 96.8% higher base moments and shear forces respectively, when compared to the average depth variable time series analyses. Additionally, acceleration, rotation and displacement values are 114.3%, 16.1% and 117.8% larger than the depth variable TSA's respectively.

In comparison to the trends found by the time series analyses, the modal analysis is conservative. This is probably due to a significant difference in damping between the two methods. Additionally, the response of the modal analysis is based on combining the maxima for the two first eigenmodes, when calculating the ultimate response.

7.2 Further Work

The developed ANSYS model may include some numerical instability. Whether this is a result of a non-compatible dynamic input, incorrect damping or just a numerical error within the solution process of ANSYS itself, is yet to be discovered. Consequently, additional sensitivity tests could be performed to validate the reliability of the finite element model:

- As the time series analyses conducted in this thesis are limited to four input accelerograms, performing more analyses using different earthquake input would be beneficial to get a broader selection of data to assess. Additionally, a comparison between using synthetic and real accelerograms as input, as well as implementing additional soil profile data is also of interest.
- Applying additional damping either in the form of viscous dampers at the springs to account for damping at small displacements, or increasing the Rayleigh damping in the system.

The ANSYS model could be further developed to include different physical effects:

- Variation in soil stiffness due to pore pressure generation during dynamic loading conditions should be implemented. This could result in a more accurate damping during cyclic loading.
- Applying additional soil springs along the caisson skirt, as in the PISA model, to better approximate the lateral capacity of the suction caisson.

- Applying additional bi-linear springs in parallel to achieve a more accurate hysteretic damping, also at small displacements.

To improve the comparability between the two methods, some suggestions are presented:

- The program calculates an equivalent distributed length and mass of a pile, based on the total mass of the caisson, soil and module. More accurate results could be obtained by calculating the contribution of each component separately.
- Further, calculating a new HM-capacity space for the specific case to get a more accurate response. This could be done by applying combinations of static moment and horizontal force to the ANSYS model.

Modelling the soil and caisson as a continuum, and performing a full 3D finite element interaction analysis should yield the most accurate response. Hence, a comparison between the ANSYS time series analysis model, and a 3D continuum model is of interest to evaluate the accuracy of the ANSYS model.

Bibliography

(1996). *Eurocode 8: Design provisions for earthquake resistance of structures.* BSI, London. Merged with DD-ENV-1998-1-1 and DD-ENV-1998-1-2 into prEN-1998-1.

Aasen, S., Page, A. M., Skau, K. S., and Nygaard, T. A. (2017). Effect of foundation modelling on the fatigue lifetime of a monopile-based offshore wind turbine. *Wind Energ. Sci*, 25194:361–376.

API (2007). Recommended Practice for Planning , Designing and Constructing Fixed Offshore Platforms — Working Stress Design. *Api Recommended Practice*, 24-WSD(December 2000):242.

Athanasiu, C. (1999). Proposal for an anisotropic, soft clay model to be incorporated in future developement of PLAXIS. *Beyond 2000 in Computational Geotechnics*, pages 1127–1132.

Athanasiu, C., Bye, A., Tistel, J., Ribe, A., Arnesen, K., Feizikhanhandi, S., and Sørlie, E. (2015). Simplified earthquake analysis for wind turbines and subsea structures on closed caisson foundations.

Bardet, J.-P. and Tobita, T. (2001). *NERA: A Computer Program for Nonlinear Earthquake site Response Analyses of Layered Soil Deposits.*

Byrne, B. W., Mcadam, R., Burd, H. J., Houlsby, G. T., Martin, C. M., Zdravkovi, L., Taborda, D. M. G., Potts, D. M., Jardine, R. J., Sideri, M., Schroeder, F. C., Gavin, K., Doherty, P., Igoe, D., Wood, a. M., Kallehave, D., and Gretlund, J. S. (2015). New design methods for large diameter piles under lateral loading for offshore wind applications. *Frontiers in Offshore Geotechnics III*, pages 705–710.

Colasanti, R. and Horvath, J. (2010). Practical subgrade model for improved soil-structure interaction analysis: software implementation. *Practice Periodical on Structural Design . . .*, (November):1–9.

Europa.eu. 2030 climate and energy framework. https://ec.europa.eu/clima/policies/strategies/2030_en. [Online; accessed 16-Desember-2017].

Gerolymos, N. and Gazetas, G. (06a). Winkler model for lateral response of rigid caisson foundations in linear soil. *Soil Dynamics and Earthquake Engineering*, 26(5):347–361.

Gerolymos, N. and Gazetas, G. (06b). Development of Winkler model for static and dynamic response of caisson foundations with soil and interface nonlinearities. *Soil Dynamics and Earthquake Engineering*, 26(5):363–376.

Gerolymos, N. and Gazetas, G. (06c). Static and dynamic response of massive caisson foundations with soil and interface nonlinearities - Validation and results. *Soil Dynamics and Earthquake Engineering*, 26(5):377–394.

Gourvenec, S. and Randolph, M. (2011). *Offshore Geotechnical Engineering*. CRC Press.

Hanssen, S. B. (2016). *Response of Laterally Loaded Monopiles Stian Baardsgaard Hanssen Response of Laterally Loaded Monopiles Thesis for the Degree of Philosophiae Doctor*, volume 6.

Hossain, M., Lehane, B., Hu, Y., and Gao, Y. (2012). Soil flow mechanisms around and between stiffeners of caissons during installation in clay. *Canadian Geotechnical Journal*, 49(4):442–459.

Hughes, T. J., Mallet, M., and Akira, M. (1986). A new finite element formulation for computational fluid dynamics: Ii. beyond supg. *Computer Methods in Applied Mechanics and Engineering*, 54(3):341–355.

Ikhouane, F., Mañosa, V., and Rodellar, J. (2007). Dynamic properties of the hysteretic Bouc-Wen model. *Systems and Control Letters*, 56(3):197–205.

Iwan, W. D. (1967). On a Class of Models for the Yielding Behavior of Continuous and Composite Systems. *Journal of Applied Mechanics*, 34(3):612–617.

Jeanjean, P. (2009). Re-Assessment of P-Y Curves for Soft Clays from Centrifuge Testing and Finite Element Modeling. *2009 Offshore Technology Conference*, (Vm):1–23.

Kerr, A. D. (1964). Elastic and Viscoelastic Foundation Models. *Journal of Applied Mechanics*, 31(3):491.

Khari, M., Kassim, K. A. B., and Adnan, A. B. (2011). The influence of effective confining pressure on site response analyses.

Kramer, S. and Kaynia, A. (2017). *Lecture notes for BA8305 Geodynamics*. Geotechnical Group.

Kramer, S. L. (1996). *Geotechnical Earthquake Engineering*. PE, 1st edition.

Martin, C. . R. M. F. (2006). Upper-bound analysis of lateral pile capacity in cohesive soil. *Géotechnique 56, No. 2*, pages 141–145.

Matlock, H. (1970). Correlation for Design of Laterally Loaded Piles in Soft Clay. In *Offshore Technology Conference*.

Mróz, Z. (1967). On the description of anisotropic workhardening. *Journal of the Mechanics and Physics of Solids*, 15(3):163–175.

Murff, J. D. and Hamilton, J. M. (1993). P-Ultimate for Undrained Analysis of Laterally Loaded Piles. *Journal of Geotechnical Engineering*, 119(1):91–107.

O'Neill, M., Reese, L., and Cox, W. (1990). Soil behavior for piles under lateral loading. *22th Offshore technology conferenceOff*, pages 279–287.

QuakeManager. Construction of linear displacement response spectra. `https://sites.google.com/site/quakemanagerwiki/record-manager/spectra/what-is-a-response-spectrum`. [Online; accessed 17-Desember-2017].

Randolph M. F & Houlsby, G. T. (1984). The limiting pressure on a circular pile loaded laterally in cohesive soil. *Géotechnique 34, No. 4*, pages 613–623.

Stevens, J. and Audibert, J. (1979). Re-Examination Of P-Y Curve Formulations. In *Offshore Technology Conference*.

Villaverde, R. (2009). *Fundamental concepts of earthquake engineering*. CRC Press.

Vucetic, M. and Dobry, R. (1991). Effect of Soil Plasticity on Cyclic Response. *Journal of Geotechnical Engineering*, 117(1):89–107.

Yamamoto, N., Sharma, S. S., and Erbrich, C. T. (2015). Suitability of Masing rules for seismic analysis of offshore carbonate sediments. *Frontiers in Offshore Geotechnics III*, pages 1127–1132.

Zdravković, L., Taborda, D. M. G., Potts, D. M., Jardine, R. J., Sideri, M., Schroeder, F. C., Zdravkovi, L., Taborda, D. M. G., Potts, D. M., Jardine, R. J., Sideri, M., Schroeder, F. C., Byrne, B. W., Mcadam, R., Burd, H. J., Houlsby, G. T., Martin, C. M., Gavin, K., Doherty, P., Igoe, D., Wood, a. M., Kallehave, D., and Gretlund, J. S. (2015). Numerical modelling of large diameter piles under lateral loading for offshore wind applications. In *Frontiers in Offshore Geotechnics III*, number August, pages 759–764.

Zhang, Y., Andersen, K. H., and Tedesco, G. (2016). Ultimate bearing capacity of laterally loaded piles in clay – Some practical considerations. *Marine Structures*, 50:260–275.

Appendices

List of Figures in Appendices

A.1 Synthetic accelogram 1 113

A.2 Synthetic accelogram 3 113

A.3 Synthetic accelogram 5 114

A.4 Synthetic accelogram 6 114

C.1 Acceleration time series at 0, 10 m, and 17 m for EQ1. 118

C.2 Acceleration time series at 0, 10 m, and 17 m for EQ3. 119

C.3 Acceleration time series at 0, 10 m, and 17 m for EQ5. 120

C.4 Acceleration time series at 0, 10 m, and 17 m for EQ6. 121

D.1 Acceleration at seabed level versus time for EQ 1A. 123

D.2 Displacement at seabed level versus time for EQ 1A. 123

D.3 Rotation at seabed level versus time for EQ 1A. 124

D.4 Moment at seabed level versus time for EQ 1A. 124

D.5 Shear force at seabed level versus time for EQ 1A. 124

D.6 Acceleration at seabed level versus time for EQ 1S. 125

D.7 Displacement at seabed level versus time for EQ 1S. 125

D.8 Rotation at seabed level versus time for EQ 1S. 125

D.9 Moment at seabed level versus time for EQ 1S. 126

D.10 Shear force at seabed level versus time for EQ 1S. 126

D.11 Acceleration at seabed level versus time for EQ 1R. 126

D.12 Displacement at seabed level versus time for EQ 1R. 127

D.13 Rotation at seabed level versus time for EQ 1R. 127

D.14 Moment at seabed level versus time for EQ 1R. 127

D.15 Shear force at seabed level versus time for EQ 1R. 127

D.16 Acceleration at seabed level versus time for EQ 3A. 128

D.17 Displacement at seabed level versus time for EQ 3A. 128

D.18 Rotation at seabed level versus time for EQ 3A. 128

D.19 Moment at seabed level versus time for EQ 3A. 129

D.20 Shear force at seabed level versus time for EQ 3A. 129

D.21 Acceleration at seabed level versus time for EQ 3S. 129

D.22 Displacement at seabed level versus time for EQ 3S. 130

D.23 Rotation at seabed level versus time for EQ 3S. 130

D.24 Moment at seabed level versus time for EQ 3S. 130

D.25 Shear force at seabed level versus time for EQ 3S. 130

D.26 Acceleration at seabed level versus time for EQ 3R. 131

D.27 Displacement at seabed level versus time for EQ 3R. 131

D.28 Rotation at seabed level versus time for EQ 3R. 131

D.29 Moment at seabed level versus time for EQ 3R. 132

D.30 Shear force at seabed level versus time for EQ 3R. 132

D.31 Acceleration at seabed level versus time for EQ 5A. 132

D.32 Displacement at seabed level versus time for EQ 5A. 133

D.33 Rotation at seabed level versus time for EQ 5A. 133

D.34 Moment at seabed level versus time for EQ 5A. 133

D.35 Shear force at seabed level versus time for EQ 5A. 133

D.36 Acceleration at seabed level versus time for EQ 5S. 134

D.37 Displacement at seabed level versus time for EQ 5S. 134

D.38 Rotation at seabed level versus time for EQ 5S. 134

D.39 Moment at seabed level versus time for EQ 5S. 135

D.40 Shear force at seabed level versus time for EQ 5S. 135

D.41 Acceleration at seabed level versus time for EQ 5R. 135

D.42 Displacement at seabed level versus time for EQ 5R. 136

D.43 Rotation at seabed level versus time for EQ 5R. 136

D.44 Moment at seabed level versus time for EQ 5R. 136

D.45 Shear force at seabed level versus time for EQ 5R. 136

D.46 Acceleration at seabed level versus time for EQ 6A. 137

D.47 Displacement at seabed level versus time for EQ 6A. 137

D.48 Rotation at seabed level versus time for EQ 6A. 137

D.49 Moment at seabed level versus time for EQ 6A. 138

D.50 Shear force at seabed level versus time for EQ 6A. 138

D.51 Acceleration at seabed level versus time for EQ 6S. 138

D.52 Displacement at seabed level versus time for EQ 6S. 139

D.53 Rotation at seabed level versus time for EQ 6S. 139

D.54 Moment at seabed level versus time for EQ 6S. 139

D.55 Shear force at seabed level versus time for EQ 6S. 139

D.56 Acceleration at seabed level versus time for EQ 6R. 140

D.57 Displacement at seabed level versus time for EQ 6R. 140

D.58 Rotation at seabed level versus time for EQ 6R. 140

D.59 Moment at seabed level versus time for EQ 6R. 141

D.60 Shear force at seabed level versus time for EQ 6R. 141

D.61 EQ 3: Total acceleration of structure at seabed level for time series analyses using depth variable time series (A), seabed time series (S) and reference depth time series (R). 142

D.62 EQ 5: Total acceleration of structure at seabed level for time series analyses using depth variable time series (A), seabed time series (S) and reference depth time series (R). 142

D.63 EQ 6: Total acceleration of structure at seabed level for time series analyses using depth variable time series (A), seabed time series (S) and reference depth time series (R). 143

D.64 EQ 3: Total displacement of structure at seabed level for time series analyses using depth variable time series (A), seabed time series (S) and reference depth time series (R). 143

D.65 EQ 5: Total displacement of structure at seabed level for time series analyses using depth variable time series (A), seabed time series (S) and reference depth time series (R). 144

D.66 EQ 6: Total displacement of structure at seabed level for time series analyses using depth variable time series (A), seabed time series (S) and reference depth time series (R). 144

D.67 EQ 3: Rotation of structure at seabed level for time series analyses using depth variable time series (A), seabed time series (S) and reference depth time series (R). 145

D.68 EQ 5: Rotation of structure at seabed level for time series analyses using depth variable time series (A), seabed time series (S) and reference depth time series (R). 145

D.69 EQ 6: Rotation of structure at seabed level for time series analyses using depth variable time series (A), seabed time series (S) and reference depth time series (R). 146

D.70 EQ 3: Moment at seabed level for time series analyses using depth variable time series (A), seabed time series (S) and reference depth time series (R). 146

D.71 EQ 5: Moment at seabed level for time series analyses using depth variable time series (A), seabed time series (S) and reference depth time series (R). 147

D.72 EQ 6: Moment at seabed level for time series analyses using depth variable time series (A), seabed time series (S) and reference depth time series (R). 147

D.73 EQ 3: Shear force at seabed level for time series analyses using depth variable time series (A), seabed time series (S) and reference depth time series (R). 148

D.74 EQ 5: Shear force at seabed level for time series analyses using depth variable time series (A), seabed time series (S) and reference depth time series (R). 148

D.75 EQ 6: Shear force at seabed level for time series analyses using depth variable time series (A), seabed time series (S) and reference depth time series (R). 149

D.76 Comparison of peak total displacement at seabed for the various time series analyses. 149

D.77 Comparison of peak rotation of the structure for the various time series analyses. 150

D.78 Comparison of peak moment at seabed for the various time series analyses. 150

D.79 Comparison of peak shear force at seabed for the various time series analyses. 151

D.82 Force-displacement in soil spring at seabed level during EQ 1A. 153

Appendix A

Input Time Histories

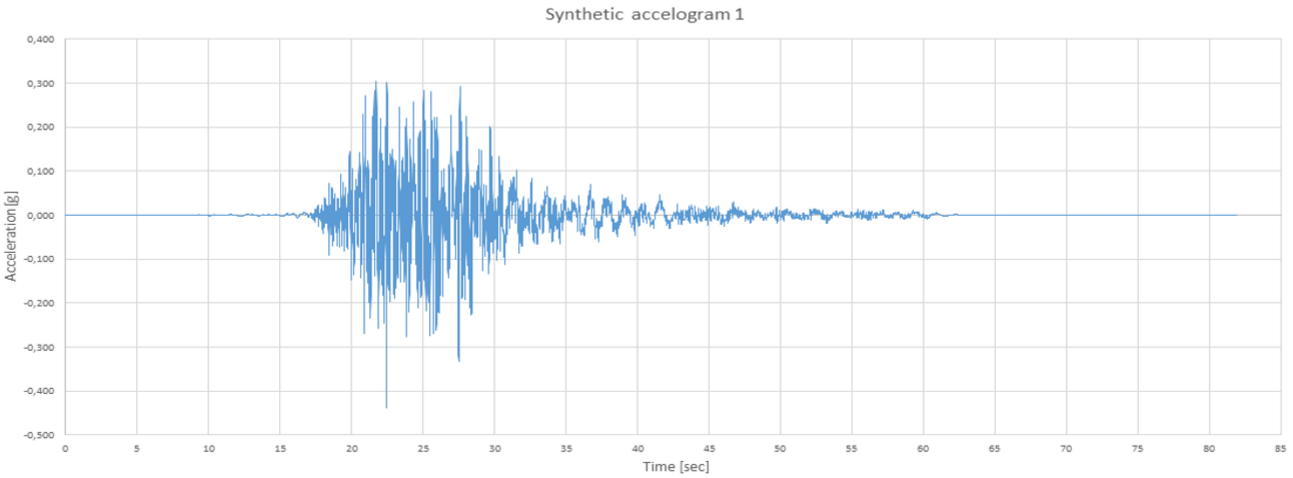

Figure A.1: Synthetic accelogram 1

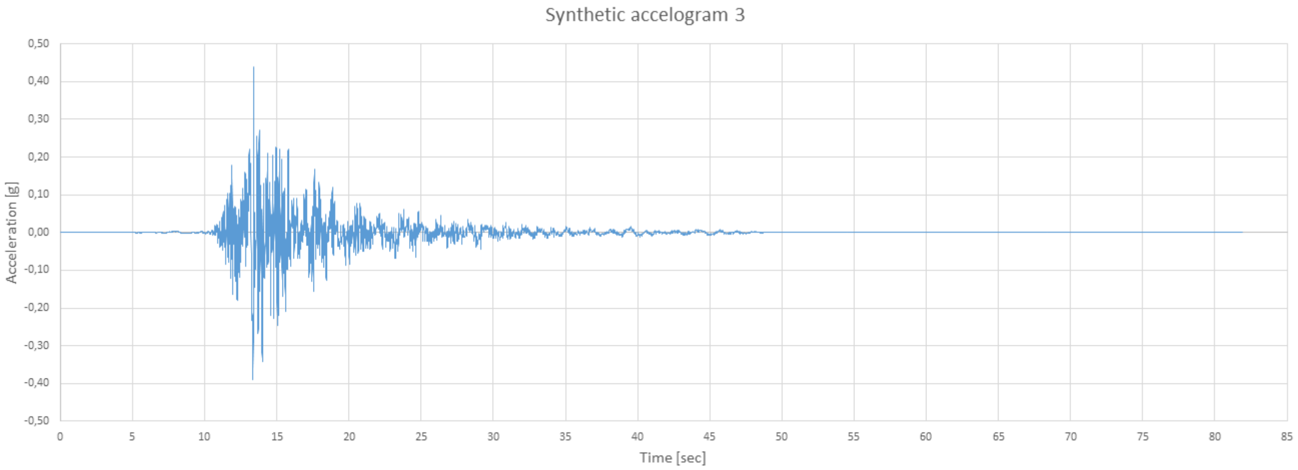

Figure A.2: Synthetic accelogram 3

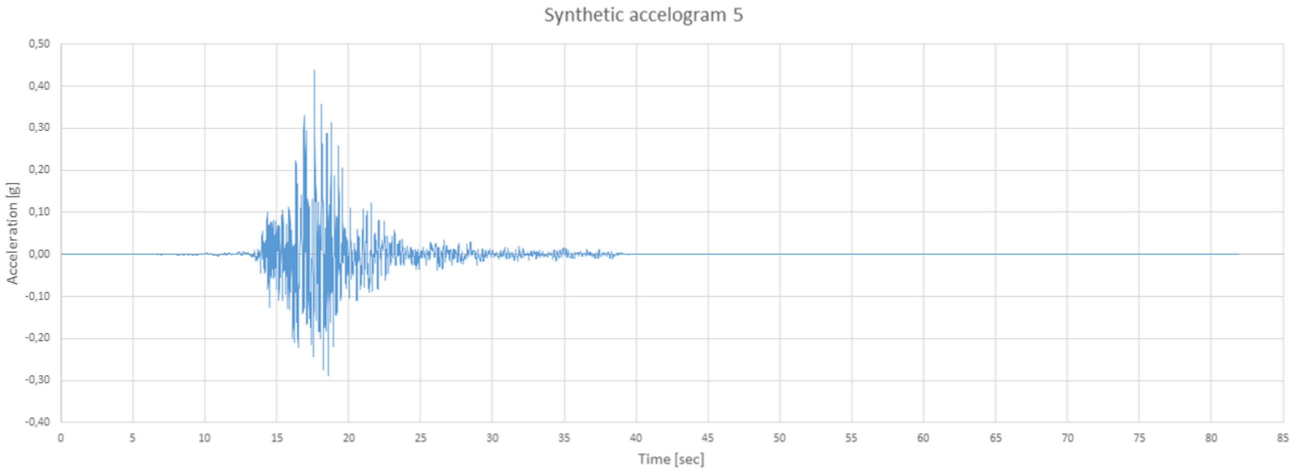

Figure A.3: Synthetic accelogram 5

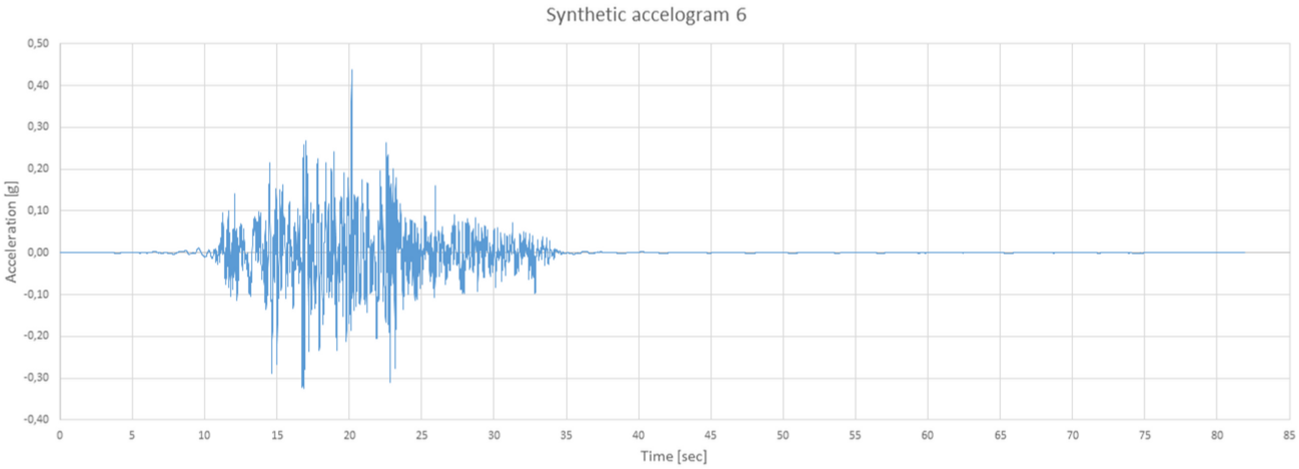

Figure A.4: Synthetic accelogram 6

Appendix B

Derivations

B.1 Undamped Natural Frequency

$$m\ddot{u} + ku = 0 \tag{B.1.1}$$

Assume solution of harmonic type:

$$u = Asin(\omega t) + Bcos(\omega t) \tag{B.1.2}$$

$$\dot{u} = A\omega cos(\omega t) - B\omega sin(\omega t) \tag{B.1.3}$$

$$\ddot{u} = -A\omega^2 sin(\omega t) - B\omega^2 cos(\omega t) = -\omega^2 u \tag{B.1.4}$$

Insert into (B.1.1) and divide by m to get:

$$-\omega^2 u + \frac{k}{m}u = 0 \tag{B.1.5}$$

Solve for ω to get

$$\omega = \omega_n = \sqrt{\frac{k}{m}} \tag{B.1.6}$$

B.2 Solution of a Free Vibrating Damped SDOF System

$$m\ddot{u} + c\dot{u} + ku = 0 \tag{B.2.1}$$

Assume a solution of the form:

$$u = Ce^{rt} \tag{B.2.2}$$

Derivate and insert into B.2.1:

$$(mr^2 + cr + k) * Ce^{rt} = 0 \tag{B.2.3}$$

Solve for r to obtain:

$$r_{1,2} = \omega_n \left(-\frac{c}{2m\omega_n} \pm \sqrt{(\frac{c}{2m\omega_n})^2 - 1} \right) \tag{B.2.4}$$

Defining c_c and ξ:

$$c = c_c = 2m\omega_n = 2\sqrt{km} \tag{B.2.5}$$

$$\xi = \frac{c}{2m\omega_n} = \frac{c}{c_c} \tag{B.2.6}$$

Appendix C

Site Response Results

C.1 NERA Results

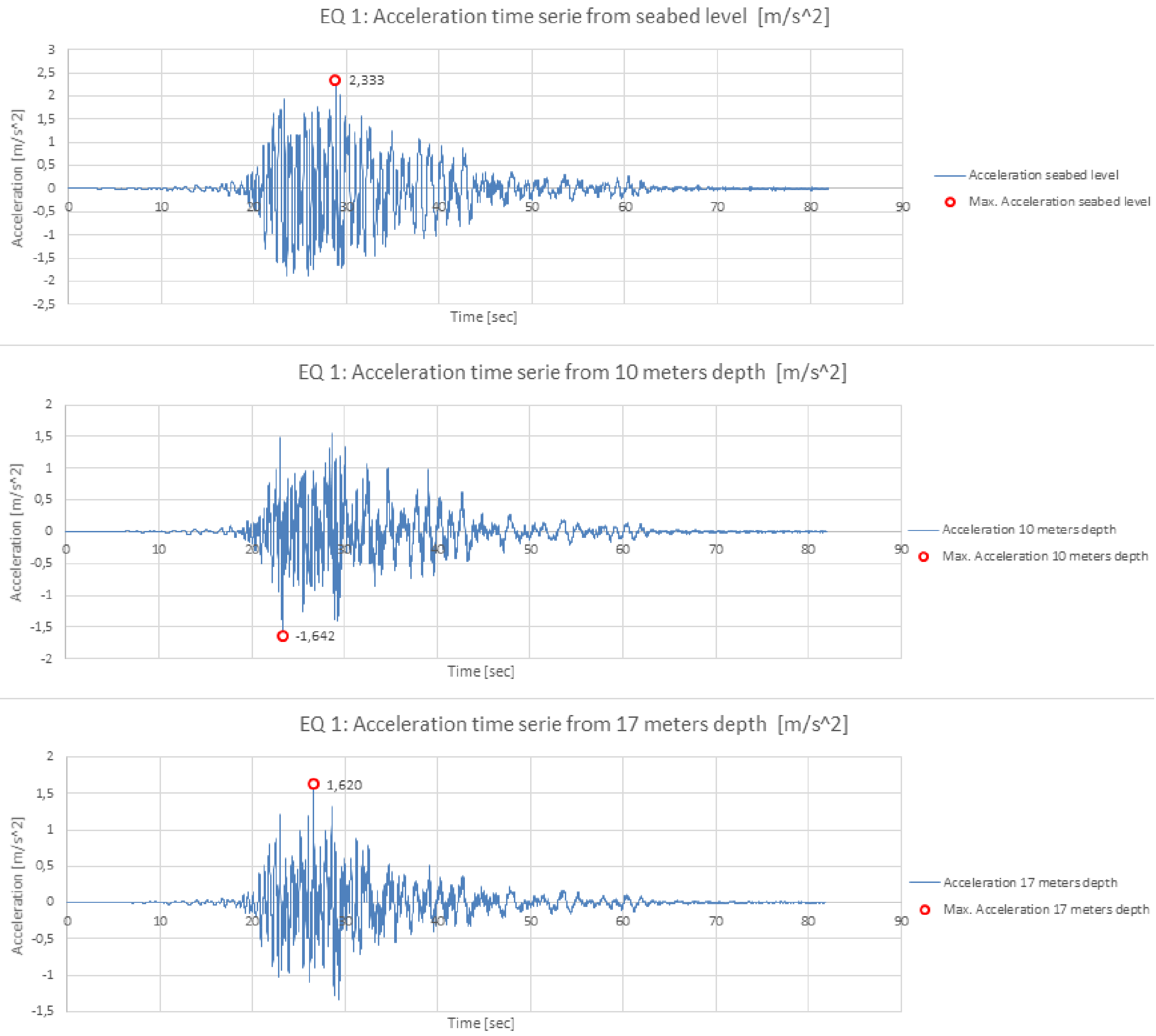

Figure C.1: Acceleration time series at 0, 10 m, and 17 m for EQ1.

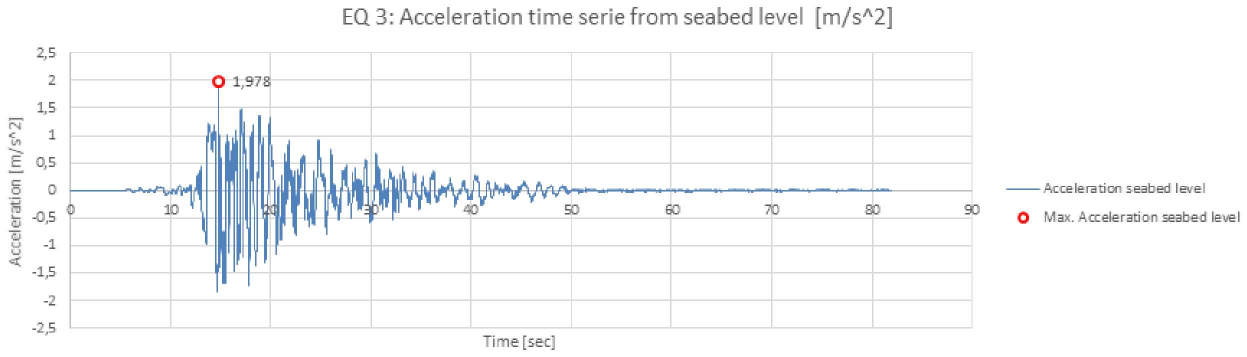

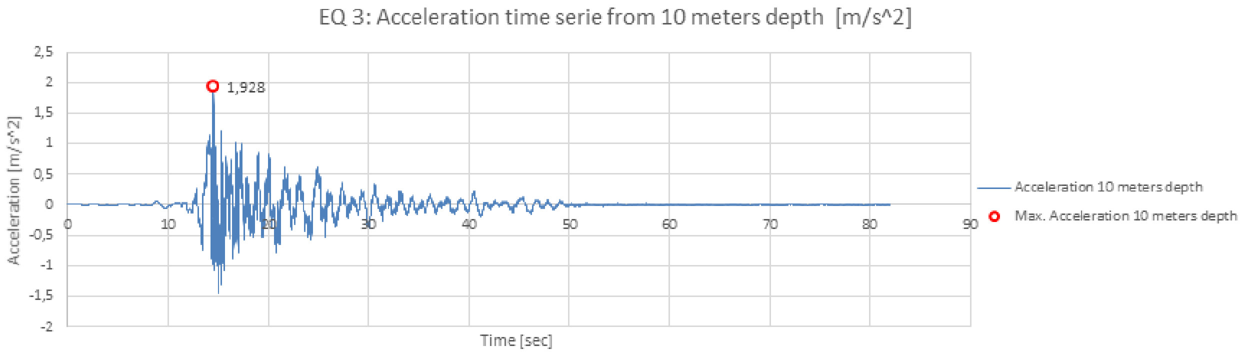

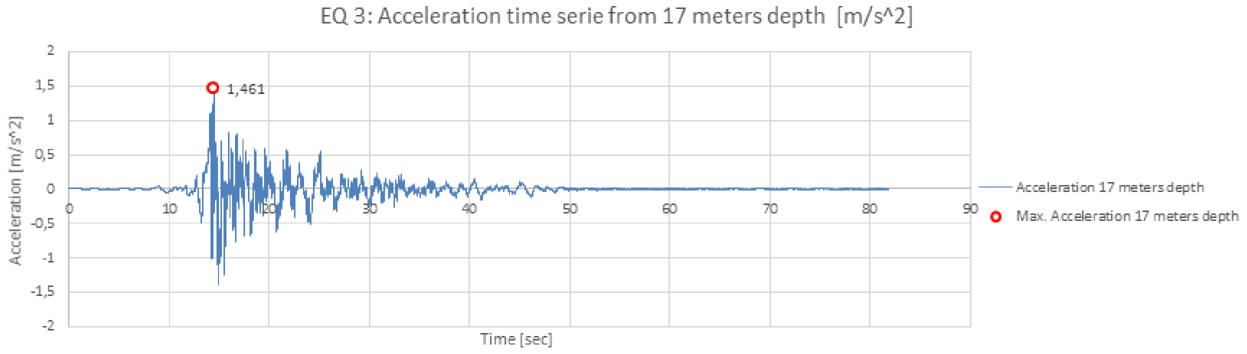

Figure C.2: Acceleration time series at 0, 10 m, and 17 m for EQ3.

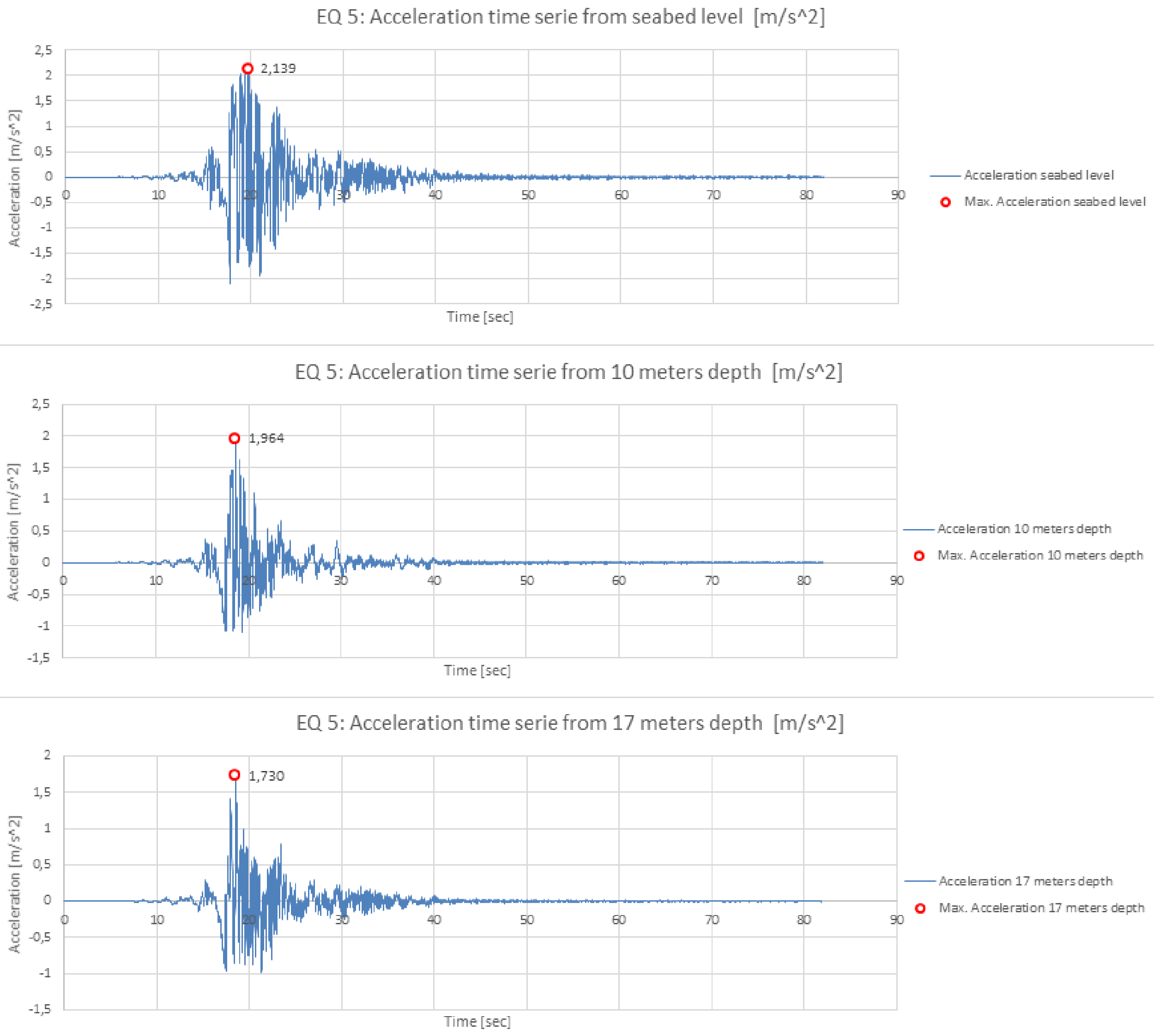

Figure C.3: Acceleration time series at 0, 10 m, and 17 m for EQ5.

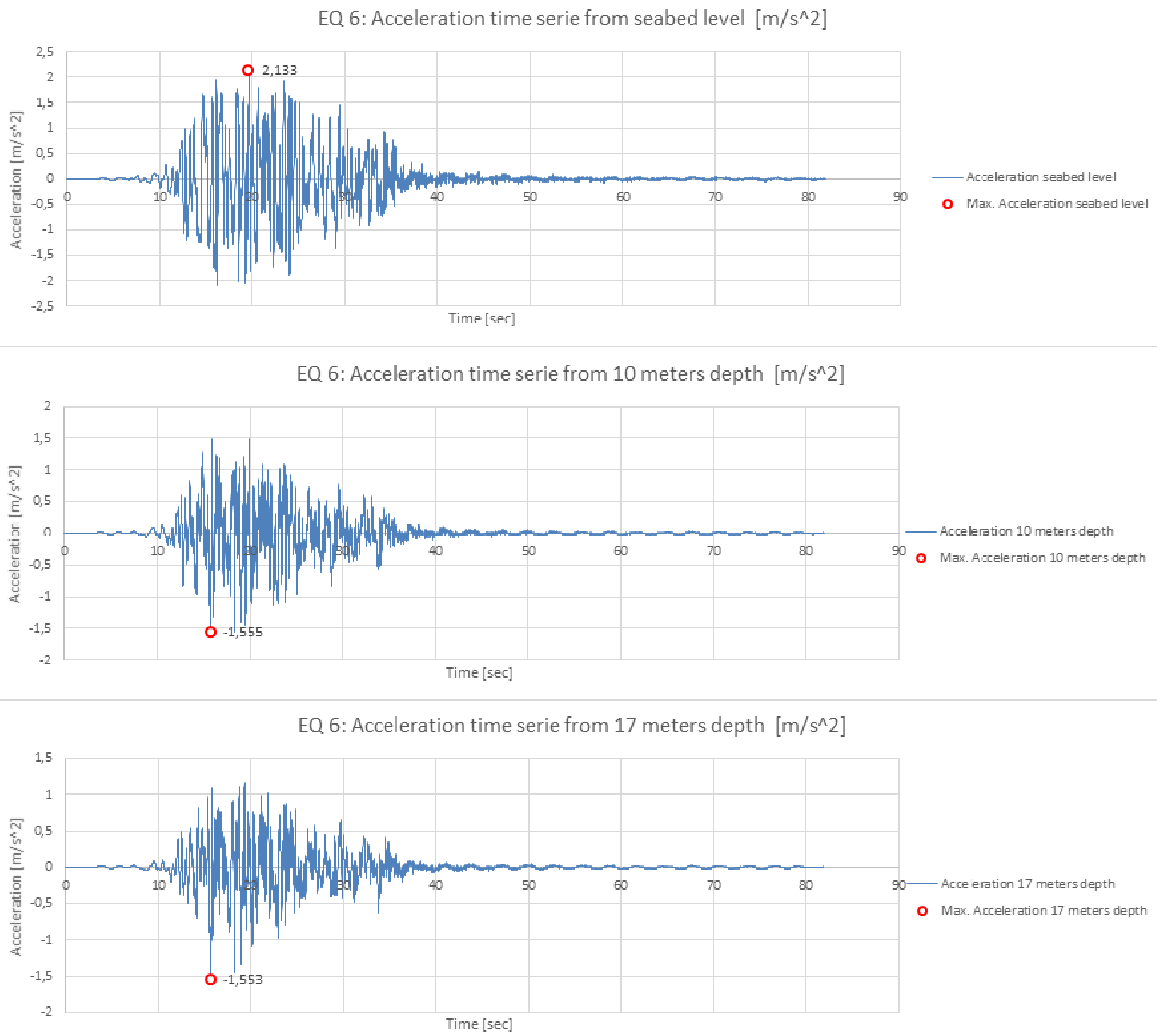

Figure C.4: Acceleration time series at 0, 10 m, and 17 m for EQ6.

Appendix D

Results From Time Series Analyses

D.1 Individual Plots

D.1.1 EQ 1A

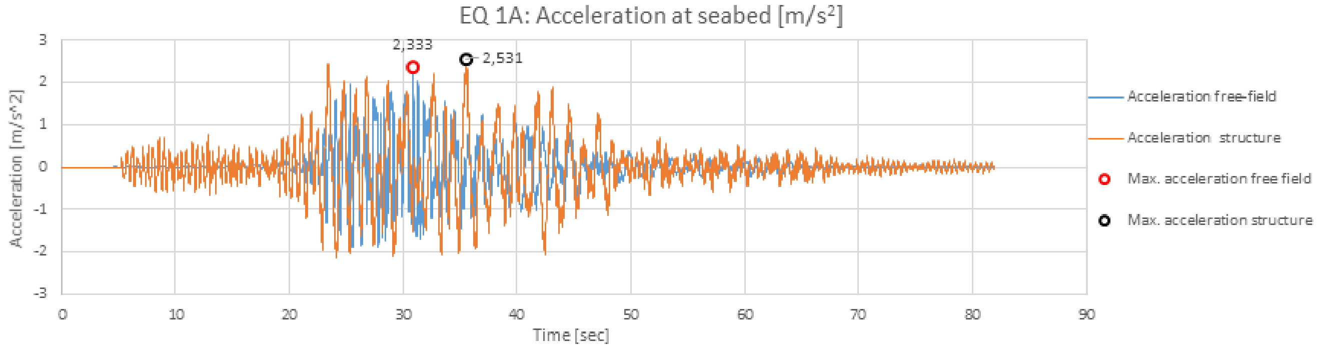

Figure D.1: Acceleration at seabed level versus time for EQ 1A.

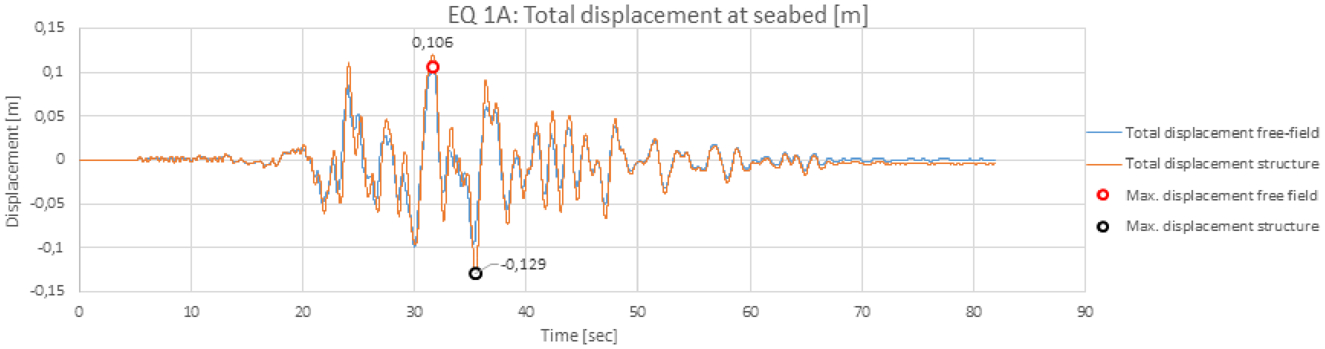

Figure D.2: Displacement at seabed level versus time for EQ 1A.

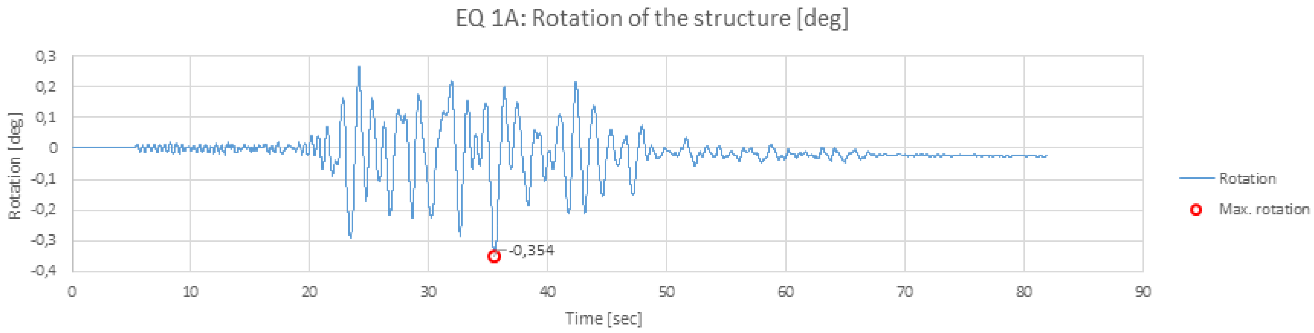

Figure D.3: Rotation at seabed level versus time for EQ 1A.

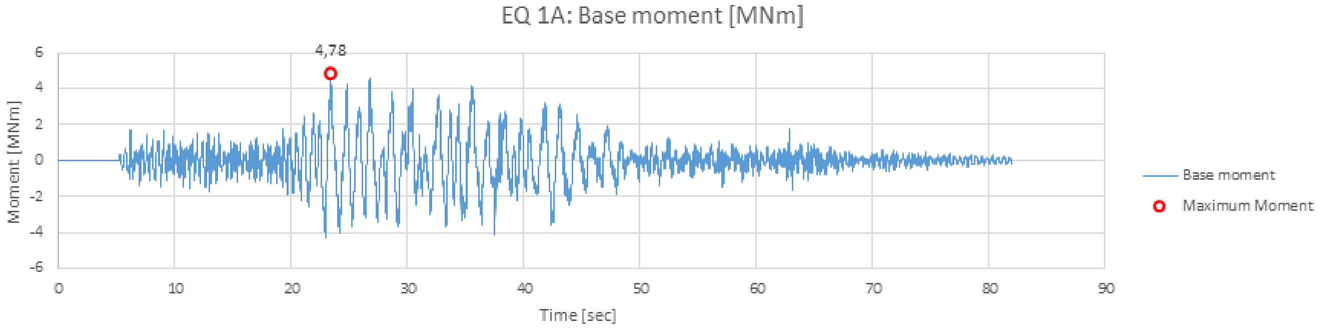

Figure D.4: Moment at seabed level versus time for EQ 1A.

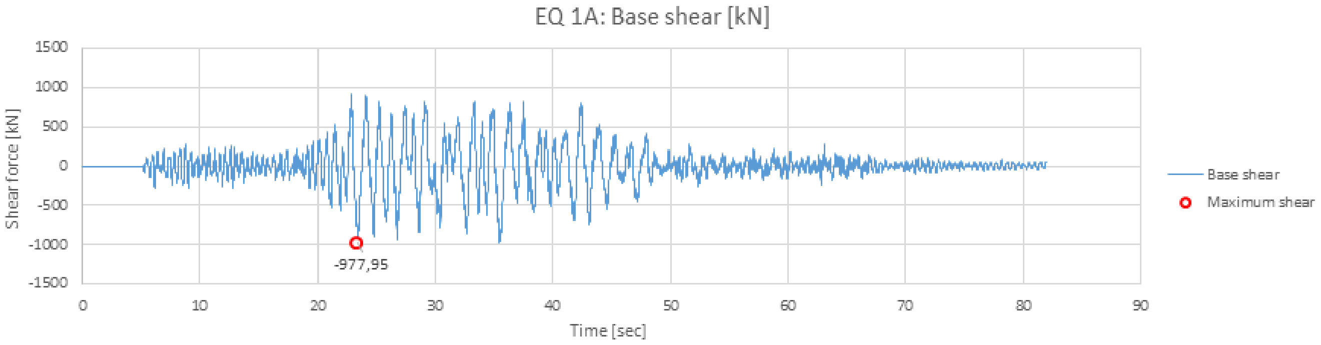

Figure D.5: Shear force at seabed level versus time for EQ 1A.

D.1.2 EQ 1S

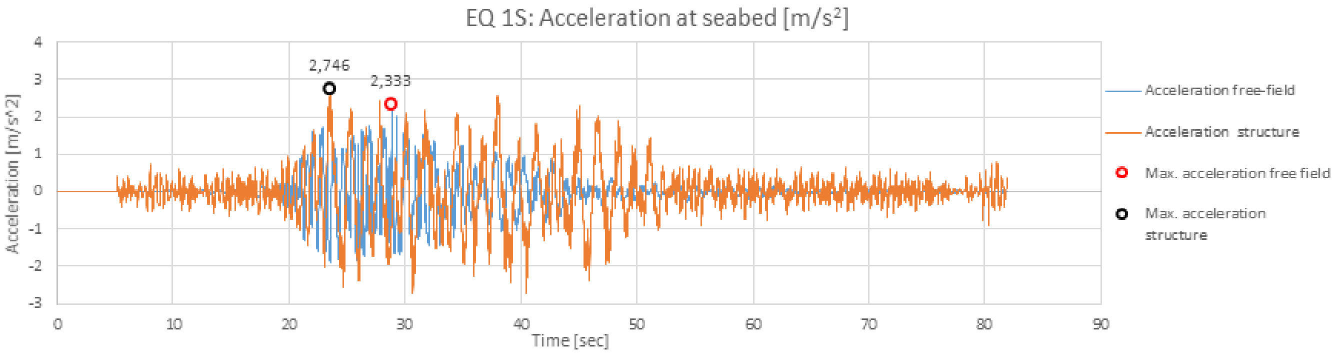

Figure D.6: Acceleration at seabed level versus time for EQ 1S.

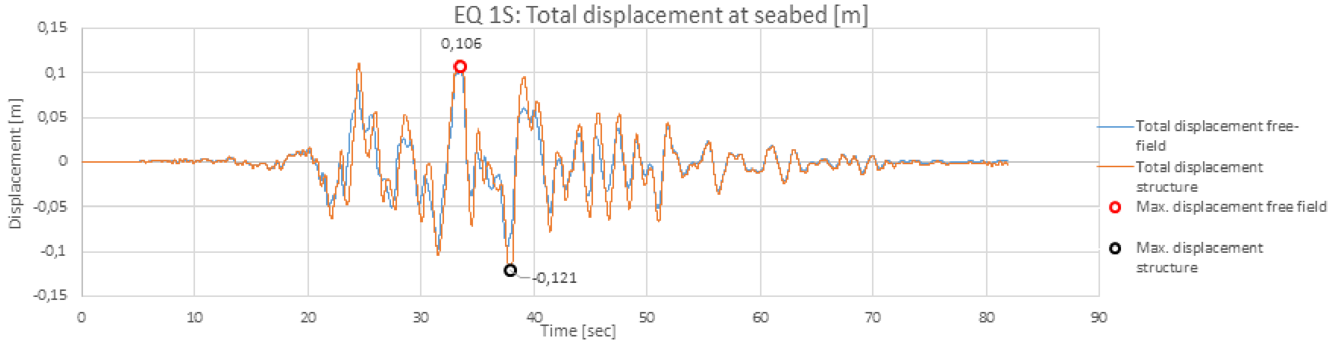

Figure D.7: Displacement at seabed level versus time for EQ 1S.

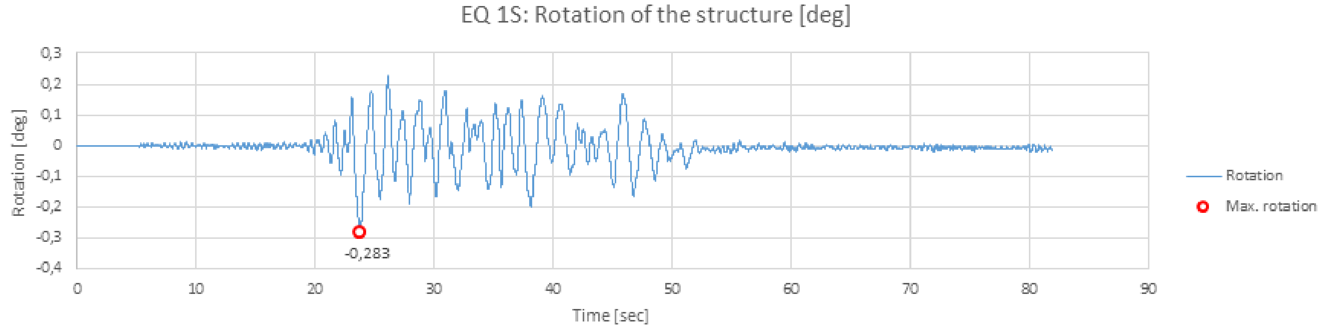

Figure D.8: Rotation at seabed level versus time for EQ 1S.

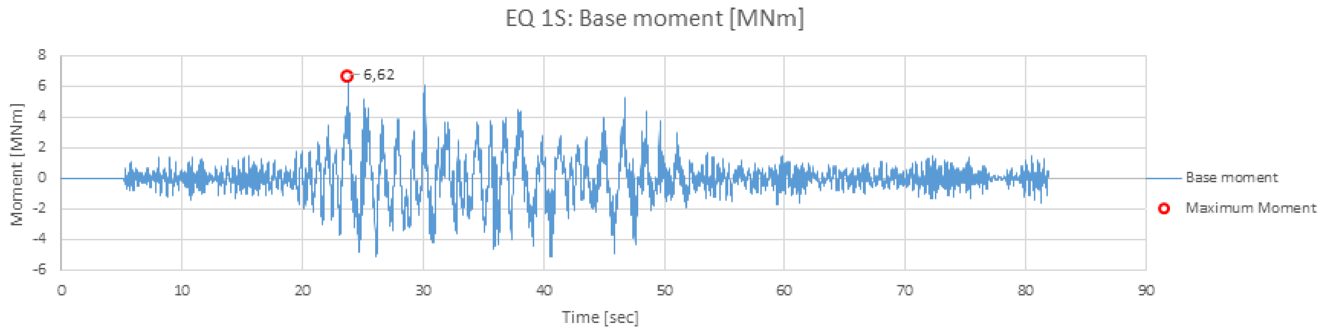

Figure D.9: Moment at seabed level versus time for EQ 1S.

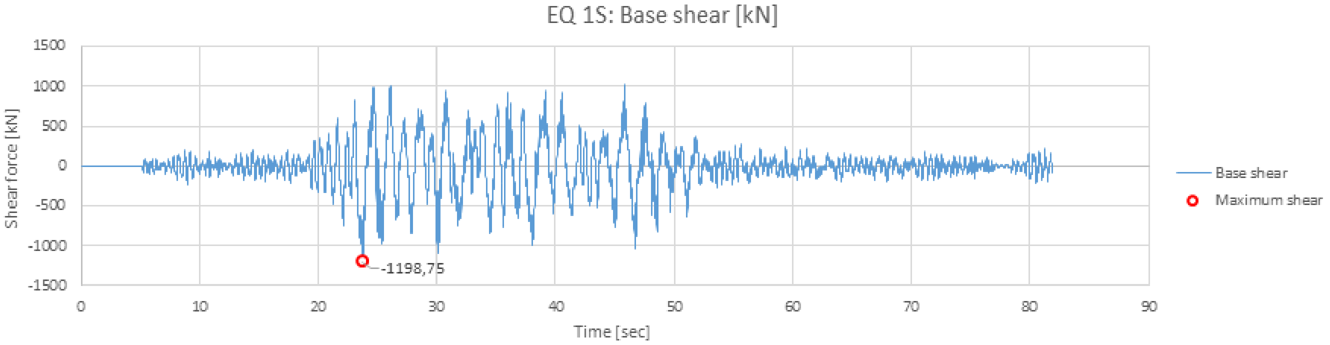

Figure D.10: Shear force at seabed level versus time for EQ 1S.

D.1.3 EQ 1R

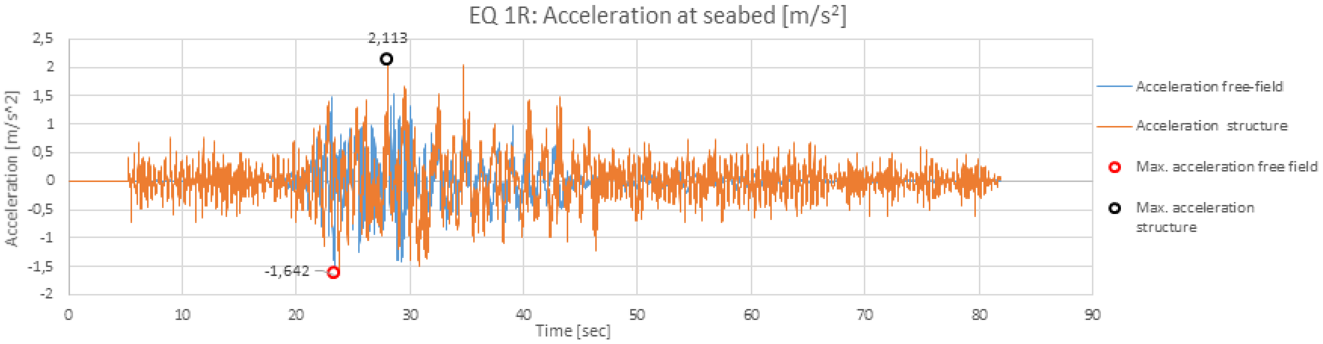

Figure D.11: Acceleration at seabed level versus time for EQ 1R.

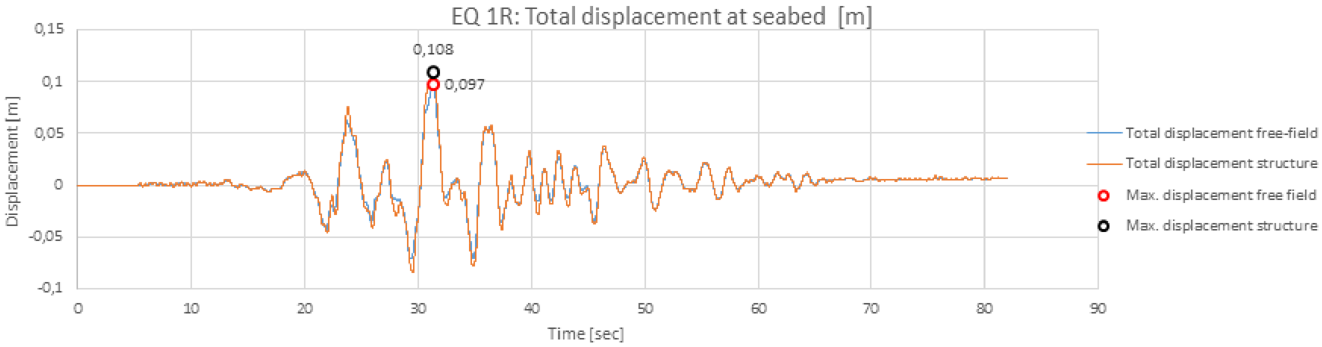

Figure D.12: Displacement at seabed level versus time for EQ 1R.

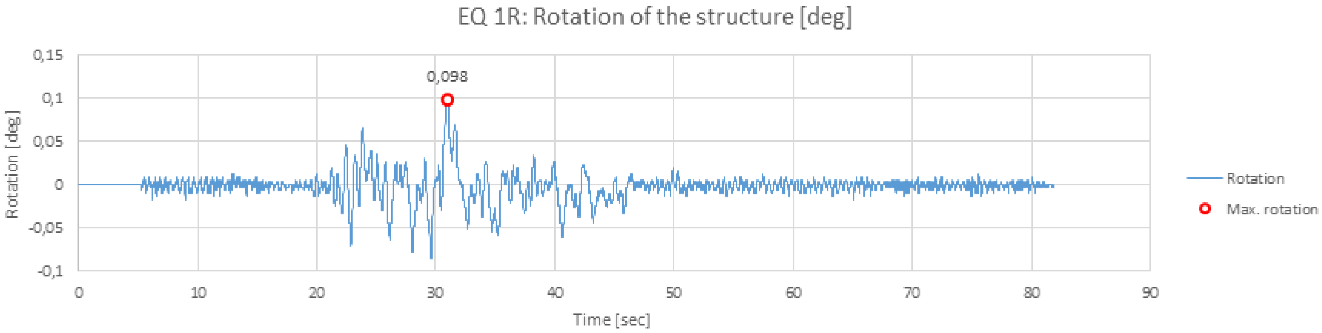

Figure D.13: Rotation at seabed level versus time for EQ 1R.

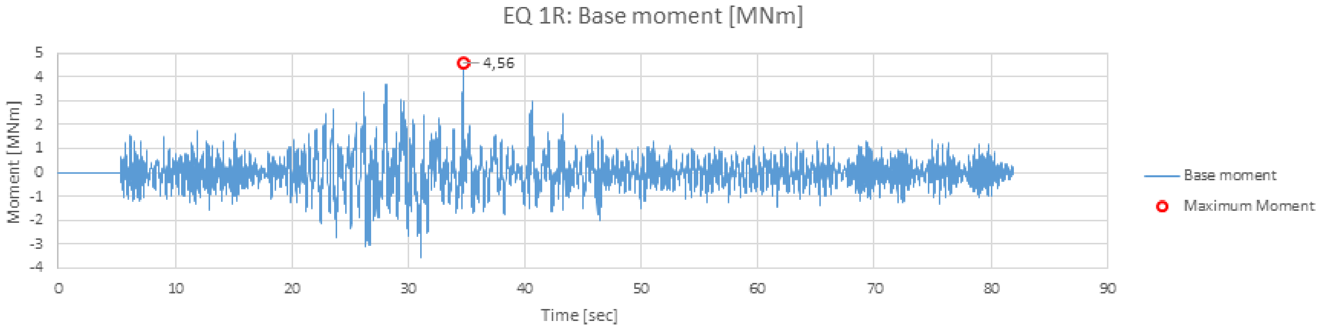

Figure D.14: Moment at seabed level versus time for EQ 1R.

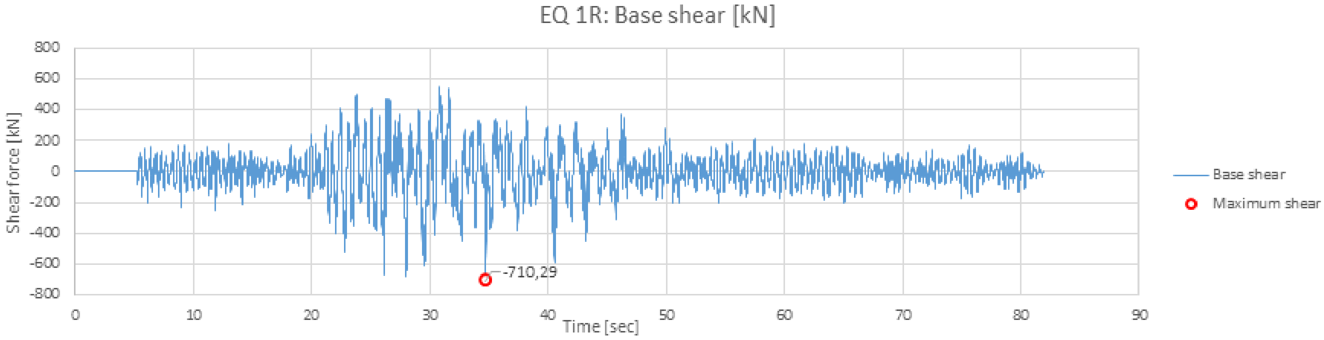

Figure D.15: Shear force at seabed level versus time for EQ 1R.

D.1.4 EQ 3A

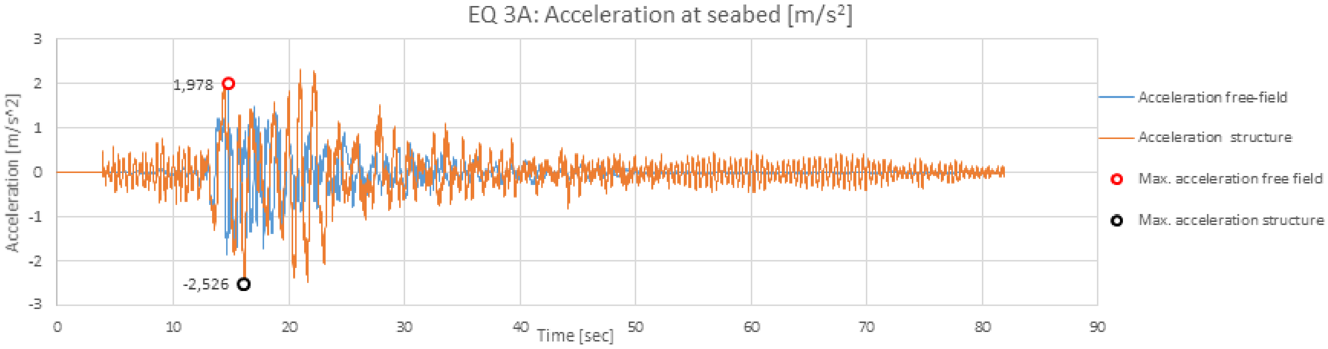

Figure D.16: Acceleration at seabed level versus time for EQ 3A.

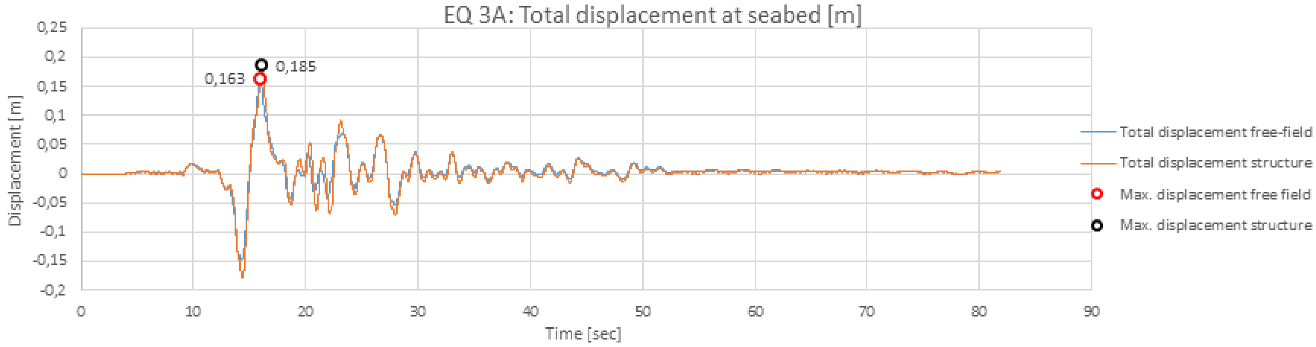

Figure D.17: Displacement at seabed level versus time for EQ 3A.

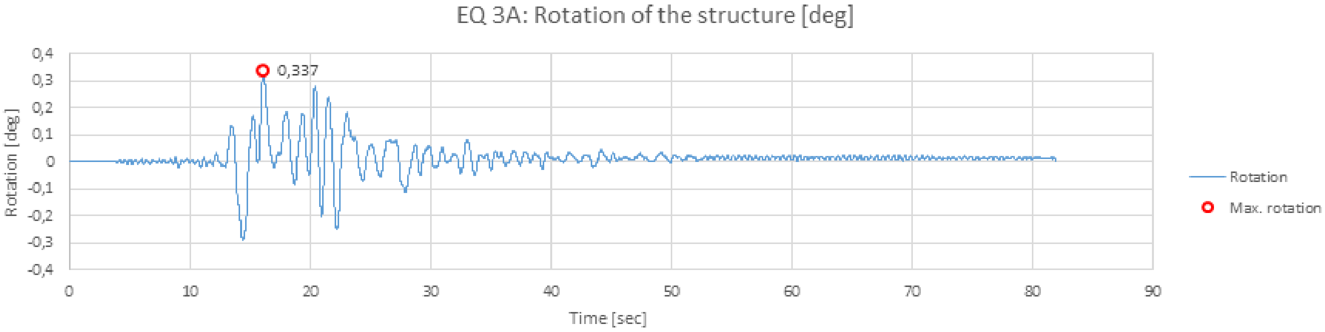

Figure D.18: Rotation at seabed level versus time for EQ 3A.

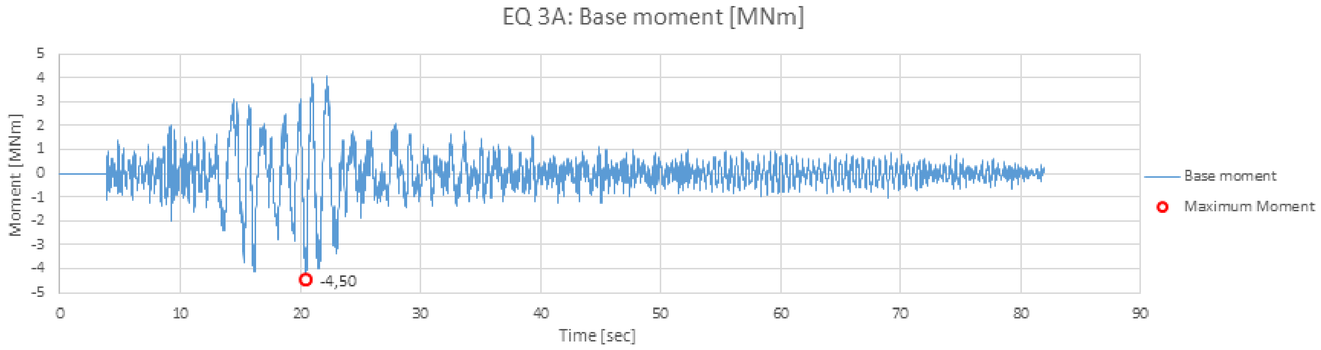

Figure D.19: Moment at seabed level versus time for EQ 3A.

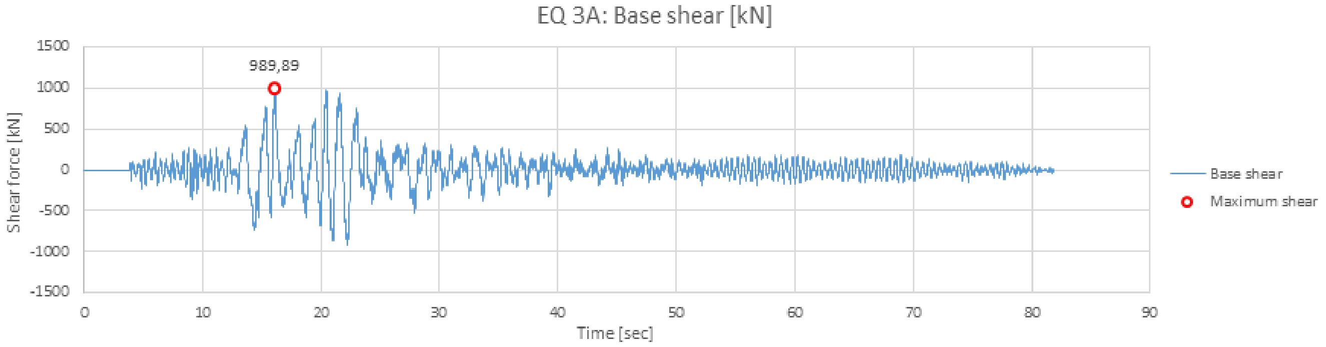

Figure D.20: Shear force at seabed level versus time for EQ 3A.

D.1.5 EQ 3S

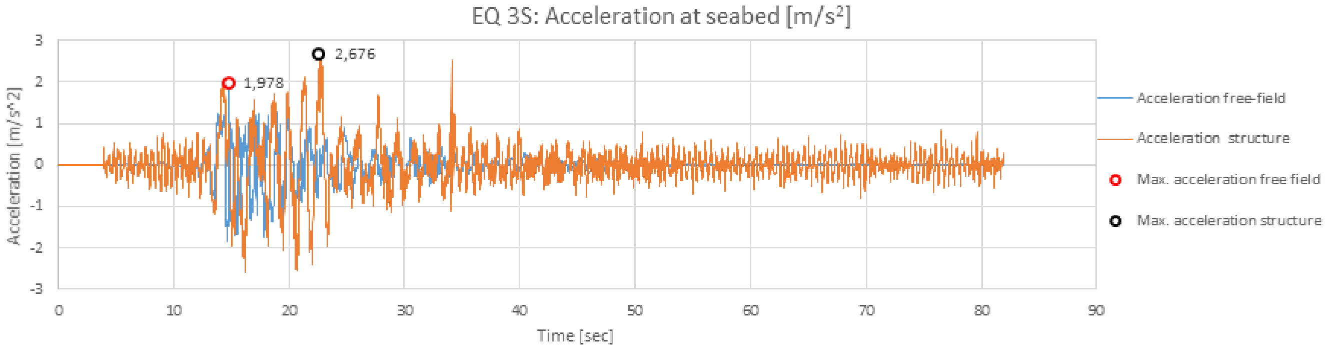

Figure D.21: Acceleration at seabed level versus time for EQ 3S.

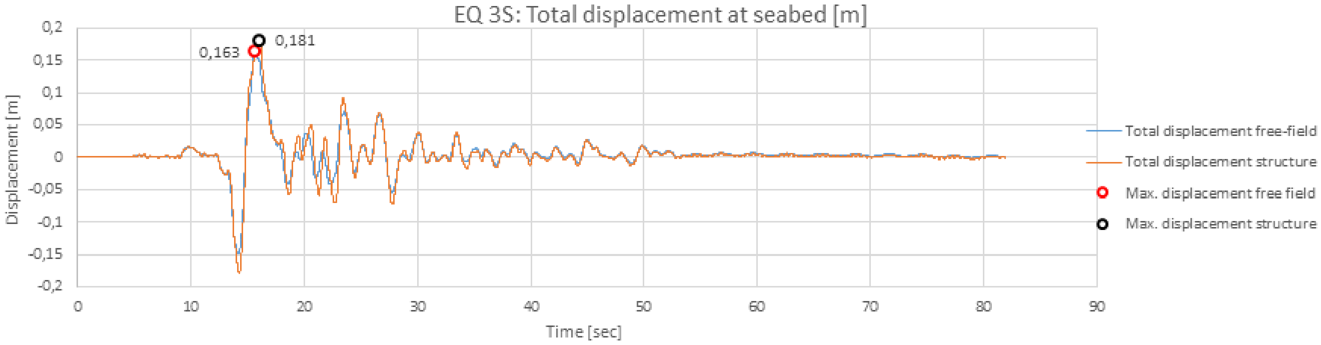

Figure D.22: Displacement at seabed level versus time for EQ 3S.

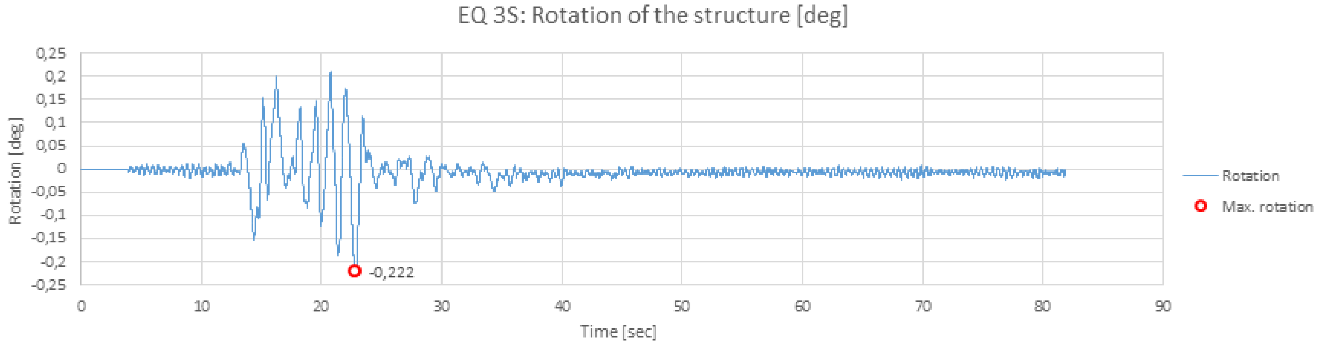

Figure D.23: Rotation at seabed level versus time for EQ 3S.

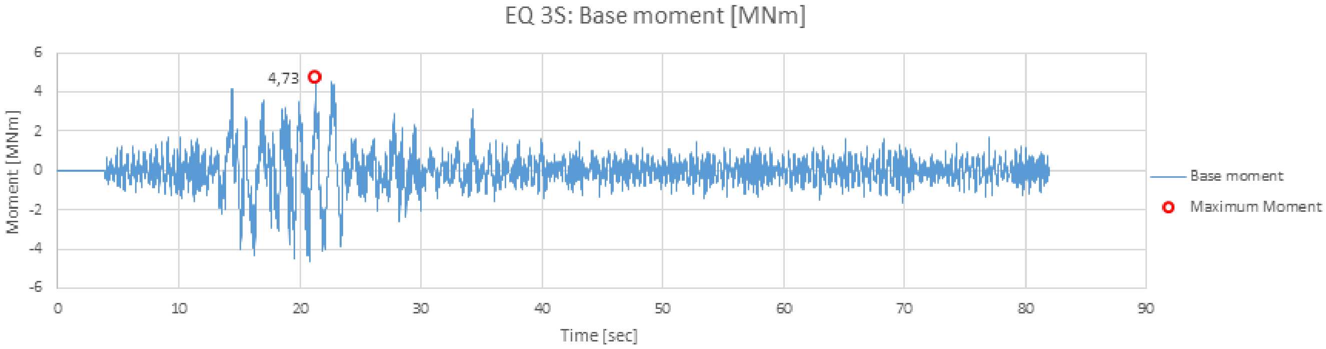

Figure D.24: Moment at seabed level versus time for EQ 3S.

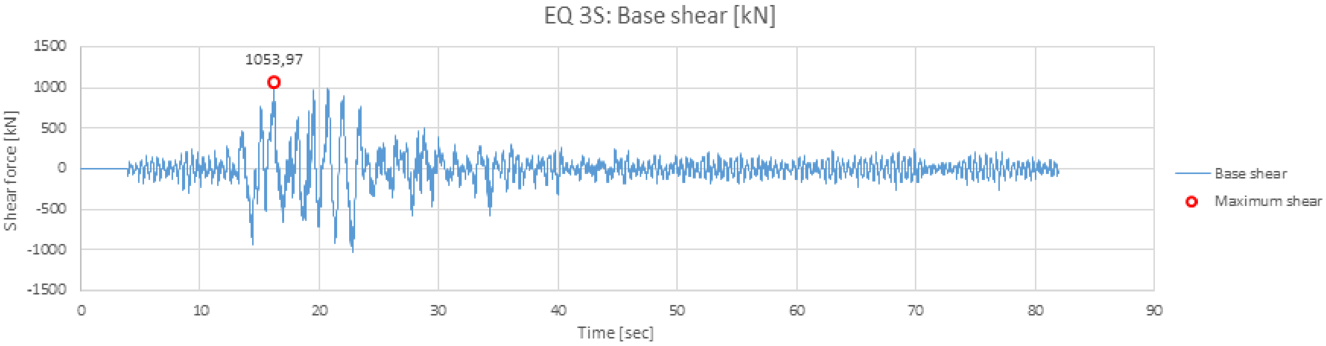

Figure D.25: Shear force at seabed level versus time for EQ 3S.

D.1.6 EQ 3R

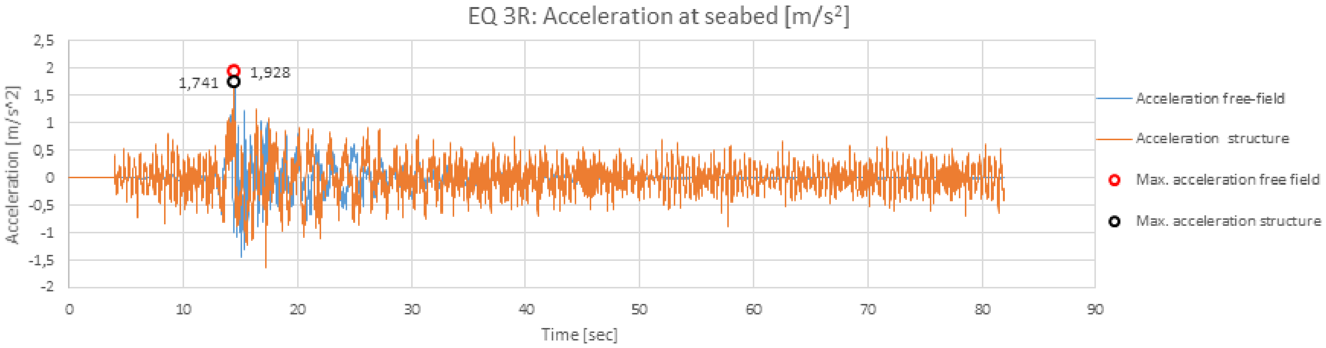

Figure D.26: Acceleration at seabed level versus time for EQ 3R.

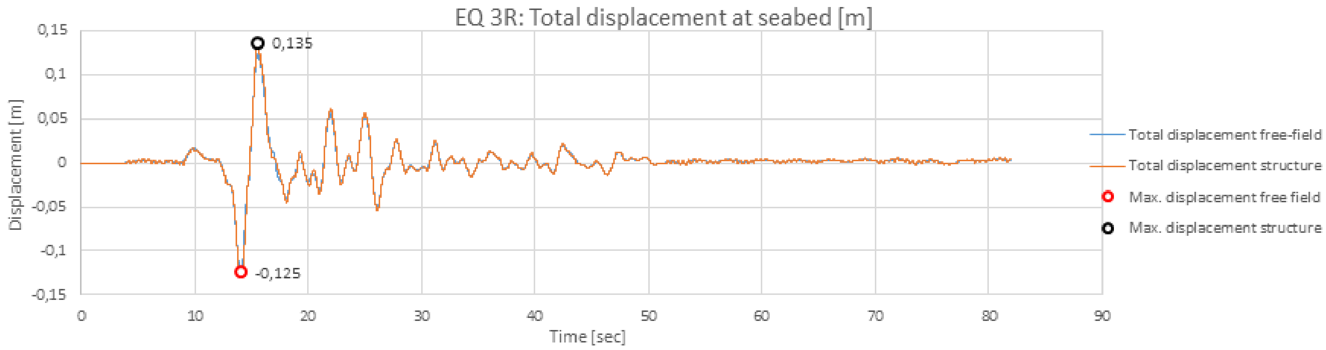

Figure D.27: Displacement at seabed level versus time for EQ 3R.

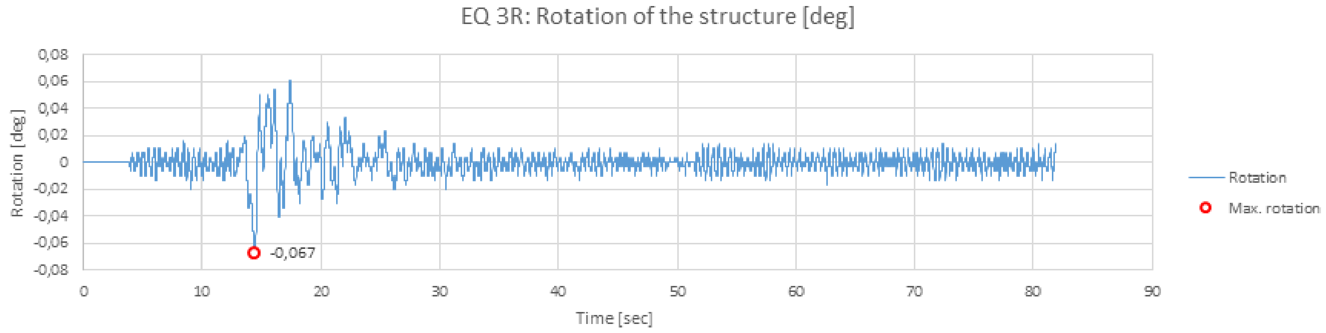

Figure D.28: Rotation at seabed level versus time for EQ 3R.

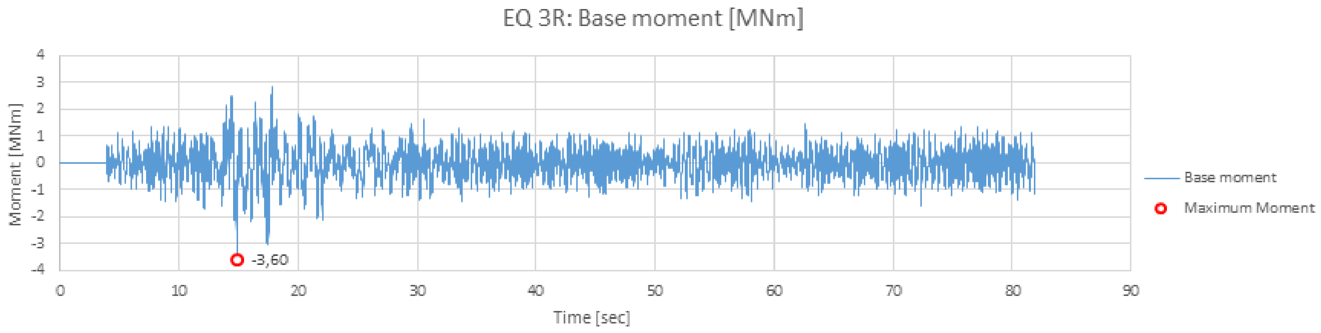

Figure D.29: Moment at seabed level versus time for EQ 3R.

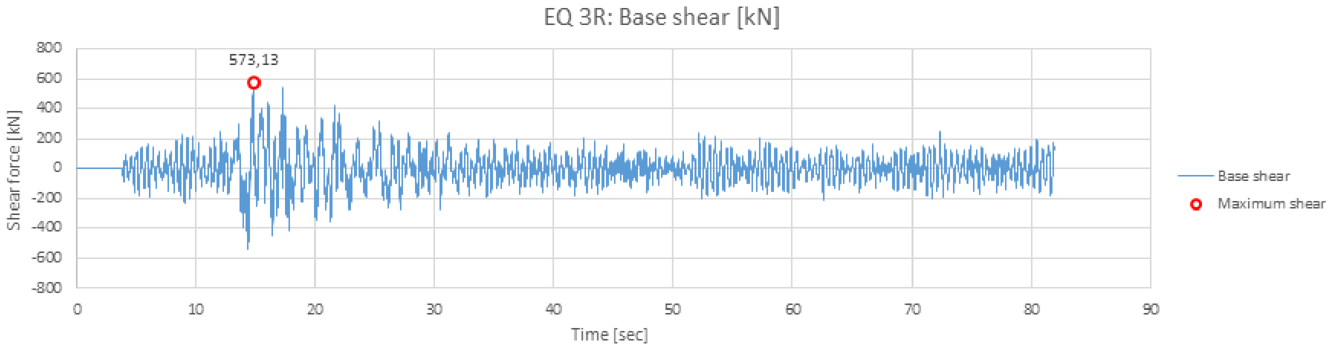

Figure D.30: Shear force at seabed level versus time for EQ 3R.

D.1.7 EQ 5A

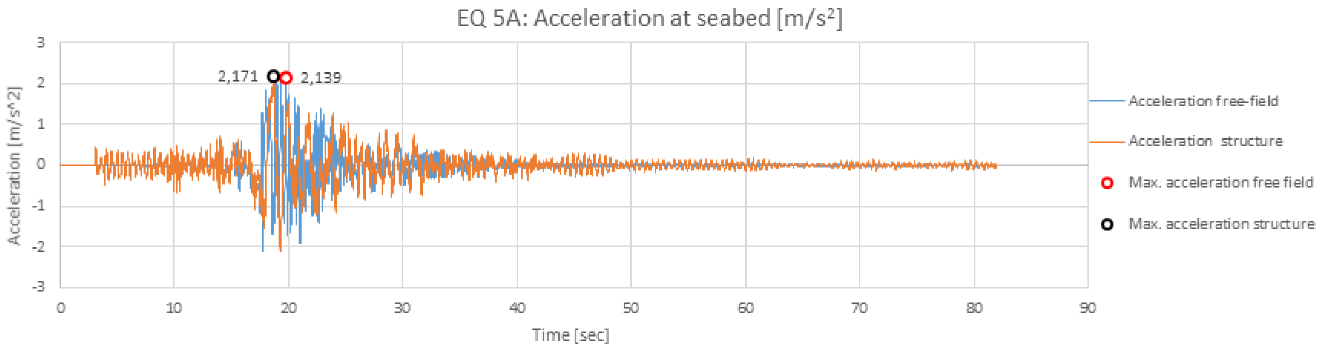

Figure D.31: Acceleration at seabed level versus time for EQ 5A.

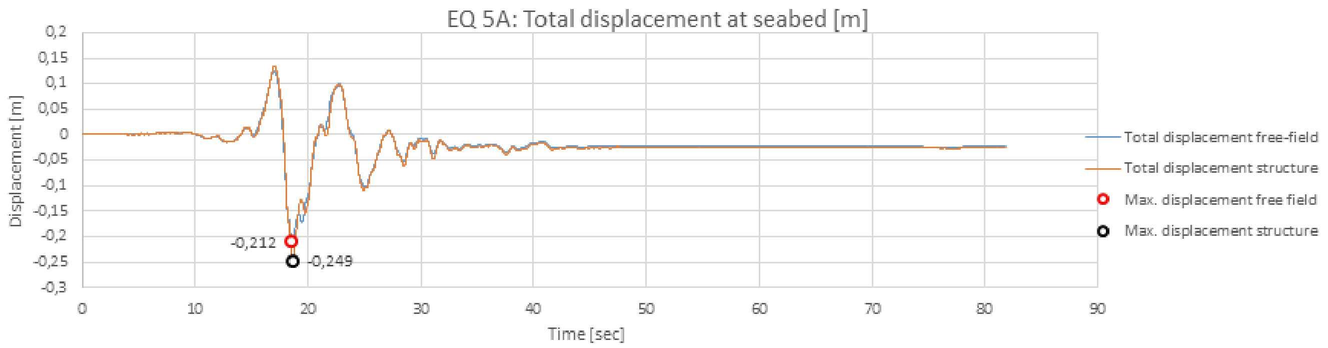

Figure D.32: Displacement at seabed level versus time for EQ 5A.

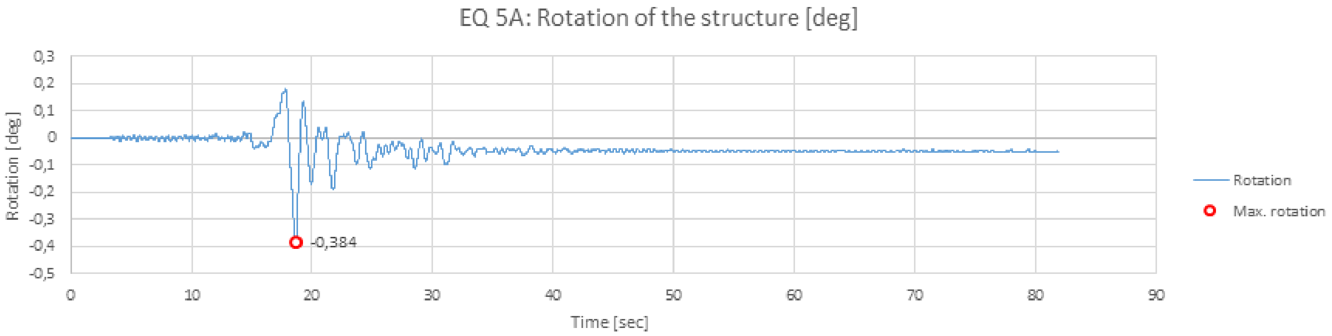

Figure D.33: Rotation at seabed level versus time for EQ 5A.

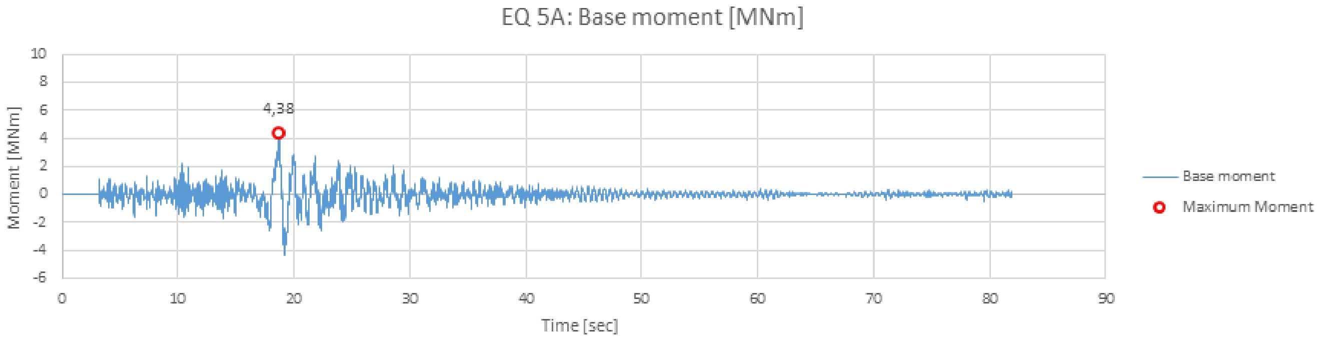

Figure D.34: Moment at seabed level versus time for EQ 5A.

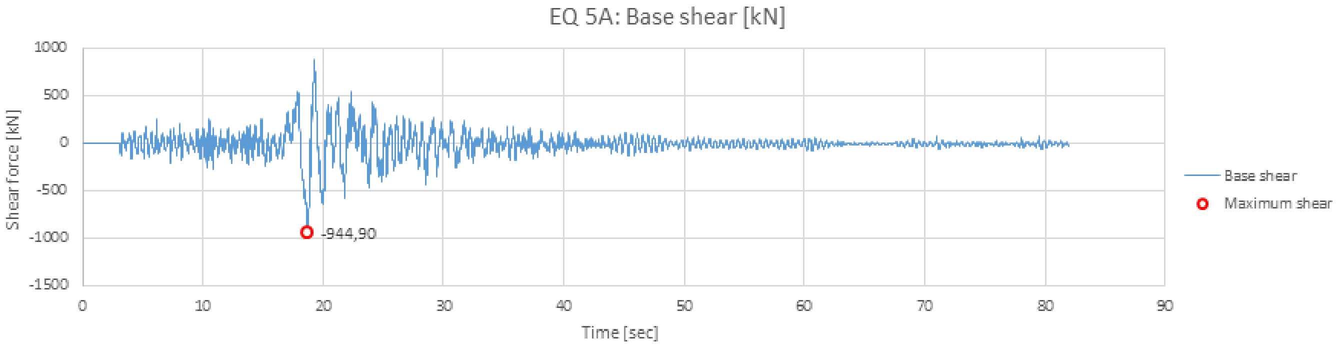

Figure D.35: Shear force at seabed level versus time for EQ 5A.

D.1.8 EQ 5S

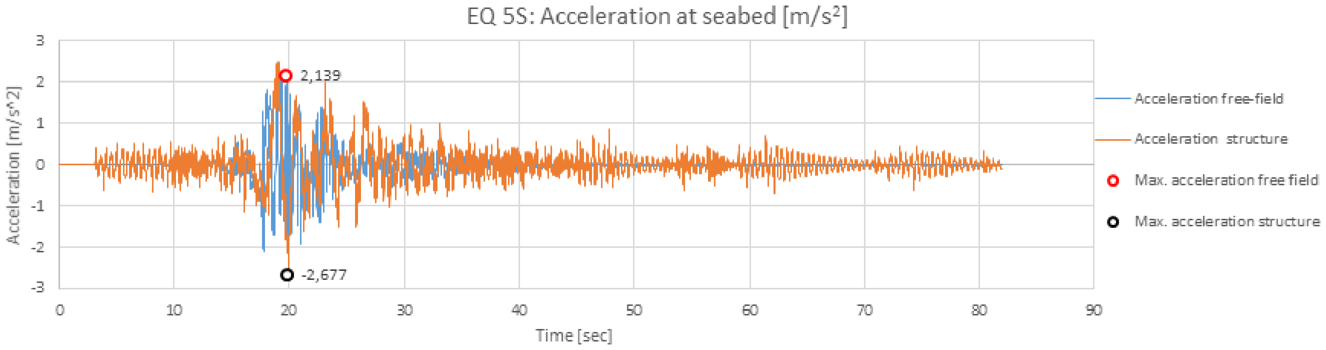

Figure D.36: Acceleration at seabed level versus time for EQ 5S.

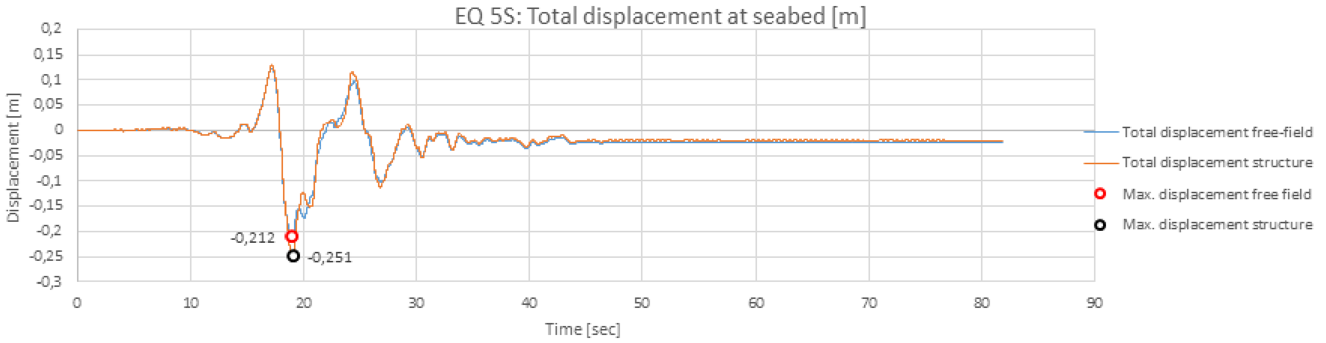

Figure D.37: Displacement at seabed level versus time for EQ 5S.

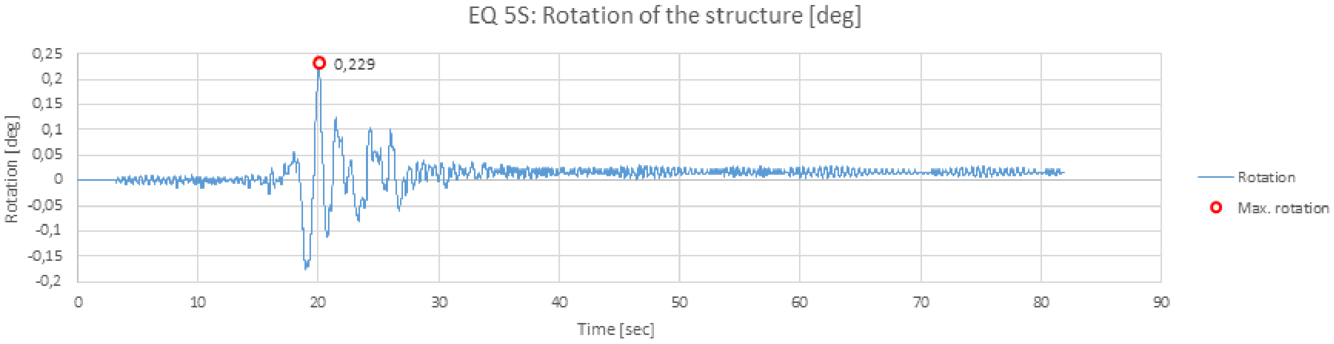

Figure D.38: Rotation at seabed level versus time for EQ 5S.

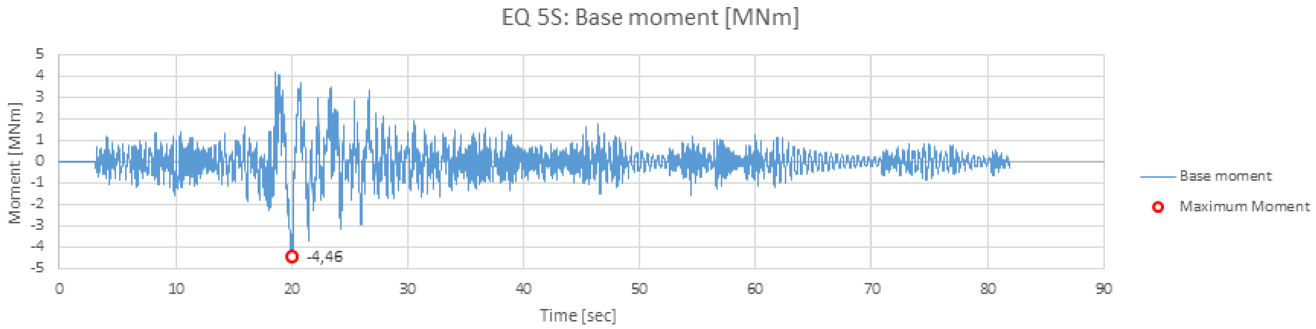

Figure D.39: Moment at seabed level versus time for EQ 5S.

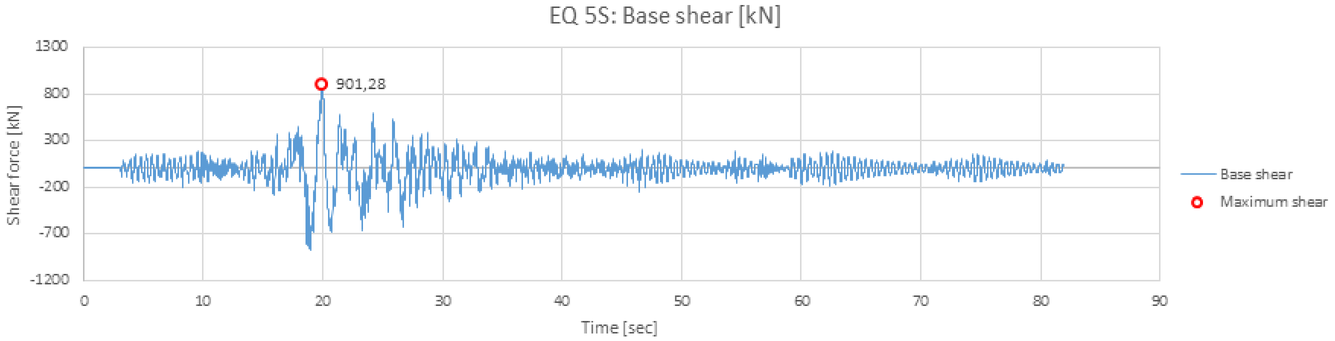

Figure D.40: Shear force at seabed level versus time for EQ 5S.

D.1.9 EQ 5R

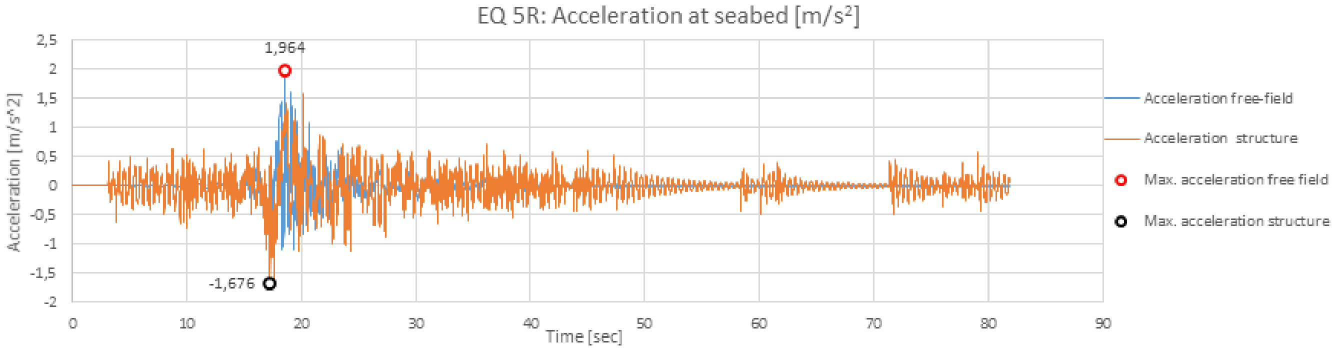

Figure D.41: Acceleration at seabed level versus time for EQ 5R.

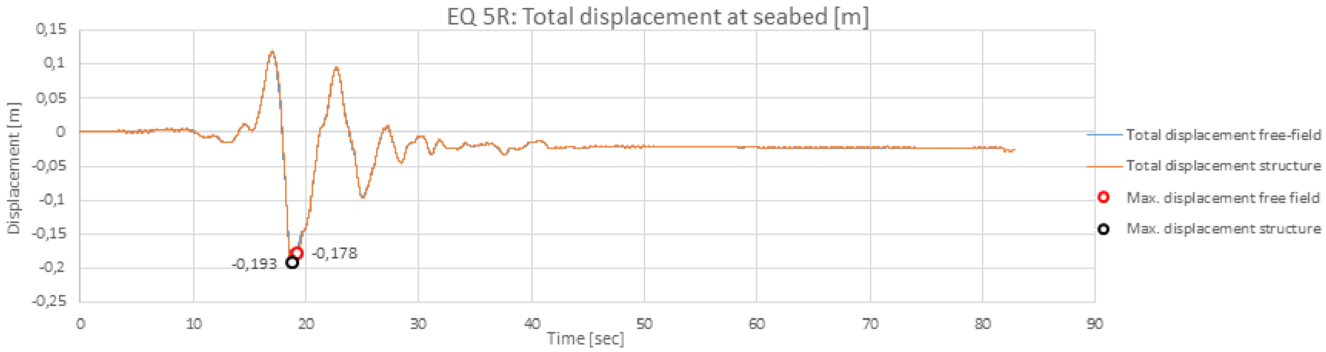

Figure D.42: Displacement at seabed level versus time for EQ 5R.

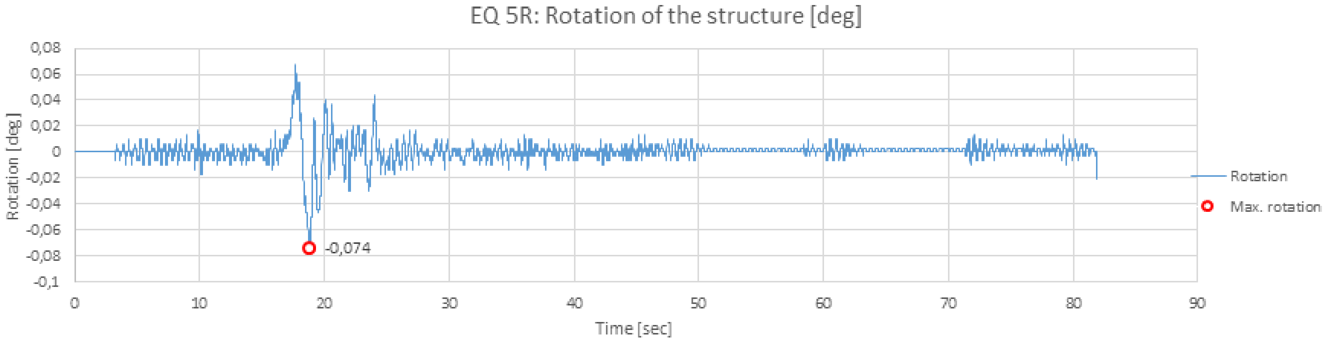

Figure D.43: Rotation at seabed level versus time for EQ 5R.

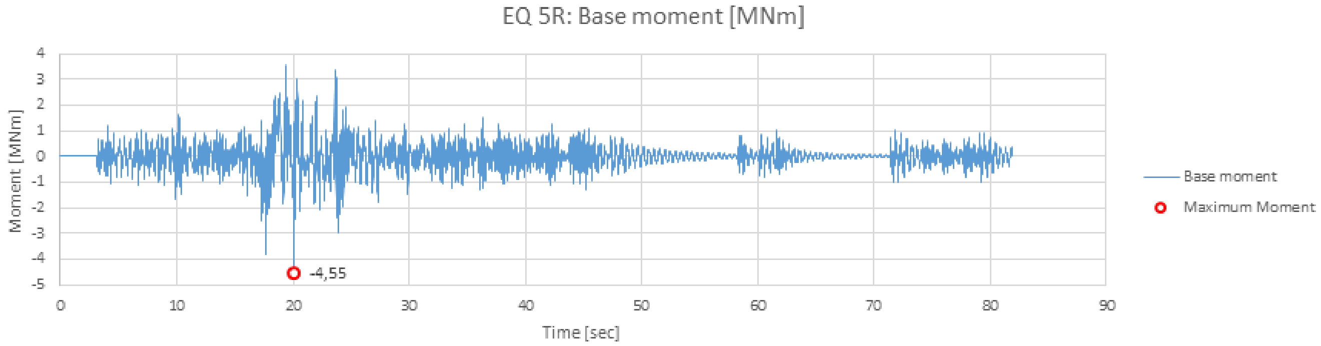

Figure D.44: Moment at seabed level versus time for EQ 5R.

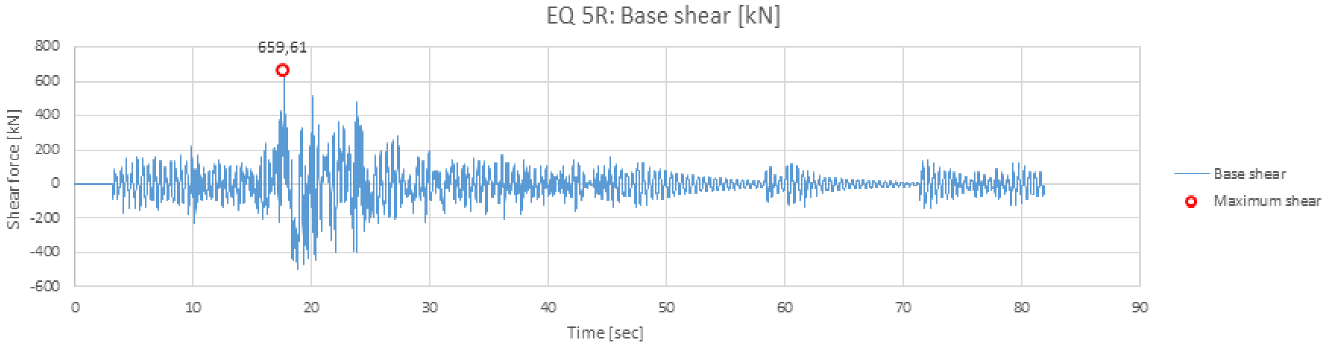

Figure D.45: Shear force at seabed level versus time for EQ 5R.

D.1.10 EQ 6A

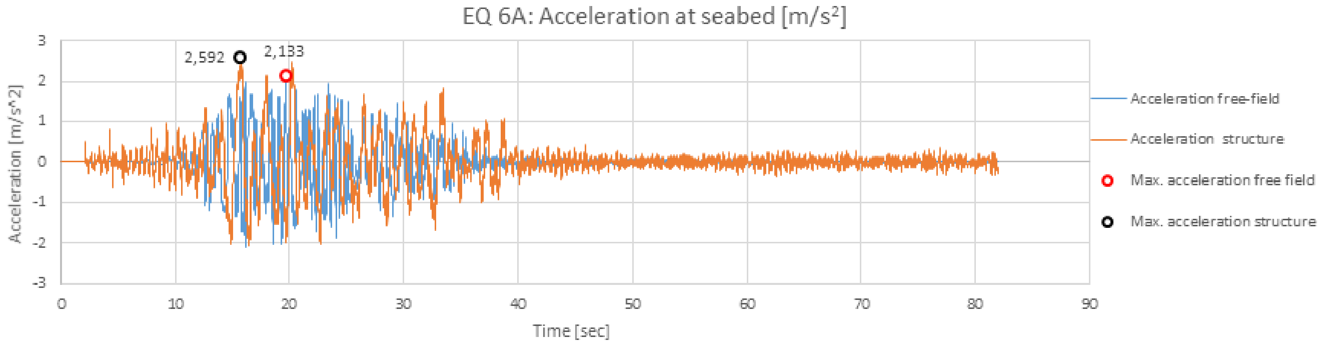

Figure D.46: Acceleration at seabed level versus time for EQ 6A.

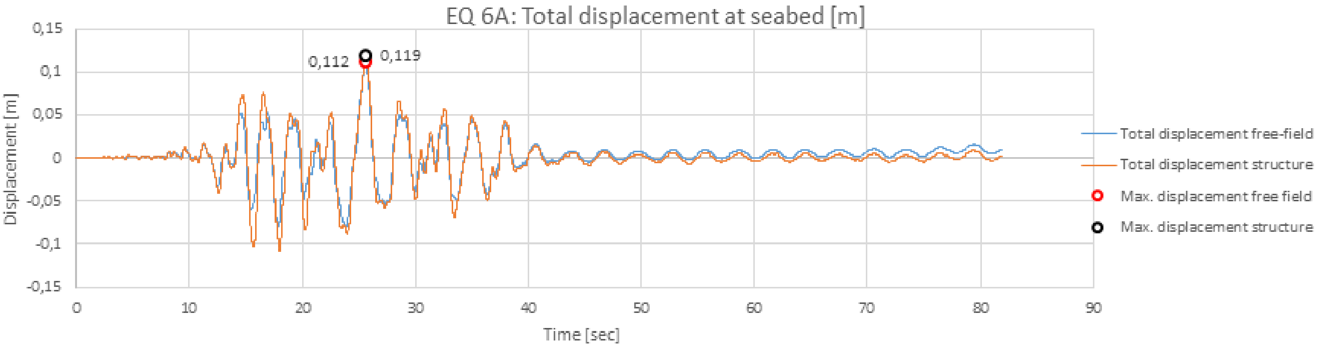

Figure D.47: Displacement at seabed level versus time for EQ 6A.

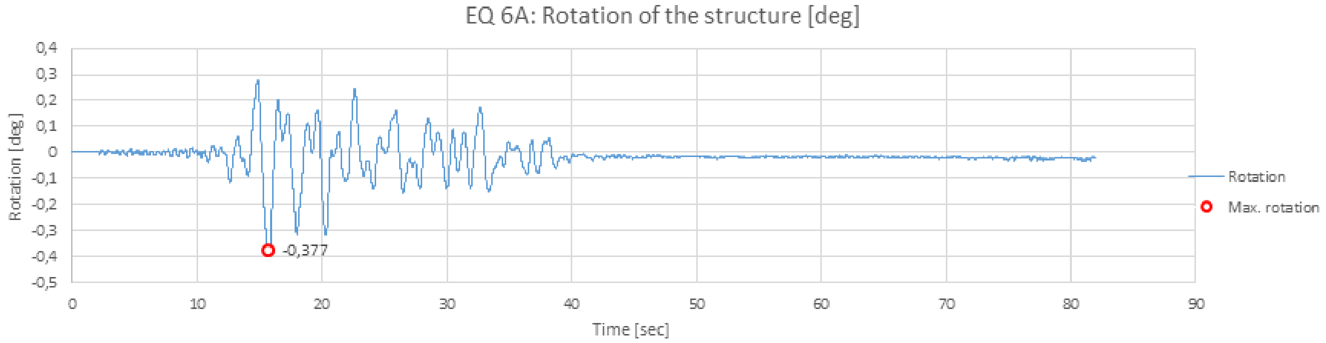

Figure D.48: Rotation at seabed level versus time for EQ 6A.

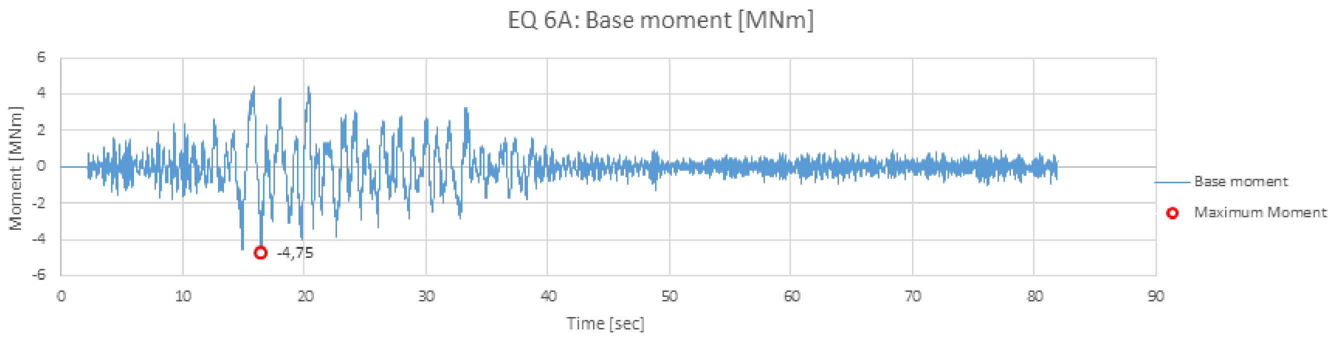

Figure D.49: Moment at seabed level versus time for EQ 6A.

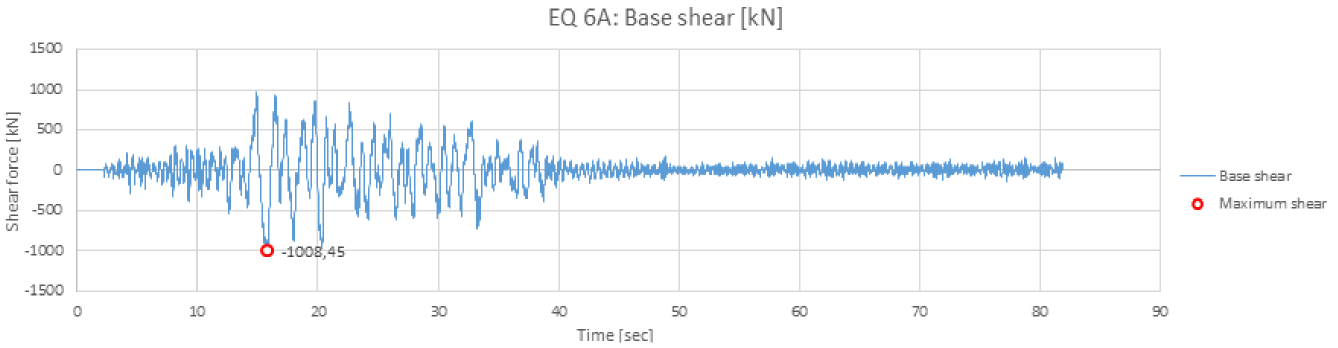

Figure D.50: Shear force at seabed level versus time for EQ 6A.

D.1.11 EQ 6S

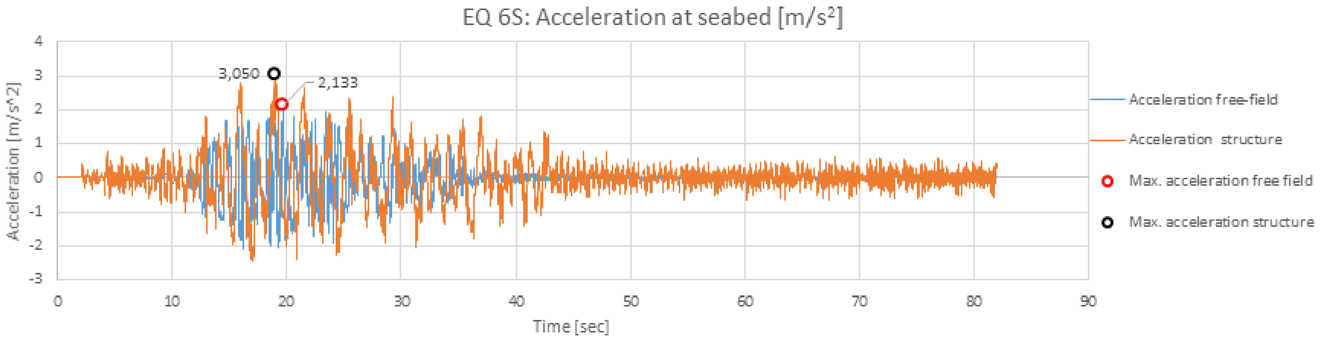

Figure D.51: Acceleration at seabed level versus time for EQ 6S.

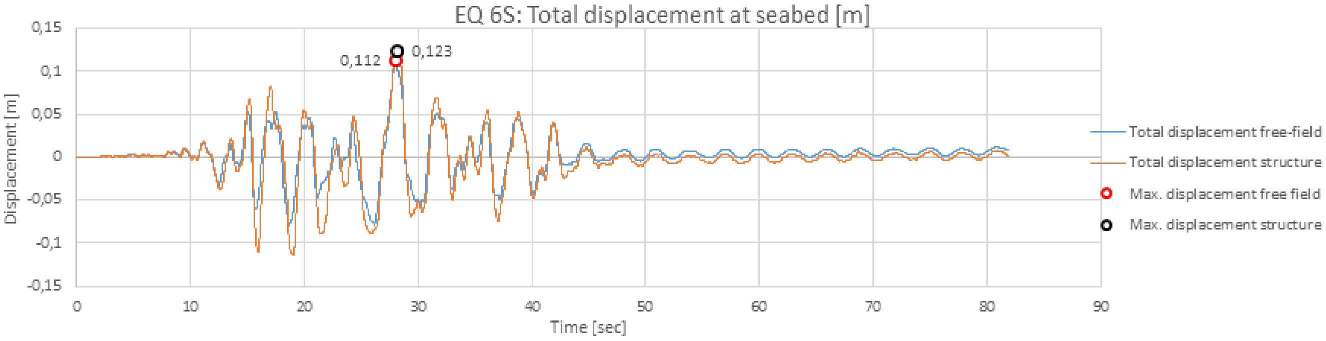

Figure D.52: Displacement at seabed level versus time for EQ 6S.

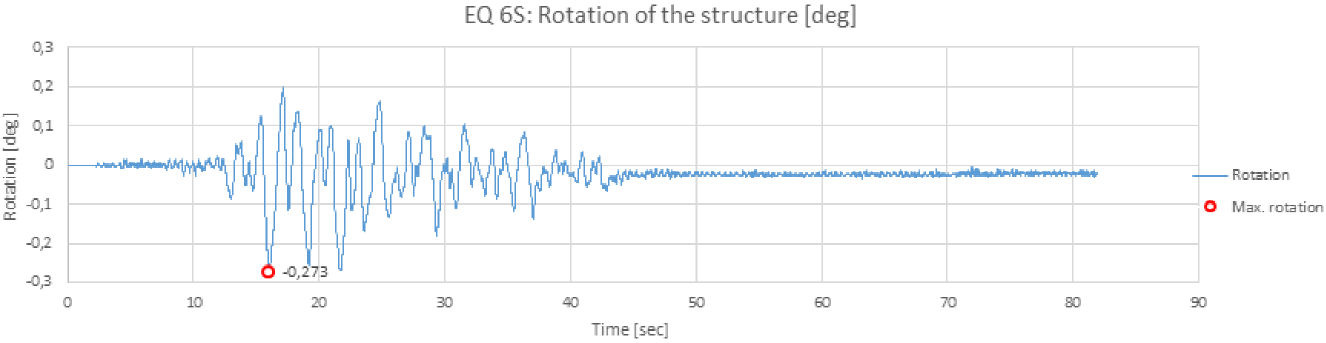

Figure D.53: Rotation at seabed level versus time for EQ 6S.

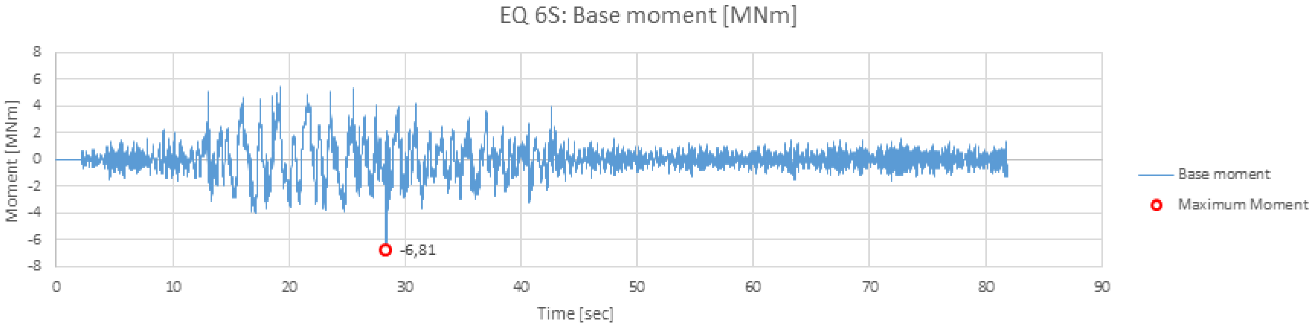

Figure D.54: Moment at seabed level versus time for EQ 6S.

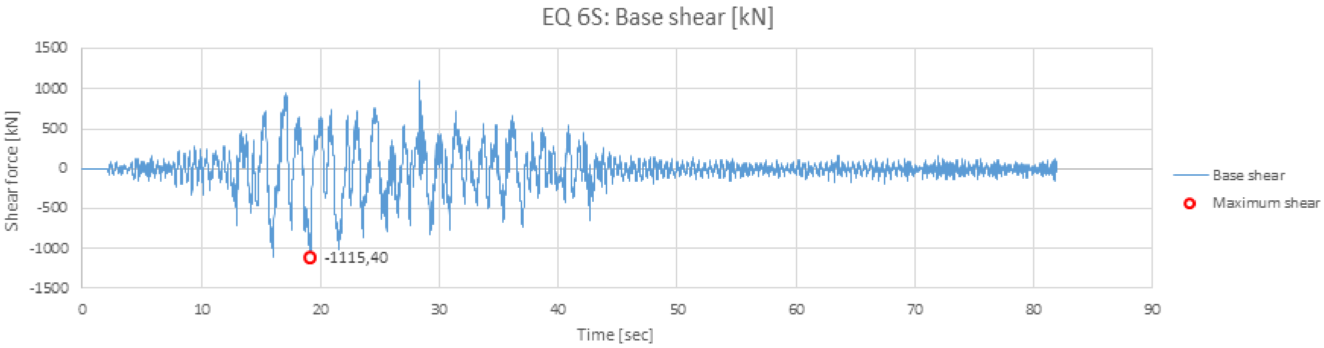

Figure D.55: Shear force at seabed level versus time for EQ 6S.

D.1.12 EQ 6R

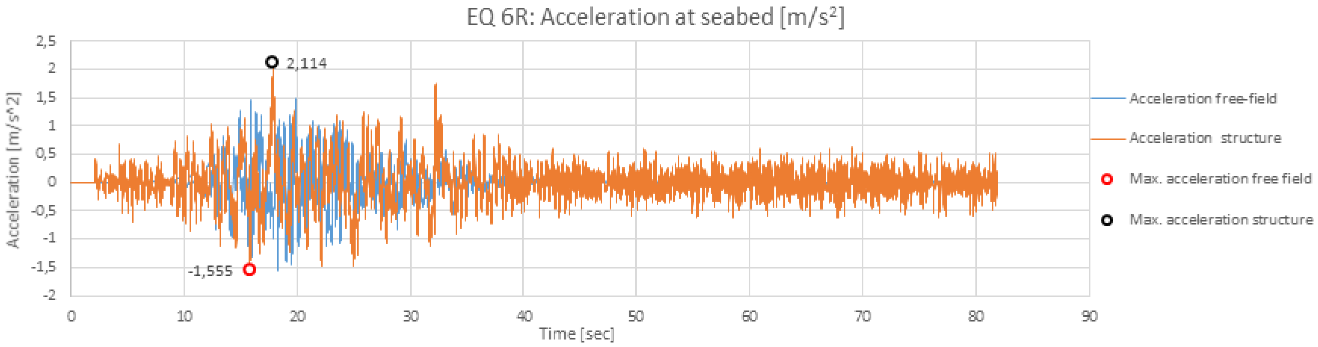

Figure D.56: Acceleration at seabed level versus time for EQ 6R.

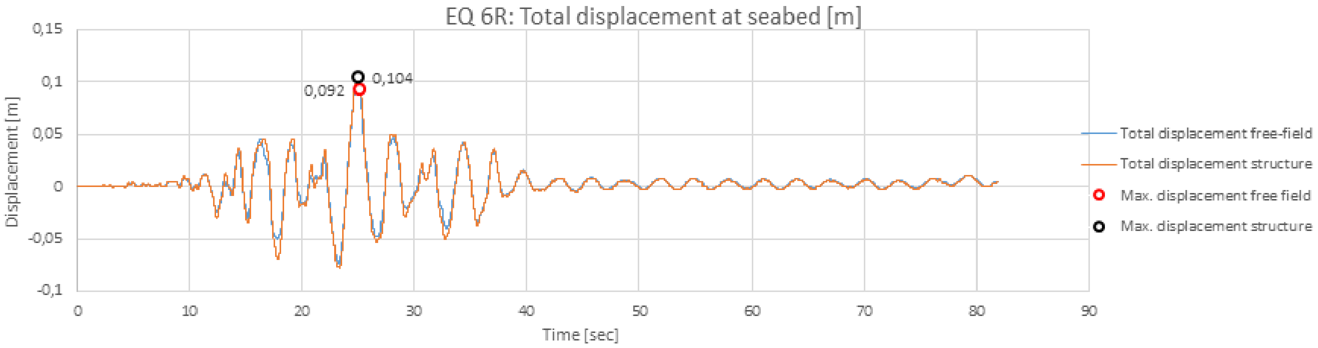

Figure D.57: Displacement at seabed level versus time for EQ 6R.

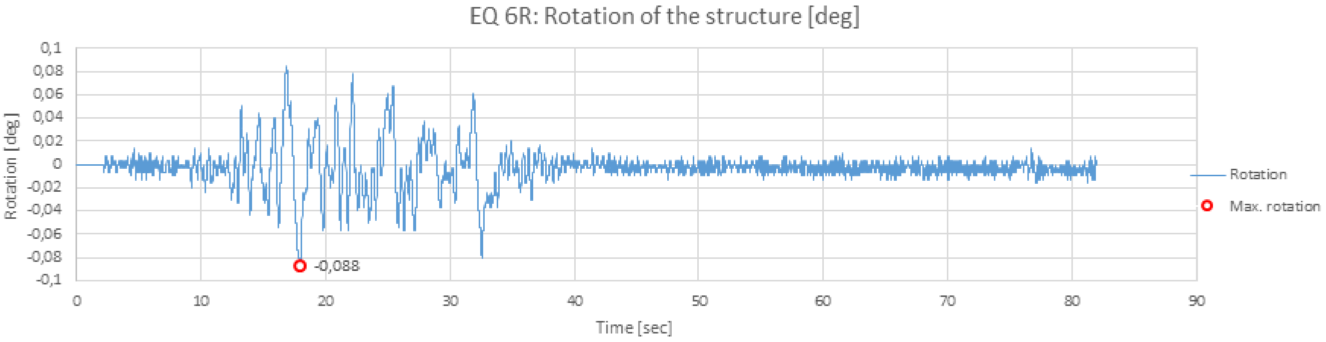

Figure D.58: Rotation at seabed level versus time for EQ 6R.

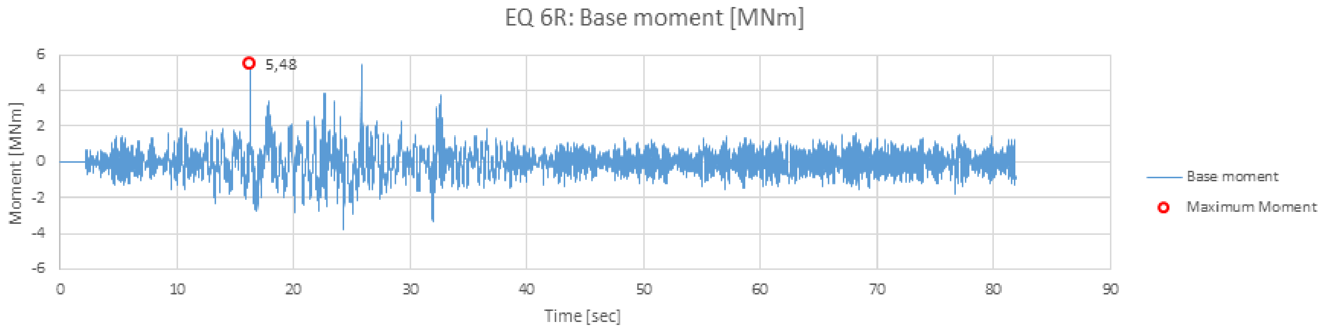

Figure D.59: Moment at seabed level versus time for EQ 6R.

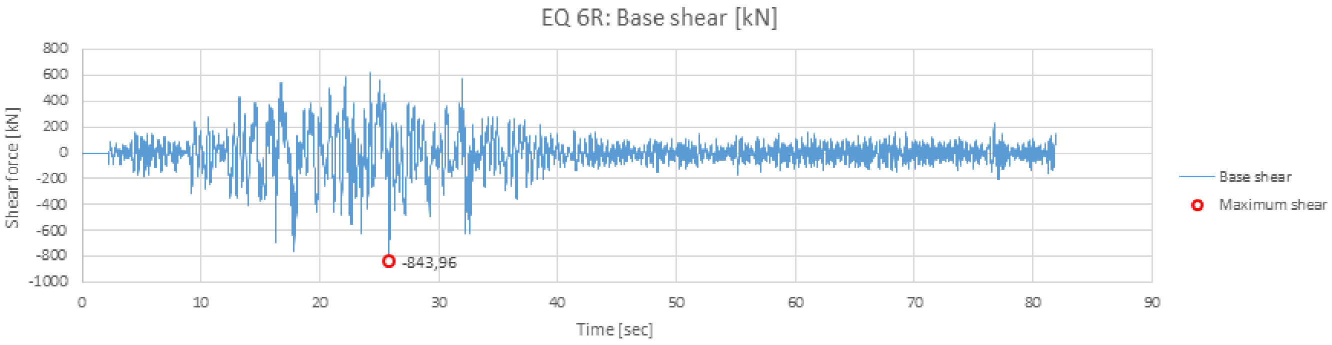

Figure D.60: Shear force at seabed level versus time for EQ 6R.

D.2 Comparison Plots

Acceleration

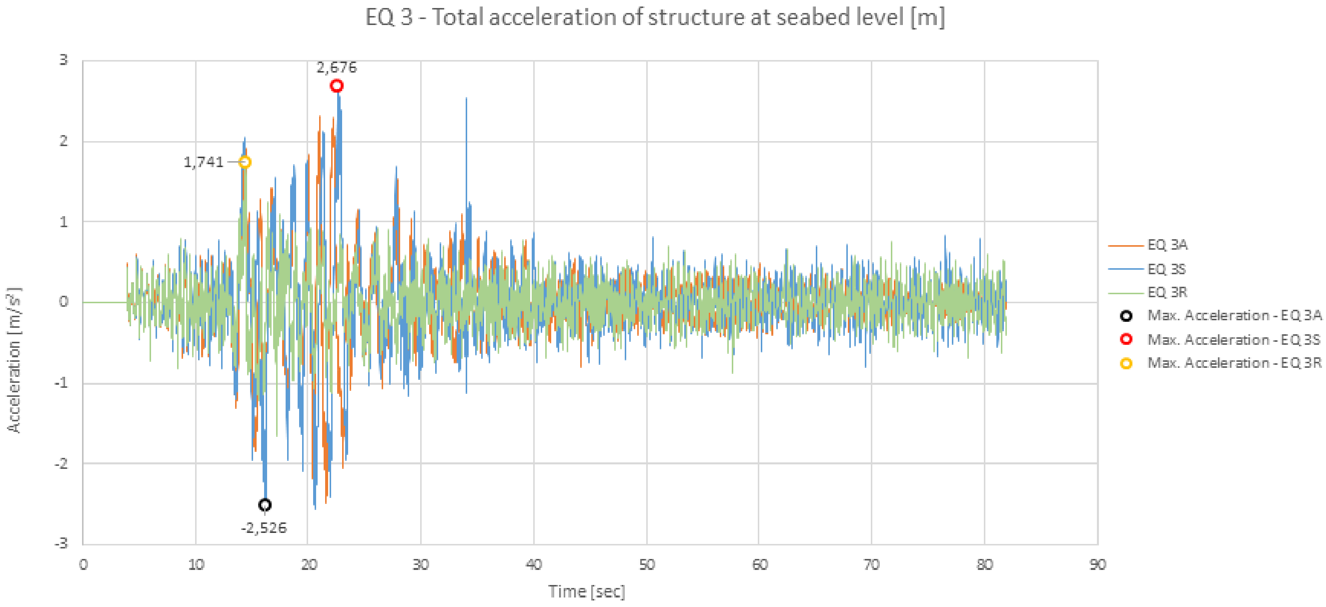

Figure D.61: EQ 3: Total acceleration of structure at seabed level for time series analyses using depth variable time series (A), seabed time series (S) and reference depth time series (R).

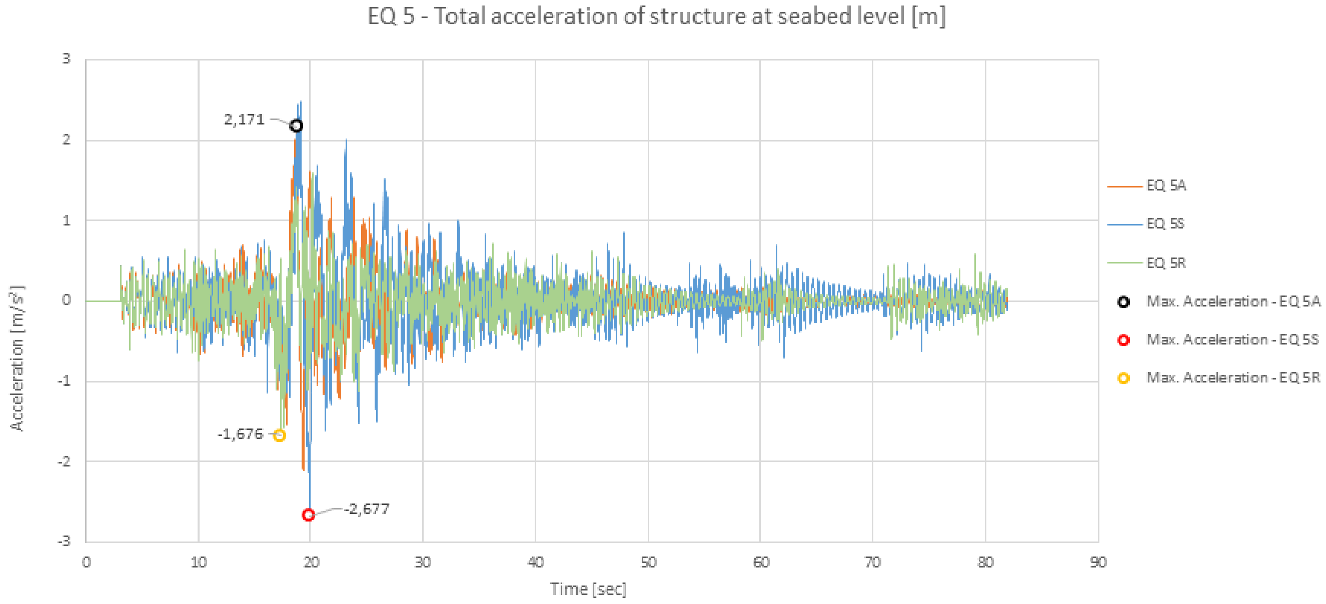

Figure D.62: EQ 5: Total acceleration of structure at seabed level for time series analyses using depth variable time series (A), seabed time series (S) and reference depth time series (R).

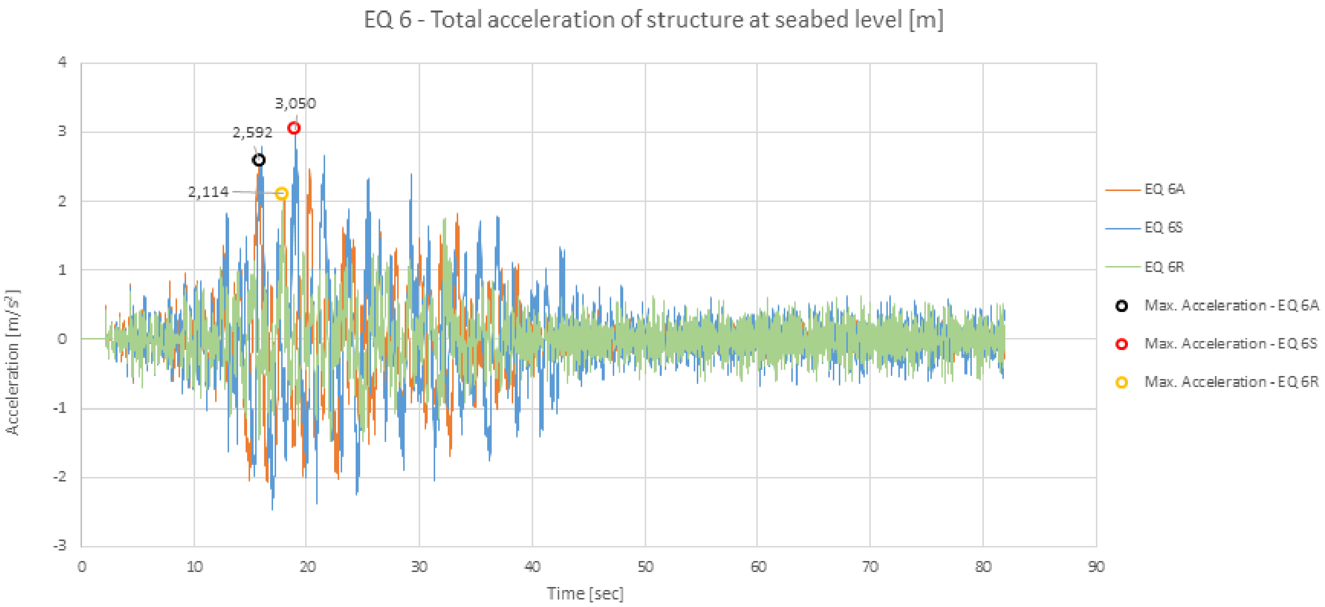

Figure D.63: EQ 6: Total acceleration of structure at seabed level for time series analyses using depth variable time series (A), seabed time series (S) and reference depth time series (R).

Displacement

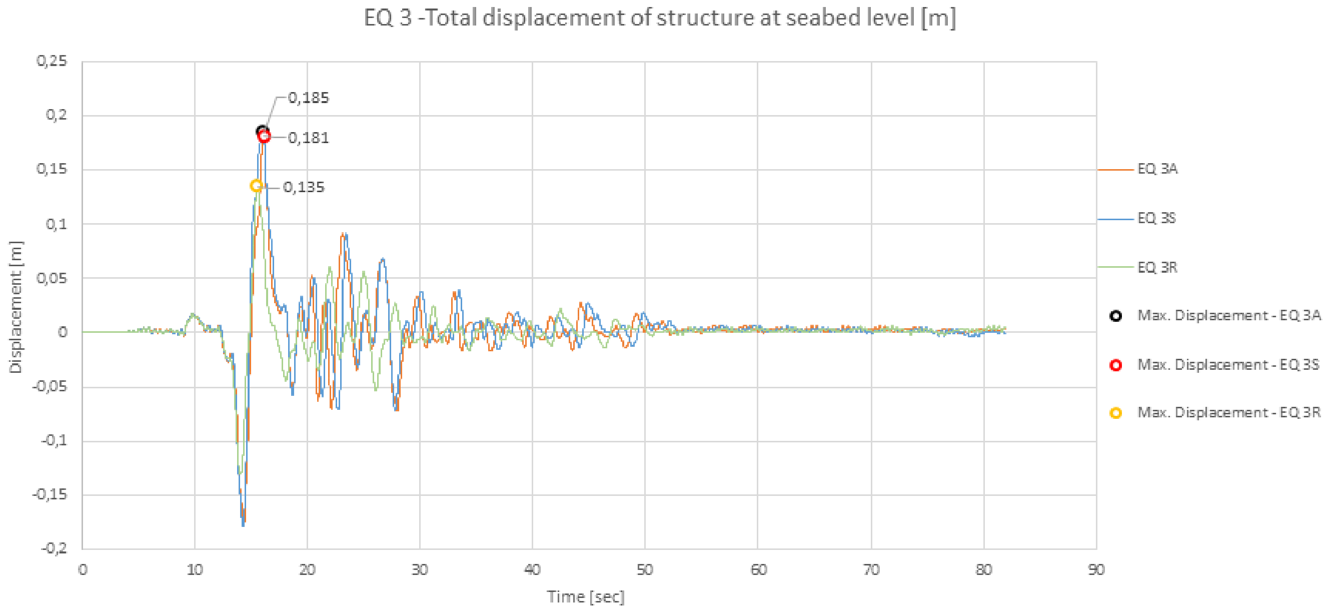

Figure D.64: EQ 3: Total displacement of structure at seabed level for time series analyses using depth variable time series (A), seabed time series (S) and reference depth time series (R).

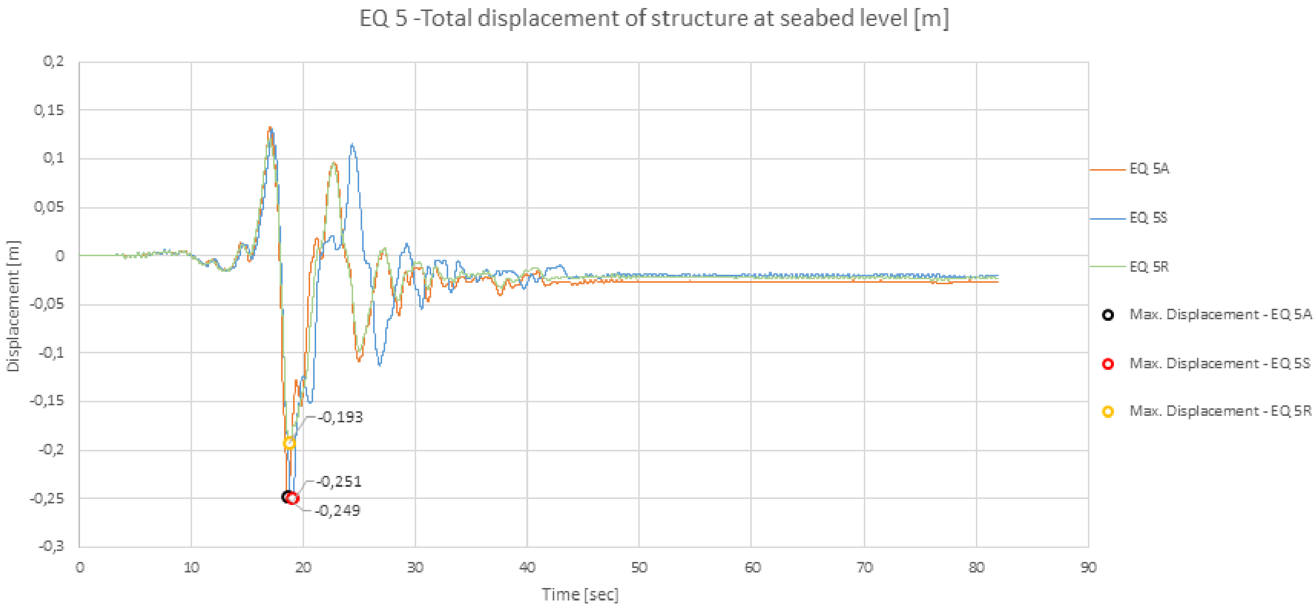

Figure D.65: EQ 5: Total displacement of structure at seabed level for time series analyses using depth variable time series (A), seabed time series (S) and reference depth time series (R).

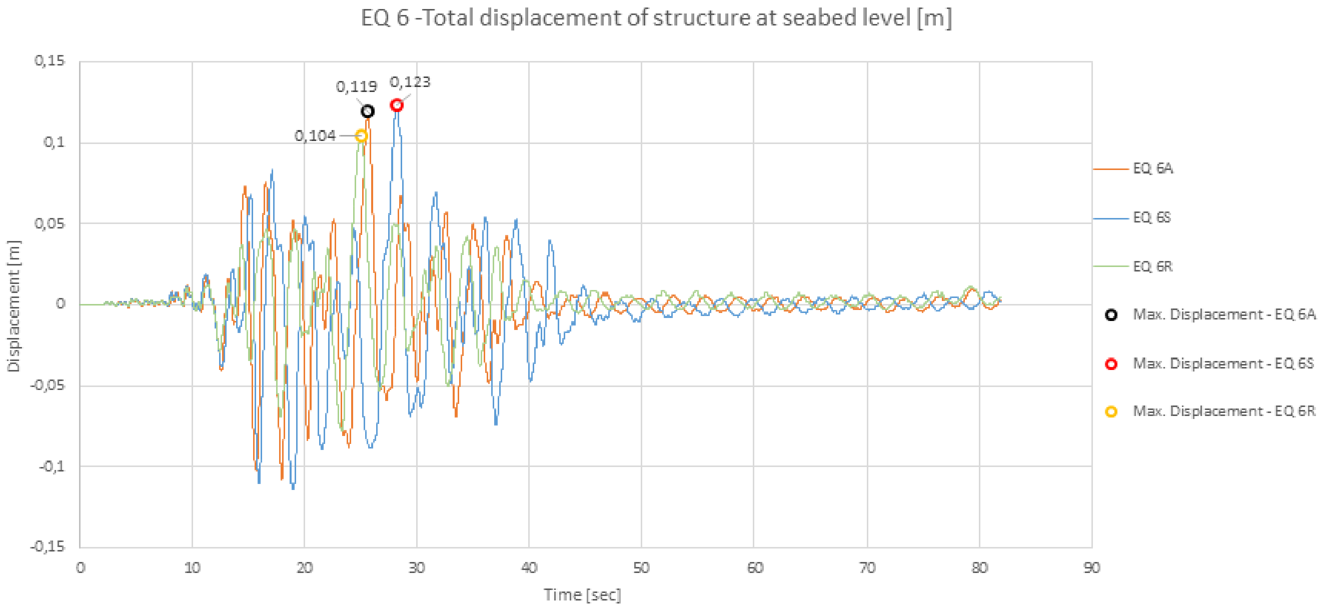

Figure D.66: EQ 6: Total displacement of structure at seabed level for time series analyses using depth variable time series (A), seabed time series (S) and reference depth time series (R).

Rotation

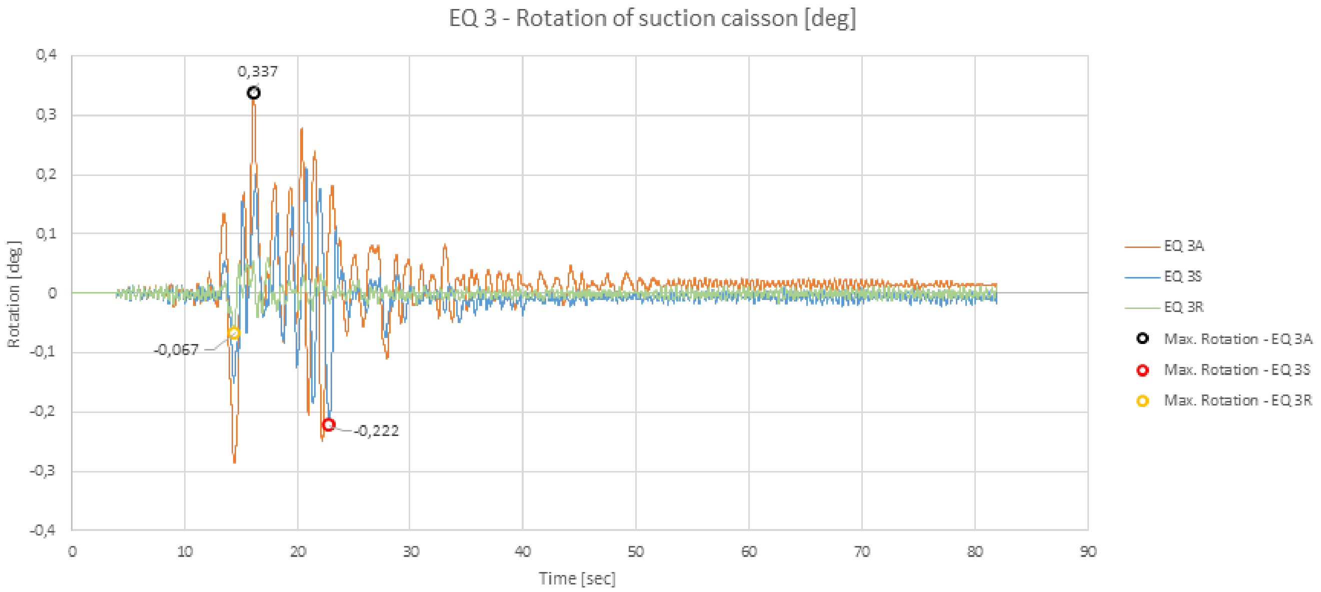

Figure D.67: EQ 3: Rotation of structure at seabed level for time series analyses using depth variable time series (A), seabed time series (S) and reference depth time series (R).

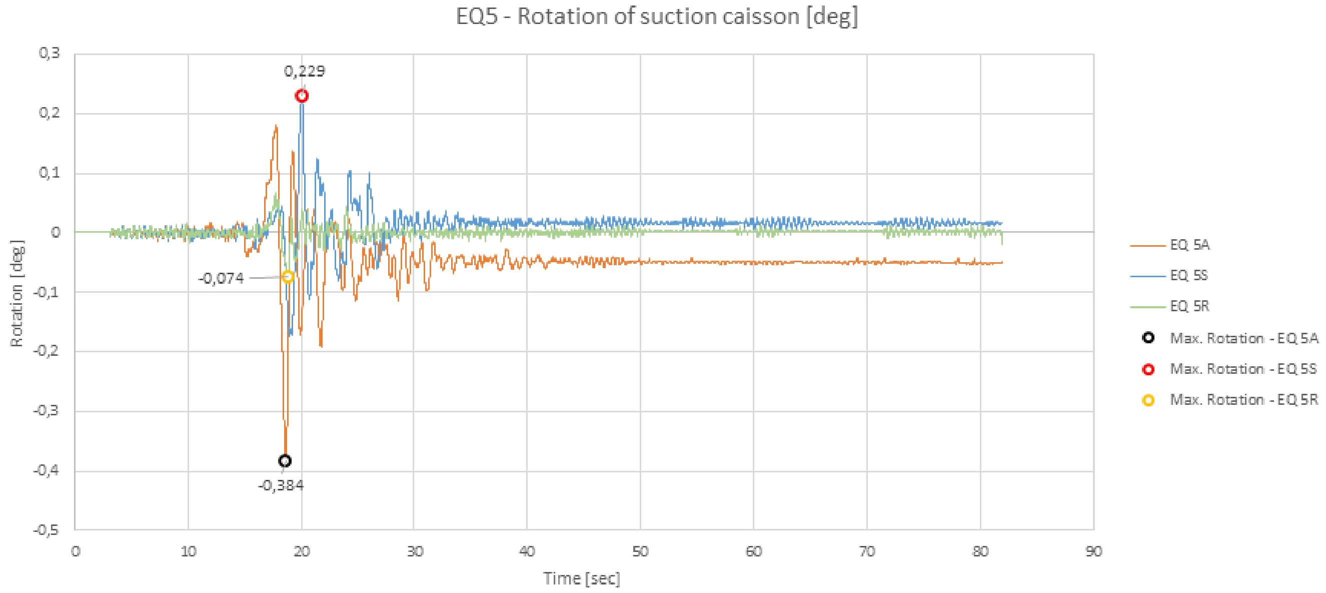

Figure D.68: EQ 5: Rotation of structure at seabed level for time series analyses using depth variable time series (A), seabed time series (S) and reference depth time series (R).

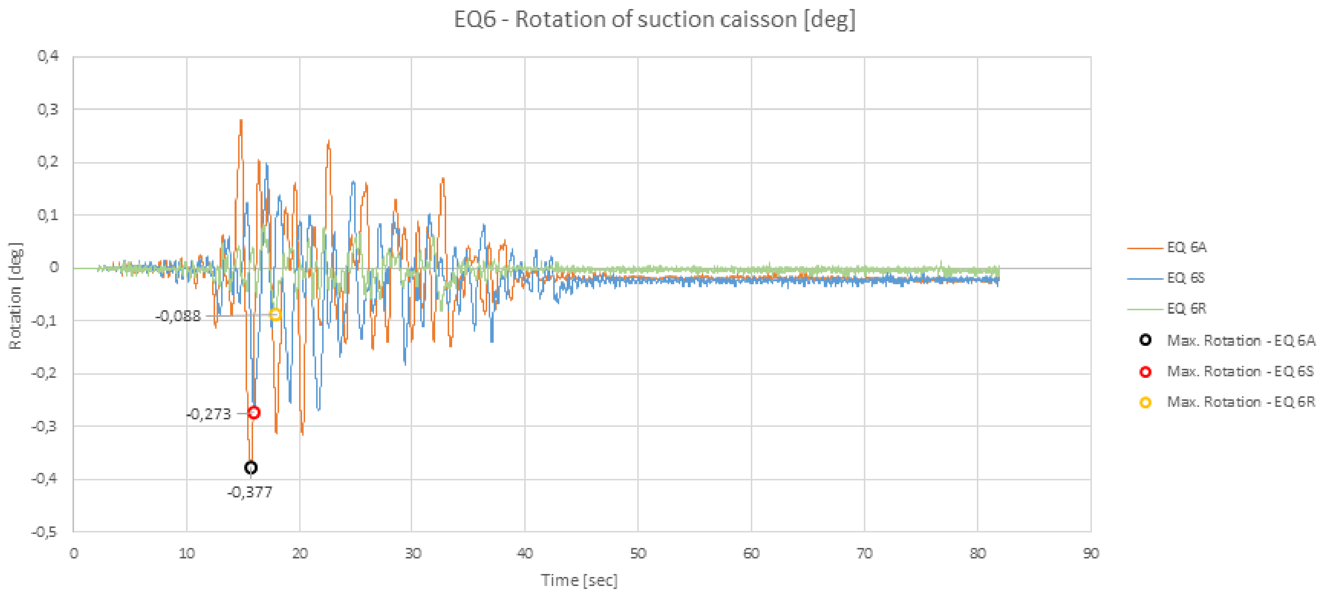

Figure D.69: EQ 6: Rotation of structure at seabed level for time series analyses using depth variable time series (A), seabed time series (S) and reference depth time series (R).

Base Moment

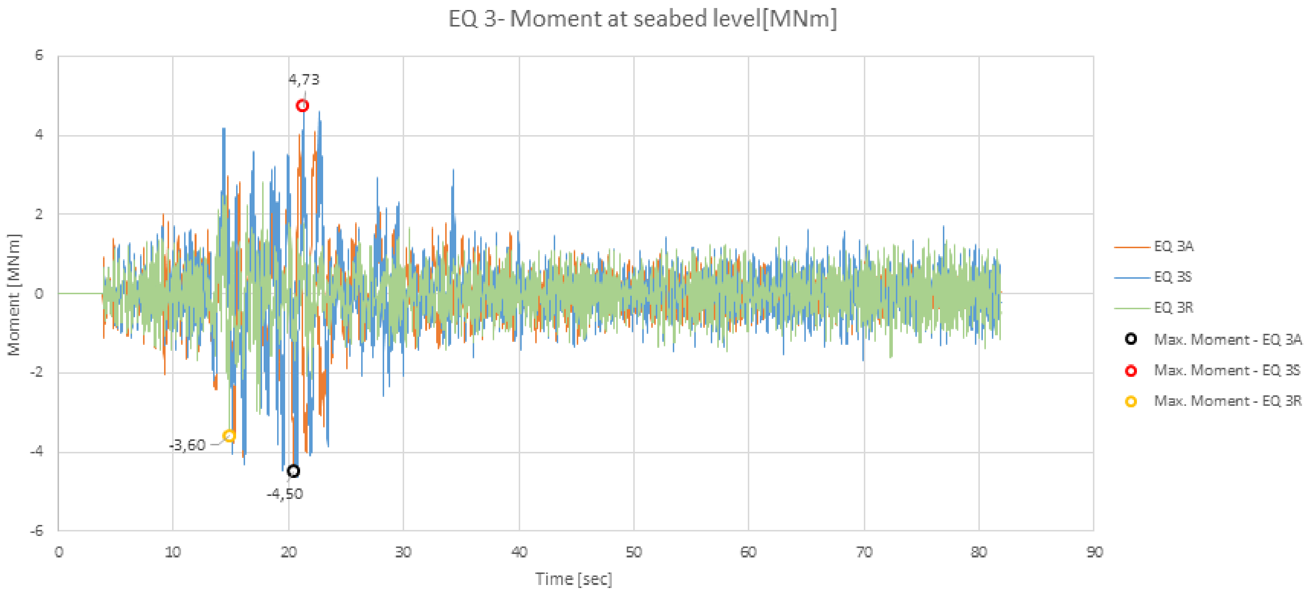

Figure D.70: EQ 3: Moment at seabed level for time series analyses using depth variable time series (A), seabed time series (S) and reference depth time series (R).

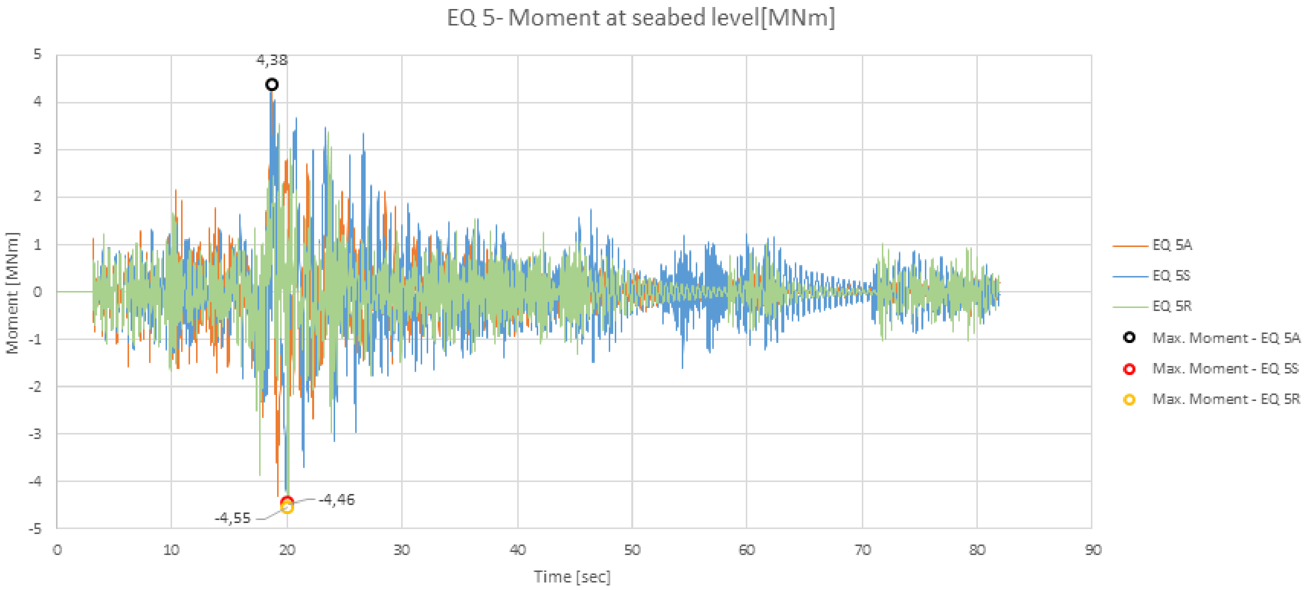

Figure D.71: EQ 5: Moment at seabed level for time series analyses using depth variable time series (A), seabed time series (S) and reference depth time series (R).

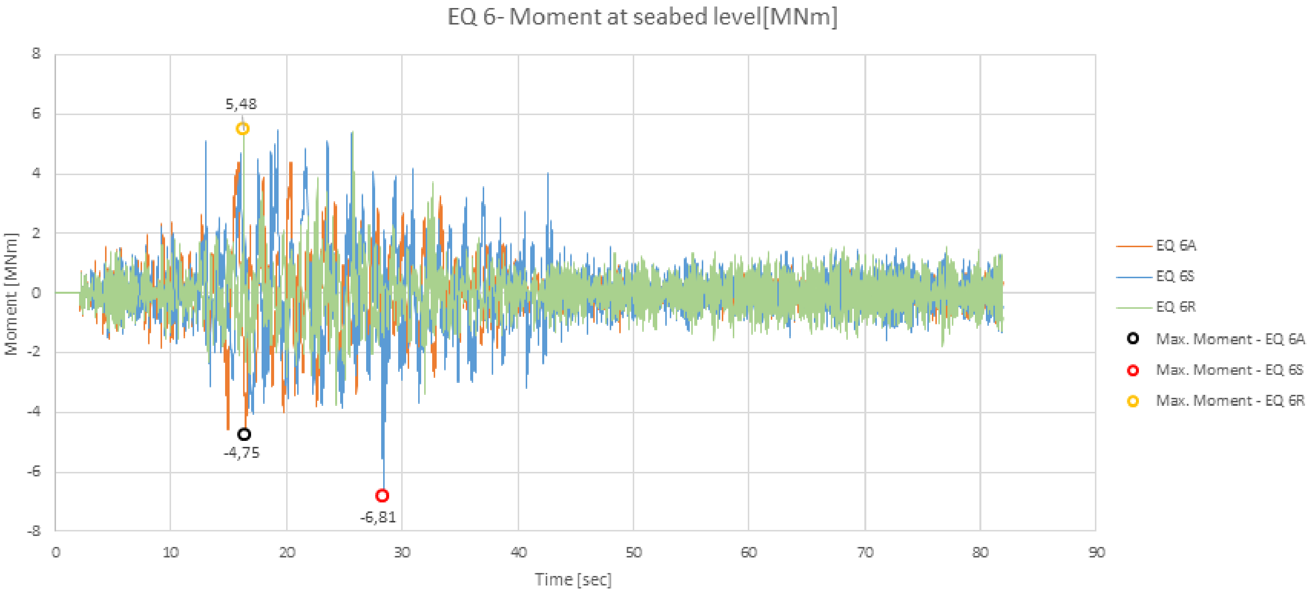

Figure D.72: EQ 6: Moment at seabed level for time series analyses using depth variable time series (A), seabed time series (S) and reference depth time series (R).

Base Shear Force

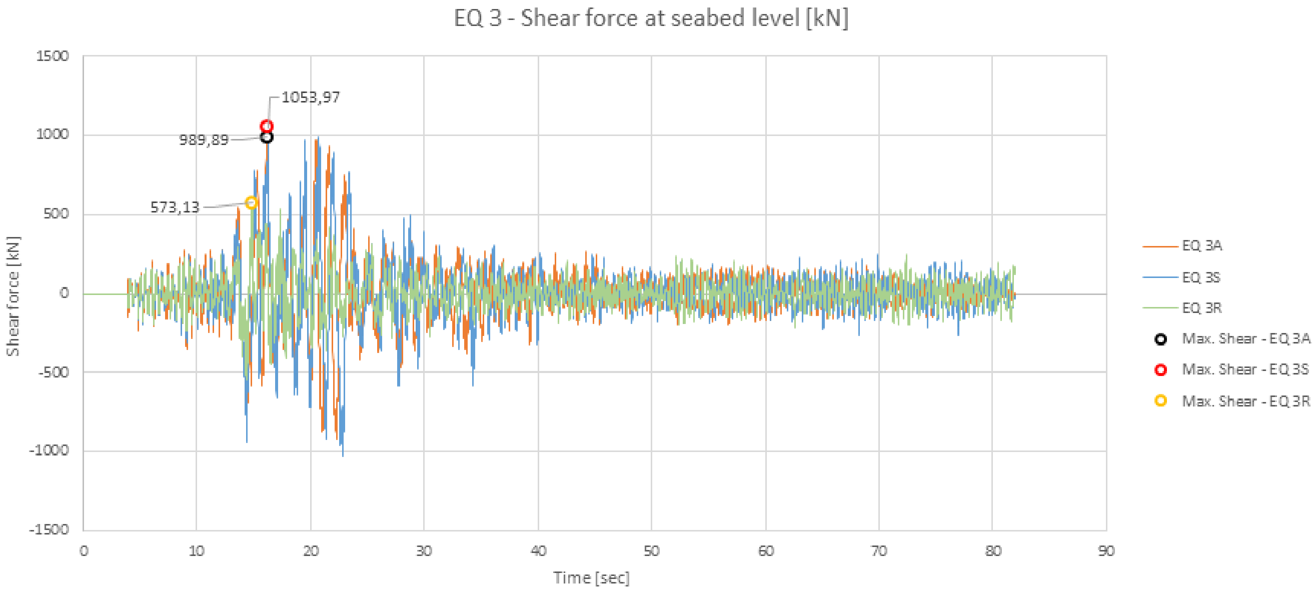

Figure D.73: EQ 3: Shear force at seabed level for time series analyses using depth variable time series (A), seabed time series (S) and reference depth time series (R).

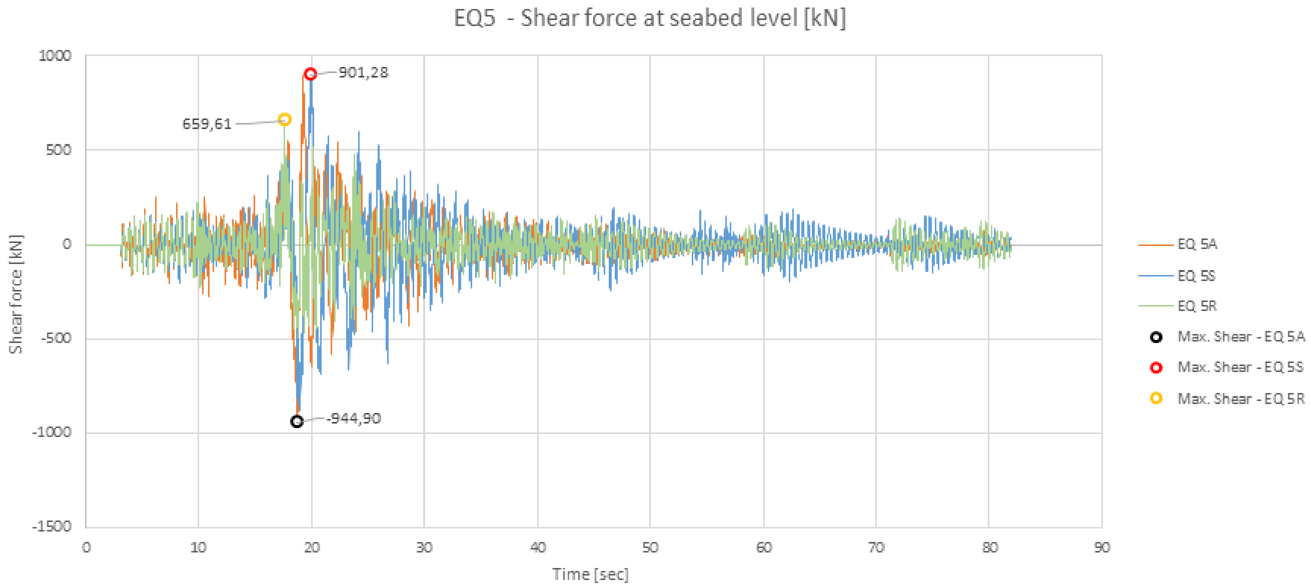

Figure D.74: EQ 5: Shear force at seabed level for time series analyses using depth variable time series (A), seabed time series (S) and reference depth time series (R).

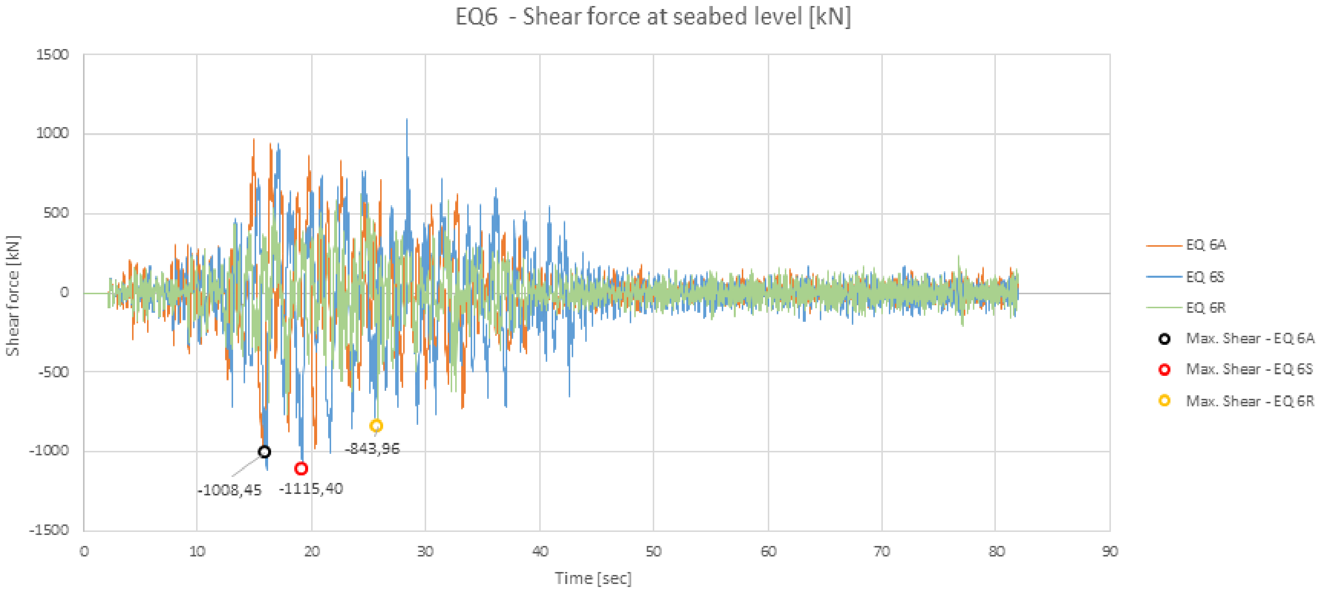

Figure D.75: EQ 6: Shear force at seabed level for time series analyses using depth variable time series (A), seabed time series (S) and reference depth time series (R).

D.3 Peak value comparisons

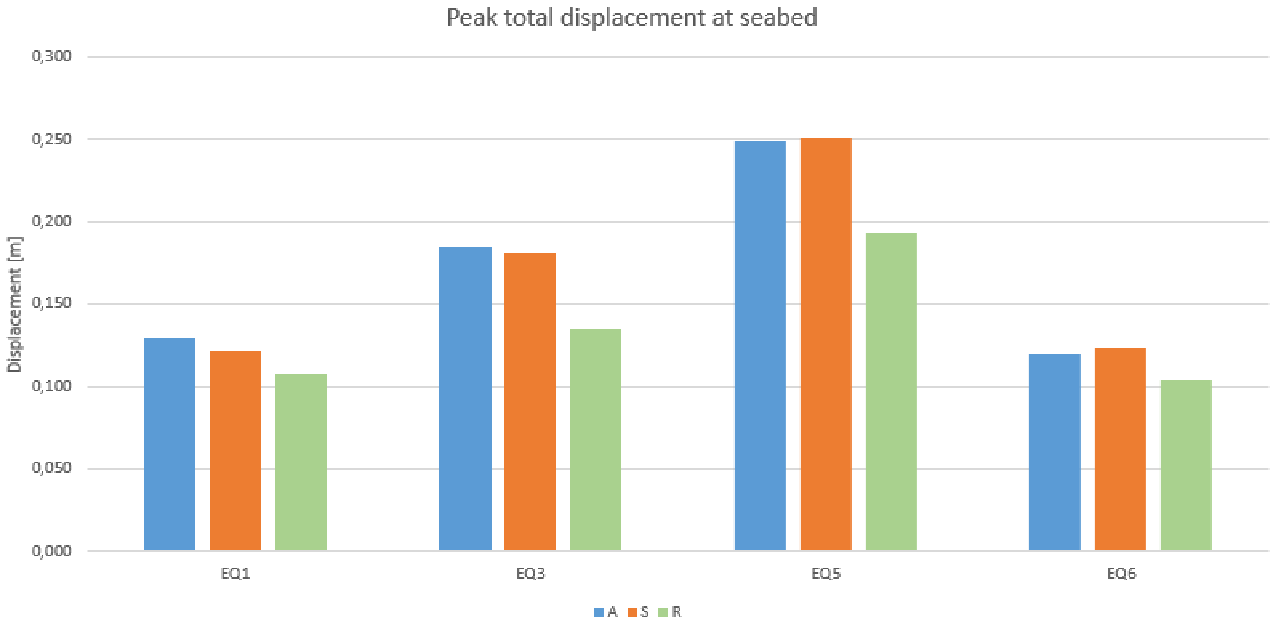

Figure D.76: Comparison of peak total displacement at seabed for the various time series analyses.

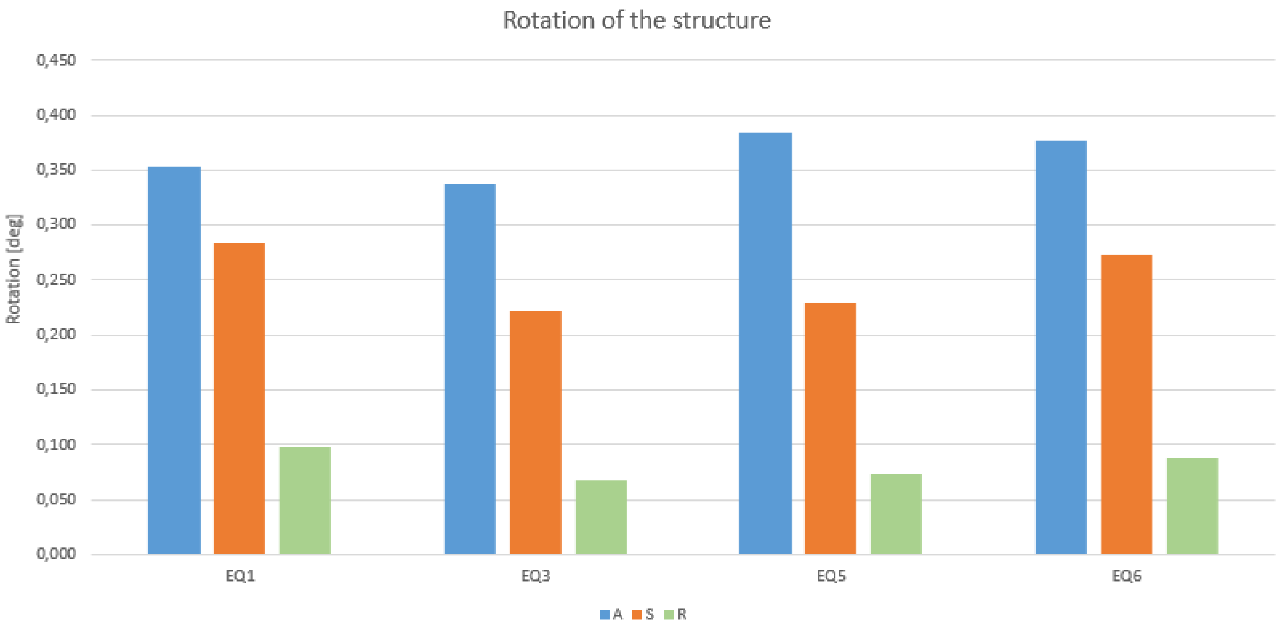

Figure D.77: Comparison of peak rotation of the structure for the various time series analyses.

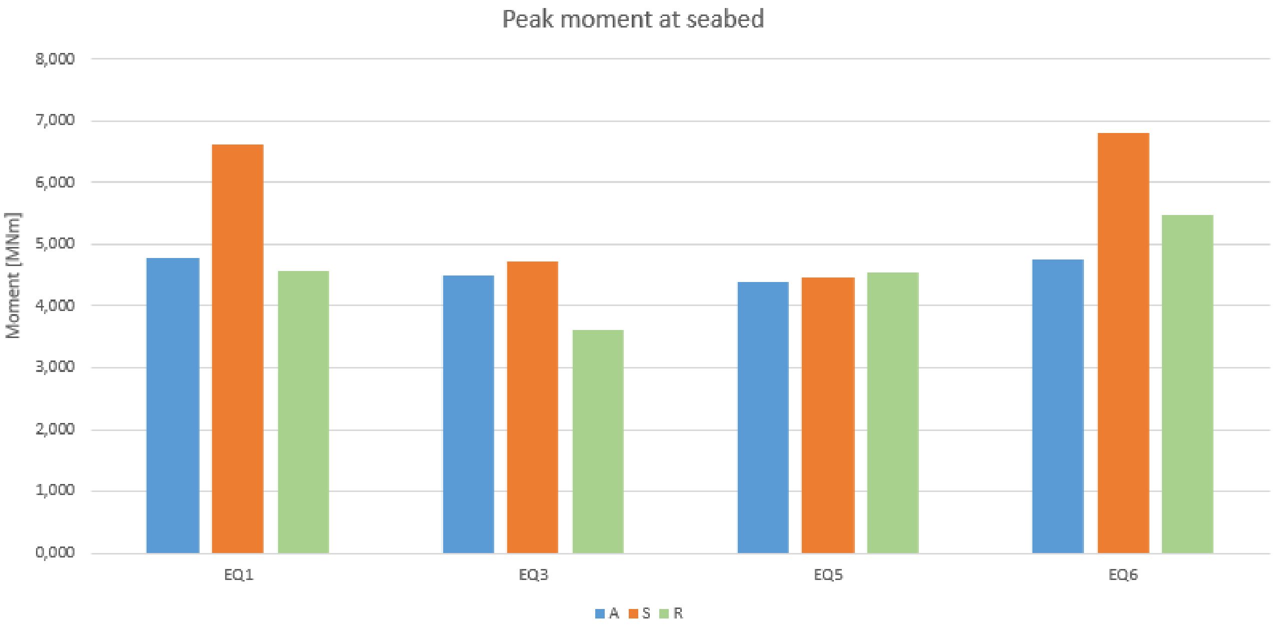

Figure D.78: Comparison of peak moment at seabed for the various time series analyses.

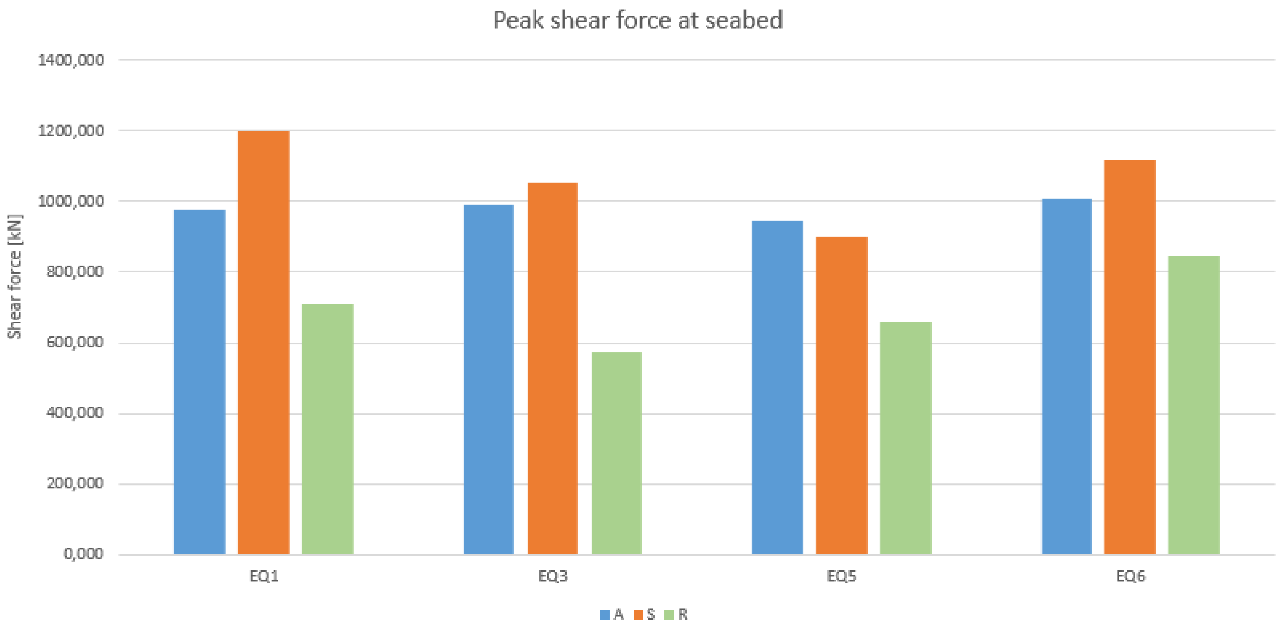

Figure D.79: Comparison of peak shear force at seabed for the various time series analyses.

D.4 Deformed Caisson & Force Diagrams

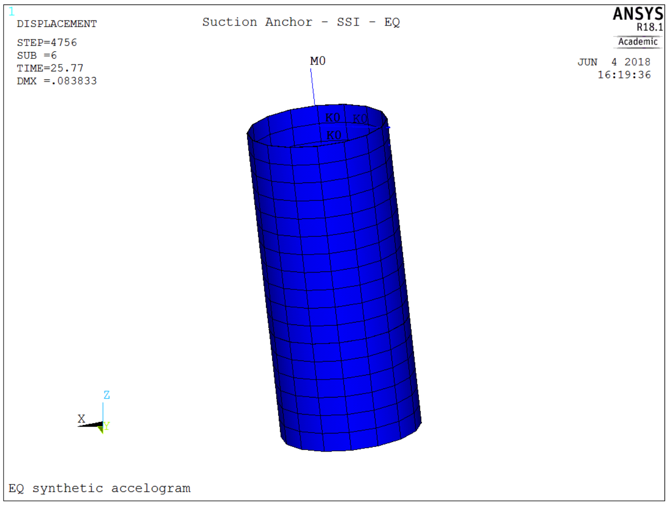
DISPLACEMENT
Suction Anchor - SSI - EQ
ANSYS
R18.1
Academic
STEP=4756
SUB =6
TIME=25.77
DMX =.083833
JUN 4 2018
16:19:36
M0
X
Z
Y
EQ synthetic accelogram

(a) Deformed beam with visual shell at 23.77 sec.

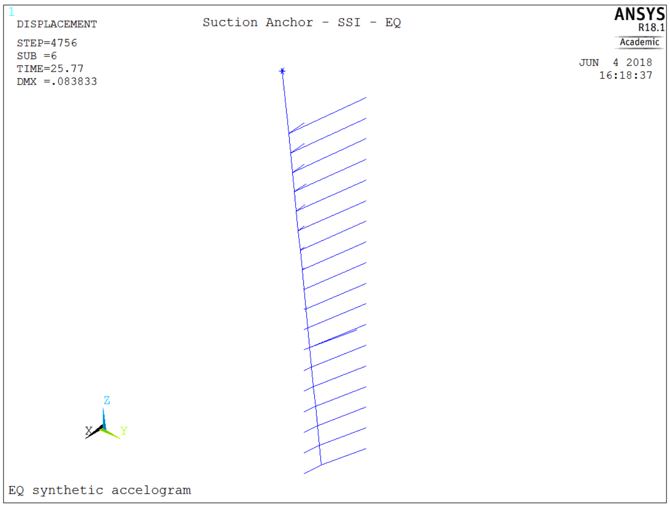
DISPLACEMENT
Suction Anchor - SSI - EQ
ANSYS
R18.1
Academic
STEP=4756
SUB =6
TIME=25.77
DMX =.083833
JUN 4 2018
16:18:37
X
Z
Y
EQ synthetic accelogram

(b) Deformed beam and springs at 23.77 sec.

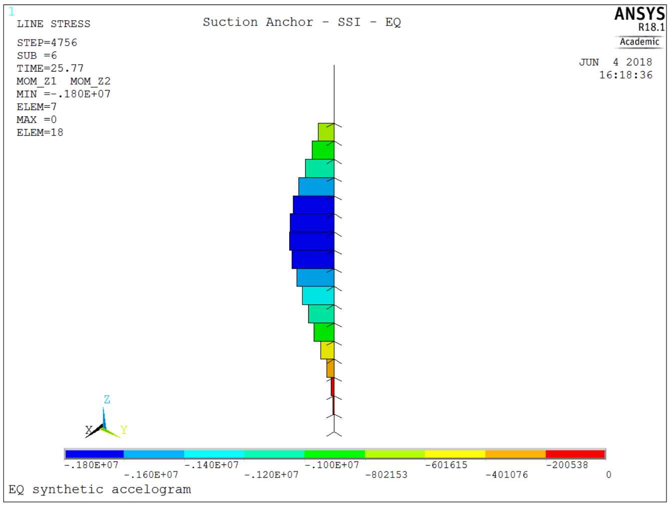

(a) Moment diagram at 23.77 sec.

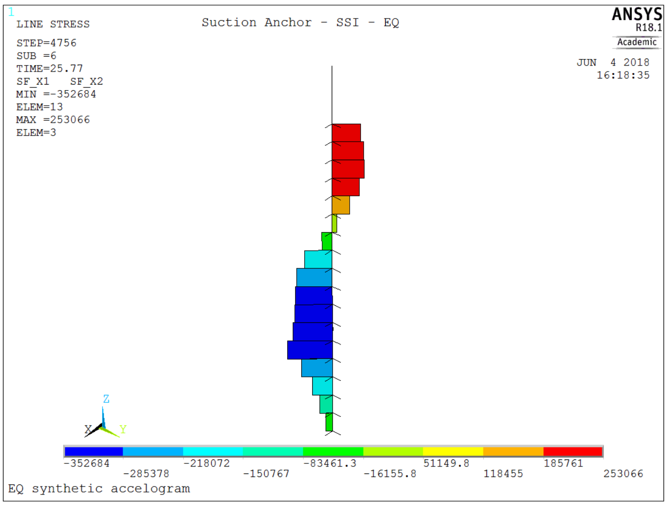

(b) Shear force diagram at 23.77 sec.

D.5 Hysteresis Plot

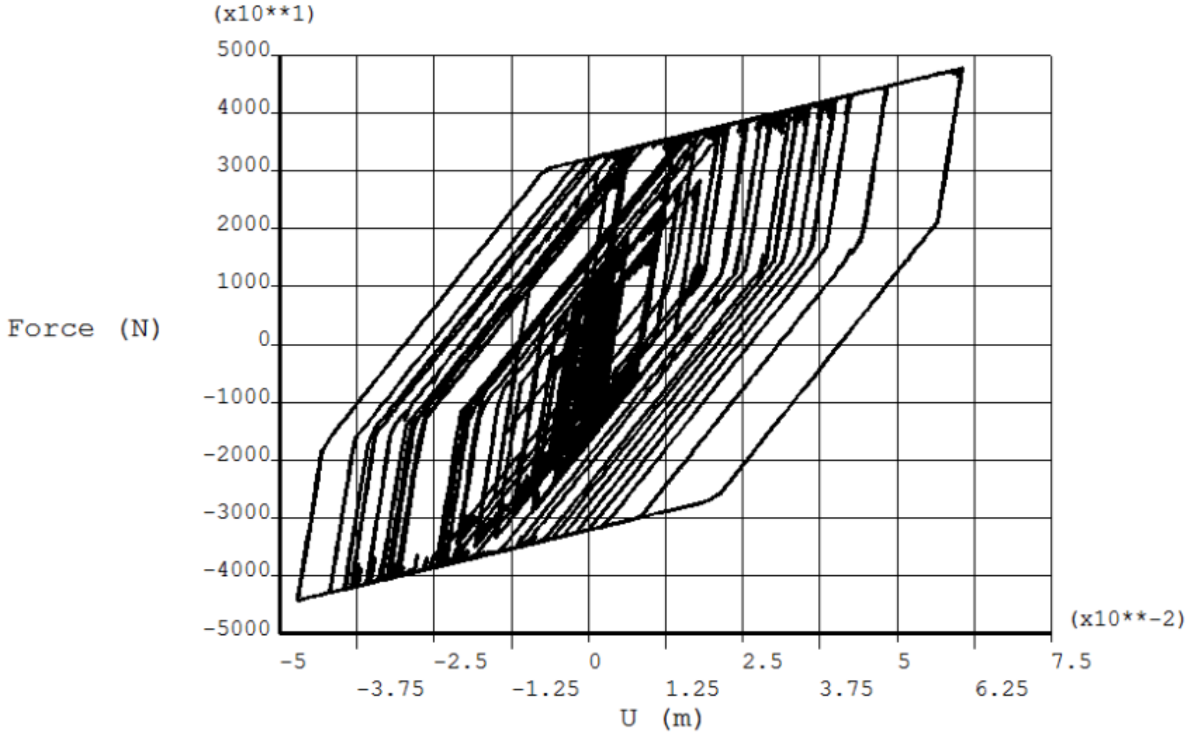

Figure D.82: Force-displacement in soil spring at seabed level during EQ 1A.